

Links with Variable Stiffness and Their Applications in Robotics

by Freddy Santiago Caro Diaz

Thesis submitted in fulfilment of the requirements for
the degree of

Doctor of Philosophy

under the supervision of Dr Marc Gary Carmichael

University of Technology Sydney
Faculty of Engineering and Information Technology

July 2024

Certificate of Original Authorship

I, **Freddy Santiago Caro Diaz**, declare that this thesis is submitted in fulfilment of the requirements for the award of **Doctor of Philosophy**, in the **School of Mechanical and Mechatronic Engineering** at the University of Technology Sydney.

This thesis is wholly my own work unless otherwise referenced or acknowledged. In addition, I certify that all information sources and literature used are indicated in the thesis.

This document has not been submitted for qualifications at any other academic institution.

This research is supported by the Australian Government Research Training Program.

Signature:

Production Note:
Signature removed prior to publication.

Date: 01-07-2024

Links with Variable Stiffness and Their Applications in Robotics

by

Freddy Santiago Caro Diaz

A thesis submitted in fulfilment of the requirements for the
degree of Doctor of Philosophy

Abstract

Robots that are able to change the stiffness of their members have become a new paradigm in robotics and have captured the attention of a big part of the research community in robotics. This paradigm considers that structural members of a robot should vary their stiffness in order to perform tasks that require different states of flexibility or rigidity. This research focuses on a method to change the stiffness known as Laminar Jamming (LJ). It has a significant potential to achieve high stiffness variation and its manufacturing is based on traditional machining processes. A new mechanism to vary the stiffness of LJ structures has been proposed. It consists of a pneumatic actuator that drives a trapezoidal pin to mechanically interfere with the layers, changing the stiffness of the LJ structure. Then, applications of Laminar Jamming in robot arms were studied. Firstly, a variable stiffness link (VSL) for robot arms was developed based on LJ structures with the trapezoidal pin mechanism. The capacity of this VSL to attenuate impacts in human-robot interactions was investigated. Secondly, the developed VSL was used to build a VSL robot arm with two degrees of freedom whose stiffness in multiple directions and poses was measured and represented through the concept of the Stiffness Envelope that explains how each VSL contributes to the stiffness of the robot arm and how this distribution of stiffness can be used to carry out a specific task. The proposed VSL robot arm was also tested to determine its destiffening time. Experiments and simulations have shown that the LJ structures with trapezoidal pin mechanism reached a maximum stiffness ratio of 3.65, which is 15% higher than the stiffness ratio of an equivalent laminar jamming with flat clamps. The VSL based on the trapezoidal pin mechanism also demonstrated its capacity to reduce the impact

force by 12% during a collision against a human being. In addition, the proposed VSL robot arm demonstrated its capacity to reduce its stiffness from a rigid state to a flexible state in approximately 173 ms, showing that the destiffening time of the proposed VSL robot arm could be short enough to be effective in the mitigation of the damage to a human being due to the impact against a cobot. The methodologies applied in this research include bending tests, torsion tests, impact tests, stiffness tests, and Finite element Simulations.

Acknowledgements

Firstly, I would like to thank and acknowledge my supervisor, Dr Marc Carmichael, for his guidance throughout my PhD. Always happy to answer questions and give great insights into the subject matter. His prompt and concise feedback was highly appreciated at all stages of the project. Marc was always ready to help at a moment's notice, and being able to simply drop into his office at any time has been incredibly helpful over the last six years. His efforts to make available the necessary technical resources are highly appreciated. I also would like to thank Professor JC Ji for accepting to be my co-supervisor during the last two years of my PhD and for his advice about publications and administrative matters. I also want to acknowledge Glenn Johnson, who is the professional editor who proofread this thesis.

This thesis represents the culmination of the six years of work in my PhD program. My academic stay in this program has been possible thanks to the support of the Australian Government Research Training Program Scholarship.

Last but not least, thanks to my parents Teresa and Efrain, sisters Ximena and Adriana, my niece Laura, my nephew Juan Jose, my brother-in-law Juan Carlos, and friends and family for your unending support. It has been a challenging time, particularly during the COVID 19 pandemic, you have helped me through the best and worst, and this thesis is dedicated to you.

Contents

Declaration of Authorship	iii
Abstract	v
Acknowledgements	vii
Contents	ix
List of Tables	xix
Nomenclature	xxiii
Glossary of Terms	xxv
1 Introduction	1
1.1 Methods of Varying Stiffness in Robotics	2
1.1.1 Variation of Material or Structural Properties	2
1.1.2 Variation of stiffness as a form of Variable impedance	2
1.1.3 Robot Arms with Elastic Links	4
1.2 Reduction of Impact in Human-Robot Interaction	5
1.3 Research Question	7
1.4 Problem Scope	8
1.5 Contributions	9
1.6 Publications	10
1.7 Thesis Outline	10
2 Literature Review	13
2.1 Methods to Vary Stiffness in Soft Robotics and Flexible Medical Devices	13
2.2 Selection of LJ as Method to Vary the Stiffness	16
2.3 Working Principle of LJ	16
2.4 Lock/Unlock Mechanisms	18
2.4.1 Mechanisms Based on Friction Force	19
2.4.1.1 Vacuum Pressure	19
2.4.1.2 Electrostatic Force	19

2.4.1.3	LJS Wrapped by Shape Memory Alloy (SMA)	19
2.4.1.4	Discrete Laminar Jamming (DLJ)	21
2.4.1.5	Mesh Sheath	21
2.4.2	Mechanisms Based on Mechanical Interference	22
2.4.3	Mechanisms Based on Miscellaneous Principles	23
2.4.3.1	LJ with Heating Blankets	23
2.4.3.2	Sliding-Layer Laminates (SLL)	24
2.5	Analysis of Performance of LJ Mechanisms	24
2.5.1	Speed of Stiffening and Destiffening	25
2.5.2	Stiffness Variation and Stiffness Range	28
2.6	Limitations of Lock/Unlock Mechanisms	30
2.7	Application of LJ in Robot Arms	32
2.8	Summary of Literature Review and Research Gap	34
3	Trapezoidal Pin Mechanism	37
3.1	Motivation for a new Lock/Unlock Mechanism for LJSs	37
3.2	Preliminary Exploration of Lock/Unlock Mechanisms	38
3.2.1	Application of Normal Force	39
3.2.2	Mechanical Interference	40
3.2.3	Conical Pin	41
3.2.4	Effect of Frames	43
3.3	LJ with Conical Pin Mechanism and Metallic Sheets	43
3.3.1	Manufacturing of the LJS with Conical Pin	45
3.3.2	Experiment Setup	47
3.3.3	Experimental Procedure	47
3.3.4	Results of Experiments	48
3.3.5	Discussion of Experimental Results	50
3.3.6	Finite Element Simulation of the Conical Pin	50
3.3.7	Experiments Versus Simulations	52
3.3.7.1	Coefficient of Friction	52
3.4	Trapezoidal Pin Mechanism	54
3.4.1	Description of the Components of the LJS with a Trapezoidal Pin	56
3.4.2	Manufacturing	58
3.5	Experiment Setup	59
3.5.1	Experimental Procedure	61
3.5.2	Results of Experiments	62
3.5.3	Discussion	63
3.6	Modelling of the Trapezoidal Pin Mechanism	66
3.6.1	Modelling of LJ Mechanisms	66
3.6.2	FE Simulation of the Trapezoidal Pin and Flat Clamp	67
3.6.3	Experiments Versus Simulations	72
3.7	Computational Studies	73
3.7.1	Effect of the Angle of the Trapezoidal Pin	74
3.7.2	Effect of Frames on the LJS	78

3.7.3	Bending of the LJS when transverse force points downwards	82
3.7.4	Large Deflections	85
3.8	Conclusions	89
4	Variable Stiffness Link	93
4.1	Motivation for the Design of a New VSL	93
4.1.1	Attaching adjacent links without locking the layers	94
4.1.2	Supporting Multiple Load Conditions	96
4.1.3	Avoiding Protrusions	98
4.2	VSL Concept A	98
4.2.1	Experiment Setup	103
4.2.2	Experiment Procedure	104
4.2.3	Finite Element Simulation of VSL Concept A	105
4.3	VSL Concept B	110
4.3.1	Bending Experiment	111
4.4	VSL Concept C	113
4.4.1	Bending Experiment	116
4.5	Torsional Stiffness of VSL Concept C	118
4.6	Manufacturing of VSLs	121
4.7	Summary of VSL Design Concepts	123
4.8	Conclusions	125
5	Application of VSLs to Mitigate Impacts	127
5.1	Impacts Between Robot Arms with VSLs and Human Beings	127
5.2	Impact Experiment	130
5.2.1	Experimental Procedure	133
5.2.2	Results of Experiments	135
5.3	Discussion	136
5.4	Conclusions	138
6	Robot arm with Variable Stiffness Links	139
6.1	Review of VSL Robot Arms	140
6.2	Stiffness Experiment on the VSL Robot Arm	141
6.2.1	Experimental Setup	141
6.2.2	Experimental Procedure	143
6.2.3	Results of the Experiment	145
6.2.4	Discussion	147
6.2.5	Use of the Stiffness Envelope in the Execution of a Task	149
6.3	Destiffening Time Experiment for the VSL Robot Arm	151
6.3.1	Experimental Setup	151
6.3.2	Experimental Procedure	153
6.3.3	Results of the Experiment	155
6.3.4	Discussion	158
6.3.5	Additional Measures to Reduce the Destiffening Time of the VSL Robot Arm	160

6.4	Conclusions	161
7	Conclusions	163
7.1	Summary of Contributions	164
7.1.1	Creation of the Trapezoidal Pin Mechanism	164
7.1.2	Design of a Variable Stiffness Link	166
7.1.3	Experimental Quantification of Impact Reduction of a VSL	167
7.1.4	Formulation and Use of the Stiffness Envelope to Analyse and Modulate the Robot Arm Stiffness	167
7.1.5	Estimation of the Destiffening Time of a VSL Robot Arm	168
7.2	Discussion and Limitations	169
7.2.1	Multiple Load Conditions Applied in VSL Robot Arms	169
7.2.2	VSL Actuators	169
7.2.3	Manufacturing of the LJS	170
7.3	Future Directions and Recommendations	171
7.3.1	VSLs for Multiple Load Conditions	171
7.3.2	Active Compliance	173
7.3.3	Improvement of Existing Lock/Unlock Mechanisms	173
7.3.4	New Lock/Unlock Mechanisms	174
7.3.5	Control of Robot Arms Composed of LJSs	175
7.3.6	Recommendations	176
	Appendices	178
A	Airstroke Actuator	179
B	Solenoid Valve	181
C	EVA Test	183
	Bibliography	187

List of Figures

1.1	MACCEPA Prototype. Image taken from [1].	3
1.2	a) The mechatronic joint design of the DLR-LWR-III, Including actuation, electronics, and sensing. b) Representation of the compliance-controlled robot as a connection of passive blocks. Image taken from [2].	4
1.3	Robot TUDOR. Images taken from [3, 4]	5
1.4	Impact test carried out with VSA and LWR robotic arms. Images taken from the video. https://www.youtube.com/watch?v=R5Gx8jpwYQ0	7
2.1	Technologies to vary the stiffness in robotics. Figure taken from [5].	15
2.2	Stiffness states of the LJS: a) side view of rigid state. b) cross-section of the LJS in the rigid state. c) Side view of the LJS in the flexible state. d) Cross-section of the LJS in the flexible state. Image adapted from [6].	17
2.3	Lock/unlock mechanisms activated by friction. (a) LJS based on vacuum pressure [7]. (b) LJS activated by electrostatic force [8]. (c) LJS activated by SMA wires [6]. (d) Discrete laminar jamming (DLJ), Figure adapted from [9]. (e) Mesh sheath, Figure adapted from [10].	20
2.4	LJ with mechanical interference. (a) LJS at high stiffness state (the black areas depict the teeth that generate the mechanical interference between layers), Figure adapted from [11]. (b) LJS at low stiffness state, Figure adapted from [11].	22
2.5	LJS with heating blanket mechanisms. (a) Components of the LJS [12]. (b) Experimental setup [12].	23
2.6	SLL. (a) Minimum and maximum stiffness state, Figure adapted from [13]. (b) Intermediate stiffness states [14].	24
2.7	Comparison of stiffness ranges for some of the fundamental lock/unlock mechanisms of LJ.	30
2.8	(a) LJ link for a robotic arm [15]. (b) Details of the parts of the VSL when it is loaded [16].	32
2.9	(a) Design of a wrist with two parallel guided beams formed by LJSs. (b) Implementation of the wrist in a robot arm [17].	33
2.10	VSL that combines airtight chamber, shape morphing, and LJ. (a) Overall view, figure adapted from [18]. (b) Cross-section view when the VSL is depressurised, figure adapted from [18]. (c) VSL cross-section when the VSL is pressurised, Figure adapted from [18].	33
3.1	LJS with solenoid applying normal force against the layers.	39
3.2	LJS with cylindrical pin mechanism.	40

3.3	Tests with cylindrical pin mechanism. a) LJS in a rigid state. b) LJS in its flexible state.	41
3.4	Tests with conical pin mechanism. a) external load is not applied to the LJS b) external load is applied to the LJS.	42
3.5	Buckling of some sheets of the LJS between 2 frames.	43
3.6	LJS with conical pin mechanism and metallic sheets.	44
3.7	a) Longitudinal section of the mechanism when the conical pin is disengaged from the LJS b) Longitudinal section of the mechanism when the pin is engaged in the LJS.	45
3.8	Burrs on the metal sheets due to laser cutting process.	46
3.9	Deflection of the layers due to the rolling shape of the raw material.	46
3.10	Experimental Set up	47
3.11	Results of the experiments at 0 bar	49
3.12	Results of the Experiments	49
3.13	Resulting shape of LJS at 7 bar and COF 0.32 from FE simulation	51
3.14	Force-Deflection curves for 7 bar pressure and COF 0.32 from FEM simulation and Experiment	52
3.15	Comparison of stiffness from experiments and simulations with different COF between the layers	53
3.16	LJS with trapezoidal pin mechanism.	55
3.17	Front and right side view a) Trapezoidal pin b) Flat clamp. The other components of the proposed mechanism are hidden in this figure. All dimensions in mm.	56
3.18	Zig-Zag and step patterns that may occur if layers are machined separately.	58
3.19	Manufacturing of the trapezoidal slots.	59
3.20	Experimental Set up.	61
3.21	Results of the experiments, a) LJS with trapezoidal pin at 50 kPa. b) LJS with trapezoidal pin. c) LJS with flat clamp.	62
3.22	Results of the experiments and linearisation when LJS with trapezoidal pin is at 50 kPa.	63
3.23	Resulting shape of LJS with trapezoidal pin mechanism at 800 kPa from FE simulation a)Perspective view of one half of the LJS. b) Side view of the LJS.	68
3.24	FE simulation of LJS at 600 kPa and 40 mm of deflection at the free end. a) contact between layers and trapezoidal pin. b) Detail view of the contact zone. c) Detail view of the no-contact zone in the rear of the pin. The support of the pneumatic cylinder is hidden in this figure.	69
3.25	Von-Mises stress in the sheets of the LJS with trapezoidal pin at 800 KPa and 40mm of deflection. a) side view of LJS. b) Detail of the location of maximum stress. The other components of the trapezoidal pin mechanism are hidden.	71
3.26	Force-deflection curves for 50 kPa of pressure from FE simulation and experiment in the LJS with trapezoidal pin.	72
3.27	Comparison of stiffness from experiments and FE simulations.	73
3.28	Trapezoidal pins with different angles. a) 30° Trapezoidal pin b) 45° Trapezoidal pin c) 75° Trapezoidal pin d) Straight pin. All dimensions are in mm.	74
3.29	Position of frames for the LJS investigated through FE simulations.	75

3.30	LJS with straight pin. a) Straight pin inside the LJS. b) Longitudinal cross-section of the LJS with straight pin.	76
3.31	Stiffness of the LJS as a function of air pressure for multiple angles of the trapezoidal pin.	78
3.32	Distribution of the frames along the LJS with trapezoidal pin a) 1 frame. b) 3 frames. c) 6 frames. d) 13 frames.	79
3.33	Comparison of stiffness range of the LJS for different numbers of frames.	80
3.34	Stiffness ratio in function of the number of frames.	81
3.35	Deflection in Y axis in the LJS with no frames.	81
3.36	Resulting shape of LJS with trapezoidal pin when is bent upward	82
3.37	a) Contact between the trapezoidal pin and the layers when LJS is bent upward. b) Detail view of the contact zone. c) Detail view of the no-contact zone in the front of the pin. The support of the pneumatic cylinder is hidden in this figure.	83
3.38	LJS bent upwards. a) Overall Side view. b) Detail of the contact between the trapezoidal pin and the layers.	84
3.39	Results of the FE simulation for LJS when is bent upward and downward.	85
3.40	LJS with trapezoidal pin under 100mm deflection at the free end.	86
3.41	Results of the Simulations of LJS under 100 mm deflection at the free end.	86
3.42	Detail of the pin section a) LJS with no transverse load b) LJS when deflection is 100 mm at the free end. The pressure in the pneumatic cylinder is 500 kPa in both cases.	87
3.43	Detail of contact between the pin and the layers when deflection is 100 mm at the free end.	88
3.44	Von-Mises stress in the sheets of the LJS with trapezoidal pin at 500 KPa and 100 mm of deflection at the free end. a) side view of LJS. b) Detail of the location of maximum stress. The other components of the trapezoidal pin mechanism are hidden	89
4.1	Constraint of the slip between the layers in a LJS. a) bolt joint in the proximal end. b) bolt joint at both ends.	95
4.2	Use of only one layer to attach a distal joint.	95
4.3	Interlocking LJS. Figure taken from [19].	96
4.4	Single beam and parallel guided beam a) under transverse vertical force. b) under torsion about the longitudinal axis. Figure taken from [20]	97
4.5	VSL Concept A. a) Components. b,c) Detail of the Airstroke actuators in the VSL. d) Diagram of minimum and maximum stroke of the Airstroke actuator (50-P-10).	99
4.6	Airstroke actuator a) depressurized state b) pressurized state.	101
4.7	a) Transverse force applied to interlocking LJS without frames and Airstroke support. b) Axial force applied to the interlocking LJS with frames and Airstroke support.	102
4.8	Location of frames in the interlocking LJS of VSL Concept A.	102
4.9	Experimental setup of bending test. a) components of the experimental setup. b) Deformation of VSL Concept A due to lateral deflection imposed by the load frame.	103
4.10	Results of the force-deflection experiment for VSL Concept A at 0 kPa.	104

4.11	Results of the force-deflection experiment for all values of pressure in the Airstroke actuators.	105
4.12	CAD model of the Airstroke a) general view of CAD model. b) cross sections of CAD model. c) real sample of an Airstroke actuator.	106
4.13	Mesh of the FE model of VSL Concept A.	106
4.14	Loads and boundary conditions imposed on the FE model of VSL Concept A . .	107
4.15	Resulting shape of the VSL at 69 kPa from the FE simulation when deflection of the free end is 24 mm.	107
4.16	Comparison of stiffness from experiments and FE simulations, VSL Concept A at 69 kPa.	108
4.17	Comparison of bending stiffness from experiments and FE simulations.	109
4.18	VSL Concept B. a) components. b) Detail of the actuator and the trapezoidal pin (support of pneumatic cylinder is hidden).	111
4.19	Experimental setup for measuring the bending stiffness of VSL Concept B. . . .	112
4.20	Results of the force-deflection experiment for VSL Concept B.	113
4.21	VSL Concept C. a) design of the whole link. b) Components of each LJS.	114
4.22	Bottom layer of one of the LJSs in VSL Concept C.	115
4.23	Components of the mechanism to vary the stiffness in VSL Concept C.	116
4.24	Experimental setup for measuring the bending stiffness of the VSL Concept C . .	117
4.25	Results of the force-deflection experiment for VSL Concept C.	118
4.26	Experimental setup of the torsion experiment.	119
4.27	Torsion experiment of the single beam VSL	120
4.28	Torsional Stiffness for Parallel guided Beam link and single link at 0 kPa and 345 kPa.	121
4.29	Assembly of the fixture to cut the trapezoidal slot in the LJS that formed VSL Concept C.	122
4.30	Tearing defect in the layers of the VSL Concept C generated during the machining of the trapezoidal slots	123
5.1	Types of test bench for impact between VSLs and human beings. a) Motorised design with VSL driven by an electric motor (1 is the motor, 3 is the VSL, and 6 to 10 are the components of the dummy head system). b) Pendular design with VSL driven by gravity.	129
5.2	Assembly of VSL Concept B, PLA support, and inertia plates	131
5.3	Assembly of VSL Concept B and inertia plates	132
5.4	Modification of the VSL for its application in the impact test.	133
5.5	Modification of VSL Concept B to make it completely rigid.	135
5.6	Data collected from the force sensor during one of the impact experiments at collision velocity $v=2.2$ m/s and 600 kPa of pressure in the pneumatic cylinders. a) Multiple peaks were registered during the collision. b) First force peak used to calculate the impact force.	136
5.7	Results of impact experiment.	136
6.1	Robot arm with VSLs. a) Components of the robot arm. b) Detail of joint 2. . .	142
6.2	Experimental setup to measure the stiffness of the VSL robot arm	143

6.3	Stiffness experiment layout for $\theta_2=135^\circ$	144
6.4	Data from the force sensor for one of the stiffness tests at $\theta_2=135^\circ$, L1 345 kPa, L2 345 kPa, and 45° for the direction of the displacement.	145
6.5	Results of stiffness experiment when $\theta_2=135^\circ$. The pressure in Link 1 is 345 kPa, and the pressure in Link 2 is 345 kPa.	146
6.6	Results of stiffness experiment for all poses of the 2-DoF robot arm and all states of stiffness.	147
6.7	Stiffness envelopes at $\theta_2=135^\circ$	148
6.8	Stiffness envelopes at $\theta_2=90^\circ$	149
6.9	Use of stiffness envelope when the VSL robot arm executes a task.	150
6.10	Experimental setup of the destiffening time experiment for the VSL robot arm.	152
6.11	Detail of the impact area between the VSL robot arm the UR3 robot arm.	152
6.12	Layout of the destiffening experiment during a collision. a) Positions of the UR3 robot arm in experiment 1. b) Positions of the UR3 robot arm in experiment 2. X-Y is the base coordinate system of the UR3.	154
6.13	Data collected from the force sensor during one of the experiments at impact velocity $v=0.84$ m/s and deactivation angle equal to -39° (-0.055 s). a) Multiple force peaks were registered during the collision. b) First force peak used to calculate the maximum impact force (MIF).	156
6.14	Results of the destiffening time experiment at impact velocity $v=0.58$ m/s. a) including the switching time of the solenoid valve. b) without including the switching time of the solenoid valve.	157
6.15	Results of the destiffening time experiment at impact velocity $v=0.84$ m/s. a) including the switching time of the solenoid valve. b) without including the switching time of the solenoid valve.	158
A.1	Airstroke actuator	179
B.1	Solenoid Valve	181
C.1	Compression test of EVA Foam	184
C.2	Sample of EVA Foam for tension test	184
C.3	Tension test results of EVA foam	185

List of Tables

- 2.1 Classification of Variable Stiffness Technologies, table adapted from [21] 14
- 2.2 Performance of the fundamental lock/unlock mechanisms of LJ, and some combinations between them (qualitative evaluation scale: ++, +, -, - - from the highest to the lowest values). 26
- 3.1 Stiffness for each state of air pressure in the pneumatic cylinder 49
- 3.2 Experimental Specifications 60
- 3.3 Bending stiffness for each state of air pressure from the experiments. (units in N/mm) 64
- 3.4 Most Relevant settings of the FE simulations in Ansys 70
- 4.1 Error from the simulations results relative to experimental results in the VSL Concept A 109
- 4.2 Results of the torsion experiment 120
- 4.3 Summary of VSL concepts 124
- 5.1 Parameters of impact test bench and impact experiment 132
- 6.1 Parameter of destiffening time experiments 155

Acronyms & Abbreviations

LWR	Lightweight robot
DLR	German Aerospace Center
SEA	Series Elastic Actuator
VSA	Variable Stiffness Actuation
LJ	Laminar Jamming
LJS	Laminar Jamming Structure
VSJ	Variable Stiffness Joints
VSL	Variable Stiffness Link
HIC	Head Impact Criterion
SMA	Shape Memory Alloy
DLJ	Discrete Laminar Jamming
SLL	Sliding-layer Laminates
ABS	Acrylonitrile Butadiene Styrene
PLA	Polylactic Acid
FS	Full Scale
FE	Finite Element
FEA	Finite Element Analysis

COF	Coefficient of Friction
EVA	Ethylene-Vinyl Acetate
DoF	Degrees of freedom
UR	Universal Robots
MIF	Maximum Impact Force

Nomenclature

General Notations

N	Number of layers
I	Area moment of inertia
E	Young's modulus
L	Beam Length
k	Stiffness
A	Cross section area
h	Thickness of the layer
w	Width

Glossary of Terms

Stiffness ratio	Measurement to evaluate the capacity of a technology or structure to change its stiffness. It is defined as the maximum stiffness divided by the minimum stiffness or the stiffness in a given state divided by the minimum stiffness. The term “stiffness variation” has the same meaning as stiffness ratio, and it was also used in this thesis.
Destiffening speed	Time to transition from a high to a low stiffness. It usually means the time to transition from maximum stiffness to minimum stiffness.
Stiffening speed	Time to transition from a low stiffness state to a high stiffness state. It usually means the time to transition from minimum stiffness to maximum stiffness.
Lock/unlock mechanism	The mechanism to vary the stiffness of a Laminar Jamming structure. The change could be between discrete states or a continuum value within a stiffness range.
VSL	This refers to robotic links that can change their stiffness.
Large Deflection	In the context of a beam under bending, it is a deflection that is higher than 10% of the length of the beam.

Chapter 1

Introduction

Machines that are able to change the stiffness of their components have emerged during the last twenty years to meet a number of needs, namely:

- for compliance during interaction with human beings;
- to be able to control position and stiffness independently;
- to be adaptable to changing operating conditions; and
- to solve traditional problems in machinery such as control of vibrations or working in confined spaces.

During recent decades, many research fields have studied methods to change the stiffness, among them are soft robotics [5], morphing aero-structures [22], medical devices [21], and compliant actuators [23].

One of the characteristics of traditional mechanical design has been the design of structural elements with constant and high stiffness in order to withstand high loads with minimum deformation. However, this type of object also has limitations in being able to accomplish other desirable functions such as being adaptable to variable operating conditions or to be able to grasp objects with irregular shapes. On the other hand, structures with low stiffness could perform properly in those functions where rigid components are not useful, but they do not have

the capacity to support high loads without yielding or presenting significant deformation. Variable stiffness has emerged as a promising approach to solve this duality between high and low stiffness: having a structural element that can change its stiffness accordingly with the situation will make it possible to take advantage of both conditions.

1.1 Methods of Varying Stiffness in Robotics

This section presents an overview of the strategies to change the stiffness of robotic elements, particularly in robot arms. The advantages and limitations of these methods are described to explain the motivation for this research.

Robotics engineering has developed multiple solutions for the problem of the duality between low and high stiffness. The classification that is presented in this section is based on the essence of the solution in terms of the principles that are applied to change the stiffness. The specific technologies to change stiffness in robotics will be extensively reviewed in Chapter 2.

1.1.1 Variation of Material or Structural Properties

The stiffness of a robot can be changed by varying the properties of the material and/or the relation between its structural components. Some of the technologies to achieve the change of stiffness through this method have been developed in the field of soft robotics. These technologies will be explained in Chapter 2.

1.1.2 Variation of stiffness as a form of Variable impedance

Mechanical impedance is a dynamic relation that generates a force as a function of displacement [24]. Variable impedance in robotics can involve the variation of the stiffness, damping, and inertia. Therefore, there are strategies to vary the stiffness that are part of a wider strategy to vary the impedance of a robot. There are multiple variable impedance strategies that involve variation in stiffness. Two of these strategies are described as follows.



FIGURE 1.1: MACCEPA Prototype. Image taken from [1].

- **Inherent Compliance:** This strategy consists in using an intrinsic or compliant element as part of the robot. This strategy can include springs, pulleys, levers, and cables, between the robot links. These elements can be configured in different ways, such as mechanical impedance adjusters or antagonistic-controlled stiffness mechanisms as described in [23]. A good example of this mechanical method to change stiffness is the MACCEPA design [1]. This design consists of a mechanism to adjust stiffness, the mechanism having compliant elements that are attached to the structure with attachment points that can be changed. As a consequence, there is a change in the pretension or preload of a spring that is attached to two links with a common joint, and this change is the variation of the compliance between these two links. The MACCEPA design has some advantages, such as completely independent control of compliance and equilibrium position. However, it also presents some disadvantages, such as the fact that friction in the joints depends on the setting of the compliance and the additional volume that is occupied by servomotors. Figure 1.1 illustrates the MACCEPA prototype.

Another strategy to achieve variable stiffness consists in having an elastic element, such as a spring, between the transmission output and the joint. This strategy is called a series elastic actuator (SEA). One particular sub-family of SEAs is called variable stiffness actuation (VSA) [25]; it consists of elastic elements that are integrated into the joints so that the motor is detached from the link by the elastic element. Consequently, compliance behaviour is attained by control and mechanical components. Multiple examples and variations of VSA technology are presented in [26–29]. The main advantages of this technology are the robustness of the mechanism to external impact, which allows the protection of sensors, gear transmission and motors; task adaptability at the mechanical level; and increased

dynamic performance and energy efficiency since the capability to store mechanical energy can be utilised to overcome motor velocity limitations [27].

- **Active Impedance by control:** This strategy consists of actuators that imitate the impedance behaviour using software control. Based on the measured output state, a correction is calculated by the controller and set by the actuator [24]. One representative example of this strategy is the torque-controlled lightweight robot (LWR) technology developed by the German Aerospace Center (DLR). The joints in LWR robots have mechanical compliance generated mainly by the torque sensors and the gearboxes, getting stiffness values about 10000-20000 Nm/rad [2]. Figure 1.2 illustrates the components of the LWR joint as well as the torque control system. The torque acting on the robot is measured by sensors, and a control loop is implemented to achieve compliance. The limitation of this technology is that software compliance is limited by sensor bandwidth and precision, motor dynamics, and model inaccuracy [27].

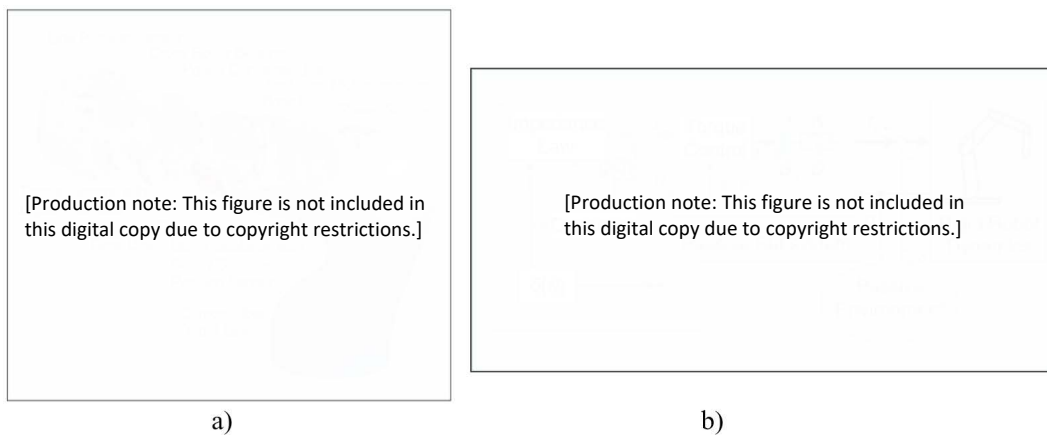


FIGURE 1.2: a) The mechatronic joint design of the DLR-LWR-III, Including actuation, electronics, and sensing. b) Representation of the compliance-controlled robot as a connection of passive blocks. Image taken from [2].

1.1.3 Robot Arms with Elastic Links

Robot arms with elastic links are a new strategy to provide compliance that has been investigated over the last 15 years. The increased elasticity of the links does not come from the choice of materials since these robots are made of the same hard materials used in industrial rigid robots, such as aluminium or steel. Instead, the elasticity of the links is achieved by the small dimensions

of their cross-sections. One of the most representative examples of robots with elastic links is the 3-DoF flexible link robot arm TUDOR (Technische Universität Dortmund Omni-elastic Robot) [30] which is shown in Figure 1.3. The links in this robot are made of steel with a cross-section measuring 4 mm by 15 mm [4]. Robots with elastic links have advantages over rigid robots. The mass and inertia of robots with elastic links are significantly less than rigid robots. Consequently, this type of robot can be safer in the case of a collision between robots and human beings, and the energy consumption and torque requirements are lower as well [31]. There are also disadvantages, such as static deformations due to gravity, lower load capacity, and vibrations that prevent controlled motion of the end effector with good precision [30].

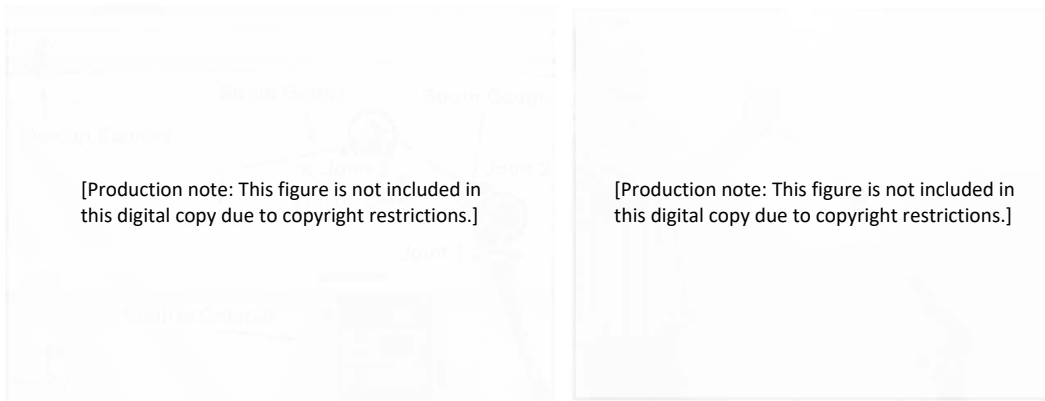


FIGURE 1.3: Robot TUDOR. Images taken from [3, 4]

It is important to note that most robot arms with elastic links do not have a mechanism to change their stiffness. They have been designed to be compliant, which is particularly useful in the case of collision because the energy of the impact is lower than in the case of rigid robot arms. Research on this technology focuses on mitigating the negative effects of such compliance through modelling and control. For instance, the static deformation due to gravity is taken into account to model or predict direct and inverse kinematics [30, 31], and vibration problems are addressed through control loops to reduce structural oscillations [4].

1.2 Reduction of Impact in Human-Robot Interaction

There has been a desire for humans and robot arms to work in the same space, but due to safety concerns, robot arms have been kept isolated in cages. Only in the relatively recent past,

collaborative robots that can work with humans have come to market. These robots are also known as cobots; they have been widely used in multiple applications where they share the same working space with human operators. These applications include surgical assistance [32], automotive industries [33], exoskeletons [34].

The use of cobots has raised a set of problems about how robots and humans interact. The problems related to safety between cobots and people are a major concern. Cobots should not injure human beings in normal operation, operational error, or mechanical failure [35]. One safety problem is the reduction of damage during an impact between a human being and a robot arm. This problem is critical because human beings could suffer serious or even fatal injuries if they received a rigid impact from a robot. In addition, the impact could cause serious damage to the mechanical adjustment of the robot.

Cobots with flexible structures could be a practical solution to reducing the damage during an impact with human beings. On the other hand, cobots have to be rigid to carry payloads and move with accuracy. These two conflicting requirements generate the necessity of implementing variable stiffness capabilities in cobots.

As mentioned previously, some technologies have been developed to reduce the damage of an impact during human-robot interactions with relative success. However, these technologies have considerable limitations and are not able to reduce the damage completely. This is the case of the VSA and the LWR technologies described in Section 1.1.2. In the case of rigid impact between a VSA robot and a human being at 2 m/s, the VSA technology is able to avoid damage to the robot components in the joints of the robot arm but there is no reduction in the impact force and thus the potential injury of a human being. The explanation for this effect is that rigid impacts are practically over before the stiffness variation system begins to work [2]. In terms of inertia, this means that link inertia is dominant in rigid and hard impacts. Figure 1.4 illustrates the type of impact test that is conducted in the German Aerospace Center (DLR), it uses robots with VSA or LWR technology and standard automobile crash-test facilities.

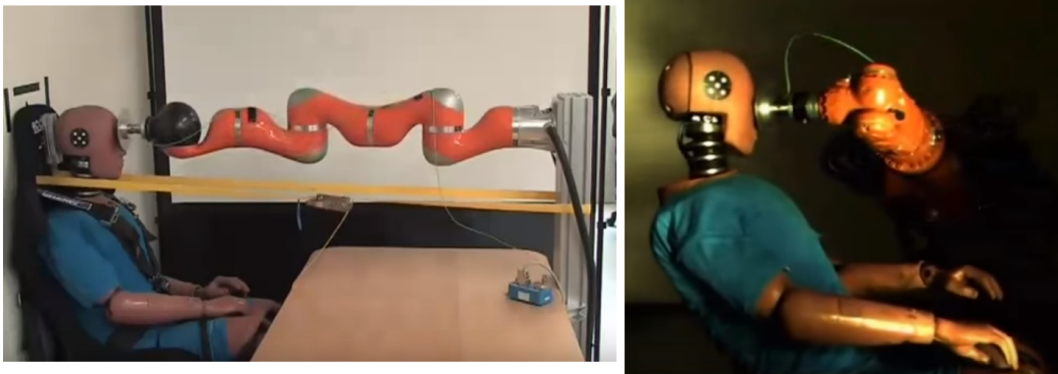


FIGURE 1.4: Impact test carried out with VSA and LWR robotic arms. Images taken from the video. <https://www.youtube.com/watch?v=R5Gx8jpwYQ0>

1.3 Research Question

Robots that can vary their stiffness fall between the rigid and elastic robot categories. In rigid robots, researchers have focused on providing compliance to rigid robots through the control of joints. In the area of elastic robots, the research has focused on mitigating their limitations through control, such as high amplitude vibrations and static deformation due to gravity. Comparatively, the capabilities of robots that can vary the stiffness of their members have not been widely explored. Therefore, this research aims to explore the implementation of variable stiffness in robot arms and their applications through the following questions.

- High-level question 1: How to create robot links with variable stiffness?

Solving this question implies solving the following question as well:

Lower level question 1: what will be their mechanical behaviour?

- High-level question 2: How to exploit the robot links with variable stiffness to improve the performance of a robot in human-robot interactions, particularly in the attenuation of impacts between robot arms and human beings?

Solving this question implies solving the following question as well:

Lower level question 2: What would be the performance of these robot links in attenuating impacts between robot arms and human beings?

1.4 Problem Scope

Multiple technologies to change stiffness in robotics have been identified. Among these technologies, laminar jamming (LJ) is selected for this research because of its high stiffness ratio and manufacturability through conventional methods. The existing mechanisms to vary the stiffness of a laminar jamming structure (LJS) have significant limitations. Particularly, there are difficulties in making the change of stiffness fast enough to be applied in reducing the impact between a human being and a robot arm. Therefore, one of the main problems explored in this thesis is developing and investigating a new mechanism to change the stiffness of laminar jamming structures (LJSs) that allows a rapid change of stiffness.

The second problem this thesis covers is the mechanical design of a variable stiffness link (VSL) that can be implemented in a robotic arm. This VSL must be based on the proposed mechanism to vary the stiffness of LJSs. This problem involves aspects not usually presented in generic LJSs, such as the capacity to be attached to other links, restrictions on maximum volume and proportions, and the capacity to vary the stiffness for bending while keeping an acceptable stiffness for axial and torsion loads.

Most of the VSLs proposed in the literature have been evaluated under quasi-static conditions to determine their stiffness range. Still, very few studies have been carried out to characterise the VSLs in terms of their capacity to attenuate impacts. Therefore, the third problem covered in this thesis is evaluating the performance of the proposed VSL in terms of its capacity to reduce the impact force during a collision against a human being.

There are very few studies in the literature about robot arms with VSLs; most research focuses on the mechanical behaviour of only one VSL. Therefore, the last problem covered in this thesis is the evaluation of the mechanical performance of a robot arm that incorporates the proposed VSL. The mechanical performance must be evaluated in two aspects. First, how the VSLs affect the stiffness of the whole arm, and second, how fast and effective is the response of the proposed VSL in reducing its stiffness and attenuating the impact force due to a collision.

The methodologies implemented to solve these problems include bending tests, impact tests, and finite element simulations. Conducting experiments involves arduous manufacturing work.

Therefore, finite element simulations were developed to investigate some design aspects of the proposed mechanism to vary the stiffness of the LJS and to evaluate the proposed VSLs.

The scope of this thesis is limited to the mechanical performance of the proposed LJ mechanism and the proposed VSLs. This thesis does not cover an extensive investigation of the materials that can be employed to build LJSs, the manufacturing process of LJSs, or the control techniques for the proposed VSLs or the proposed VSL robot arm. However, some exploration of LJSs made of metallic sheets is carried out, and the lessons from this exploration are documented to support future developments in this field. Similarly, some insights about the control of the proposed VSL robot arms are provided to contribute to future work in this area.

1.5 Contributions

The contributions of the thesis can be summarised in the following points:

- The creation of the trapezoidal pin mechanism, which is a new mechanism to vary the stiffness of LJSs, and demonstrating that it has better mechanical performance than flat clamps in terms of stiffness ratio and maximum stiffness. The proposed mechanism consists of a pneumatic actuator that drives a trapezoidal pin to mechanically interfere with the layers, changing the stiffness of the LJ structure.
- The creation of three designs of Variable Stiffness Links (VSLs) that are based on LJSs. The last VSL design incorporates ideas from the previous VSL designs such as the concept of the trapezoidal pin mechanism, frames distributed along the beam, and Airstroke actuators. This link is appropriate for its implementation in a VSL robot arm since it is slender, does not have protrusions, and avoids the axial separation of both parts of the link.
- Experimental quantification of the reduction of impact force during a collision of a VSL with trapezoidal pin mechanism against the head of a human operator. The experiments demonstrate that the reduction of impact force can reach 12% despite a stiffness ratio of 1.34.

- Formulation and use of the stiffness envelope to analyse and modulate the robot arm stiffness. The stiffness envelope is a method to visualise the stiffness of the proposed 2-DoF robot arm in different poses and multiple directions. The stiffness envelope allows us to visualise how the stiffness of the VSL robot arm is distributed between the links and how this distribution could be used in a particular task.
- Experimental estimation of the destiffening time of the proposed 2-DoF robot arm and its capacity to reduce the impact force within the period where the damage to human beings occurs due to a collision against a cobot. The experiment demonstrates that the destiffening process starts at about 38 ms and finishes at about 173 ms after a solenoid valve has switched. Considering that the damage to human beings due to collisions against robot arms takes place within 0.1 s, the proposed VSL robot arm can react fast enough to reduce the damage to a human being during an impact.

1.6 Publications

- Freddy Caro and Marc G. Carmichael. A review of mechanisms to vary the stiffness of laminar jamming structures and their applications in robotics. *Actuators*, 13(2), 2024. ISSN 2076-0825. doi: 10.3390/act13020064.
- Freddy Caro and Marc G. Carmichael. Laminar jamming with trapezoidal pin mechanism for variable stiffness robotic arms. In *2022 IEEE International Conference on Robotics and Biomimetics (ROBIO)*, pages 1061–1066, 2022. doi: 10.1109/ROBIO55434.2022.10011709.
- Freddy. Caro and Marc G. Carmichael. A novel multi-layer beam mechanism for variable stiffness robotic arms. *Australasian Conference on Robotics and Automation, ACRA*, 2021-December, 2021. ISSN 1448-2053.

1.7 Thesis Outline

The thesis is organised as follows.

Chapter 2

In Chapter 2, a review of the work is presented. The review focuses on three main areas. First, the technologies to vary the stiffness of robot structures. Second, the mechanisms to vary the stiffness of LJSs. Finally, the application of LJSs in robot arms and the use of VSLs to mitigate the effects of impacts between human beings and robot arms.

Chapter 3

Chapter 3 presents the trapezoidal pin mechanism, which is a mechanism to vary the stiffness of a laminar jamming structure. The bending stiffness of LJSs is evaluated through bending tests and finite element simulations. Computational case studies are carried out to investigate the effect of the number of frames, the angle of the trapezoidal pin, behaviour in both bending directions, and large deflections on the LJSs activated by the proposed mechanism.

Chapter 4

Chapter 4 discusses the challenges of designing VSLs based on LJSs and the solutions to these challenges. Three designs of VSLs based on LJSs are presented. These designs incorporate some of the elements of the trapezoidal pin mechanism presented in Chapter 3. The mechanical behaviour of the proposed designs is evaluated through bending tests and finite element simulations.

Chapter 5

Chapter 5 presents the application of a VSL with trapezoidal pin mechanisms to mitigate the effects of impacts between human operators and robotic arms. The capacity of the VSL is evaluated through an impact test that measures the impact force between the proposed VSL and a human head dummy.

Chapter 6

Chapter 6 investigates the stiffness of a two-degrees-of-freedom robot arm whose links are VSLs with trapezoidal pin mechanisms. The robot arm is built and used to carry out a stiffness test. The robot arm is placed in five different poses, and four stiffness states are studied in each pose. The result of the experiment is the stiffness envelope of the robot arm in each pose. The potential use of the stiffness envelope in the operation of robot arms is discussed. In addition, impact tests are carried out to measure the destiffening time of the proposed robot arm and its

capacity to effectively reduce the impact force within the period where human damage occurs due to the collision against a cobot.

Chapter 7

Chapter 7 outlines the conclusion of this research, its limitations, and the future work that could be done to advance the knowledge in this field.

Chapter 2

Literature Review

The work in this thesis covers a wide range of research areas, including methods to vary the stiffness in soft robotics, LJ, applications of LJ in robot arms, and attenuation of impact between human beings and robot arms. The following sections describe relevant research in these areas, the state of the art, and gaps in the literature that this thesis aims to improve upon.

2.1 Methods to Vary Stiffness in Soft Robotics and Flexible Medical Devices

Soft robotics technologies consist of a set of technologies to vary the stiffness of the robot structure through two strategies. The first strategy consists in changing the properties of the material, while the second strategy consists in changing the internal properties of the structure of the member. Research in this field gets inspiration from animals such as octopuses, elephants [5], and kangaroos [10]. The octopus can embrace objects with irregular shapes, and simultaneously stiffen sections of its arms to utilize them as a modifiable skeleton. Elephants can do the same with their trunk achieving the transmission of high loads. Therefore, a significant part of the applications in robotics looks at imitating the properties of these animals in the design of continuum robots, soft actuators, mobile robots, and robots that interact with humans.

The medical field investigates variable stiffness to develop instruments for Minimally-Invasive Surgery, such as endoscopes and colonoscopes. These type of tools requires low stiffness to be

TABLE 2.1: Classification of Variable Stiffness Technologies, table adapted from [21]

Classification			
General Properties	Cross Section Shaping		
	Structural Interactions	Multi-Layer Beam	Single Material Multiple Materials
Elastic Properties	Material	Phase Transition	Low Melting Point
			Low Melting Point Polymer
			Wax
			Solder
		Glass Transition	Shape Memory Alloy
			Shape Memory Polymer
			Shape Memory Gel
		Rheological Fluids	Magnetorheological
			Electrorheological
	Biomaterials		
	Structural Interactions	Bulk Locking	Granular Jamming
			Turgor Pressure
		Segment Locking	Central Wire
Multiple Wires			
Bellows Connections			
Soft Layer			
Longitudinal Locking		Layer Jamming	
	Wire Jamming		
Actuator-like Solutions	Fluid Based	Pneumatic Solution	
		Fluid Flexible Matrix Composite	
	Mechanical Solutions		
Muscle			

able to follow intricate paths without damaging organs or tissues. On the other hand, they also need high stiffness to transmit force during biopsies, punctures or grasping tasks [21]. Variable Stiffness technologies generate solutions for satisfying these opposing requirements.

Soft robotics covers a wide range of technologies, materials and control techniques. All of them serve the purpose of building robots with high compliance and deformability. There have been more than 20 technologies for soft robotics, some of these technologies are also applied to flexible medical devices.

The most common classification of soft robotics technologies is based on working principles [5, 21]. Table 2.1 shows the main technologies of controllable stiffness mechanisms in the areas of flexible medical devices and soft robotics according to [21]. It can be observed that this

classification includes up to 25 different technologies organised into three categories of working principles, namely: general properties, elastic properties, and actuator-like solutions.

It is important to note that Table 2.1 is not an exhaustive list of variable stiffness technologies because their classification among different authors could follow different criteria. In addition, variable stiffness has been a very active research field over the last 10 years. Therefore, new technologies appear frequently in this field, and some of them are very difficult to classify because they are a new combination of previous ideas or they are completely new ideas. For example, LJmechanisms have been combined with McKibben actuators to create a new type of variable stiffness actuator [36]. McKibben actuators are a type of pneumatic artificial muscle that were invented in the 1950s and are also widely used in soft robotics.



FIGURE 2.1: Technologies to vary the stiffness in robotics. Figure taken from [5].

A comparison of soft robotics technologies can be based on aspects of critical importance for the application. As is shown in Figure 2.1, these aspects include (among others) scalability, stiffness variation, and speed of stiffening and destiffening. The comparison shows that each technology

has significant advantages and disadvantages, making each technology suitable only for certain applications. Due to this balance between advantages and disadvantages, there is no dominant soft robotics technology at the moment according to [5].

2.2 Selection of LJ as Method to Vary the Stiffness

It is essential to note that the terms “laminar jamming structure” and “multi-layer beam” are equivalent in this document and refer to the same variable stiffness technology. However, before 2019, the term “laminar jamming” was more commonly used to designate devices activated by vacuum pressure. Nowadays, LJ covers multiple methods of actuation, and it is the most widely used term. In contrast, the term “multi-layer beam” is rarely used in the context of soft robotics.

LJ is a method of varying stiffness that has attracted the attention of the robotics community over the last 10 years. A compelling argument for choosing LJ over other variable stiffness methods is the large change in stiffness possible. There are LJ technologies that can achieve a stiffness variation of at least ten, as seen in Figure 2.1, which means that the maximum stiffness is ten times larger than the minimum stiffness. In addition, the speeds of stiffening and destiffening of some LJ technologies are high. Other technologies, such as low melting-point materials, have larger stiffness variation, but their speeds of stiffening or destiffening are low [5]. Some types of LJ also have the significant advantage of requiring traditional and simple manufacturing processes, such as machining or laser cutting, making them relatively easy to manufacture [6]. Additionally, it has been demonstrated that LJSs can be applied in various robotic fields such as grippers, continuum robots, wearable robots, robot arms and others [37].

2.3 Working Principle of LJ

The LJS consists of a beam that is made of thin sheets and a mechanism to lock/unlock the sheets. When the mechanism locks the sheets, the bending stiffness is high, and the whole beam behaves similarly to a rigid member, as can be seen in Figure 2.2a and Figure 2.2b. When the mechanism unlocks the sheets, they can slide between themselves, the bending stiffness is low, and the beam becomes flexible, as can be observed in Figure 2.2c and Figure 2.2d. In this state,

the layers are not coupled, and they are free to slip. This working principle is the same for all LJSs regardless of the lock/unlock mechanism utilised.

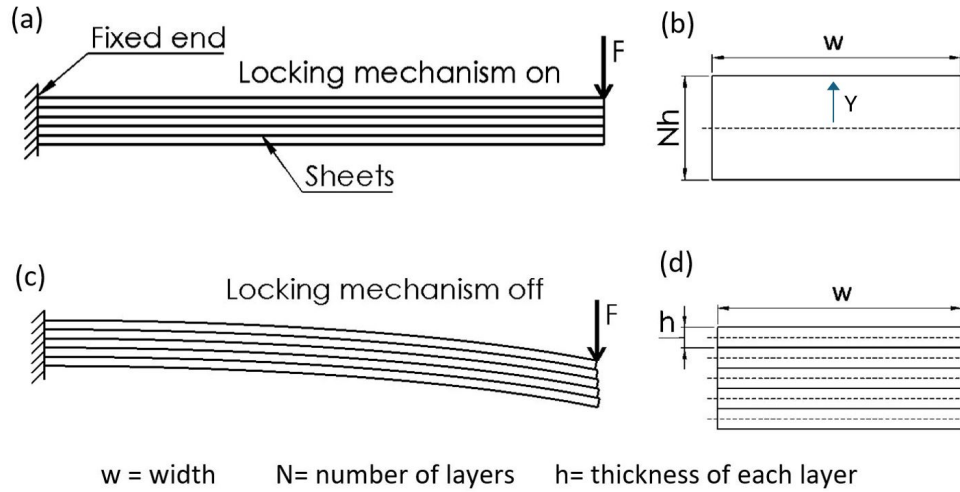


FIGURE 2.2: Stiffness states of the LJS: a) side view of rigid state. b) cross-section of the LJS in the rigid state. c) Side view of the LJS in the flexible state. d) Cross-section of the LJS in the flexible state. Image adapted from [6].

The fundamental phenomenon that allows the variation of bending stiffness in the LJS is the change in the area moment of inertia I . The bending stiffness k depends linearly on I , in the case of a cantilever beam of length L and Young's modulus E , this relation is given by Eq. (2.1)[38].

$$k = \frac{3EI}{L^3} \quad (2.1)$$

Figure 2.2b and Figure 2.2d illustrate the cross-sectional area (A) of an LJS, w is the width of the beam, h is the thickness of each layer, and N is the numbers of layers. When the mechanism locks the layers, they form a solid beam as illustrated in Figure 2.2b, all the layers bend around the neutral axis of the stack and the beam has maximum bending stiffness, or in other words, the LJS is stiff. The I of the beam in this case is defined by Eq. (2.2).

$$I_{rigid} = \int_{-\frac{Nh}{2}}^{\frac{Nh}{2}} y^2 dA = N^3 \frac{wh^3}{12} \quad (2.2)$$

When the mechanism unlocks the layers, each individual layer bends around its own neutral axis, the whole beam has the minimum bending stiffness, and the layers slide freely as it can be

seen in Figure 2.2c. In other words, the beam is in a flexible state. The I of the beam in this case is defined by Eq. (2.3).

$$I_{flexible} = N \int_{-\frac{h}{2}}^{\frac{h}{2}} y^2 dA = N \frac{wh^3}{12} \quad (2.3)$$

It can be observed in Eq. (2.2), that I of the LJS in the rigid state depends on the number of layers raised to the 3rd power (N^3). In contrast, Eq. (2.3) shows that I of the beam in the flexible state depends on the number of layers (N). The ratio of stiffness or the stiffness variation can be calculated by comparing the area moments of inertia in the flexible and rigid state, which yields:

$$\frac{I_{rigid}}{I_{flexible}} = \frac{N^3}{N} = N^2 \quad (2.4)$$

As Eq. 2.4 shows, the stiffness ratio in an LJS depends on the number of layers raised to the second power [6, 39]. This generates, at least in theory, the possibility of obtaining very high stiffness variation by only adding more layers to the beam [6]. However, this is a theoretical value because other factors, such as friction and efficacy of the lock/unlock mechanism, would reduce the stiffness ratio that can be achieved.

2.4 Lock/Unlock Mechanisms

The LJ principle is relatively simple, consisting of a lock/unlock mechanism that couples or decouples the bending stiffness of the layers to render a bending stiffness change for the whole beam. However, this locking/unlocking is not trivial and requires the development of mechanisms to facilitate this action. Several mechanisms to lock/unlock LJSs have been proposed during the last 20 years. We categorise these mechanisms by the following operating principles: friction, mechanical interference, and miscellaneous principles that differ from the previous two categories.

2.4.1 Mechanisms Based on Friction Force

Friction-based mechanisms function by modifying factors determining the friction forces, such as a normal force. The following section explains these mechanisms.

2.4.1.1 Vacuum Pressure

Jamming generated by vacuum pressure is the most developed technology based on friction to lock/unlock LJSs. Figure 2.3a illustrates a typical LJS. It consists of a stack of compliant layers, an airtight chamber that envelops the layer stack, and a vacuum pump that applies negative pressure inside the chamber. When the vacuum is activated, atmospheric pressure compresses the chamber and the LJS that is inside. As a result, the friction force between the layers increases, which leads to the locking of the sheets and the corresponding increase in the bending stiffness.

There are multiple variations of vacuum-pressure-activated LJS that have been developed to be applied in robotics [7, 15–17, 19, 20, 39–54]. These variations will be described in Section 2.7 and Section 4.1.1.

2.4.1.2 Electrostatic Force

Another method to increase the friction is through electrostatic force, as shown in Figure 2.3b. This mechanism consists of a stack of thin, flexible polyimide layers with patterned nickel electrodes [8]. These electrodes are connected to a high-voltage source in an alternating polarity. Consequently, the electrostatic force between the layers generates a friction force. The final result is the increment in the bending stiffness of the entire stack. The principle of using electrostatic force to lock/unlock the layers is currently known as electro-bonded lamination [55] or electrostatic layer jamming [56–58].

2.4.1.3 LJS Wrapped by Shape Memory Alloy (SMA)

This locking mechanism consists of an array of SMA wires that are wrapped around the LJS, as shown in Figure 2.3c. When an electric current is passed through the wire, the increase in

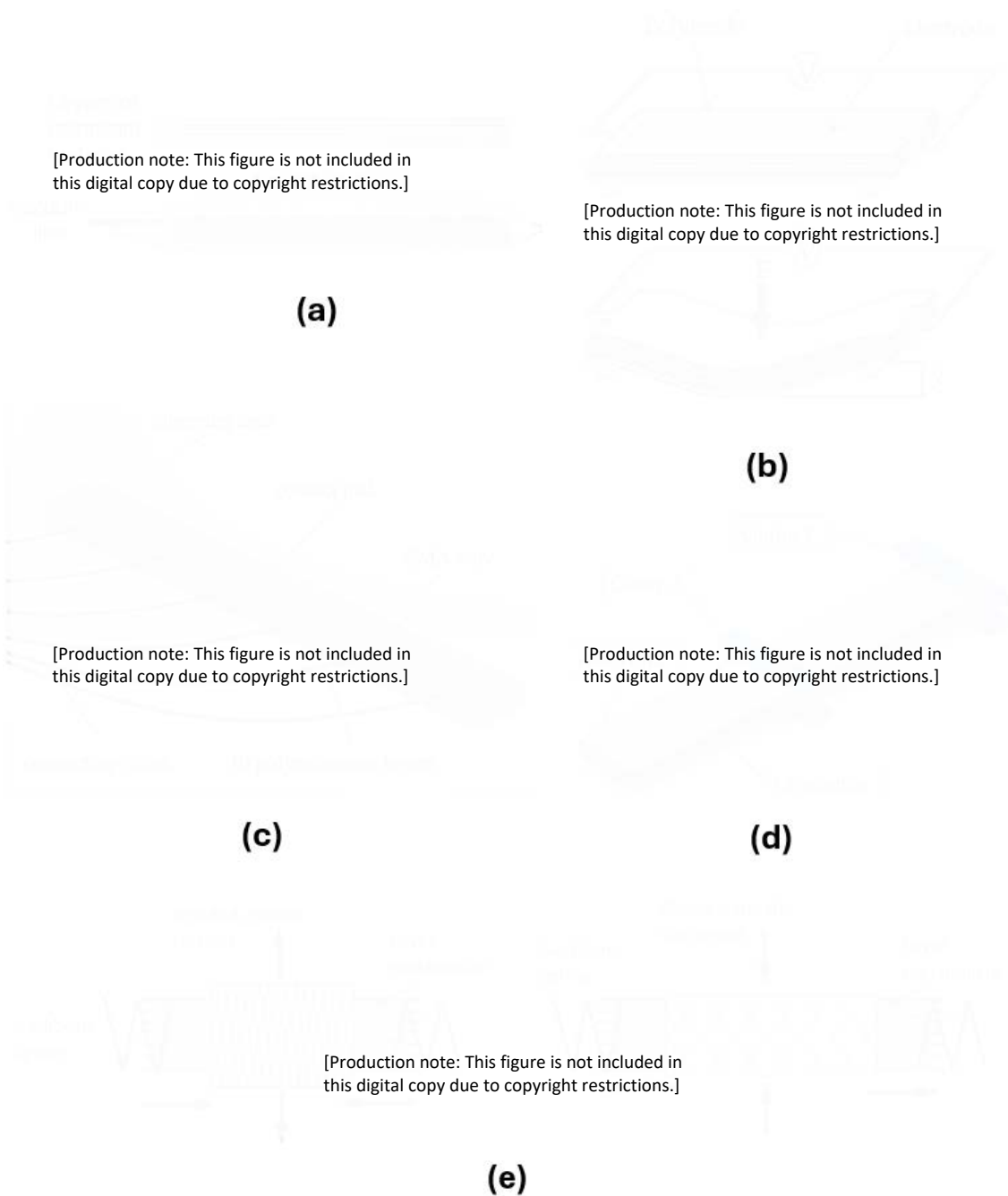


FIGURE 2.3: Lock/unlock mechanisms activated by friction. **(a)** LJS based on vacuum pressure [7]. **(b)** LJS activated by electrostatic force [8]. **(c)** LJS activated by SMA wires [6]. **(d)** Discrete laminar jamming (DLJ), Figure adapted from [9]. **(e)** Mesh sheath, Figure adapted from [10].

temperature causes the SMA wires to contract, which, in turn, tightens the stack of layers and increases the inter-layer friction force, incrementing the bending stiffness. Experiments were carried out with this mechanism, and the results of the experiments showed that the stiffness changed by a factor of 60 [6], meaning the maximum stiffness was 60 times larger than the minimum stiffness.

2.4.1.4 Discrete Laminar Jamming (DLJ)

DLJ is another mechanism to lock/unlock the LJS utilised to build robot links with variable stiffness capabilities. DLJ does not have an elastic membrane that contains the layers. Instead, this mechanism has multiple variable pressure clamps placed discretely along the LJS, as illustrated in Figure 2.3d. The pressure in the clamps is set by bolts [9, 59] or rubber bands [60]. Furthermore, piezoelectric actuators are being considered to drive the pressure in the clamps [9]. The pressure clamps increase the friction force between the layers by applying normal force to the LJS. There are potential advantages of this concept in comparison with LJ based on vacuum pressure, such as faster actuation, better portability, no sealing issues due to a lack of vacuum pressure, and no use of an elastic membrane, which implies a lower probability of being damaged due to contact or impact against rough edges. In addition, LJSs based on vacuum pressure are limited by the differential pressure between full vacuum and atmospheric pressure, while DLJ does not have this limitation.

2.4.1.5 Mesh Sheath

This mechanism is illustrated in Figure 2.3e and consists of a spring backbone contained within a layer-jamming structure that is formed by flaps that are sewn together. Jamming of the flaps is achieved by using a woven mesh sheath that encases the flaps. The sheath decreases and increases in radius when it is extended or contracted longitudinally by a cable coupled at its ends. When the mesh sheath decreases in radius, it tightens the flaps against a steel spring backbone, which increases the friction force between the flaps and stiffens the structure [10].

2.4.2 Mechanisms Based on Mechanical Interference

The lock/unlock mechanism based on the principle of mechanical interference consists of an object that passes through the layer of the LJS, which prevents relative slip between the layers. Typically, there is an actuator that thrusts the object into the layers to increase the stiffness and pulls the object out of the layers to reduce the stiffness. The layers often have a cutout or slot to accommodate the object that goes through them.

Figure 2.4 shows an example of a mechanism based on mechanical interference. The mechanism consists of layers with teeth that are aligned and form gaps between them, as illustrated in Figure 2.4a. A mechanism driven by SMA wires [11], or a mechanism based on electroactive polymers [61], introduces teeth inside the gaps of the layers. This generates a mechanical interference that prevents slipping between the layers and, therefore, increases the bending stiffness, as shown in Figure 2.4a. The same mechanism can remove the teeth that generate the interference, allowing slip between the layers, which, in turn, generates the minimum bending stiffness, as can be seen in Figure 2.4b. Intermediate values of the bending stiffness can be achieved by varying the number and location of the teeth that are introduced in the gaps along the LJS.

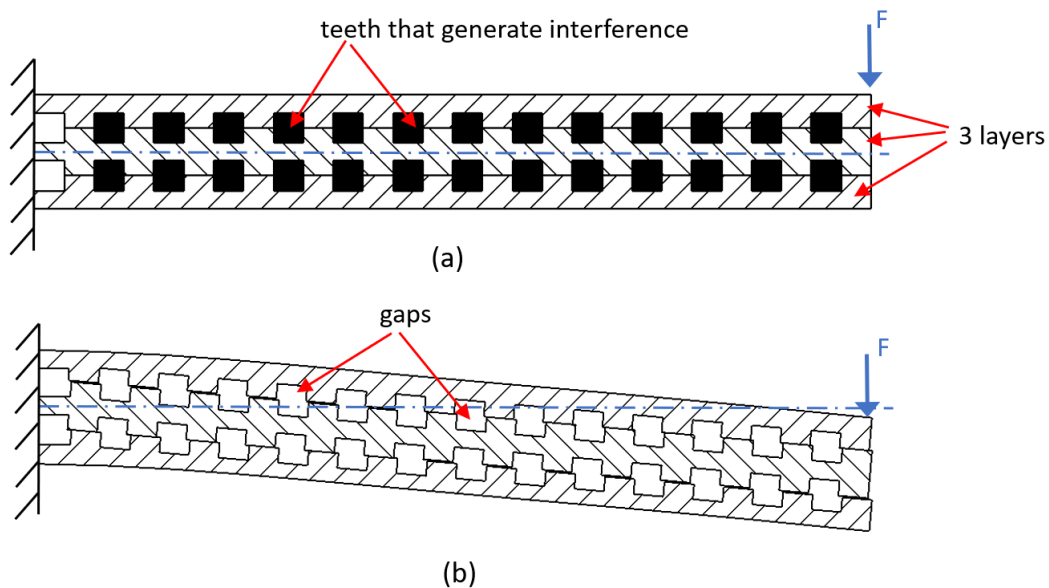


FIGURE 2.4: LJ with mechanical interference. (a) LJS at high stiffness state (the black areas depict the teeth that generate the mechanical interference between layers), Figure adapted from [11]. (b) LJS at low stiffness state, Figure adapted from [11].

2.4.3 Mechanisms Based on Miscellaneous Principles

Currently, multiple research projects on LJ are exploring different concepts and mechanisms to facilitate variation in stiffness. Furthermore, some of these ideas are presented with various names. Therefore, defining a strict classification method is challenging because some LJ concepts are unique regarding their working principle. This section presents lock/unlock mechanisms that do not classify as mechanisms based on friction or based on mechanical interference.

2.4.3.1 LJ with Heating Blankets

This mechanism consists of aluminium sheets with polymer sub-layers between them, as illustrated in Figure 2.5a. The polymer sub-layers have ultra-thin electric heating blankets embedded in them. The aluminium cover sheets are coupled with the base aluminium sheet when the polymer layers are rigid, and the LJS bends as a whole unit. When the embedded ultra-thin heating blankets are activated by an electric current generated by a temperature controller (Figure 2.5b), the increment in the temperature provokes a reduction in the shear modulus of the polymer, resulting in the decoupling of the aluminium cover layers and the base aluminium layer. The ultimate consequence is a decrease in the bending stiffness of the beam [12].



FIGURE 2.5: LJS with heating blanket mechanisms. (a) Components of the LJS [12]. (b) Experimental setup [12].

2.4.3.2 Sliding-Layer Laminates (SLL)

SLL comprise a stack of layers forming a beam. Each layer is composed of sections of two different materials that are arranged periodically. One of the materials is soft, and the other one is rigid. When the layers are aligned, as shown in Figure 2.6a, the beam is flexible because the layers bend around their soft sections. When the layers are not aligned, each soft section is accompanied by a rigid section, causing the beam to become more rigid. It is possible to obtain intermediate bending stiffness values by sliding the layers with an appropriate proportion of overlapping between the rigid and the soft sections, as seen in Figure 2.6b. The layers are slid manually before every test [13], or by the action of a linear motorised stage [14].



FIGURE 2.6: SLL. (a) Minimum and maximum stiffness state, Figure adapted from [13]. (b) Intermediate stiffness states [14].

2.5 Analysis of Performance of LJ Mechanisms

The analysis of the performance of any variable stiffness technology depends on the intended applications. Each application often targets a particular capability or set of capabilities. For example, some applications focus on enhancing the dynamic capabilities of the structures, particularly for a fast change in stiffness to produce a fast dynamic response. This is the case of impact mitigation in human-robot interaction where robots with variable stiffness capabilities can be safer than rigid robots in the case of a collision against a human operator [62]. Another example is the application of haptic devices for the teleoperation of robots that require quick variable stiffness to change the perception of the human operator at the moment of grabbing soft or hard objects [45].

Furthermore, some applications implement variable stiffness techniques without focusing on a rapid dynamic response. For instance, the aerospace industry focuses on how to achieve efficient shape adaptability, high load-carrying capacity, reversible strain, and a broad range of rigidity levels while prioritising criteria like low weight, efficient use of energy, and manufacturability [22].

The performance of various lock/unlock mechanisms of each LJS are presented in Table 2.2 and are partially based on the evaluation presented in [5]. In this section, the lock/unlock mechanisms of an LJS will be compared in terms of the performance in the application of impact mitigation between human beings and robots. Table 2.2 presents four criteria that were used in the comparison: speed of stiffening, speed of destiffening, stiffness variation, and stiffness range. These are considered the most relevant criteria to evaluate the performance of this application. Other criteria are not useful for evaluating the performance of LJ mechanisms in mitigating impacts between human beings and robot arms. For example, the criterion of scalability defines how well a variable stiffness mechanism can be adapted to applications in different scales. Since this discussion focuses on a particular application defined in the dimension range of current cobots or industrial robotic arms, scalability is not useful when comparing the performance of lock/unlock mechanisms in this particular application.

It is important to note that the majority of LJSs have lengths that do not exceed 400 mm [9]. These LJSs are suitable for research purposes; however, they would need to be scaled up to be applicable in fields where collaborative robots and industrial robots have been implemented, such as in the manufacturing industries. These applications need heavier and larger robot arm links than the LJSs that have been developed so far.

A performance comparison of the lock/unlock mechanisms for LJ structures according to the criteria mentioned above is discussed below.

2.5.1 Speed of Stiffening and Destiffening

This criterion is crucial to generate a fast dynamic response. This is especially critical in active compliant robots where the change in stiffness must be faster than the duration of the collision to mitigate the effects of the impact on human beings. In this regard, it can be seen in Table 2.2

TABLE 2.2: Performance of the fundamental lock/unlock mechanisms of LJ, and some combinations between them (qualitative evaluation scale: ++, +, -, -- from the highest to the lowest values).

Lock/Unlock Mechanism	Speed of Stiffening	Speed of Destiffening	Actuation/Power Source	Stiffness Variation	Example of Stiffness Range (N/mm)	Applications
LJ wrapped by SMA [6]	--	--	Electric Power/Thermal Conditions	60 ×	0.03–1.8	No specific application
Electrostatic Force [8, 56–58, 63–66]	--	++	Electric Power	18 ×	No data available	-robotic fingers -continuum robots -wearable robots -haptic gloves
Vacuum Pressure [7, 15–17, 19, 20, 39–53, 67–69]	++	++	Vacuum Pump	10 – 180 ×	0.008–1.522 [42]	-grippers and fingers -wearable robots -robot arms -landing gear of UAVs
Mechanical Interference [11, 61]	-	-	Electric Power/Thermal Conditions	14.6 ×	0.11–1.72 [11]	No specific application
LJ with Heating Blankets [12, 70]	--	-	Heat Source/Thermal Conditions	2.25 – 4 ×	5–18 approx [12]	No specific application
Sliding Layer Laminate [13, 14]	+	+	Linear Actuator	3 – 7 ×	0.005–0.035 [14]	Underwater robots
Mesh Sheath [10]	No data available	No data available	Mechanical Motion	1.5 ×	No data available	Continuum robots
DLJ [9, 59, 60]	Not applicable	Not applicable	Mechanical/Pressure Clamps	17×	0.024–0.4 [9]	Robot arms

that lock/unlock mechanisms based on thermal effects as a working principle have low scores for stiffening and destiffening speeds. For instance, LJ based on SMA wires has a limitation in the maximum switching velocity between different stiffness states that is determined by the heating and cooling processes of the SMA wire, which take 100 s and 200 s to reach thermal equilibrium, respectively [6].

LJ based on electrostatic force also exhibits a low speed of stiffening. The research presented by [66] does not directly measure the stiffening time. However, the experiments include a 60 s period of voltage application to the layers before starting the application of force on the beam. This period is necessary to accumulate enough electric charge on the layers to achieve the increment in stiffness. The study report makes no mention of the destiffening time. However, a recent development has shown that LJSs based on electrostatic force have actuation and release

times that are less than 5 ms and 15 ms, respectively, which makes this mechanism adequate for haptic gloves [64].

The best performance in terms of stiffening and destiffening speeds corresponds to LJSs that are activated by vacuum pressure, as seen in Table 2.2. The research on vacuum pressure-activated LJ does not focus on these aspects, and the information is scarce. Concerning the devices presented in [7, 19, 40], the authors do not mention any measure of the stiffening or destiffening speed. The only measure in this regard is presented in [45]. That investigation reports that the necessary time to change the stiffness of the haptic glove completely is characterised by a time constant of about 0.5 s. This time is much shorter than the typical time of stiffening and destiffening of the LJ wrapped by SMA wires (hundreds of seconds) [6]. However, it is still too large for collision applications considering that the damage due to impacts between industrial robotic arms and humans takes about 0.1 s [2]. Therefore, the current LJSs that are activated by vacuum pressure seem ineffective in mitigating the effects of an impact in an active compliant robot arm because their reaction times are too long.

Furthermore, it should be noted that the transition of vacuum pressure-activated LJSs from the rigid state to the flexible state may not be immediate nor complete, as was revealed in the experiments presented in [7]. In these experiments, after each test the LJ sample was disconnected from the vacuum regulator and flexed multiple times to accelerate its return to ambient pressure. These limitations could be potentially overcome if the DLJ structures implement piezoelectric actuators to drive the pressure clamps located along the LJS, as has been considered in [9, 59] for future research. The LJSs based on SLL also demonstrate a high speed of stiffening and destiffening since the change from maximum to minimum stiffness and vice versa is about 4 s, as can be observed in the supplementary videos presented in [14].

Despite vacuum pressure-activated LJ being seemingly ineffective for active compliant robots, it may be used for implementation in passive compliant robot arms, as was proposed in [9, 15, 20, 59]. Additionally, LJ based on vacuum pressure can be used to mitigate the effect of impacts in UAVs, seat belts, and robot arms, respectively [18, 19, 49]. In these applications, the LJSs do not change their stiffness in response to the impact. Instead, they work as passive elements whose stiffness is tuned before operating the devices where they are used. However, impacts against

solid bodies could tear the envelope that generates the vacuum pressure on the laminates, which may eliminate the variable stiffness capabilities of the LJS.

2.5.2 Stiffness Variation and Stiffness Range

Table 2.2 presents two different columns for the stiffness variation and stiffness range. However, these two criteria are highly associated. The stiffness variation, also known as the stiffness ratio, is a relative quantity that can be calculated from the stiffness range since it is the ratio between the maximum stiffness and the minimum stiffness (maximum stiffness/minimum stiffness). Therefore, it can be considered that the stiffness variation is just a metric of the stiffness range.

A large stiffness variation means that the studied lock/unlock mechanism is very useful since it can take advantage of the characteristics of a high stiffness state (e.g., more load capacity) and of the characteristics of a low stiffness state (e.g., the ability to be deformed by an external force or conform to object shapes).

A large stiffness variation is desirable in the mitigation of impacts between human beings and robots because it indicates that the robot can have acceptable performance in normal tasks, such as carrying heavy weights and moving with accuracy, and can become flexible or soft enough to be effective in the mitigation of impact forces between a human being and a robot.

Table 2.2 shows that lock/unlock mechanisms based on friction have the largest stiffness variation. For example, the LJS wrapped by SMA wires reaches a stiffness variation of $60 \times [6]$, which means that its maximum stiffness is 60 times its minimum stiffness, while a gripper composed of vacuum pressure-activated LJSs exhibits a variation of stiffness of $180 \times [42]$. In contrast, LJ with heating blankets has the lowest stiffness variation, ranging from 2.25 to $4 \times$. LJ with electrostatic force mechanisms and LJ with mechanical interference mechanisms have intermediate values of the stiffness ratio of $18 \times [65]$ and $14.6 \times [11]$, respectively. Although the mechanisms based on friction have the highest stiffness ratio, one of them also has the lowest stiffness ratio, which is the case of LJ with a mesh sheath [10], which has a stiffness ratio of $1.5 \times$.

In addition to the stiffness ratio, the stiffness range of the LJ mechanisms should be considered to determine how a particular locking mechanism can satisfy diverse requirements associated with

stiffness. Table 2.2 and Figure 2.7 show the stiffness range of the fundamental LJ mechanisms that were described in Section 2.4. For example, LJ wrapped by SMA has a stiffness range between 0.03 N/mm and 1.8 N/mm [6]. The stiffness values of the lock/unlock mechanisms cover various orders of magnitude, as shown in Figure 2.7. A significant difference in the order of magnitude of stiffness between some mechanisms is observed. For instance, the minimum stiffness achieved by the heating blankets mechanism is two orders of magnitude larger than the maximum stiffness achieved by the SLL mechanism.

Table 2.2 and Figure 2.7 illustrate that LJ based on vacuum pressure has the best performance in terms of the stiffness range because it ranges from low values of stiffness (0.008 N/mm) to high values of stiffness (1.522 N/mm). As was demonstrated in [16], a vacuum pressure-activated LJ can generate stiffnesses low enough to be useful to mitigate impacts between a robot arm link and a human being whilst also being able to produce a stiffness state that is high enough to allow the manipulation of significant payloads. In contrast, LJ with heating blankets has the worst performance in terms of stiffness range since its minimum stiffness is too large to mitigate the impact between a robot link and a human being [12].

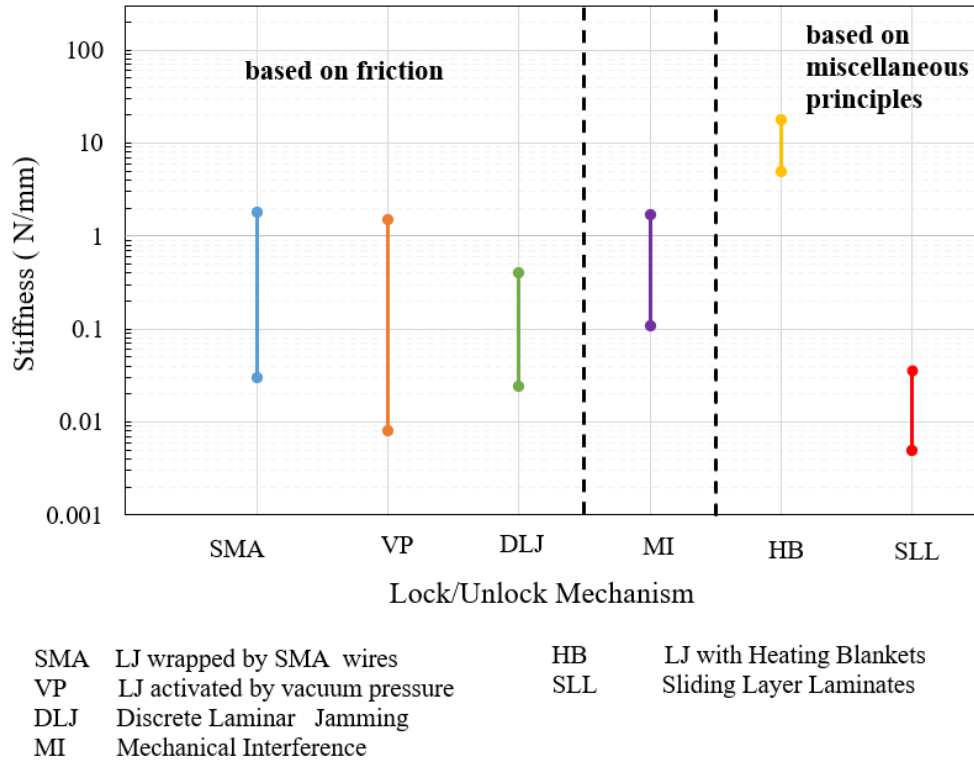


FIGURE 2.7: Comparison of stiffness ranges for some of the fundamental lock/unlock mechanisms of LJ.

2.6 Limitations of Lock/Unlock Mechanisms

All lock/unlock mechanisms to activate stiffness changes in LJSs have limitations. Some limitations are inherent in the working principle of each mechanism. Other limitations are determined by technical factors in the manufacture or the assembly. An example of the former is LJ based on vacuum pressure, which is not able to keep its high stiffness state at high loads because of the transition from the pre-slip regime to the full-slip regime. An example of the latter happens in LJ wrapped by SMA wires [6]. The wire is wrapped around the stack of layers manually, which results in small gaps between the stack and the wires, especially in the first loops. This manufacturing error and the relaxation of the wires after the first thermal cycle may cause a reduction in friction in certain parts of the LJS, thus reducing the stiffness and the variation of stiffness.

It should be noted that other limitations of the lock/unlock mechanisms are related to their applications in cobots. For instance, LJ based on electrostatic force might not be suitable for human-robot interaction because it requires voltages of the order of hundreds of volts [8] or thousands of volts [66] to generate changes in stiffness of the LJS. High voltages could be dangerous, considering that the links of the robots could contact a human being during the normal operation of the robot arm or during an impact. However, this problem may have been solved recently since LJ based on electrostatic forces has been implemented in wearable robots [63] and haptic gloves [64]. The solution to this problem consists of limiting the maximum current that energises the LJS. In a haptic glove with LJSs based on electrostatic forces, the current was limited to 1 mA [64] to increase safety for the user.

The limitations of the lock/unlock mechanisms of LJ could also have some applicability. For instance, the transition from the pre-slip regime to the full-slip regime in vacuum pressure-activated LJ could have some utility in the case of impact between a robot and a human being. The stiffness in the pre-slip regime could be considerably larger than the stiffness of the full-slip regime. Therefore, if the impact force is larger than the transition force, the LJS will pass from a high-stiffness state to a low-stiffness state without deactivating the vacuum pressure. In this case, the destiffening process would be faster than the normal destiffening process that happens because of the deactivation of the vacuum pressure. However, if the full-slip stiffness is too low, the LJS will yield catastrophically upon collision if the external load is maintained [7].

The importance of the limitations of LJ mechanisms depends on the application. In the case of LJSs that are applied to wearable robots, such as haptic gloves, the LJS should be as thin as possible to ensure user comfort. LJSs based on vacuum pressure have been implemented in haptic gloves, but it remains a challenge to produce the required output force and stiffness ratio that this application requires while keeping a small thickness of the LJS. Researchers are trying to solve this problem by combining different locking mechanisms for LJ: for example, haptic gloves that combine vacuum pressure and mechanical interference [71]. The mechanical interference mechanism generates a higher stiffness ratio than an equivalent LJS based only on vacuum pressure while the glove remains thin enough to be comfortable.

2.7 Application of LJ in Robot Arms

Changing the stiffness of robotic arms is another application of LJ. The purpose of this application is the development of robot arm links to achieve the load capabilities and precision of a traditional rigid robotic arm with the safety of a compliant soft robot. One strategy to introduce compliance capabilities in robot arms is the implementation of VSLs. Figure 2.8 presents a novel VSL that has a dual parallel beam configuration [15, 16, 20]. The lateral beams comprise a solid centre support, layers on both sides and a sealed enclosure. The solid centre support is made of a rigid material, but it is compliant due to the thin sections along it. When there is vacuum pressure inside the bags, the lateral beams are rigid, and the link reaches high stiffness. When there is atmospheric pressure in the bags, the whole link becomes compliant since the solid centre supports are not constrained to move due to the flexibility of the thin centre sections. This idea of having a solid centre or a *backbone* with adjacent LJSs has also been applied to build fingers of robotic grippers with variable stiffness [42]. The key role of the backbone is to increase the stiffness variation by increasing the distance between the LJSs on both sides and the neutral axis, which increases the opposing moment coming from friction forces in the LJSs.

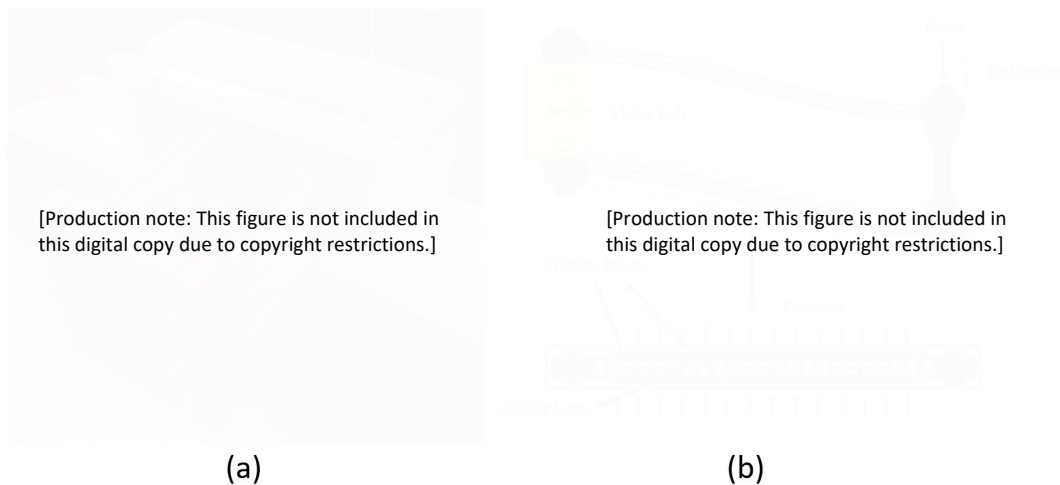


FIGURE 2.8: (a) LJ link for a robotic arm [15]. (b) Details of the parts of the VSL when it is loaded [16].

Parallel guided beams composed of LJSs have also been implemented in robot arms to change the stiffness of the joints rather than the stiffness of the links [17]. The construction of the joint consists of two sets of parallel guided beams that form a wrist that provides variable stiffness

in two perpendicular axes of rotation, as can be seen in Figure 2.9. The LJSs are activated by vacuum pressure.



FIGURE 2.9: (a) Design of a wrist with two parallel guided beams formed by LJSs. (b) Implementation of the wrist in a robot arm [17].

There are other methods to build VSLs that have been combined with LJSs. This is the case of the VSL illustrated in Figure 2.10, which combines three types of variable stiffness methods: an airtight chamber, shape morphing, and LJ [18]. This VSL consists of a cloth cover that contains two spring steel plates and a TPU (thermoplastic polyurethane) air bladder. When the air bladder is not pressurised, the VSL has minimum stiffness. When the air bladder is pressurised, the link is inflated and the cross-section becomes circular, which increases the bending stiffness. When the VSL is not pressurised, the link has a rectangular cross-section and behaves like an LJS with unlocked layers.

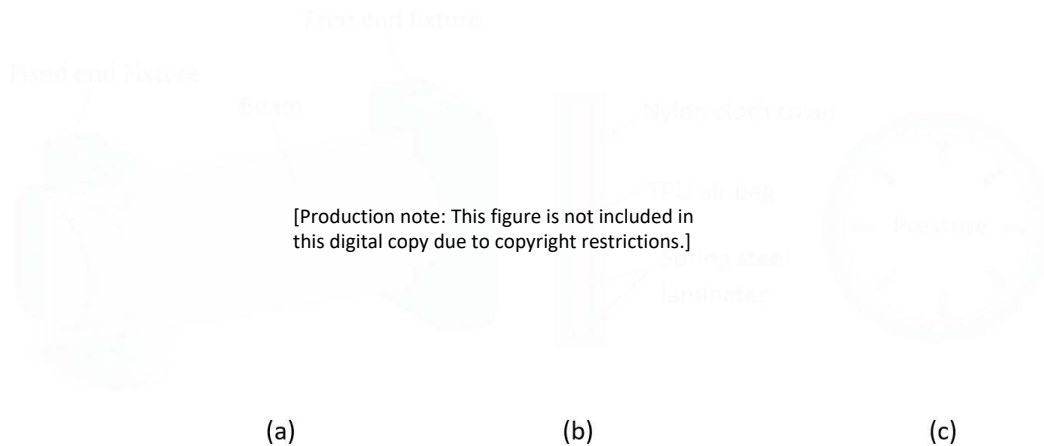


FIGURE 2.10: VSL that combines airtight chamber, shape morphing, and LJ. (a) Overall view, figure adapted from [18]. (b) Cross-section view when the VSL is depressurised, figure adapted from [18]. (c) VSL cross-section when the VSL is pressurised, Figure adapted from [18].

2.8 Summary of Literature Review and Research Gap

There are about 25 technologies that can vary the stiffness of robots. Each technology has advantages and disadvantages, making each technology suitable only for certain applications. As a consequence, there is no dominant technology at the moment. However, LJ was chosen for this research because it has a large stiffness ratio and high speeds of stiffening and destiffening. In addition, LJSs can be manufactured through conventional processes like machining, and they have already been applied in multiple robotic fields such as grippers, wearable robots, robotic arms and others.

There are multiple mechanisms to vary the stiffness of LJSs, including SMA wires, electrostatic force, vacuum pressure, mesh sheath, mechanical interference, heating blankets, and others. Vacuum pressure is the dominant mechanism because it has the highest stiffness ratio (about 180) and high stiffening and destiffening speeds that are characterised by a time constant of 0.5 s. In addition, most of the LJSs that have been applied to robotics are based on the vacuum pressure mechanism.

There are few studies about the application of LJ in robotic arms. These studies focus on implementing LJSs in robotic arms with VSLs and variable stiffness joints (VSJs). In both cases, vacuum pressure is the mechanism used in the LJSs. However, in most of the reviewed robot arms, the vacuum pressure mechanism has been modified by introducing a solid centre that works as a backbone, increasing the stiffness ratio of the VSLs significantly.

LJSs based on vacuum pressure have also shown limitations in their application to robot arms. Particularly in the mitigation of impacts against human beings. First, the time of stiffening and destiffening (time constant=0.5 s) is much shorter than the typical time of many other lock/unlock mechanisms for LJSs, but it is still too large for collision applications considering that the damage due to impacts between industrial robotic arms and humans takes about 0.1s. Second, there are problems with the envelope, such as damages that can easily be caused by contact with rough edges during impacts. Third, the device must be manually returned to ambient pressure after transitioning from the rigid state to the flexible state. Fourth, the LJSs are limited by the differential pressure between full vacuum and atmospheric pressure, which also limits the variation of stiffness that can be achieved.

The limitations of LJSs based on vacuum pressure represent a research gap that must be filled by developing a new mechanism to vary the stiffness of LJSs. This new lock/unlock mechanism must rapidly change the stiffness of the LJS to be useful in attenuating the impact between robot arms and human beings. This gap is the initial motivation of this research.

Chapters 4 to 6 will identify other research gaps related to robot arms with VSLs. Chapter 4 describes the research gaps in the current designs of VSLs. Chapter 5 discusses the limitations of impact tests to determine the injury severity in a human being due to a collision with a VSL. Chapter 6 reviews the strategies and limitations of current VSL robot arms to vary their stiffness.

Chapter 3

Trapezoidal Pin Mechanism

This chapter presents a novel lock/unlock mechanism to vary the stiffness of a LJS. The creation of this mechanism began with qualitative experiments to test the behaviour of simple concepts, followed by the formulation of the conical pin mechanism, and finalised with the study of the trapezoidal pin through bending tests and finite element (FE) simulations.

Computational case studies based on FE simulations were also carried out to study the effect of two main parameters in the LJS with the trapezoidal mechanism, as well as to investigate the behaviour of this mechanism when the LJS is bent in both directions and the behaviour of the LJS in large deflections.

Chapter 2 showed various technologies to vary the stiffness in robotics. Among these technologies, LJ stands out because of its high stiffness ratio, high stiffening and destiffening speeds, and relatively easy manufacturing. Many mechanisms to change the stiffness of the LJSs were reviewed. The limitations of these mechanisms motivate the creation of the new lock/unlock mechanism presented in this chapter. This new mechanism, known as the trapezoidal pin, will be applied to create new types of VSL presented in Chapter 4.

3.1 Motivation for a new Lock/Unlock Mechanism for LJSs

The literature review in Chapter 2 shows that vacuum pressure is the dominant lock/unlock mechanism for LJSs. The main limitation of vacuum pressure LJSs in their application in cobot

arms is the long time taken to change from high stiffness to low stiffness (destiffening). In addition, the transition during destiffening is incomplete and requires manual manipulation to return the LJS to the ambient pressure. The airtight envelope can also have sealing problems in the case of collisions with other objects.

The limitation of the LJS based on vacuum pressure and other lock/unlock mechanisms motivates the creation of a new mechanism to vary the stiffness of LJSs. The creation of this new mechanism looks for a change in the variation of stiffness as well as simple manufacturing and robustness in the application to cobots.

3.2 Preliminary Exploration of Lock/Unlock Mechanisms

This preliminary exploration aimed to develop an impression of the performance of the LJS, its technical problems in manufacturing and testing, and potential lock/unlock mechanisms that overcome the limitations of the alternatives described in Chapter 2.

An LJS was built to conduct the initial exploration. The LJS consisted of ten layers of polycarbonate with a thickness of 0.8 mm. Two bolts at the fixed end keep the sheets together. In terms of manufacturing, these layers were cut with industrial scissors since laser cutting was not possible due to the toxic fumes of the process and the possibility of burning the material. The holes in the layers were made using a conventional machining process. The material, the thickness and the number of layers were the same as the LJS activated by SMA that was presented in [6], that study demonstrated that a LJS with these features was flexible and easy to manufacture by conventional methods.

The lock/unlock mechanisms that are proposed are essentially mechanical because they are more likely to have fast stiffening and destiffening speeds. One of the main limitations that were identified in the Section 2.4 of the literature review was the low speed to achieve the change of stiffness with the lock/unlock mechanisms that have been developed so far.

Two main ideas for the lock/unlock mechanism were tested. They are solenoids that apply normal-pressure force, and solenoids that generate mechanical interference with the layers. Both

solutions involve solenoids because they are one of the most simple linear actuators that can be implemented in this experiment.

3.2.1 Application of Normal Force

The application of normal-pressure force consists of a solenoid that pushes against the layers. The solenoid is mounted in a frame bonded to the lower layer of the beam, as can be seen in Figure 3.1. Two solenoids were mounted along the beam, and three frames were fitted in the beam to allow the alignment of the sheets. The solenoids can be mounted to push or pull against the beam when they are energised, and a compression spring pushes the solenoid back to its original position when it is de-energised.

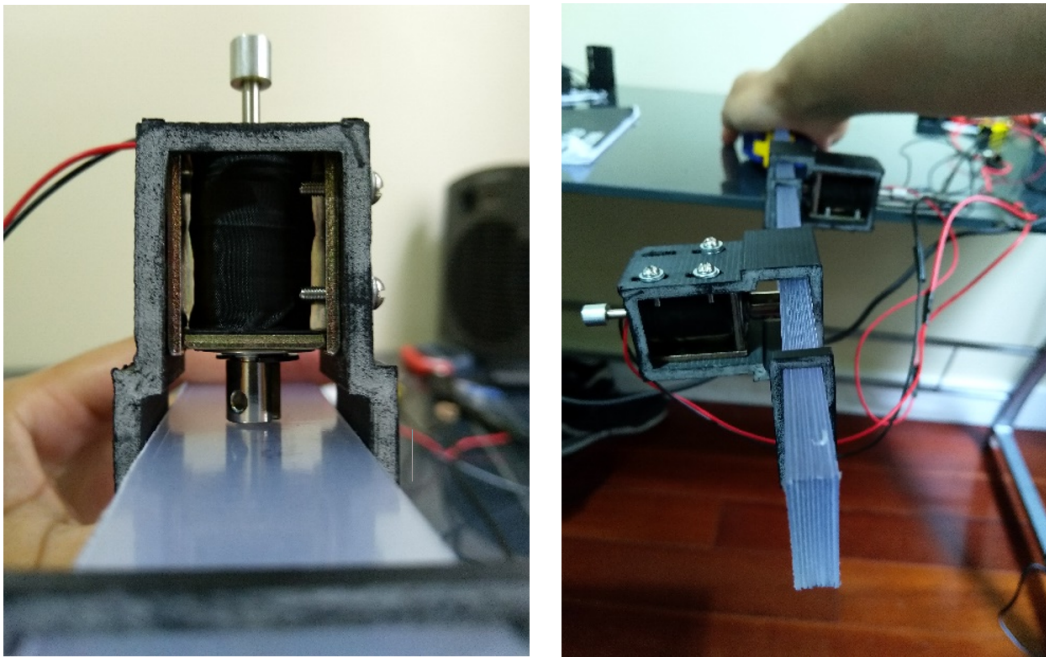


FIGURE 3.1: LJS with solenoid applying normal force against the layers.

Qualitative analysis of the experimental setup led to the following conclusions:

- The solenoid cannot provide or generate enough normal force to stiffen the beam completely. The only significant difference in stiffness occurred when the distance from the top layers to the end of the solenoid core was 10 mm.

- In general, the difference or variation in stiffness generated by solenoids (by spring or electromagnetic field) is not significant.

The use of stronger solenoids could increase the normal force applied to the LJS. However, a stronger solenoid would be significantly larger and heavier, which would increase the volume and the weight of the LJS. Therefore, mechanisms using a different working principle were pursued, such as the mechanical interference mechanism presented in the following section.

3.2.2 Mechanical Interference

The mechanical interference method consists of coupling a pin with the solenoid tip in order to move the pin across the LJS. The LJS has a hole through all its layers with the shape of the solenoid core tip. When the core of the solenoid goes through the LJS, the relative slipping between the layers is prevented. Thus, the LJS is locked and becomes rigid. When the core tip of the solenoid moves out of the LJS, the slipping between the layers is possible, and the LJS is in the flexible state.

Figure 3.2 illustrates a specific case of the mechanical interference mechanism where the cylindrical shape of the solenoid core is directly used to interfere with the layers. The sheets of the LJS also have circular holes that fit with the cylindrical shape of the solenoid core.

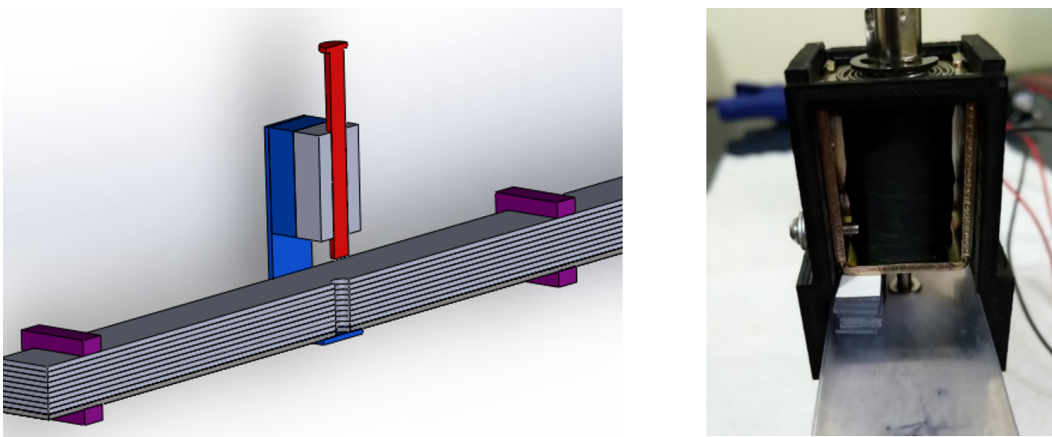


FIGURE 3.2: LJS with cylindrical pin mechanism.

The results of the experiments with this configuration are illustrated in Figure 3.3 and summarised as follows.

- The reliability or effectiveness of the pin motion is low due to the misalignment of the holes in the layers. Even a small misalignment leads to the pin not being properly inserted through the layers, ineffectively locking the LJS.
- The LJS cannot pass from the rigid state to the flexible state when loaded. Figure 3.3a shows the LJS when it is rigid and loaded by its own weight. When the solenoid is deactivated, the cylindrical core cannot disengage from the layers and gets stuck in the circular holes of the layers. It was necessary to reduce the load in the LJS by manually pushing the free end up, which allowed the cylindrical pin to disengage, leading to the flexible state of the LJS, illustrated in Figure 3.3b. When the LJS is loaded, the layers apply lateral forces to the cylindrical core, and the solenoid could not generate enough force to overcome these lateral forces and release the pin.

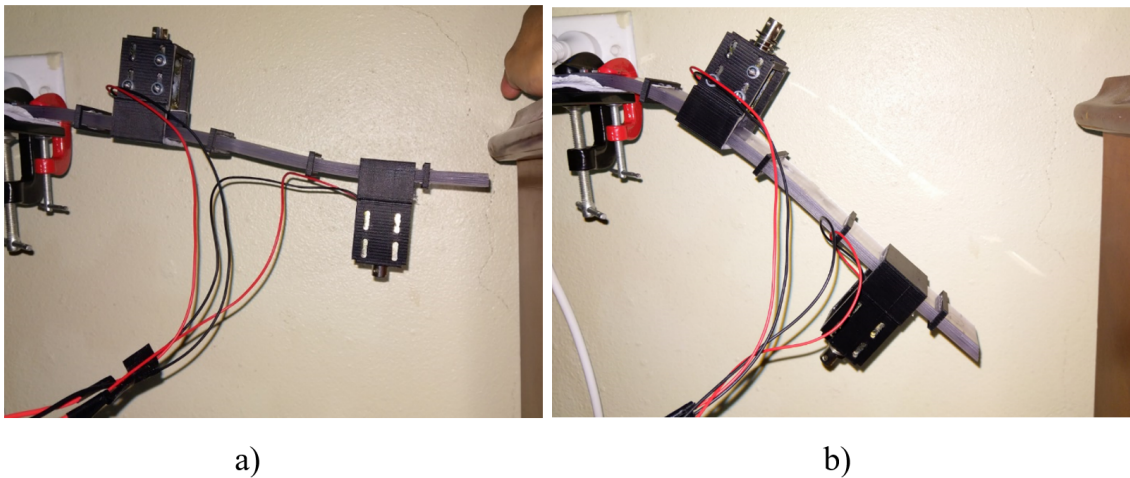


FIGURE 3.3: Tests with cylindrical pin mechanism. a) LJS in a rigid state. b) LJS in its flexible state.

3.2.3 Conical Pin

The purpose of the conical pin is to overcome the main problems observed in both the normal force method and the cylindrical pin mechanism. The first problem was the issue of generating enough interference force with the solenoid to effectively lock the LJS in a rigid state. The second problem was the impossibility of the LJS to pass from the rigid state to the flexible state when the structure is loaded.

A conical pin was attached to the core of the solenoid, and a conical hole was machined on the polycarbonate sheets. The first experiment was similar to the experiment carried out with the cylindrical pin and consisted on thrusting the conical pin in the holes and then allowing the structure to bend under the effect of its own weight. In this situation, the LJS was rigid and loaded by the gravity force. Then, when the solenoid was de-energised, the conical pin was released, and the LJS transitioned to its flexible state, which generated larger deflection because of gravity. This experiment demonstrates that the conical pin solves the problems observed with the previous two lock/unlock mechanisms.

Another experiment was carried out in order to visualise how the conical pin works. The conical pin was initially engaged in the conical holes as can be seen in Figure 3.4a. Then, the free end of the LJS was pushed up manually, as illustrated in Figure 3.4b. It can be seen that the LJS bends, and the relative slip between the sheets pushes the conical pin up. In other words, the deformation of the LJS contributes to disengaging the pin from the layers due to its conical shape.

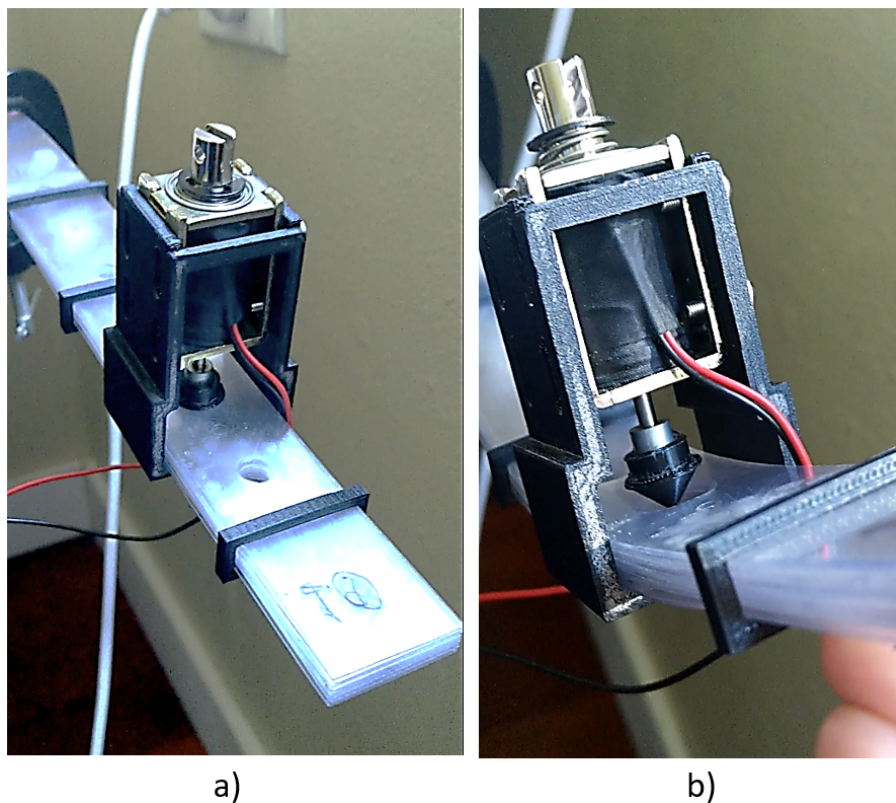


FIGURE 3.4: Tests with conical pin mechanism. a) external load is not applied to the LJS
b) external load is applied to the LJS.

These preliminary experiments showed how the conical pin works. The solenoid has to thrust the conical pin into the layers in order to generate the rigid state. If the LJS is bent under the action of an external load, the thrusting force of the solenoid acts against the slipping of the layers that pushes the pin up. It should be noted that the LJS is still in a rigid state. Then, when it is necessary to transition from the rigid state to the flexible state, the solenoid must be de-energised, and the conical pin is disengaged from the layers by combining two actions. First, the solenoid retracts the conical pin. Second, the relative slip of the layers pushes the conical pin up.

3.2.4 Effect of Frames

Frames are rigid components distributed along the LJS, they keep the layers together without preventing the axial slip between them. The preliminary experiments demonstrate that the main function of the frames is to avoid the independent buckling of the sheets. Without the frames, the sheets can buckle independently when the beam is locked because slipping between the layers is not allowed. Figure 3.5 shows how two layers buckle independently due to the lack of a frame in this section of the LJS.

It was also noted that a fit press between the frames and the layers significantly increases the stiffness of the LJS.



FIGURE 3.5: Buckling of some sheets of the LJS between 2 frames.

3.3 LJ with Conical Pin Mechanism and Metallic Sheets

The preliminary experiments demonstrated the benefits of the conical pin mechanism in comparison with the cylindrical mechanism. Therefore, the conical pin concept was selected to be

extensively investigated through quantitative experiments and FE Simulations [72]. However, challenges associated with the manufacture of the concept were identified. This section focusses on the description of the problems in the manufacturing of this LJS.

The LJS that is presented in this section is very similar to the LJS presented in Section 3.2.3. The main differences between them are the material of the layers, the type of actuator, and the number of frames. Figure 3.6 and Figure 3.7 show the components of this mechanism and the LJS. It consists of a conical pin that is coupled with the rod of a pneumatic cylinder. Figure 3.7b shows that when the cylinder is pressurised, the conical pin is thrust into a conic hole formed by the circular holes in the layers. The conical pin compresses the layers and increases the friction force between them in that area. When the conical pin is disengaged, the LJS has the lowest stiffness (Figure 3.7a). When the pin is engaged, the stiffness depends on the force that is applied to the pin, which in turn depends on the air pressure in the pneumatic cylinder (Figure 3.7b).

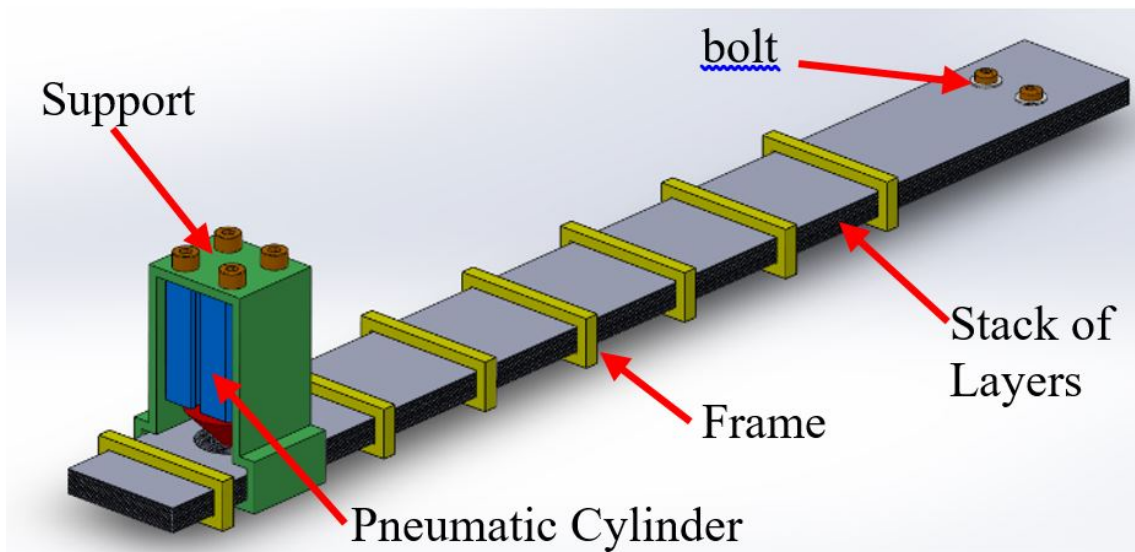


FIGURE 3.6: LJS with conical pin mechanism and metallic sheets.

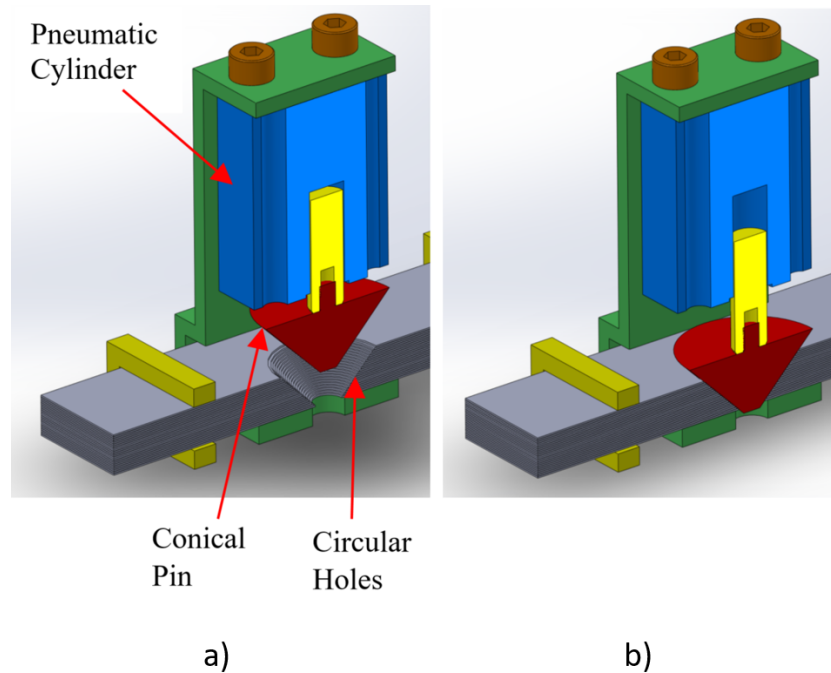


FIGURE 3.7: a) Longitudinal section of the mechanism when the conical pin is disengaged from the LJS b) Longitudinal section of the mechanism when the pin is engaged in the LJS.

This LJS has 22 layers that are made of stainless steel shims with a length of 350 mm (300 mm for LJS length and 50 mm for holding with C-clamp), width of 35 mm, and thickness of 0.318 mm. Each layer has a hole with a different diameter to accommodate the conical pin. The conical pin was made of industrial nylon. The angle of the tip of the cone is 90° . More details of the components of this LJS can be found in [72] and in Section 3.4.1 since some of these components were also used in another type of LJS mechanism called “Trapezoidal Pin”.

3.3.1 Manufacturing of the LJS with Conical Pin

The layers are the components that require the most work and attention. The raw material is a large sheet that, due to common manufacturing processes, typically comes in rolls. To cut the sheets of the LJS from this raw material, it is necessary to cut the roll in smaller rectangles and then place them in a laser cutting machine that cuts each layer of the LJS. The laser cutting process is accurate, and it does not deform the sheets. However, it generates burrs on the edges of the sheets, as can be seen in Figure 3.8. These burrs are small, but they were high enough to

prevent the correct contact between the sheets. Therefore, it is necessary to deburr the edges with a pedestal grinder and a handheld grinding tool.

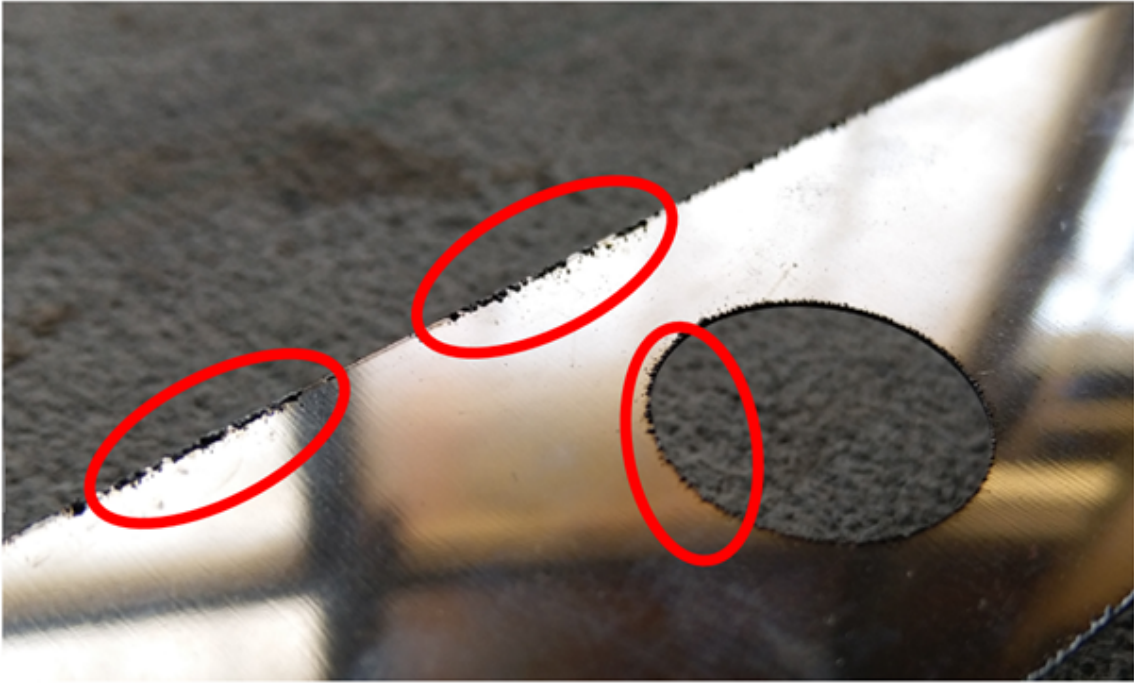


FIGURE 3.8: Burrs on the metal sheets due to laser cutting process.

The fact that the raw sheet material comes in rolls generates a curved shape of the layers, as illustrated in Figure 3.9. When the sheets are assembled in the LJS, the curvature of the sheets generates gaps between them, which may affect the mechanical behaviour of the proposed LJS.



FIGURE 3.9: Deflection of the layers due to the rolling shape of the raw material.

3.3.2 Experiment Setup

The purpose of the experiment was to determine the variation of stiffness of the LJS as a function of the air pressure in the pneumatic cylinder. The experiment setup was completely assembled on the table of a vertical milling machine in order to take advantage of the high stiffness of its structure. A similar setup was used by [62] to carry out static experiments in VSLs. Figure 3.10 illustrates the components of the experiment setup. The force was measured by a YUTON HDM2006LS load cell that has a resolution of 0.019N and nonlinearity of 0.02%. The deflection was measured by a height gauge with 0.02mm resolution.

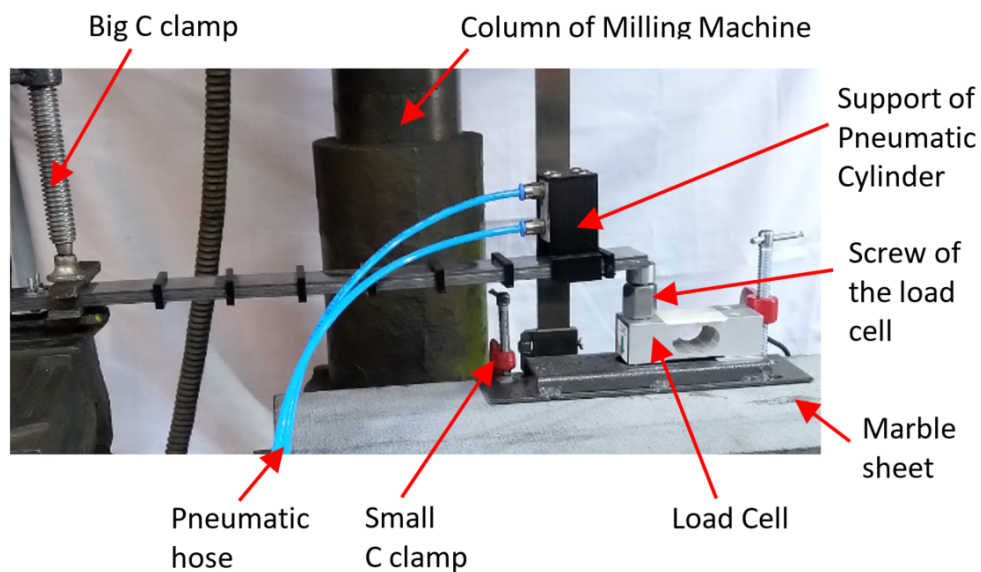


FIGURE 3.10: Experimental Set up

3.3.3 Experimental Procedure

At the beginning of each test, the LJS is deflected by its own weight. This deflection prevents the correct accommodation of the conical pin in the circular holes of the LJS. In consequence, the LJS is not locked properly. To solve this problem, the LJS is manipulated manually to properly accommodate the conical pin in the holes of the LJS.

The procedure to generate the deflection of the LJS and measure the force is similar to the procedure presented by [12]. The deflection of the beam is generated through the manual

rotation of the screw of the load cell. The contact force between the screw and the LJS is measured by the load cell. For every value of deflection, there is a corresponding value of force.

The force is measured every two revolutions of the screw which correspond to approximately 3 mm of axial motion of the screw. However, as there is no precise control of the manual rotation of the screw, the height gauge was used to measure the deflection of the free end of the beam. It is important to know that these values have to be recorded after the force has reached a stable value. For this reason, it can be considered that the LJS is loaded and unloaded quasi-statically. This type of static experiment is necessary before conducting dynamic tests and provides valuable inputs for dynamic models of VSLs composed of LJSs [16].

The experiment of force vs deflection consisted in the application of a complete load-unload cycle at 0, 2, 4, 6 and 7 bar of pressure in the pneumatic cylinder. The test begins with the loading procedure where the deflection increases from zero until reaching a maximum value about 30mm. Then, the unloading procedure begins by reducing the deflection until the straight position of the LJS, reaching a deflection very close to zero.

3.3.4 Results of Experiments

Figure 3.11 illustrates the results of this experiment for a locking pressure of 0 bar in the pneumatic cylinder. The upper branch of the curve is the loading procedure. The lower branch of the curve represents the unloading procedure. Three trials were conducted at each pressure value. Similar Experiments carried out in DLJ [9] and LJ based on vacuum pressure [15] also carried out three trials at each pressure value. The points illustrated in Figure 3.11 correspond to the average of the forces obtained in the 3 trials for a given deflection. The error is illustrated in Figure 3.11 through the error bars that reflect the range of force values obtained across the 3 trials for a given deflection. A similar procedure to illustrate the error in stiffness tests was implemented by [73].

The stiffness of the LJS is the slope of the curve Force vs Deflection. Figure 3.11 and Figure 3.12 show hysteresis in the LJS which means that there is not a unique value of stiffness for a given pressure. This phenomenon is also reported by [6] and [7]

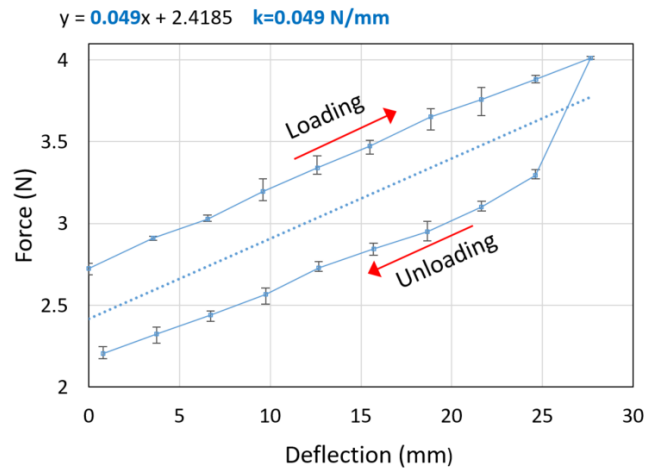


FIGURE 3.11: Results of the experiments at 0 bar

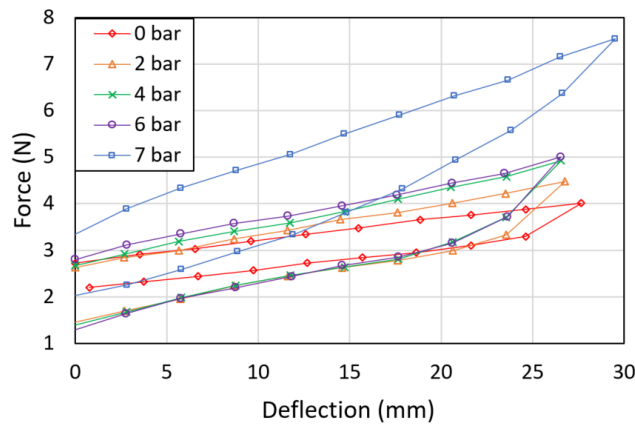


FIGURE 3.12: Results of the Experiments

TABLE 3.1: Stiffness for each state of air pressure in the pneumatic cylinder

Pressure (bar)	0	2	4	6	7
Stiffness (N/mm)	0.049	0.076	0.091	0.091	0.153

In order to compare the stiffness of the LJS for different air pressures in the pneumatic cylinder, it is necessary to calculate a unique value of stiffness for each pressure. Therefore, following the same procedure that is applied by [6, 9]. The results of the experiment at each value of pressure were linearized by the method of least square which yields a straight line whose slope is the stiffness k . The linearization includes the loading and unloading data.

Table 3.1 shows the stiffness calculated from the linearization of the results at each state of

pressure in the pneumatic cylinder. It can be observed that the minimum stiffness is 0.049 N/mm and corresponds to 0 bar. The maximum stiffness is 0.153 N/mm and corresponds to 7 bar. The stiffness ratio is calculated as the ratio between the maximum stiffness and the minimum stiffness, which yields 3.12 for this novel lock/unlock mechanism.

The calculation of stiffness from the experiments could be calculated through other methods. For example, the stiffness can be calculated only for the loading part of the cycle (the upper branch of the curve). This is the method adopted by [12, 39]. If we apply this method to the previous experimental results, the maximum stiffness ratio is 2.95. The difference with the value calculated by considering the complete load-unload cycle (3.12) is 5.4%.

3.3.5 Discussion of Experimental Results

The proposed lock/unlock mechanism of the LJS achieves a stiffness ratio of 3.12. The measured stiffness ratio is much less than the theoretical maximum that could be achieved if all the LJS layers were joined to form one solid member (484 for $N=22$) as it was explained in Section 2.3. In this experiment, the maximum pressure that the air compressor can supply is 8 bar. If the air compressor can supply 10 bars, which is the operative limit of the pneumatic cylinder, the maximum stiffness ratio could be higher.

3.3.6 Finite Element Simulation of the Conical Pin

LJSs with other lock/unlock mechanisms have been modelled by analytical methods or finite element (FE) methods in order to study the mechanical behaviour of the LJS with such mechanisms [7, 9, 11, 70]. In the case of LJS with many layers, FE methods would be preferred over analytical methods because analytical methods are algebraically taxing [7]. This section presents FE Simulations of the LJS mechanism proposed in this section.

A FE model was built in Ansys with the same dimensions and components as the experiment setup. The FE model has the same load and boundary conditions that were implemented in the experiment. These conditions are the following: the LJS model is fixed in one of its ends; gravity force is considered; deflection is imposed at the free end following the same values that were imposed in the experiment; the pressure in the pneumatic cylinder is implemented as a

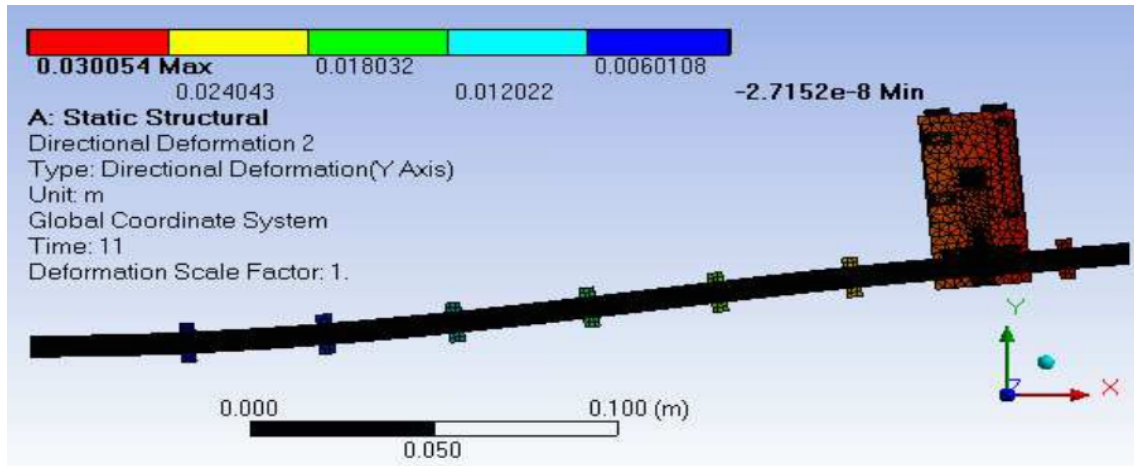


FIGURE 3.13: Resulting shape of LJS at 7 bar and COF 0.32 from FE simulation

pair of forces that are applied to the cylinder rod and the cylinder body, the value of these forces correspond to the forces applied by the cylinder when it is pressurized at the same values of pressure of the experiment (0 bar, 2 bar, 4 bar, 6 bar, 7 bar). The result of the simulation is the force associated with each value of the enforced deflection.

The most relevant details about the pre-process of the simulation are mentioned as follows: Only one half of the LJS sample is modeled, and symmetry along the longitudinal plane was imposed, as can be seen in Figure 3.13. The mesh of the layers is composed of elements of quadratic order and all the layers have one element across the thickness. *Large deflection* is turned on considering that the maximum deflection in the experiment was about 10 % of the length of the beam. The setup of the contact among the layers, and between the layers and the pin had a determinant role in the convergence of the simulation. In this aspect, the most important parameters are the Contact Formulation which was selected as Augmented Lagrange, the normal stiffness factor is set up as 0.01, and the stiffness is updated in each iteration.

Figure 3.13 illustrates the shape of the LJS at a locking pressure of 7 bar when it reaches the maximum deflection of the free end that was imposed in the experiment. It can be appreciated that the curvature of the LJS is very low in the section that is close to the conical pin mechanism. In other words, the action of the conical pin makes that section of the LJS straight.

3.3.7 Experiments Versus Simulations

Figure 3.14 illustrates the results of the FEM simulations and the experiment for the LJS at 7 bar and a coefficient of friction (COF) of 0.32. It can be observed that the simulation results agree with experimental results very well for the loading part of the cycle but differ significantly in the unloading part of the cycle. Both results were linearized, which yields a stiffness of $k=0.15$ N/mm in the simulation, and a stiffness of $k=0.153$ N/mm in the experiment. It can be appreciated that the stiffness values of the simulation and the experiments were very close.

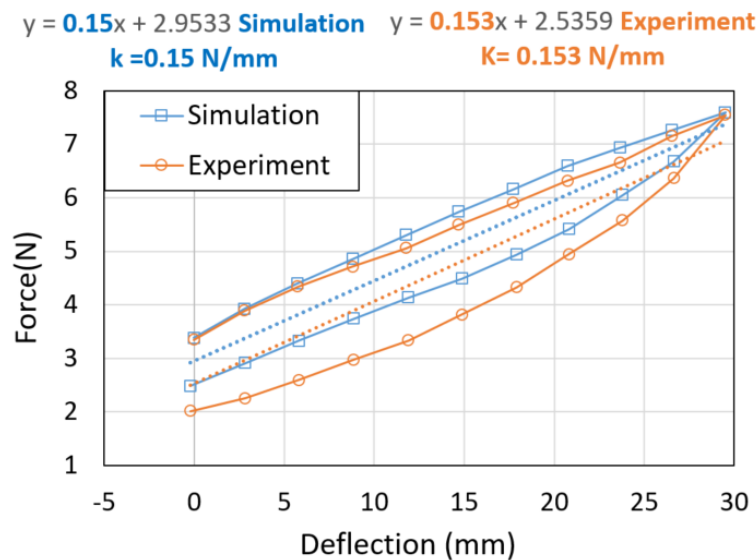


FIGURE 3.14: Force-Deflection curves for 7 bar pressure and COF 0.32 from FEM simulation and Experiment

Despite the good match between the FE simulations and the experiments illustrated in Figure 3.14. The Investigation on LJ mechanisms based on friction force indicates that the stiffness of the structures is highly dependent on the COF [7, 9]. Therefore, the following section presents a study of the effect of the COF on the LJS with a conical pin in order to evaluate the match between FE simulations and the experiment.

3.3.7.1 Coefficient of Friction

The coefficient of friction between the components of the LJSs is an important parameter in the LJS behaviour. Measuring the COF between the layers is a difficult task because of the

curvature of the sheets and the lack of uniform surface finishing of the sheets that results from the elimination of burrs. Despite these difficulties, a first approach to define the COF among the layers was carried out by conducting some experiments. A sample of three pairs of layers was selected for these tests. The COF between the layers was measured by the method described by [74] which uses an inclined-plane friction apparatus. The same experiment was carried out between the layers and the conical Pin. The results of these experiments indicate that the COF between the layers is 0.39 and the COF between the layers and conical pin is 0.25.

Figure 3.15 compares the experimental and the simulation stiffnesses for all the pressure values that were tested in the experiment. The first set of FE simulations was run with the COF values that resulted from the friction experiments (0.39 between the layers and 0.25 between the layers and the conical Pin). The results of these simulations agree well with the experiment at 0 bar and 7 bar, but results differ considerably at 2, 4, and 6 bar.

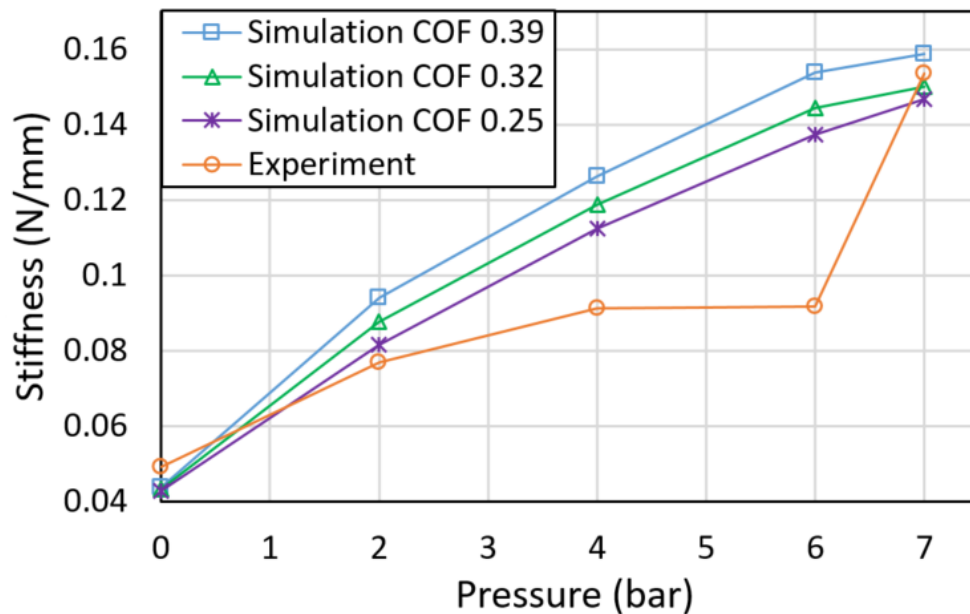


FIGURE 3.15: Comparison of stiffness from experiments and simulations with different COF between the layers

It is hypothesised that the discrepancies were probably caused by the curved shape of the sheets. As it was explained in Section 3.3.1, the sheets keep a curved shape due to the manufacturing process of the raw material, when they are assembled in the LJS, the curvature of the sheets generates gaps between them which reduces the area of contact. As a consequence, the friction force between the layers decreases as well. Including this phenomenon in the FE simulation by

altering the geometries of the sheets is very difficult since it would require knowing where the gaps are with accuracy.

The difference between simulation and experimental results at 4 and 6 bar could have another explanation apart from the gaps between the sheets. As it was explained in the section 3.3.3, the experiment requires the manual accommodation of the conical pin in the holes of the LJS before each test. At 4 and 6 bar, the manual accommodation of the pin could not have been appropriate, which may have an effect in the stiffness of the beam at these pressures.

Figure 3.15 also shows that the bending stiffness of the LJS with a conical pin increases when the COF between the layers increases. This behaviour was also observed in DLJ [9] for the case of only one clamp located at the free end of the DLJ structure. At low pressure, the friction force is small because the normal force between the layers is low. Therefore, the effect of variation in COF is not significant in the stiffness. At high pressure (7 bar), the best COF that fits the experimental results is 0.32 which suggests that this could be the actual average of COF between the layers of the LJS.

As a result of the manufacturing difficulties and their effect on the LJS performance, LJS with metallic layers was no longer investigated. Instead, future sections of this thesis use layers constructed using acrylonitrile butadiene styrene (ABS) plastic to overcome the aforementioned manufacturing challenges.

3.4 Trapezoidal Pin Mechanism

The trapezoidal pin mechanism is an evolution of the conical pin mechanism concept. This evolution is characterised by a change in the shape of the pin and a change in the material of the sheets in order to avoid the manufacturing problems that occurred with the conical pin mechanism.

The working principle of the trapezoidal pin mechanism and the conical pin mechanism are the same. Both mechanisms are based on the combination of the principles of mechanical interference and friction. The components of the trapezoidal pin mechanism can be seen in Figure 3.16. It consists of a trapezoidal pin that is coupled to the rod of a pneumatic actuator. Figure 3.17a

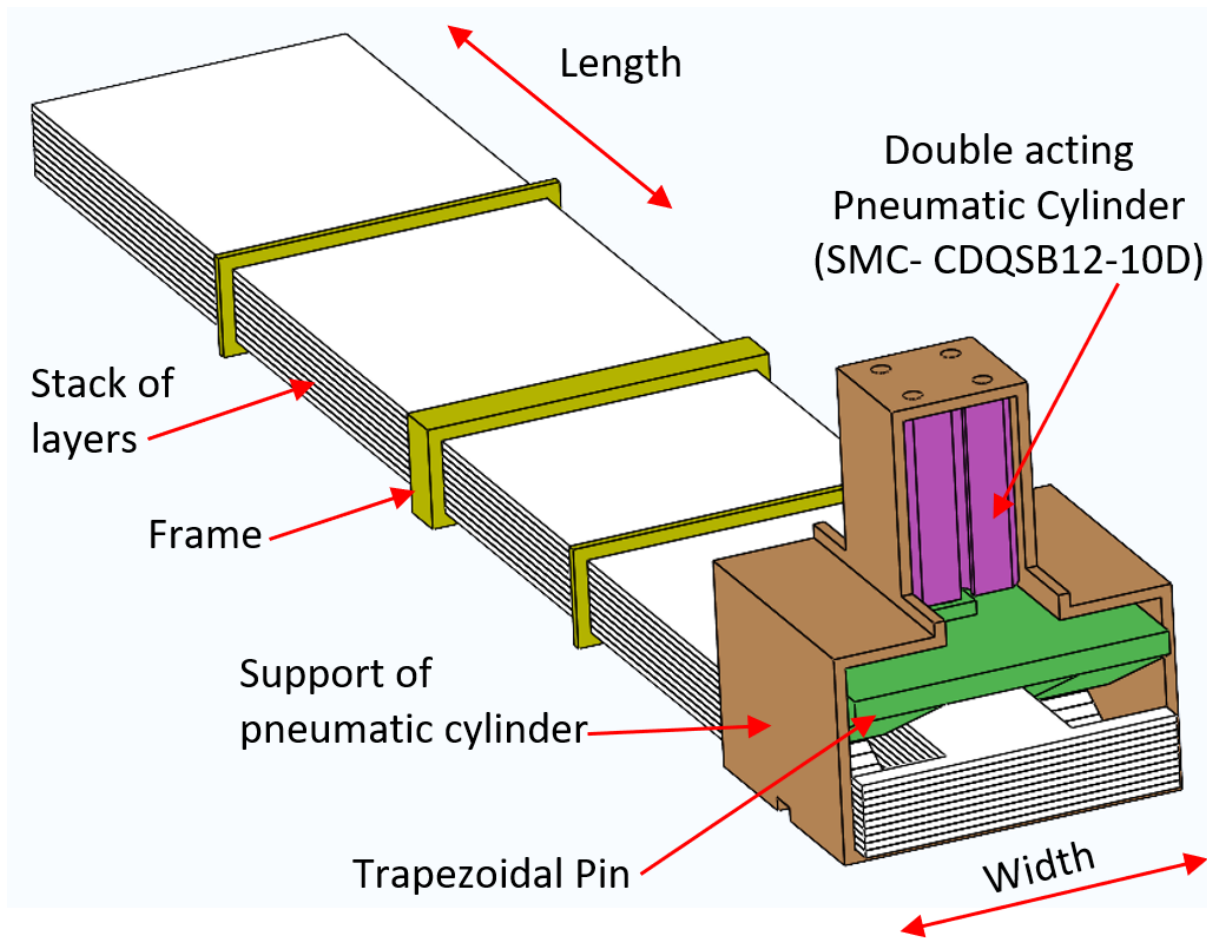


FIGURE 3.16: LJS with trapezoidal pin mechanism.

shows that when the pneumatic cylinder is pressurised, the trapezoidal pin is thrust into the trapezoidal slots formed in the sheets. The trapezoidal pin compresses the layers and raises the friction force between them in that section. The fact that the pin comes in and out of the LJS produces mechanical interference. When the trapezoidal pin is disengaged, the LJS has the lowest stiffness (Figure 3.16). When the trapezoidal pin is engaged, the stiffness of the LJS depends on the force that is applied to the pin, which in turn depends on the air pressure in the pneumatic actuator (Figure 3.17a).

The LJS with trapezoidal pin was compared to an LJS with a flat clamp that is illustrated in Figure 3.17b. Both LJSs have the same parts and dimensions and were simulated and tested under the same conditions. The concept of the flat clamp is similar to the concept of DLJ, which consists of many variable pressure clamps placed discretely along the LJS [9, 59]. The

main difference between these two LJ mechanisms is the width of the clamp. The clamps in DLJ have the same width as the stack of layers and make contact with them along the entire width. Instead, the proposed flat clamp has two contact areas whose width (20 mm) and length (59.08 mm) in the horizontal plane are identical to the contact areas in the trapezoidal pin to enable a fair comparison, as shown in Figure 3.17.

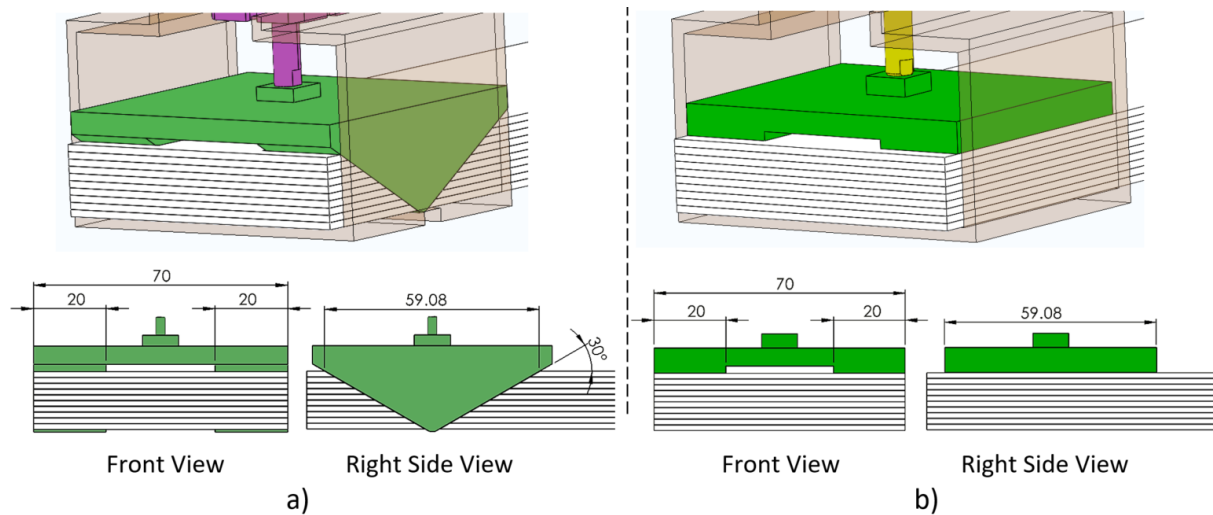


FIGURE 3.17: Front and right side view a) Trapezoidal pin b) Flat clamp. The other components of the proposed mechanism are hidden in this figure. All dimensions in mm.

3.4.1 Description of the Components of the LJS with a Trapezoidal Pin

The general characteristics of each component of the proposed LJ mechanism are described as follows.

Frames: As can be seen in Figure 3.16, three frames were placed along the LJS. Their main function is to avoid independent buckling of the sheets by keeping them together in one stack. The frame in the middle is notably longer than the other two frames. This feature was implemented to resemble the DLJ design that has a clamp of similar length in the same position [9, 59]. The frames do not constrain the relative slipping of the sheets because some of the frames are bonded to the top layer and others to the bottom layer, but none are bonded to both. In addition, a small clearance between the frames and the stack of sheets ensures they do not apply pressure on the LJS.

The performance of the trapezoidal pin mechanism will be compared against the DLJ, which only has one clamp at the free end of the structure. However, the middle clamp of the DLJ stiffens the structure in the middle section even when no pressure is applied to the clamp. Therefore, the length of the frame in the middle of the proposed LJS replicates the presence of the middle clamp in the DLJ in order to make a fair comparison between these two LJ mechanisms. The other two frames in the proposed LJS are shorter than the frame in the middle to minimize the stiffening effect in these locations.

Layers: The LJS has 10 layers made of ABS plastic with a thickness of 1.5 mm, length of 405 mm, and width of 70 mm. The material has a density of 1030 Kg/m^3 and a Young's modulus of 180 GPa. Each sheet has a cutout with a different length to accommodate the trapezoidal pin.

In order to make a fair comparison between the DLJ mechanism and the proposed mechanism in this section. The number, overall dimensions, and material of the layers are the same as the layers used in the DLJ mechanism.

Pneumatic Cylinder Support: This support, which is attached to a bottom layer, has enough height to let the trapezoidal pin completely emerge from the stack of sheets. Thus, it does not prevent the slip between the sheets.

Pneumatic Cylinder (SMC- CDQSB12-10D): This double-acting pneumatic cylinder was selected because of its high force per weight output compared to other actuators, such as solenoids. This pneumatic cylinder was manufactured by SMC (Tokyo-Japan).

Trapezoidal Pin The trapezoidal pin sits in the trapezoidal cutouts of the layers in such a way that it comes into contact with all the layers of the LJS. The pin has two trapezoidal protrusions that come in contact with the stack of layers in two areas that have a width of 20 mm each, as can be seen in Figure 3.16. The rod of the pneumatic cylinder is attached to the trapezoidal pin with a threaded connection.

The trapezoidal pin, the support of the pneumatic cylinder and the frames were manufactured by 3D printing (fused deposition modelling technology), and the material was polylactic acid (PLA).

Pneumatic Circuit: The pneumatic circuit has a 5/2 pneumatic valve with manual actuation that controls the motion of the cylinder rod. The circuit also has a pressure regulator that allows the control of the pressure in the whole circuit including the pneumatic cylinder.

3.4.2 Manufacturing

The layers are the components that require the most work and attention. The external shape of the layers was cut with a saw/router machine. The machining of trapezoidal cutouts in the layers is a critical task. Milling the trapezoidal slot in each layer separately was not a viable solution since any variation in the machining process of each layer would generate a step or a zig-zag pattern in the trapezoidal slots, as can be seen in Figure 3.18, which in turn would generate contact with the trapezoidal pin that occurs only in one specific layer instead of contact occurring in all the layers.

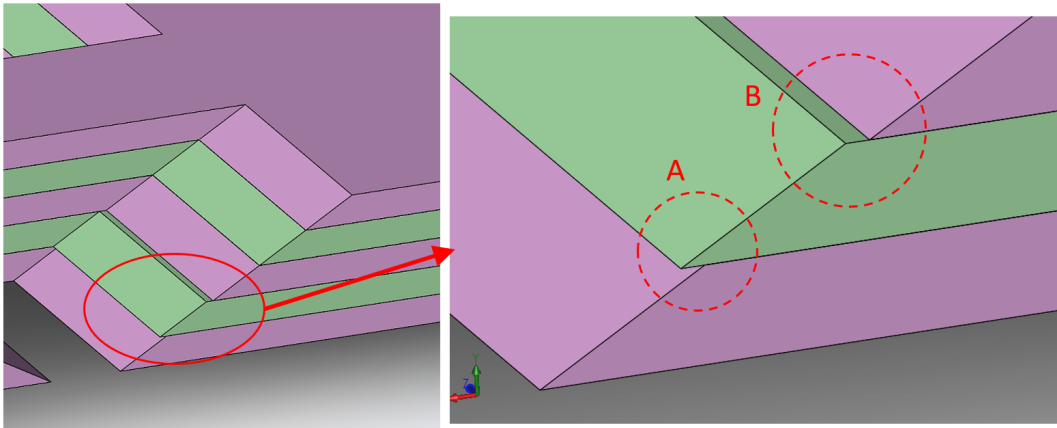


FIGURE 3.18: Zig-Zag and step patterns that may occur if layers are machined separately.

The solution to cut the trapezoidal slot in the LJS consisted on machining all the layers at the same time, as can be seen in Figure 3.19. A fixture comprising two sacrificial brass plates was implemented to achieve this purpose, all the layers and the brass plates are joined by bolts on one end of the LSJ. These plates have two functions. First, they keep the sheets together during the machining. Second, it allows to fix the LJS on the milling machine or the machining centre. As a result, there was no flutter or vibration of the ABS layers when the milling tool cut the trapezoidal slot.

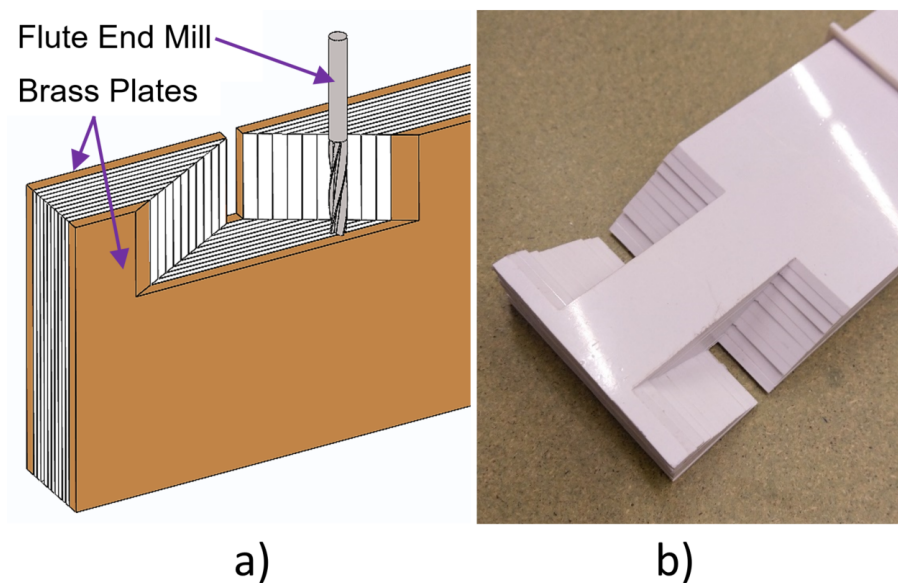


FIGURE 3.19: Manufacturing of the trapezoidal slots.

Machining was preferred over Laser cutting for layer manufacture because laser machines are not usually able to cut a chamfer since the laser is always perpendicular to the sheets. In addition, laser cutting produces toxic fumes when cutting ABS. Furthermore, machining would be more appropriate for manufacturing the layers in metallic materials, which is one of the directions of future work that is envisioned for LJS with a trapezoidal pin mechanism.

3D printing for layer manufacture was not selected due to insufficient dimensional accuracy, rough surface finish, and low repeatability of material and mechanical properties that characterize most of the 3D printing technologies of plastic materials [75], which does not give the researchers good confidence to replicate the results through experiments or FE simulations.

3.5 Experiment Setup

Table 3.2 summarises the main properties and dimensions of the LJS and the parameters of the bending test. The objective of the experiment was to determine the variation of bending stiffness of the LJS as a function of the air pressure in the pneumatic actuator. Figure 3.20 shows the components of the experimental setup. The LJS was fixed by a clamp at one end and deflected at the other end in the horizontal direction by a ZHIQU ZQ-21A-10 tensile testing machine

(manufactured by ZHIQU-mainland China). The load applied at the free end was measured by a ZHIQU DS2-20N force gauge that has an accuracy of $\pm 0.2\%$ FS and a resolution of 0.01 N (manufactured by ZHIQU-mainland China). The tip deflection was measured by a digital caliper that has a resolution of 0.01 mm.

TABLE 3.2: Experimental Specifications

Specification	Value
Layer length	400 mm
Layer width	70 mm
Layer thickness	1.59 mm
Total thickness of LJS	15.9 mm
Number of layers	10
Layer material	ABS plastic
Youngs modulus of ABS	1.8 GPa
Density of ABS	1030 kg/m ³
Friction coefficient between layers	0.253
Friction coefficient between layers and the trapezoidal pin	0.126
Pressure in the pneumatic cylinders	0, 50, 200, 400, 600, 800 kPa

The pneumatic cylinder is controlled by a pneumatic circuit that has a 5/2-way valve with manual actuation, as can be seen in Figure 3.20. The circuit also has a pressure regulator that controls the pressure in the whole circuit, including the pneumatic actuator.

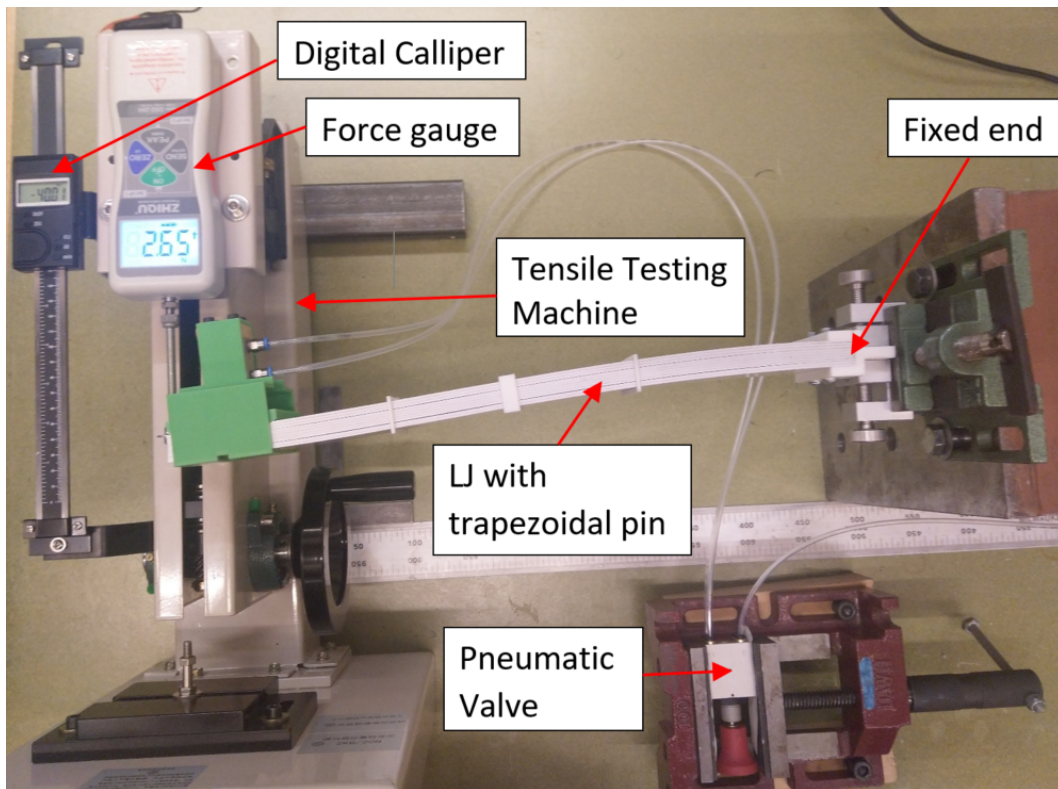


FIGURE 3.20: Experimental Set up.

3.5.1 Experimental Procedure

The experiment of force vs deflection consisted in the application of a complete load-unload cycle at 800, 600, 400, 200, 50, and 0 kPa of pressure in the pneumatic actuator. In the LJS with trapezoidal pin, the experiment starts with the loading procedure, where the deflection rises every 4 mm, from 0 mm to 40 mm, which is about 10% of the total length of the LJS. Then, the unloading procedure starts by diminishing the deflection in steps of 2 mm, from 40 mm until a deflection where the force gauge measures 0 N. The experimental procedure for the LJS with flat clamp was the same, except for the loading procedure where the deflection is incremented every 2 mm from 0 mm to 12 mm, and then every 4 mm up to 40 mm. When the pressure in the pneumatic cylinder is zero, the cylinder rod is retracted so that the flat clamp or the trapezoidal pin is not in contact with the stack of layers.

For both LJSs, the values were recorded after the force had reached a stable value. For this reason, it can be considered that the LJS are loaded and unloaded quasi-statically.

3.5.2 Results of Experiments

Figure 3.21a illustrates the results of the experiments for the LJS with trapezoidal pin at 50 kPa in the pneumatic cylinder. The loading procedure is represented by the upper branch of the curve. The unloading procedure is represented by the lower branch of the curve. Three trials were carried out at each pressure value. Similar Experiments carried out in DLJ [9] and LJ based on vacuum pressure [15] also carried out three trials at each pressure value. The average force obtained for a given deflection is represented by the points in Figure 3.21, and the error is illustrated through the error bars that reflect the range of force values obtained for a given deflection. A similar procedure to illustrate the error in stiffness experiments was implemented in robots with leg locomotion [73].

Figure 3.21 shows the presence of the hysteresis phenomenon in the LJS. The presence of hysteresis is likely due to the friction force between the LJS components. The friction force is a non-conservative force that dissipates energy during the loading cycle. This phenomenon is also present in other lock/unlock mechanisms of LJS [6, 7, 9, 72].

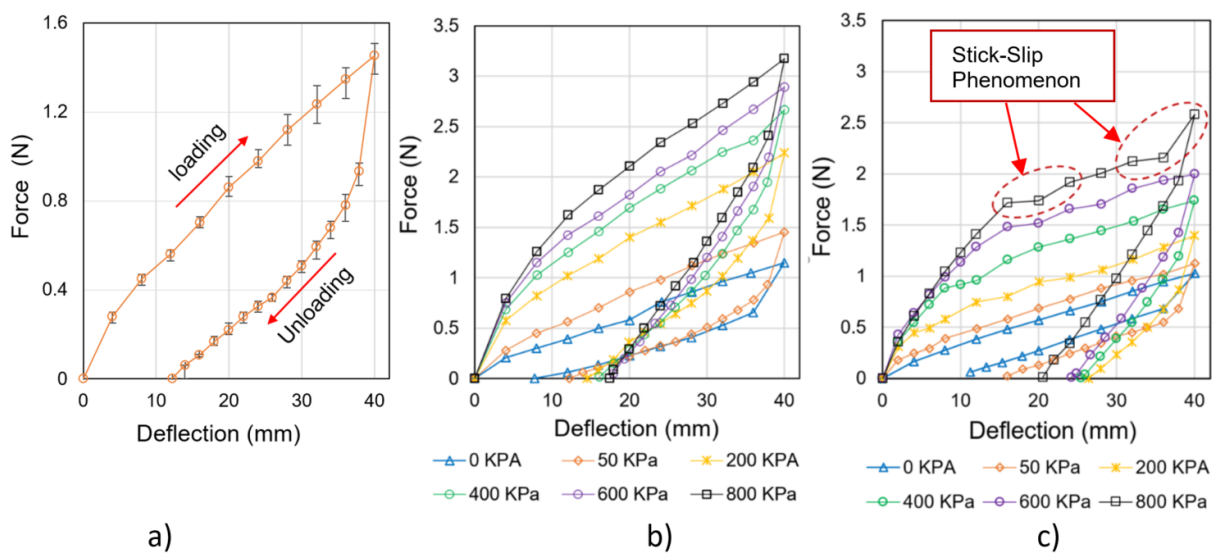


FIGURE 3.21: Results of the experiments, a) LJS with trapezoidal pin at 50 kPa. b) LJS with trapezoidal pin. c) LJS with flat clamp.

The bending stiffness of the LJS is calculated from the slope of the force vs deflection curve. To compare the bending stiffness of the LJS at different air pressures in the pneumatic cylinder, the results of the experiment at each pressure value were linearised using the least squares method

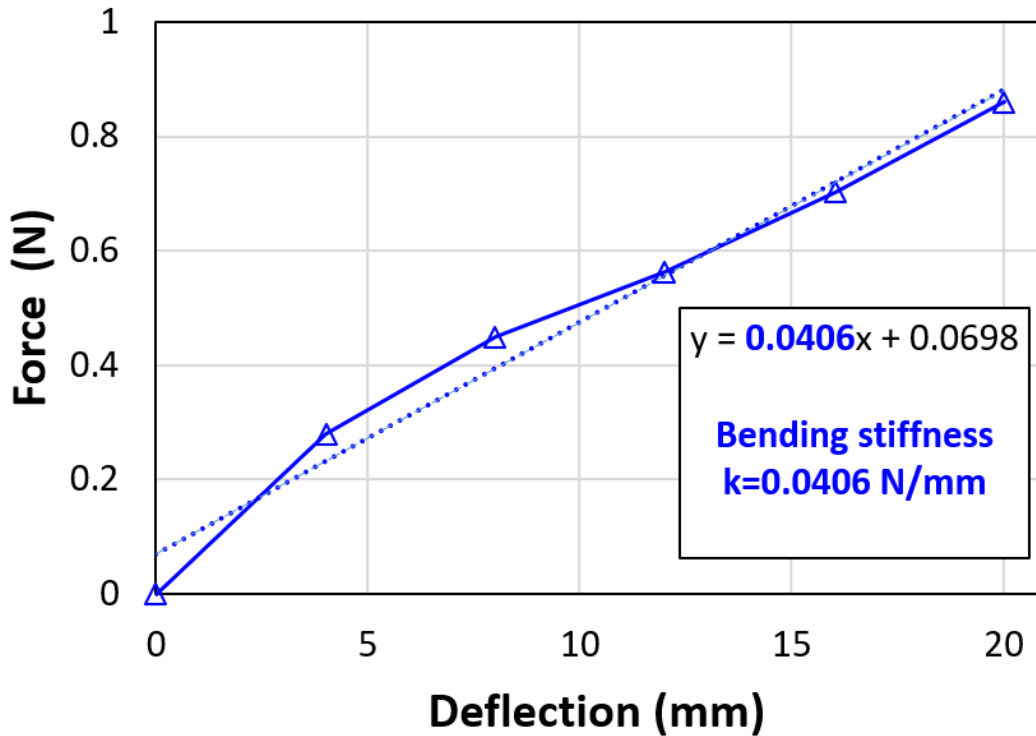


FIGURE 3.22: Results of the experiments and linearisation when LJS with trapezoidal pin is at 50 kPa.

to generate a straight line whose slope is the bending stiffness k [6, 9, 39]. Figure 3.22 shows that the linearisation includes only the points from 0 mm to 20 mm in the loading part of the cycle, which was the same range that was considered in the linearisation of the DLJ experiments [9, 59].

The bending stiffness calculated from the linearisation of the results at each state of pressure is illustrated in Table 3.3. It can be observed that, as expected from the working principle of the LJS, the maximum stiffness and minimum stiffness correspond to the maximum (800 kPa) and minimum (0 kPa) air pressure, respectively. The maximum stiffness ratio is calculated as the ratio between the maximum stiffness and the minimum stiffness [59], which yields 3.17 for the LJS with flat clamp and 3.65 for the LJS with trapezoidal pin.

3.5.3 Discussion

The stiffness ratio of the LJS with trapezoidal pin (3.65) is much less than the theoretical maximum that could be reached if all the layers were joined to form one solid beam (100 for

TABLE 3.3: Bending stiffness for each state of air pressure from the experiments. (units in N/mm)

Stiffness (N/mm)	Pressure (kPa)					
	0	50	200	400	600	800
Trapezoidal pin	0.0276	0.0406	0.0646	0.0788	0.0887	0.1008
Flat Clamp	0.0279	0.0313	0.0407	0.0582	0.0731	0.0886

N=10). This difference in the stiffness ratio exists because of multiple factors that affect the effectiveness of the trapezoidal pin mechanism. Some of these factors are discussed later in this section and in Section 3.7. The limitation in reaching a higher stiffness ratio in this test is purely technical. In this case, the stiffness ratio is limited by the maximum pressure that the air compressor is able to supply (800 kPa). If the air compressor were able to supply 1000 kPa, which is the maximum operative pressure of the pneumatic actuator, the stiffness ratio may be higher.

Figure 3.21b and Figure 3.21c show an important difference in the loading part of the cycle between the flat clamp and the trapezoidal pin. The LJS with a trapezoidal pin has a nearly constant stiffness (slope of the curve), whereas the LJS with a flat clamp has sections where the stiffness declines and then rises again, as can be observed in the encircled areas in Figure 3.21c. This behaviour demonstrates that the phenomenon of stick-slip intermittent motion is present in the LJS with the flat clamp. In this case, the layers stick together for a while, then they slip suddenly, and then stick again, repeating this cycle. When the layers slip abruptly, the LJS stiffness decreases. Then, when the layers stick again, the LJS stiffness increases. This stick-slip motion was also observed visually during the flat clamp experiment and is present in other LJSs with friction mechanisms applied to VSLs [20, 59]. No stick-slip was noticed during experiments utilising the trapezoidal pin.

Table 3.3 and Figure 3.27 show that the LJS with the trapezoidal pin reaches larger stiffness values than the LJS with the flat clamp for almost all the pressure states in the pneumatic cylinder. Thus, the maximum stiffness ratio for the LJS with a trapezoidal pin is about 15% larger than the stiffness ratio of the LJS with a flat clamp.

The behaviour of the LJS with a trapezoidal pin also depends on other parameters, such as the number of layers, the location of the actuators, the number of actuators, and COF. These parameters were not included in this research because they have been extensively investigated in relation to DLJ [9, 59]. The conclusions obtained in DLJ studies can be applied to the trapezoidal pin mechanism because both mechanisms have in common the concept of discrete actuators placed in particular locations of the LJS. For example, the stiffness ratio of DLJ increases when the number of clamps placed along the beam increases. Similarly, if multiple trapezoidal pin mechanisms are placed along the LJS, the stiffness will increase significantly.

Although the effect of the COF was not investigated in the trapezoidal pin mechanism and the flat clamp mechanism, this parameter was studied in the LJS with the conical pin mechanism as presented in Section 3.3.7.1. It should be noted that the trapezoidal pin mechanism is an evolution of the conical pin mechanism. Therefore, the conclusion obtained for the effect of COF in the conical pin mechanism can be applied to the trapezoidal pin mechanism.

DLJ reaches a stiffness ratio of 5 when only the end clamp is implemented [59]. This mechanism surpasses the stiffness ratio of the LJS with a trapezoidal pin and the LJS with flat clamps. However, it is necessary to consider important differences between these LJ mechanisms, such as the contact areas between the clamp and the layers and the presence of frames along the LJS. Therefore, it is not possible to definitely conclude that the LJ mechanisms presented in this chapter are less effective than DLJ.

The speed of the stiffness change in the LJS with a trapezoidal pin mechanism proposed in this chapter was not measured. However, the time that the piston rod takes to enter the cylinder at 1000 kPa is roughly estimated at 0.02 s based on calculations that took into account the speed of the piston (500 mm/s) and the stroke (10 mm). This time is shorter than 0.1 s, which is the duration in the human body of the dynamic effects caused by an impact against a robot manipulator [76], showing that this pneumatic system has the potential to attenuate the effects of this type of collision. This will be explored in Chapter 6 in which the speed of destiffening of an LJS with a pneumatic trapezoidal pin mechanism is measured through experiments. The tests demonstrate the capacity to attenuate the impact force due to collisions within a period shorter than 0.1s.

3.6 Modelling of the Trapezoidal Pin Mechanism

The following section presents the analysis of trapezoidal pin mechanics using the FE simulation. This section begins with a review of the methods to model LJSs, then FE simulations of the trapezoidal pin mechanism are presented, followed by a comparison of the FE simulation results and the experimental results presented in Section 3.5.2.

3.6.1 Modelling of LJ Mechanisms

Modelling of the LJ mechanism typically focuses on finding the relation between the applied force and the deflection of the LJS. Additionally, researchers are concerned with how this relationship can be modulated by the lock/unlock mechanism utilised.

The research on LJ based on friction has adopted two approaches to modelling the behaviour of the LJS. The first approach consists of the use of the Coulomb model of friction [6, 19, 39]. The second approach is the energy method to calculate the relation between the force and the deflection of the LJS. This method formulates how the work done by the external force is transformed into deformation energy due to bending and the work done by the inter-layer friction. Examples of this method are the research presented in [6], which only calculates the deformation energy due to bending for a cantilever LJS, and the work presented in [8] that calculates the elasticity energy due to bending and work done by the inter-layer friction in a LJS in which both ends are fixed.

Finite element analysis (FEA) has been employed to study multiple lock/unlock mechanisms for LJ. This tool has proven to be a useful and accurate method to predict the performance of many LJ mechanisms. For instance: FEA simulations in 3D were carried out for LJS wrapped by SMA [6], for DLJ [9]; FEA simulations in 2D were carried out for the LJSs that are activated by vacuum pressure [7, 77]; LJ with heating blankets was simulated in 2D using FEA as well [70].

FEA has been carried out to study the effect of critical design inputs on the performance of the LJSs. For instance, the effects of changing the number of layers, vacuum pressure, and coefficient of friction of the layers have been analysed extensively in LJSs that are activated by vacuum

pressure to extract the stiffness and damping values of the LJSs [7]. Another example occurred in LJSs with heating blankets where FEA simulations allowed the exploration of the possible improvement in performance through the appropriate combination of factors that characterise this type of LJ mechanism [70]. In addition, FE simulations were also employed to study the design variables that affect the DLJ mechanisms, such as clamp width, middle clamp location, number of clamps, number of layers, and friction coefficient between the laminates [9, 59].

The following subsection explains how FE simulations were used to investigate the mechanical behaviour of the LJS with a trapezoidal pin mechanism. In particular, the FE simulations were used to calculate the bending stiffness of the LJS and to describe the contact between the trapezoidal pin and the layers during the deformation of the structure. This mechanism has not been studied through FE simulations before because of its novelty.

3.6.2 FE Simulation of the Trapezoidal Pin and Flat Clamp

FE simulations were selected as the methodology to investigate the trapezoidal pin mechanism. There are two main reasons for this choice. First, FE simulations have been used successfully to study other mechanisms to vary the stiffness of LJSs, as explained in the previous section. Second, similarly to the case of LJ with a vacuum pressure mechanism, FE analysis would be favoured over analytical models because analytical methods are algebraically taxing. Developing analytical methods for the trapezoidal pin mechanism could be even more difficult since this new mechanism combines the principles of friction and mechanical interference. Analytical models are also difficult to formulate in this case because the contact between the layers and the trapezoidal pin was unknown. Similar to the case of the conical pin mechanism presented in Section 3.2.3, the trapezoidal pin experiments showed that the deformation of the LJS contributes to disengaging the pin from the layers due to its trapezoidal shape, but the details of the contact between the trapezoidal pin and the layers could not be observed because the support of the pneumatic cylinder hid the contact zone. Therefore, FE simulations were the only viable alternative to visualize how the contact between the trapezoidal pin and the layers occurs during the deformation of the beam

The FE models were developed in Ansys with the same components and dimensions as the experimental setup presented in Section 3.4.1 and Section 3.5. The FE model has the same

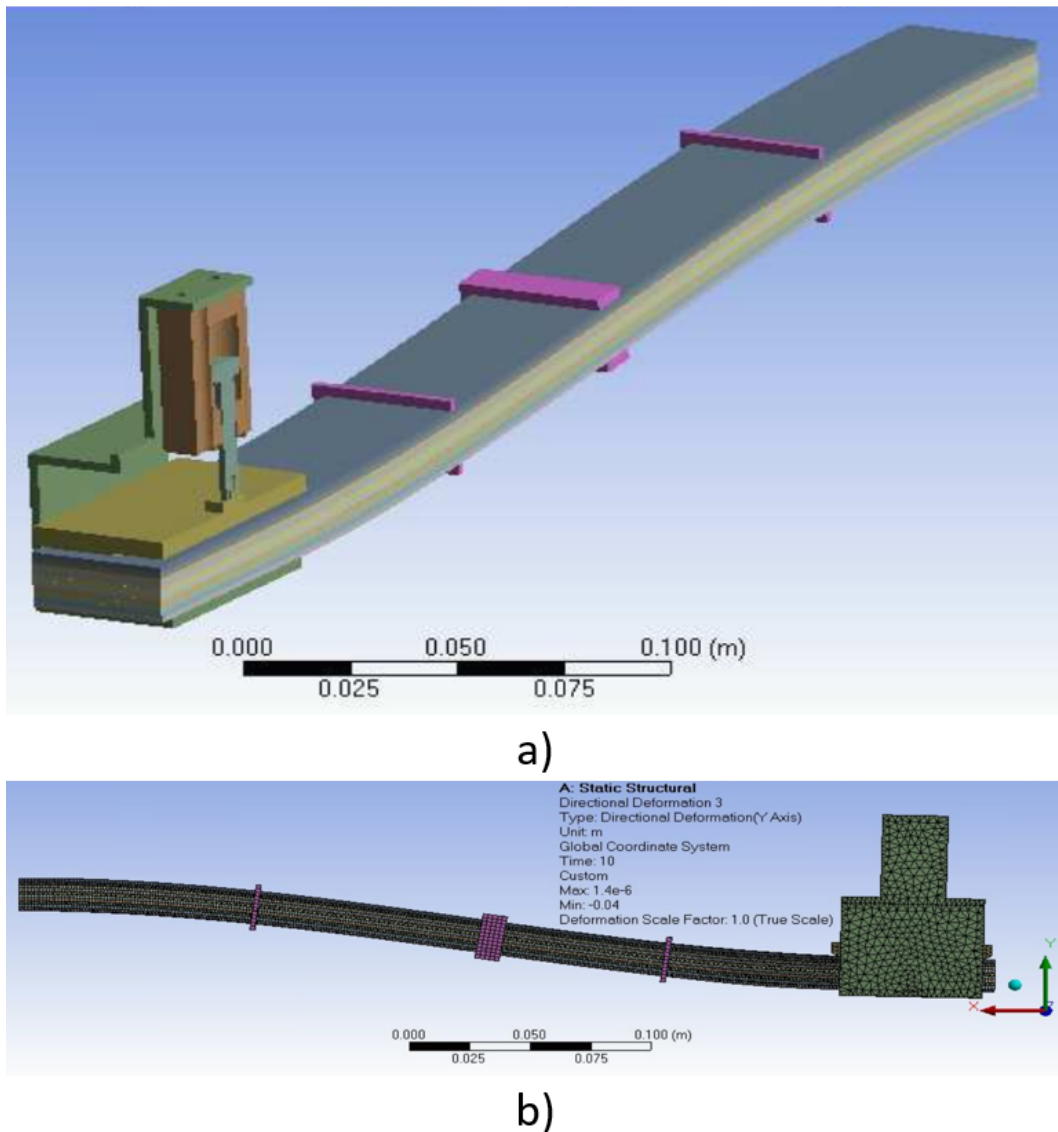


FIGURE 3.23: Resulting shape of LJS with trapezoidal pin mechanism at 800 kPa from FE simulation a) Perspective view of one half of the LJS. b) Side view of the LJS.

geometry, materials, boundary conditions and load conditions that were implemented in the experiment. This means that the LJ model is fixed at one of its ends, the deflection is applied at the free end following the same values that were imposed in the test, the pressure in the pneumatic cylinder is implemented as a pair of forces that are applied to the cylinder body and the cylinder rod, the value of these forces corresponding to the forces applied by the cylinder when it is pressurised at the same values of pressure of the experiment. The result of the simulations was the force associated with each value of the applied deflection.

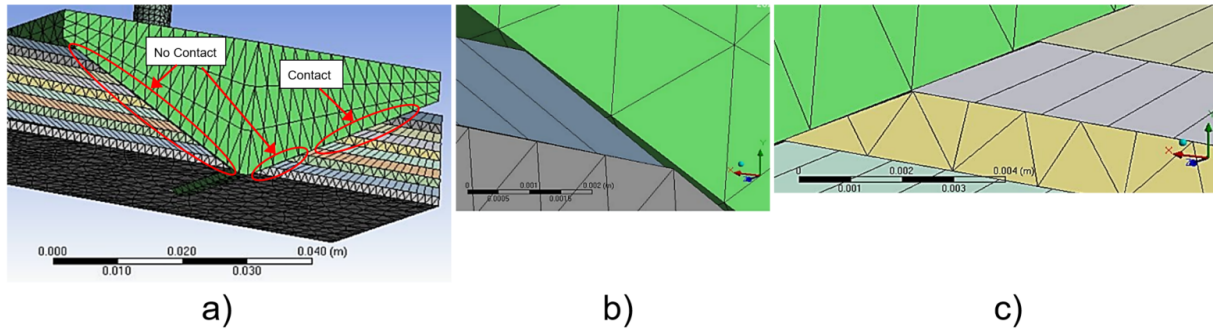


FIGURE 3.24: FE simulation of LJS at 600 kPa and 40 mm of deflection at the free end. a) contact between layers and trapezoidal pin. b) Detail view of the contact zone. c) Detail view of the no-contact zone in the rear of the pin. The support of the pneumatic cylinder is hidden in this figure.

The coefficient of friction (COF) between the sheets was measured using an inclined-plane friction device [74]. The same experiment was conducted between the layers and trapezoidal pin, as well as between the sheets and flat clamp. The results of these tests indicate that the COF between the sheets is 0.253, the COF between the layers and flat clamp, and the COF between the layers and trapezoidal pin is 0.126. These COF values were used in the FE simulations.

The most relevant details about the pre-processing of the simulation are described as follows: Only one half of the LJS is modelled, and symmetry along the longitudinal plane was imposed, as can be observed in Figure 3.23a. The mesh of the sheets is composed of elements of quadratic order, and all the layers have one element across the thickness. The Static Structural Solver was selected to carry out the simulation because the experiment was conducted in quasi-static conditions. *Large deflection* is turned on, considering that the maximum deflection in the experiment was about 10% of the length of the LJS. The setup of the contact among the sheets, and between the sheets and the pin had a critical role in the convergence of the solution. In this aspect, the most relevant parameters are the Contact Formulation which was selected as Augmented Lagrange, the stiffness is updated in each iteration, and the normal stiffness factor is set up as 0.01. The maximum number of equilibrium iterations per solution step is 50 and was defined through the command NEQIT. These settings are summarised in Table 3.4.

Figure 3.23b shows the shape of the LJS with trapezoidal pin at a locking pressure of 800 kPa when it reaches 40 mm of deflection, which is the maximum deflection of the free end that was applied in the experiment and replicated in the simulation. It can be seen that the LJS structure under transverse load has an "S" shape, which means that the curvature of the LJS reverses

TABLE 3.4: Most Relevant settings of the FE simulations in Ansys

Parameter	Value
Large Deflection	on
Maximum number of equilibrium iterations	50 (using the command NEQIT)
Mesh	
Element Order	Quadratic
Number of elements across the thickness of each layer	1
Contact between layers and between layers and trapezoidal pin	
Type	Frictional
Contact Formulation	Augmented Lagrange
Normal Stiffness Factor	0.01
Update Stiffness	Each Iteration

along the structure. This phenomenon occurs because the trapezoidal pin mechanism reduces the relative slip between the layers and makes the LJS straight in that section. The relative slip between the layers is also constrained in the clamp end, which makes the LJS straight in that section as well. As a result of these constraints in the clamp end and the free end of the LJS, the bending deformation concentrates in the middle part of the beam where the relative slip between the layers is not constrained, and the curvature can have high values. The same phenomenon was observed in the LJS with conical pin [72] and the DLJ [9].

Figure 3.24 illustrates some details that were impossible to observe in the bending test. Figure 3.24a and Figure 3.24c show that the trapezoidal pin only keeps contact with some of the top sheets in the front of the pin. Figure 3.24b illustrates how the contact between the layers and the trapezoidal pin is missing in the back part of the pin. This figure also shows the relative slip between the sheets. The areas of contact and no-contact are more evident in Figure 3.43. The consequences of the existence of these areas are also explained in the section 3.7.4.

The cause for the existence of the contact and no-contact zones is the fact that slip between the layers depends on the distance from the clamp end to the position of analysis along the LJS. When the LJS is bent, the slip between the layers in the clamp end is zero, then the slip differs from zero as the point of analysis moves along the beam [7]. In addition, the slip between the layers also depends on the position of the layers in relation to the bottom layer. It is necessary to remember that trapezoidal pin is ultimately attached to the bottom layer. In other words, the trapezoidal pin can move perpendicularly to the bottom layer, but both components remain

in the same position along the beam. Therefore, when the LJS is bent, all the layers move, or try to move, in relation to the trapezoidal pin, except for the bottom layer.

Another aspect that was investigated through the FE simulations is the possibility of plastic deformation of the ABS sheets during the bending experiments. Figure 3.25 illustrates the Von-Mises stresses of the ABS laminates when air pressure in the cylinders is 800kPa and the deflection in the free end of the LJS is 40 mm (the same simulation as Figure 3.23), which was the maximum deflection in the experiment. It can be seen that the maximum stress in the sheets is 10.8 MPa and occurs in the trapezoidal slots in the top layers. The maximum stress at this point is probably caused by the contact between the trapezoidal pin and the top layers. Another cause of the maximum stress in this location is the proximity to the edge where the trapezoidal slot starts, which generates a stress concentration factor. This stress value is less than the yield strength of ABS (39 MPa according with the sheets manufacturer). Therefore, plastic deformation does not occur in the ABS sheets. This result matches the experiment where no damage or plastic deformation in the ABS sheets was observed after the bending tests.

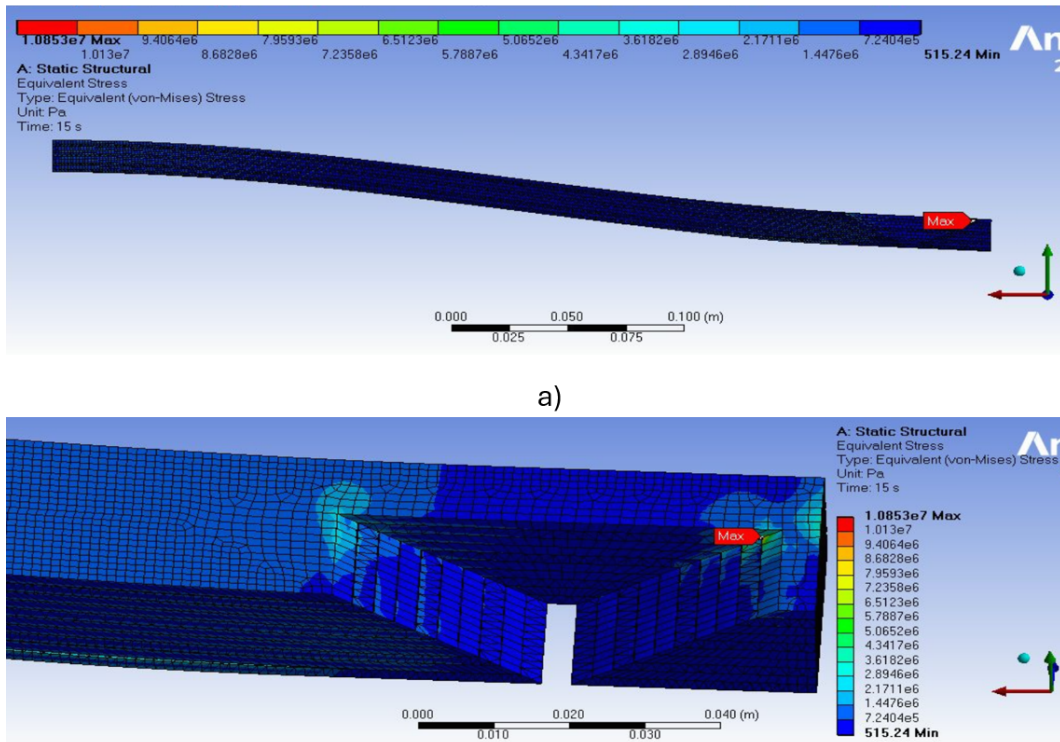


FIGURE 3.25: Von-Mises stress in the sheets of the LJS with trapezoidal pin at 800 KPa and 40mm of deflection. a) side view of LJS. b) Detail of the location of maximum stress. The other components of the trapezoidal pin mechanism are hidden.

3.6.3 Experiments Versus Simulations

Figure 3.26 shows the results of the experiment compared with results from the FE simulations for the LJ with trapezoidal pin at 50 kPa. It can be seen that the simulation results agree well with the experimental results. The results are compared from 0 mm to 20 mm in the loading part of the cycle, as the same range was considered in the studies about DLJ [9, 59]. The results were a stiffness of $k=0.0369$ N/mm in the simulation, and a stiffness of $k=0.0406$ N/mm in the experiment. Thus, the simulation error relative to the test is about 9.1% in this case.

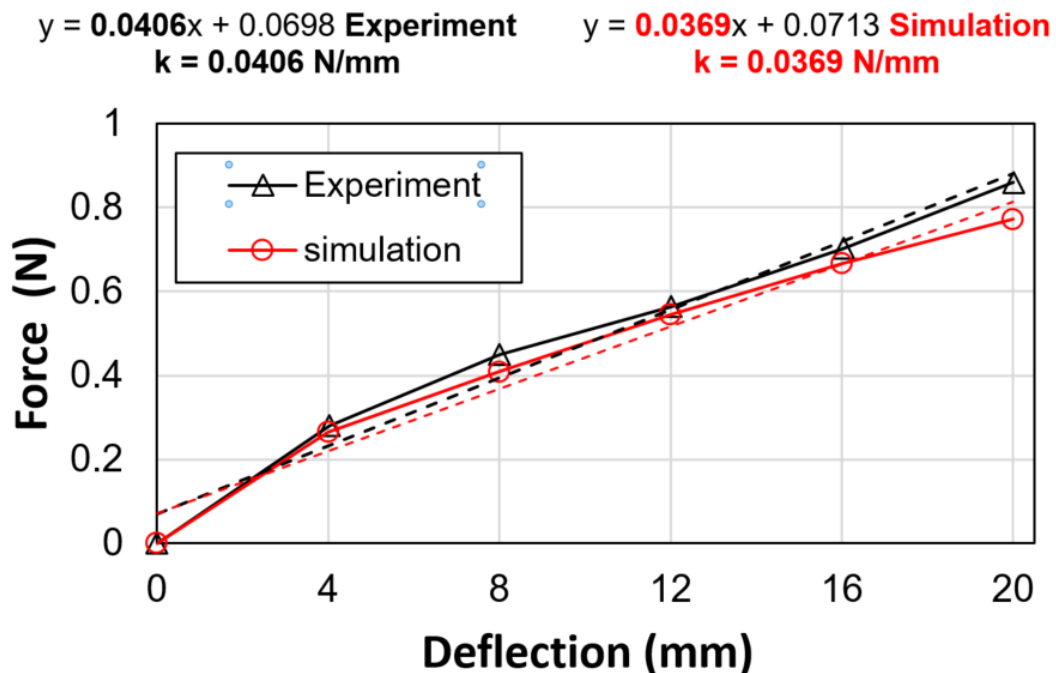


FIGURE 3.26: Force-deflection curves for 50 kPa of pressure from FE simulation and experiment in the LJS with trapezoidal pin.

Figure 3.27 shows a comparison of the simulation and the experimental stiffness values for all pressure states that were tested in the experiments. For the case of the LJS with trapezoidal pin, it can be seen that the results of the simulations match well with the results of the experiment. The maximum difference is about 10% and occurs at 0 kPa. This difference occurs because the ABS layers are not totally flat which results in gaps between the sheets when there is not any locking force that keeps them together. On the other hand, the ABS layers in the simulations are modelled as totally flat and they remain together even when there is not any locking force on them. For the case of the LJS with a flat clamp, it can be seen that the results of the

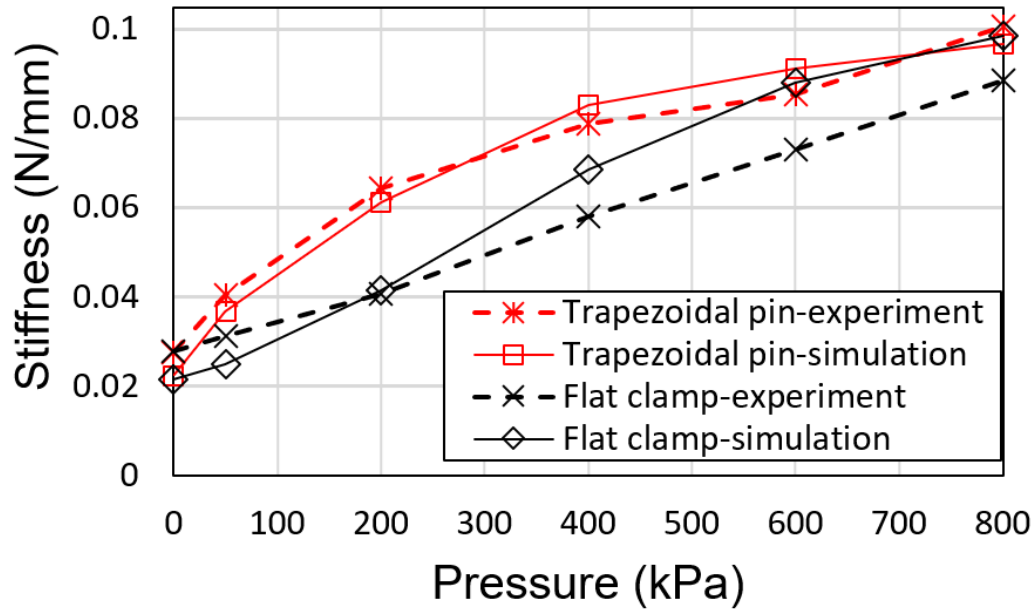


FIGURE 3.27: Comparison of stiffness from experiments and FE simulations.

simulation follow the same trend of the experiment but with a maximum error of about 20%. The FE simulations do not present the stick-slip phenomenon that occurs in the tests of the LJS with flat clamp, which may be the cause of the difference between the experimental and the simulation results in this case.

3.7 Computational Studies

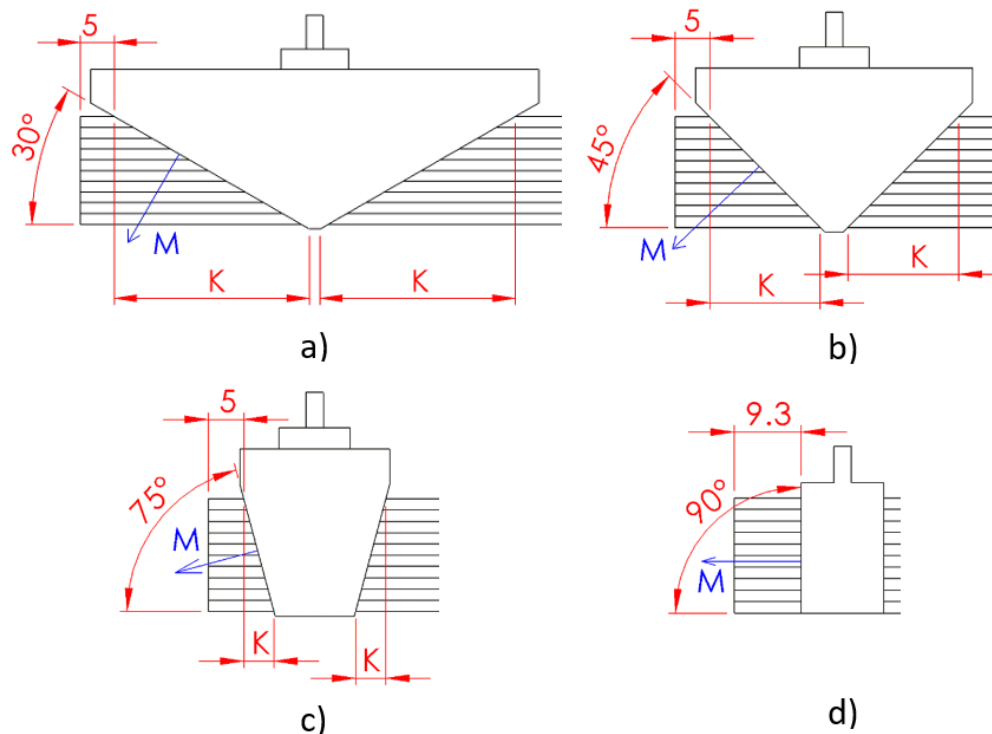
Section 3.6.3 demonstrated that the FE simulations match well the results of the experiment in the case of the trapezoidal pin. Therefore, FE simulations of the trapezoidal pin were validated as an analysis tool. In consequence, this section presents more studies of the trapezoidal pin based on the use of FE simulations

A series of computational studies were carried out in order to optimise the design of the LJS with trapezoidal pin and develop an understanding of how some design parameters affect the bending stiffness. The key parameters that were analysed through FE simulations were the angle of the trapezoidal pin and the number of frames. In addition, the behaviour of the LJS with trapezoidal pin when it is bent upward and its behaviour at high deflections were also

analysed through FE simulations. Other parameters such as the number of layers, the number of actuators, the location of the actuators and the effect of the friction coefficient between the layers were not simulated because they have been extensively studied in similar mechanisms such as the DLJ [9, 59] and the conical pin mechanism [72].

3.7.1 Effect of the Angle of the Trapezoidal Pin

To study the effect of the angle of the trapezoidal pin on the LJS stiffness, FE simulations with various pin angles were performed. The setup of this case study is illustrated in Figure 3.28. The overall dimensions of the LJS, the number of sheets, the materials, the load conditions and the settings of the FE simulations for all trapezoidal pins are equal to the LJS described in Section 3.4.1 and Section 3.6.2.



M = Direction of the contact between layers and pin
K = Section of the LJS under the effect of the locking force applied by the pin

FIGURE 3.28: Trapezoidal pins with different angles. a) 30° Trapezoidal pin b) 45° Trapezoidal pin c) 75° Trapezoidal pin d) Straight pin. All dimensions are in mm.

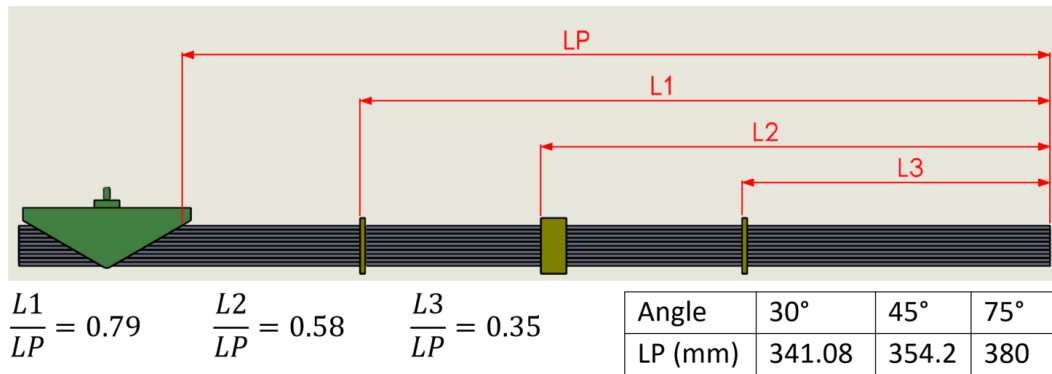


FIGURE 3.29: Position of frames for the LJS investigated through FE simulations.

As it will be explained in Section 3.7.2, three frames generate the maximum stiffness ratio in the LJ with trapezoidal pin. Therefore, all of the LJSs that were studied have three frames. The frames are placed along the beam at lengths that keep the same proportion in relation to the distance LP that is illustrated in Figure 3.29.

Figure 3.28 shows four different pin angles that have been studied, including 30°, 45°, 75° and the straight pin. The straight pin is considered as a trapezoidal pin with an angle of 90°. It is clear that the angle of the trapezoidal pin and the contact area between the pin and the layers are related. Therefore, they cannot be changed independently. The parameters that remain unchanged between the cases are the position of the pin and the width of the contact areas of the pin. All the pins were located at 5 mm from the free end of the LJS, except for the straight pin which cannot be placed at that position because there would not be enough space to place the support of the pneumatic cylinder. In relation to the width of the pins, they have the same two contact zones whose widths are 20 mm each and separated by a gap as illustrated in Figure 3.17. The only exception is the straight pin that only has one contact area for reasons of simplicity as can be seen in Figure 3.30. The flat clamp was not included because its FE simulation was not accurate enough according to Figure 3.27.

Figure 3.31 illustrates the results of the simulations for each pin. It can be seen in this figure that the trapezoidal pins at 30°, 45° and 75° present a growing trend between the pressure and the stiffness. The increment of the stiffness is larger at low pressures (less than 200 kPa), and then the stiffness increments are lower at large pressures (more than 400 kPa). It is important to note that the stiffness at 0 kPa corresponds to the situation when the pin is disengaged from the layers.

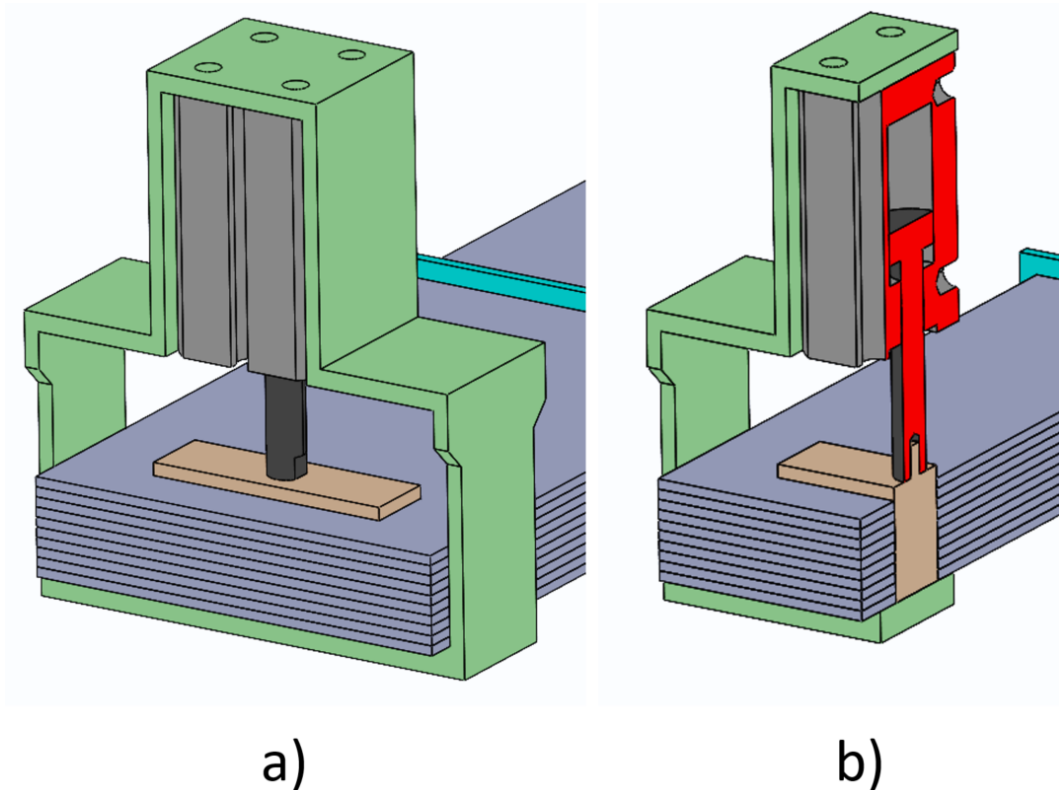


FIGURE 3.30: LJS with straight pin. a) Straight pin inside the LJS. b) Longitudinal cross-section of the LJS with straight pin.

As explained in Section 3.4.1 the trapezoidal pin mechanisms are based on a combination of the principles of friction and mechanical interference. The angle of the trapezoidal pin affects the amount of friction force versus mechanical interference generated by the pin. In relation to the friction force, it should be noted that the size of the beam section where the locking force is applied depends on the angle of the trapezoidal pin as can be seen in Figure 3.28 where the dimension K represents the section of the LJS that is affected by the trapezoidal pin. In particular, as the angle of the trapezoidal pin decreases, the pin becomes flatter and the section of the beam under the effect of the pin increases. Thus, the friction force between the layers is larger. In relation to mechanical interference, as the angle of the trapezoidal pin increases, the pin becomes steeper and the interference phenomenon grows because the direction of the contact between the layers and the pin gets close to the parallel direction to the layer as shown in Figure 3.28, where vector M is the direction of the contact between the layers and the pin. Therefore, as the angle of the pin increases, the effect of the mechanical interference becomes stronger while the effect of the friction force fades. It can be inferred that the flat clamp (angle 0°)

is the extreme case where there is only friction force and no mechanical interference. In contrast, the straight pin (angle 90°) is the extreme case where there is only mechanical interference and no friction force.

While trapezoidal pins of 30° , 45° and 75° have a growing trend between the stiffness and the pressure, the straight pin reaches its maximum stiffness at the lowest non-zero pressure tested (50 kPa), and then the stiffness remains constant for higher pressures because there is only mechanical interference and the increase in pressure does not generate additional friction force between the layers. This behaviour indicates that the straight pin works as an on-off mechanism, whereas the other trapezoidal pins work as continuous mechanisms that are able to modulate the stiffness. These observations make it clear how the interference mechanism differs from the friction force mechanism. The straight pin, which is a pure interference mechanism, can not compress the layers. Instead, it prevents the relative slip of the layers, which combined with the action of the frames that will be explained in Section 3.7.2, block the independent bending of each layer and force them to bend as a whole beam, increasing the bending stiffness.

Figure 3.31 shows that the 30° trapezoidal pin has the largest stiffness for pressures higher than 500 kPa. In contrast, the 75° trapezoidal pin and the straight pin have the largest stiffness at pressures lower than 200 kPa. This behaviour shows that the effect of the friction force is dominant at high pressures (more than 500 kPa) and the effect of mechanical interference is dominant at low pressures (less than 200 kPa). At low pressures, the 75° trapezoidal pin has the highest stiffness because most of its stiffness comes from mechanical interference, while the stiffness of the 30° trapezoidal pin is the lowest because its mechanical interference is scarce and the friction between the layers is low because the pressure is low as well. At higher pressures, the 30° trapezoidal pin has the maximum stiffness which comes mainly from the friction force that is high due to high pressure and the large area of the layers that are under the effect of the pin. In contrast, the stiffness of the 75° trapezoidal pin is lower because most of its stiffness comes from mechanical interference that does not grow significantly at higher pressures, while the generated friction force is low due to the small area of the layers under the effect of the pin.

The behaviour of the LJS with trapezoidal pin and DLJ differs considerably in terms of the relation between the contact area and the stiffness. It was explained above that the contact area increases when the angle of the trapezoidal pin decreases. However, It should be noted that

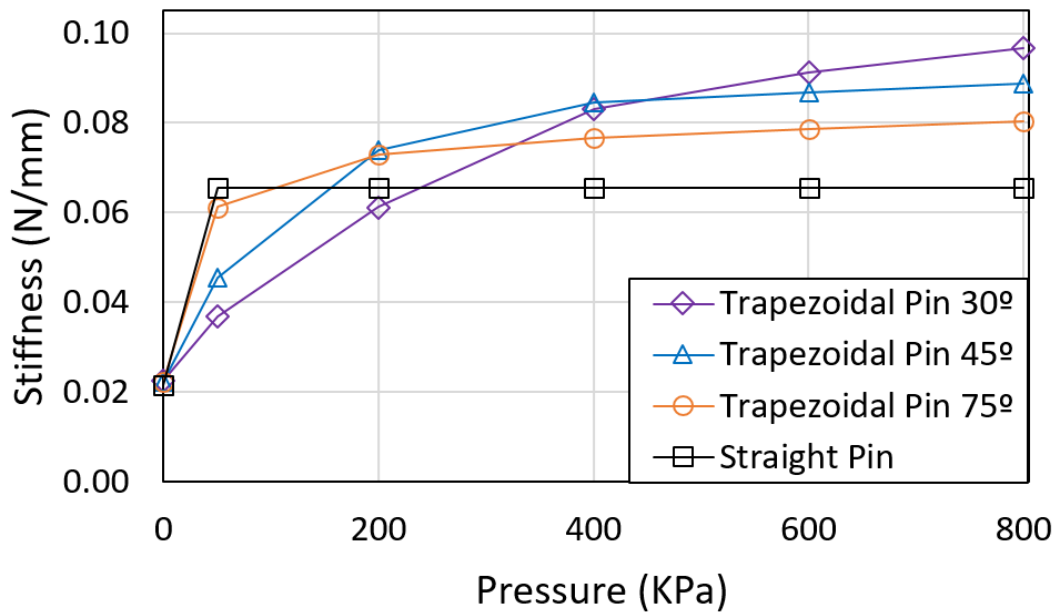


FIGURE 3.31: Stiffness of the LJS as a function of air pressure for multiple angles of the trapezoidal pin.

the increase in the contact area between the trapezoidal pin and the layers does not generate a larger stiffness at all pressures. In the DLJ, the stiffness of the LJS raises when the contact area increases by making the clamps longer [9].

3.7.2 Effect of Frames on the LJS

The LJ mechanism proposed in this chapter utilises frames, which are a novel component compared to other LJ mechanisms. For this reason, this section focuses only on the study of the effect of the number of frames in the LJS structure through FE simulations.

FE simulations were carried out on an LJS with a trapezoidal pin at the free end and with 13, 6, 3, 1 and 0 frames distributed along the LJS. The overall dimensions of the beam, the number of sheets, the materials, the load conditions, and the settings of the FE simulations for all numbers of frames are equal to the LJS described in Section 3.4.1 and Section 3.6.2, only the values of the COF between the layers and the Young's modulus of ABS have changed to 0.6 and 2.2 GPa respectively. The distribution of the frames can be seen in Figure 3.32.

For each number of frames, the simulations were run at 1000 kPa and 0 kPa of pressure in the pneumatic cylinder to calculate the maximum and minimum bending stiffness, respectively. The

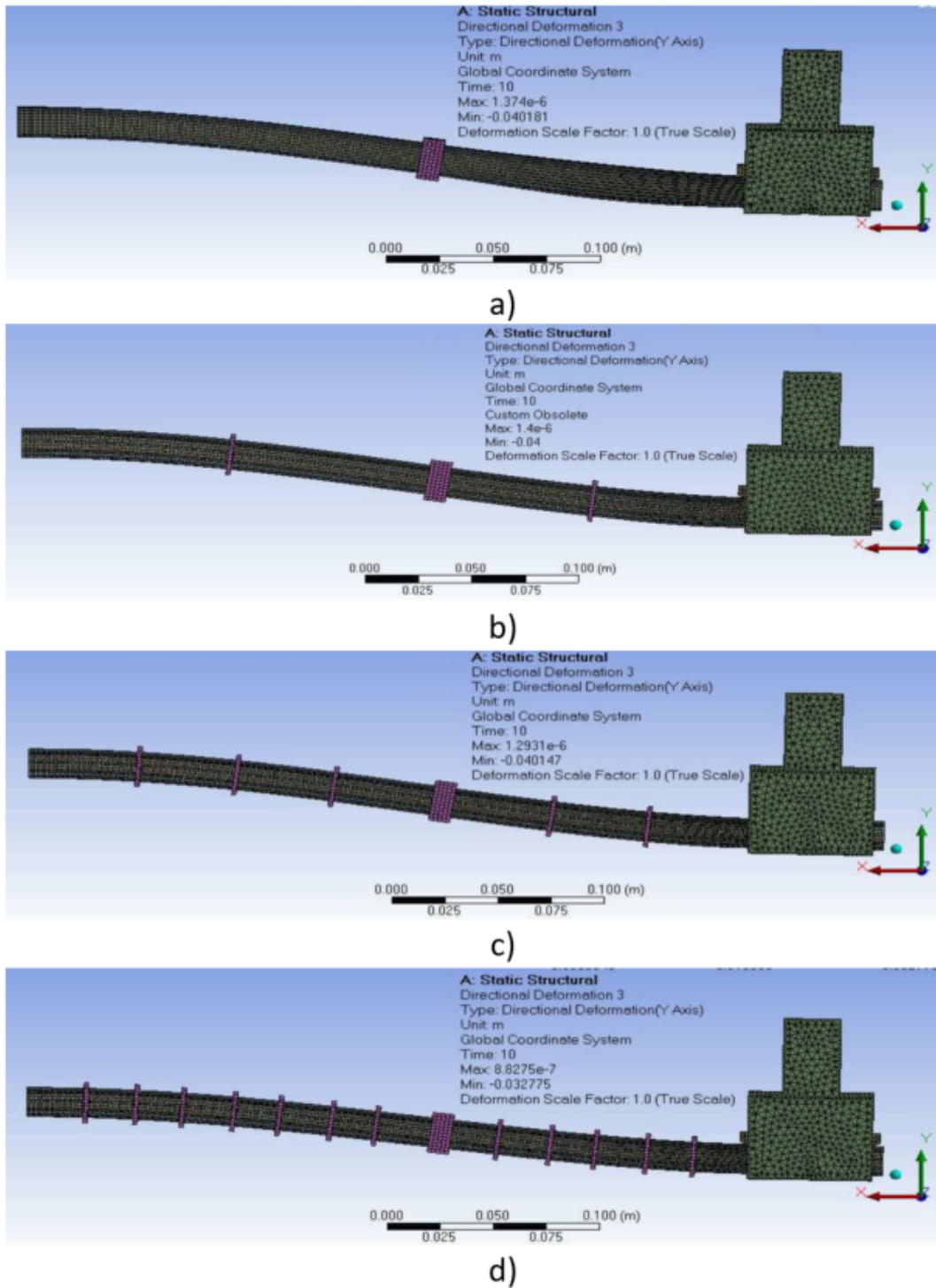


FIGURE 3.32: Distribution of the frames along the LJS with trapezoidal pin a) 1 frame. b) 3 frames. c) 6 frames. d) 13 frames.

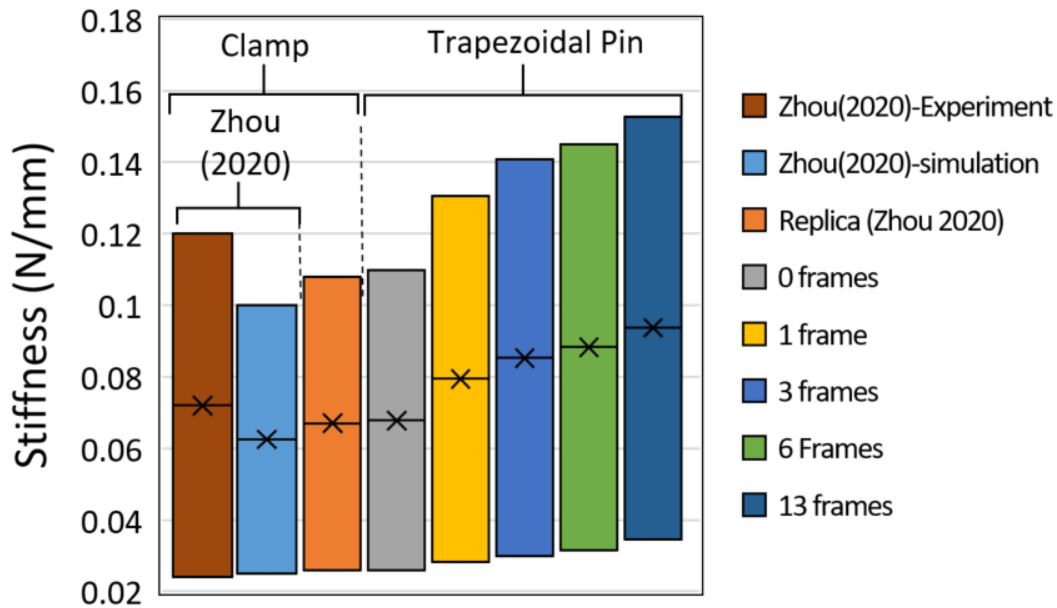


FIGURE 3.33: Comparison of stiffness range of the LJS for different numbers of frames.

results are illustrated in Figure 3.33. It can be seen that the main effect of the number of frames is the displacement of the stiffness range of the LJS. As the number of frames increases; the maximum, the minimum, and the average values of stiffness rises. For example, the comparison of the stiffness range between 0 frames and 13 frames, demonstrates that there are increments of 33.6% in the minimum stiffness and 39.3% in the maximum stiffness.

To validate the configuration of the parameters used in the FE simulation. The DLJ structure presented by [9] was also simulated in Ansys but using the parameters described in Section 3.3.6. As can be seen in Figure 3.33, the results of the simulation in Ansys have 4% error for the minimum stiffness, and 8% error for the maximum stiffness in relation to the simulations presented by [9]

Figure 3.34 shows the behaviour of the stiffness ratio as a function of the number of frames. The maximum stiffness ratio occurs when there are three frames in the LJS and represents an increase of about 11.3% in relation to the minimum stiffness ratio that occurs when there are no frames. Figure 3.33 and Figure 3.34 indicate that raising the number of frames beyond three frames increases the average stiffness of the LJS but decreases its stiffness ratio.

The frames avoid buckling of the sheets when the LJS is bent by transversal forces, as can be

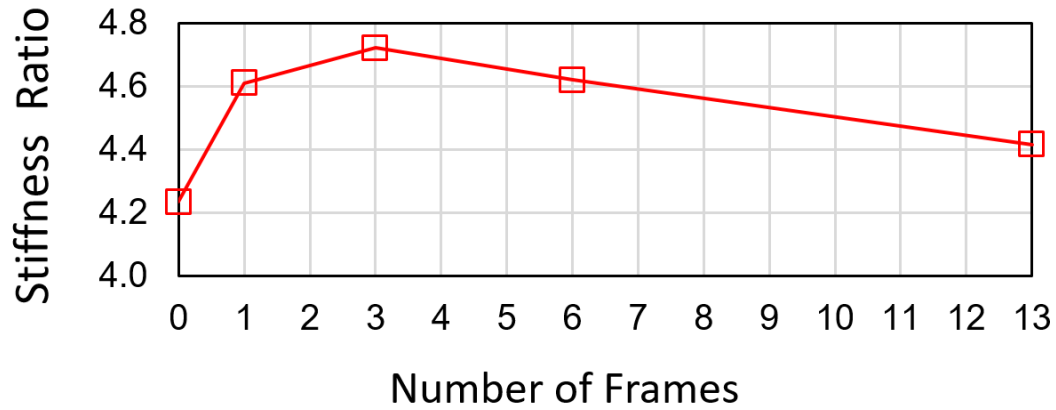


FIGURE 3.34: Stiffness ratio in function of the number of frames.

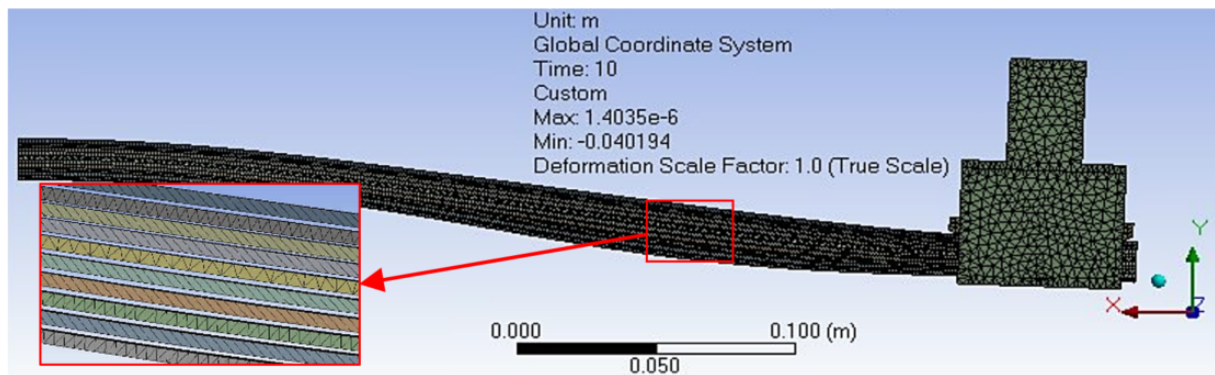


FIGURE 3.35: Deflection in Y axis in the LJS with no frames.

seen in Figure 3.23. When no frames exist and the trapezoidal pin is engaged with the sheets, the layers buckle as the transversal load is applied and deflects the LJS. Because the sheets do not have any constraint and the trapezoidal pin opposes the relative slip between the layers at the free end, the sheets buckle independently and contact between them is lost (Figure 3.35). When there are frames in the LJS, the sheets are restricted from separating, leading to a significant decrease in the buckling of the layers, as shown in Figure 3.23.

The manipulation of the stiffness range of the LJS by modifying the number of frames has two advantages. First, frames are passive elements that do not need any actuator to be effective. Second, it is a very convenient method that does not need the total disassembly of the LJS. In the context of the use of the LJS in a cobot, this method will enable variation of the stiffness range without interrupting the operation of the cobot for lengthy periods of time. Furthermore, the utilisation of frames is also possible in LJSs with other lock/unlock mechanisms, such as shape-memory alloy wires [6] and clamps [9, 59]. Other methods to vary the stiffness of the LJS,

such as changing the number of layers, require the complete disassembly of the LJS, which could cause long interruptions in the operation of the cobot.

3.7.3 Bending of the LJS when transverse force points downwards

The bending experiment and the FE simulations presented in Section 3.5.2, Section 3.6.2 and Section 3.7.2 are characterized by a traverse force that points downward. This section explores the behavior of the LJS when the traverse force is applied upward. A FE simulation was used to carry out this study. It must be noted that the terms "upward" and "downward" are relative to the page and it does not mean that the simulations were carried out in the vertical plane. Therefore, gravity force is not included in these simulations.

The LJS, the boundary conditions and the FE simulation settings are the same as the simulation of the LJS with three frames presented in Section 3.7.2. The only difference is that the deflection applied at the free end points upward. The result of the simulations was the force associated with the applied deflection.

Figure 3.36 illustrates the resulting shape of the LJS when the deflection at the free end was 40 mm. The LJS has an "S" shape that is very similar to the shape of the LJS when the deflection is applied downward.

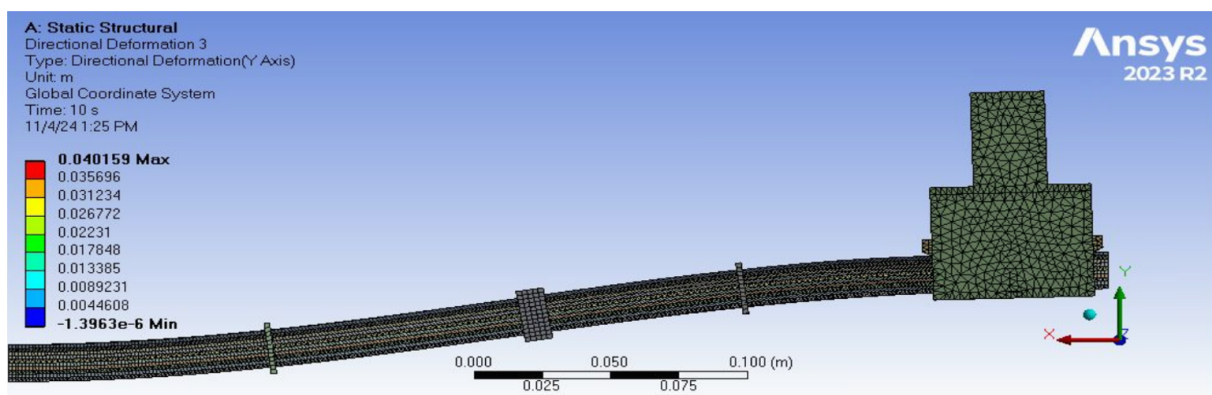


FIGURE 3.36: Resulting shape of LJS with trapezoidal pin when is bent upward

Figure 3.37 illustrates the details of the contact between the trapezoidal pin and the sheets of the LJS. It should be noted that the contact and no-contact areas flip sides in comparison to the LJS when is bent downward (see Figure 3.24 and Figure 3.43). In this case, the contact

between the top layers and the pin occurs at the back of the pin while the front part of the pin loses contact with the layers. This distribution of contact is more evident in Figure 3.38, which illustrates a LJS that is also deflected upwards and has only three sheets and a 45° trapezoidal pin.

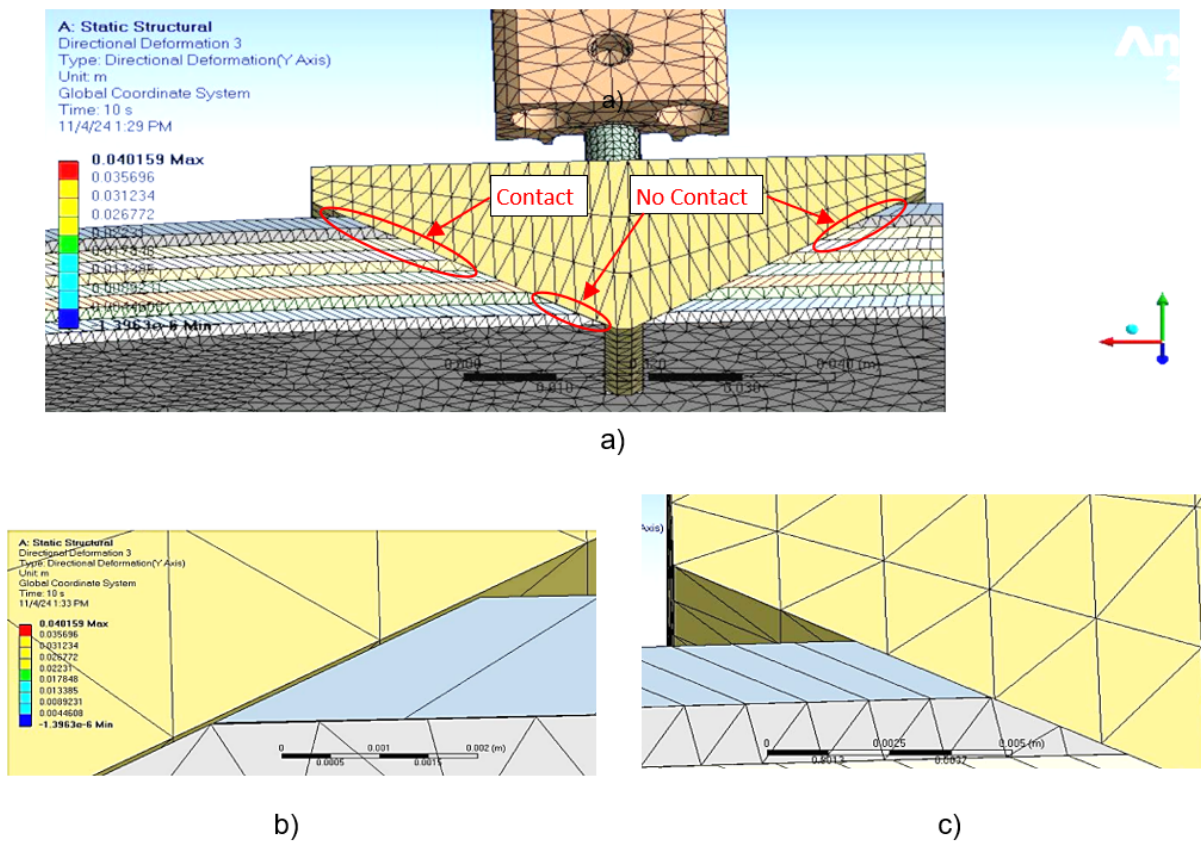


FIGURE 3.37: a) Contact between the trapezoidal pin and the layers when LJS is bent upward. b) Detail view of the contact zone. c) Detail view of the no-contact zone in the front of the pin. The support of the pneumatic cylinder is hidden in this figure.

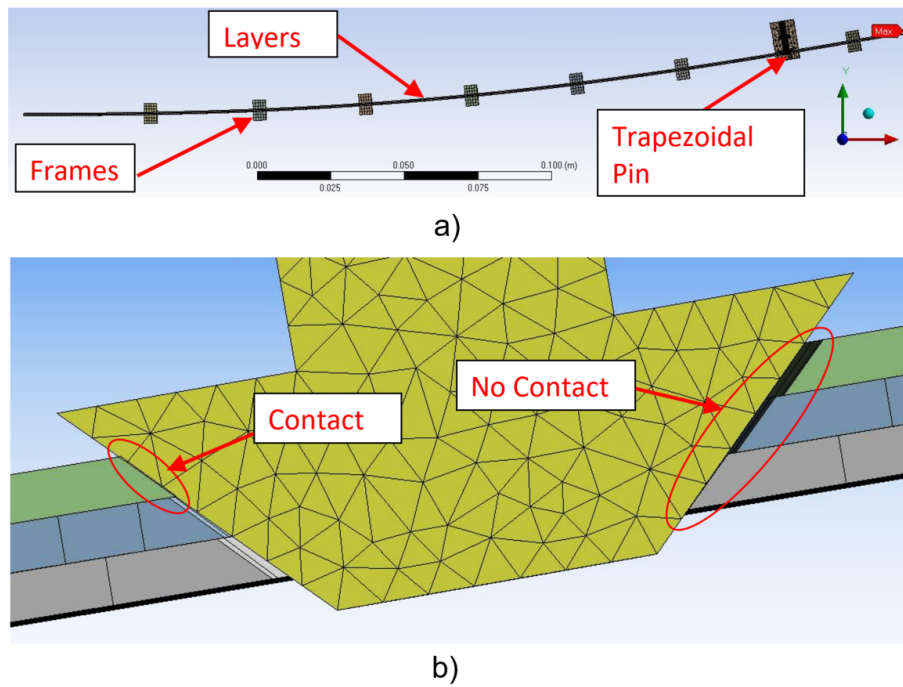


FIGURE 3.38: LJS bent upwards. a) Overall Side view. b) Detail of the contact between the trapezoidal pin and the layers.

The results of the FE simulation of the LJS when is bent upward are illustrated in Figure 3.39. The same figure also shows the result of the LJS that was presented in Section 3.7.2 and illustrated in Figure 3.32b, which corresponds to the traverse force applied downward. The results were linearized by the method of the least squares to calculate the stiffness, it can be observed that the stiffness of the LJS when it is bent upward (0.1475 N/mm) is slightly higher than the stiffness when the LJS is bent downward (0.1407 N/mm). This variation can be explained by the difference in the location of contact between the trapezoidal pin and the layers along the LJS. As was explained above, the contact occurs behind the pin when the LJS is bent upward, while the contact occurs in front of the pin when is bent downward. A similar effect was present in the DLJ where the effect of the location of the flat clamp along the LJS was studied, showing that the stiffness increases when the clamp is closer to the middle of the beam and decreases as the clamp is located closer to the ends [9].

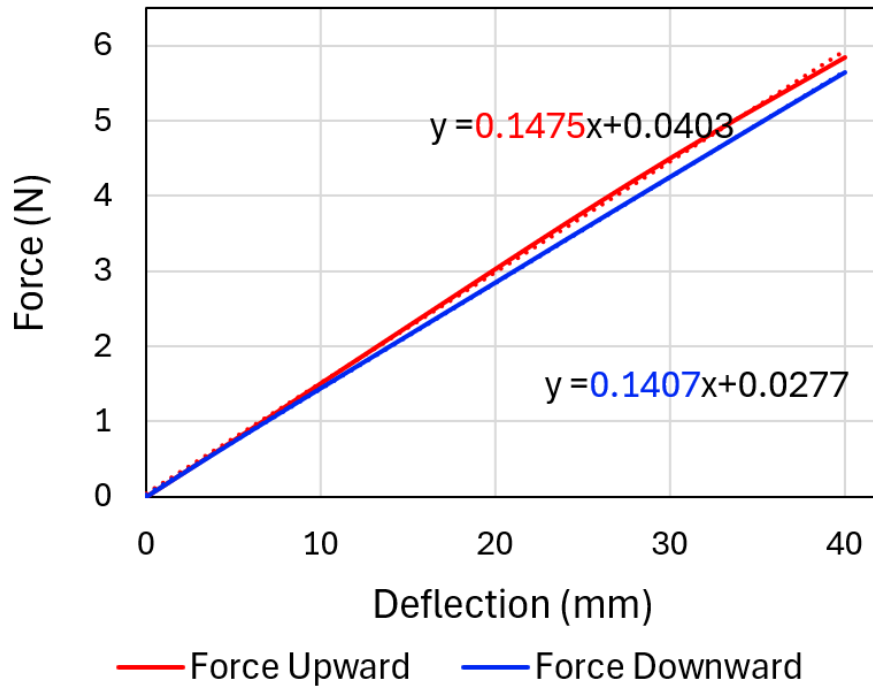


FIGURE 3.39: Results of the FE simulation for LJS when is bent upward and downward.

3.7.4 Large Deflections

The maximum deflection at the free end that was enforced in the experiments and FE simulations was 10% of the length of the LJS. In the case of a collision between a VSL and a human operator, the maximum acceleration and impact forces are expected to occur during the first part of the impact when the deflection is less than 10% of the length of the link. However, VSLs may present larger deflections during an impact with a human being, particularly at high collision velocities. Therefore, a simulation with a maximum deflection of 100 mm (25% of LJS length) is presented to investigate the behaviour of the bending stiffness for higher deflections.

Figure 3.40 illustrates the LJS under 100 mm deflection pointing downward at the free end. The LJS has the dimensions of the samples presented in Table 3.2 and the load conditions and simulation settings are the same as those described in Section 3.6.2 with the exception of when the number of frames is 13, the pressure in the pneumatic cylinder is 500 kPa, the COF between the sheets that is 0.6, and the COF between the layers and the trapezoidal pin is also 0.6.

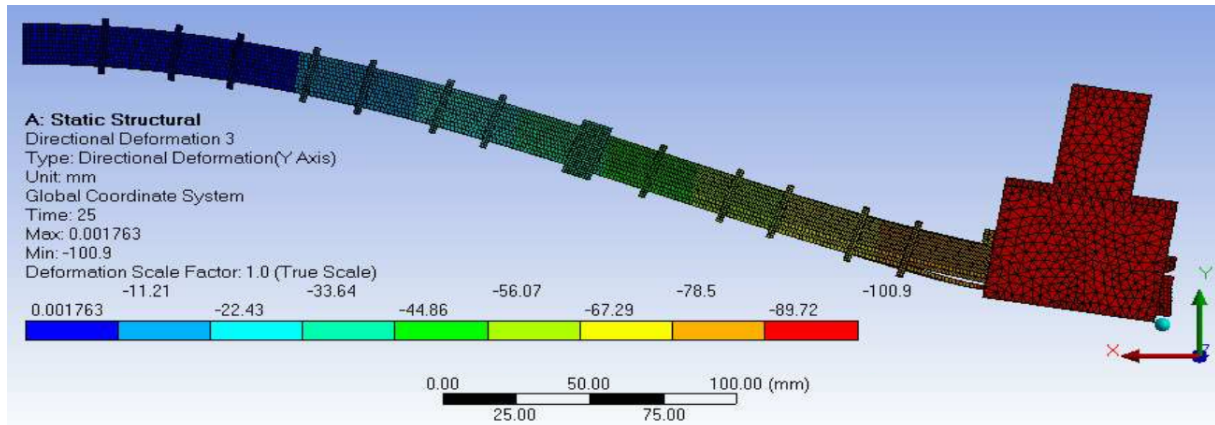


FIGURE 3.40: LJS with trapezoidal pin under 100mm deflection at the free end.

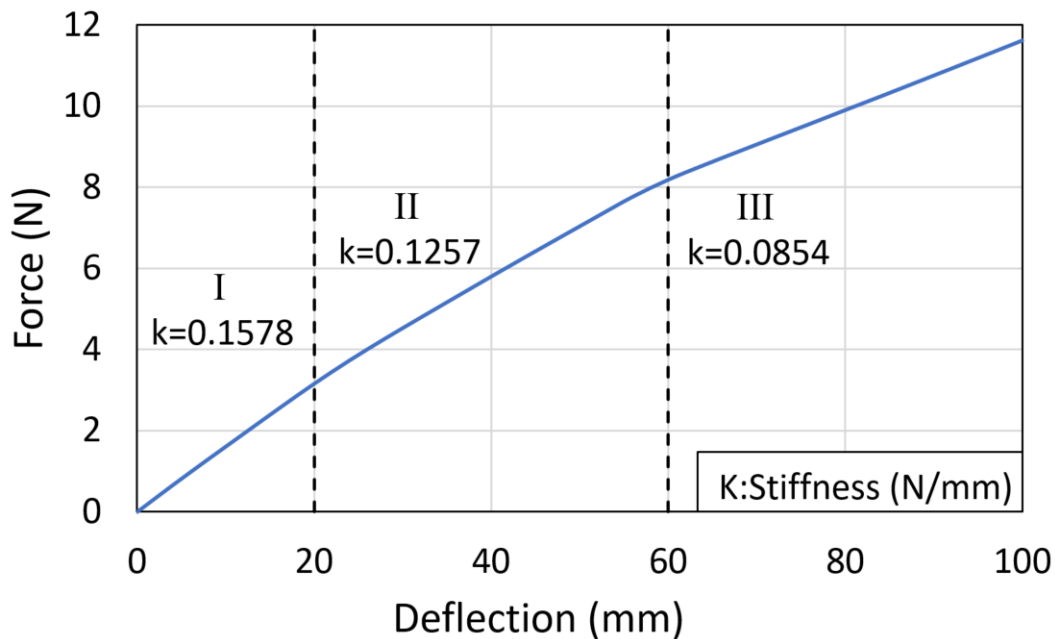


FIGURE 3.41: Results of the Simulations of LJS under 100 mm deflection at the free end.

The results of the simulation are illustrated in Figure 3.41. It can be observed that the slope of the curves decreases as the deflection grows, which means that the stiffness varies significantly during the deformation of the LJS. The graph can be divided into three regions with distinctive bending stiffness values. The bending stiffness in Region I is 0.1578 N/mm, while the bending stiffness in Region III is 0.0854 N/mm. The results show that the reduction of the stiffness is significant since the stiffness in Region III is almost half of the stiffness in Region I.

These simulations also show some details that are difficult to note in the previous simulations. One of them is the fact that the layers push the pin upwards as the LJS bends. Figure 3.42a

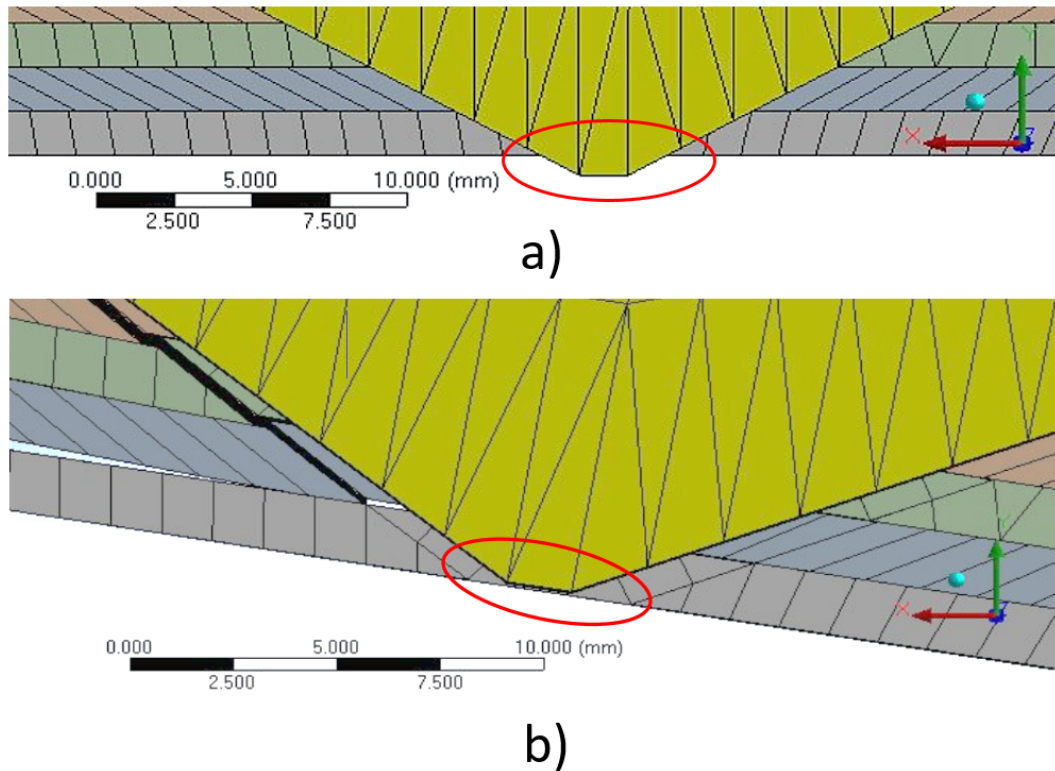


FIGURE 3.42: Detail of the pin section a) LJS with no transverse load b) LJS when deflection is 100 mm at the free end. The pressure in the pneumatic cylinder is 500 kPa in both cases.

shows the pin protrudes from the bottom layer when the LJS is straight due to no transverse load. Figure 3.42b shows the LJS when the deflection is 100 mm in the free end due to the action of the transverse load, it can be seen that the pin does not protrude from the bottom layer anymore. According to Figure 3.42, the pin moves about 0.8 mm upward. It is important to note that the pressure in the pneumatic cylinder is 500 kPa in both cases.

Another fact that is evident in this simulation is how the contact between the pin and the layers concentrates in the top layers as the deflection increases. Figure 3.43 shows that only the three top layers are in contact with the pin when the deflection is 100 mm, while Figure 3.24 shows that about six layers are in contact with the pin when the deflection is 40 mm. This behaviour may also explain the reduction in beam stiffness as deflection increases, as the contact area between the pin and the LJS reduces significantly. Another detail that is evident in Figure 3.43 is that the bottom layer buckles despite having 13 frames distributed along the beam. Therefore, the buckling in the LJS with trapezoidal pin cannot be completely avoided despite using a large number of frames.

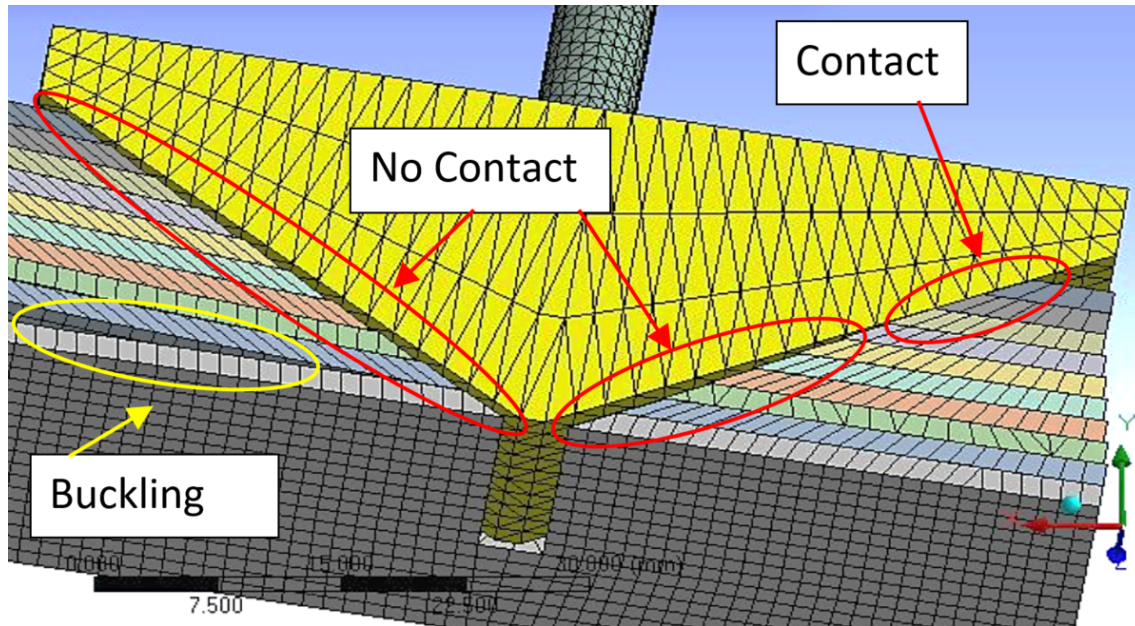
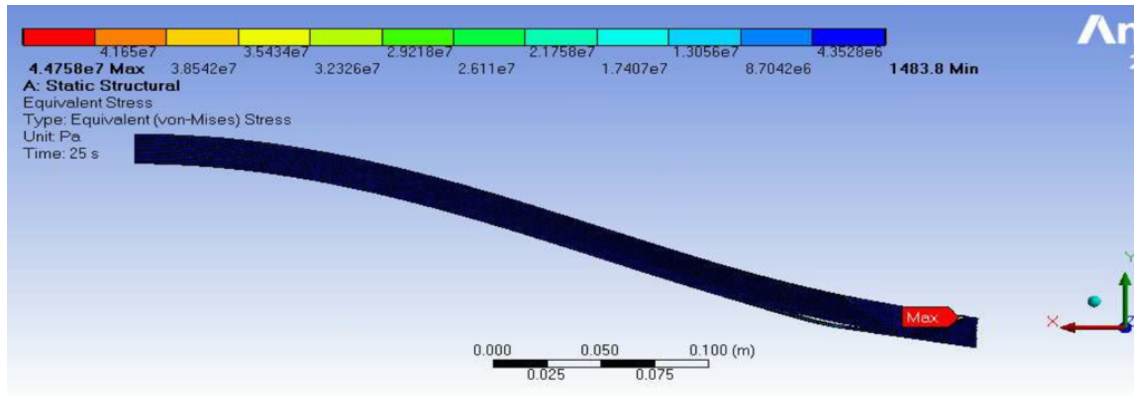
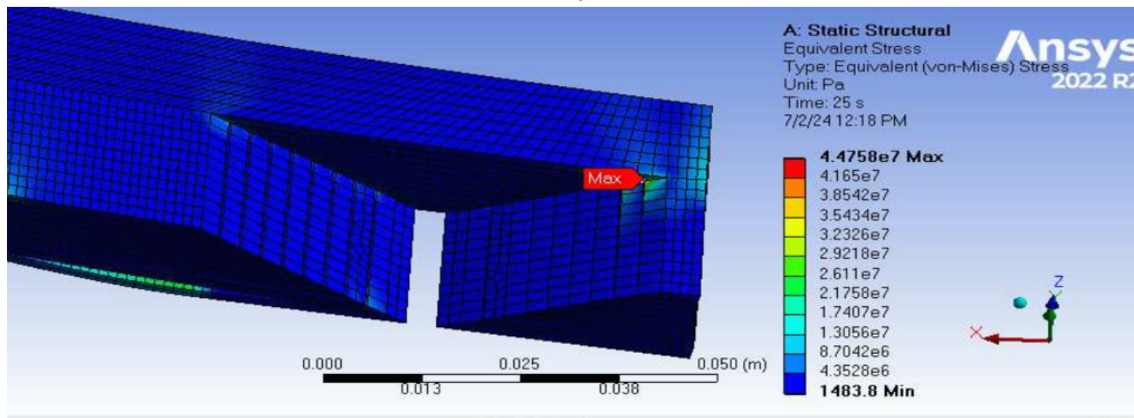


FIGURE 3.43: Detail of contact between the pin and the layers when deflection is 100 mm at the free end.

Another aspect that was investigated with this simulation is the possibility of plastic deformation of the ABS sheets under large deflection. Figure 3.44 illustrates the Von-Mises stresses of the ABS laminates when the LJS is deflected 100 mm. It can be seen that the maximum stress in the sheets is 44.7 MPa and occurs in the trapezoidal slots in the top layers. The maximum stress at this point is probably caused by the contact between the top layers and the trapezoidal pin. Another cause of the maximum stress in this position is the proximity to the edge where the trapezoidal slot starts, which generates a stress concentration factor. This stress value is higher than the yield strength of ABS (39 MPa, according to the sheets manufacturer). Therefore, plastic deformation could occur in the ABS sheets. It must be noted that the trapezoidal pin will be applied in the construction of VSLs, and the expected deflection of a VSL robot arm is much less than 25% of its length (100 mm deflection, length of 400 mm).



a)



b)

FIGURE 3.44: Von-Mises stress in the sheets of the LJS with trapezoidal pin at 500 KPa and 100 mm of deflection at the free end. a) side view of LJS. b) Detail of the location of maximum stress. The other components of the trapezoidal pin mechanism are hidden

3.8 Conclusions

In this chapter, a novel mechanism was presented to lock/unlock the sheets of an LJS with the purpose of modifying its bending stiffness and making it useful for the construction of VSL robots. The mechanism consists of a pneumatic actuator that drives a trapezoidal pin to interfere mechanically with the layers and, in turn, modulating the stiffness of the LJS. Another LJS with a flat clamp mechanism is presented to compare the mechanical behaviour of both mechanisms.

Compared with a vacuum pressure mechanism, the proposed mechanism does not require an air-tight chamber. Therefore, it is not vulnerable to sealing damage due to contact with rough edges. In addition, trapezoidal pin mechanisms have the potential to change the stiffness faster than

the vacuum pressure mechanism, which makes the proposed mechanism adequate for mitigating impacts between robot arms and human beings.

Force-deflection tests were conducted to characterise variations of bending stiffness in the LJSs due to changes in air pressure in the pneumatic cylinder. The results demonstrated that the maximum stiffness ratio of the trapezoidal pin is about 15% larger than the maximum stiffness ratio of the flat clamp. In addition, the experiments showed that the stick-slip phenomenon occurs in the flat clamp mechanism, but it is not present in the trapezoidal pin mechanism.

Both lock/unlock mechanisms were simulated using FE methods. The results of the FE simulations match well with the test results in the case of the trapezoidal pin mechanism. In the case of the flat clamp mechanism, the FE simulations differ considerably from the experiments. This difference may happen because the FE simulations do not replicate the stick-slip phenomenon that happens in the tests of the LJS with a flat clamp.

Computational case studies were carried out using FE simulations to study the effect of the angle of the trapezoidal pin in the LJS. The simulations show that the 30° trapezoidal pin has the highest stiffness for pressures greater than 500 kPa, while the 75° and 90° trapezoidal pins have the highest stiffness for pressures lower than 200 kPa.

Another computational study was carried out to investigate the effect of the number of frames placed along the LJS with a trapezoidal pin mechanism. FE simulations show that incrementing the number of frames results in an increased average of the stiffness range. Furthermore, the stiffness ratio reaches a maximum value when there are three frames in the LJS, showing an increase of about 11.5% relative to the minimum stiffness ratio. Overall, altering the number of frames is a practical and novel method of modulating the stiffness range without including more actuators in the LJS.

The behaviour of the LJS with a trapezoidal pin when it is bent upward was also studied through FE simulations. The simulations demonstrate that the contact areas between the trapezoidal pin and the layers flip sides in comparison to the LJS structure when it is bent downward. The results of the simulation also show that the stiffness of the LJS when it is bent upward is slightly higher than the stiffness of the LJS when it is bent downward. This difference in the results

occurs because of the variation in the location of the contact zones between the pin and the sheets of the LJS.

The behaviour of the proposed mechanism when deflections are large was also analysed through FE analysis. The simulations demonstrate that the stiffness of the LJS diminishes when the deflection increases beyond 10% of the length of the LJS. In addition, it is evident that at large deflections, the layers of the LJS push the pin upwards, and the pin keeps contact only with the first top layers.

The conclusions of the investigation presented in this chapter was used to formulate new designs of VSLs that are based on LJS activated by trapezoidal pin mechanisms. These new VSLs are presented in Chapter 4.

Chapter 4

Variable Stiffness Link

This chapter presents three designs of VSLs for robot arms. These VSL designs were named “VSL Concept A”, “VSL Concept B”, and “VSL Concept C”. These links are based on LJS and combine different design aspects in order to achieve a VSL that is adequate to be used in robot arms.

Chapter 3 introduced the LJS activated by a trapezoidal mechanism. This lock/unlock mechanism demonstrated its capacity to vary the stiffness of the LJS and to achieve a fast change of stiffness that can be used in VSL robot arms. This chapter implements some of the lessons from Chapter 3 to develop new VSLs.

Two of the VSL prototypes presented in this chapter will be used in Chapter 5 and Chapter 6 to investigate their capacity to reduce the impact force during a collision and to build robot arms with VSLs.

4.1 Motivation for the Design of a New VSL

Chapter 2 shows how LJ is a research topic that is drawing the attention of the research community. Most of the research on LJ is focused on the lock/unlock mechanism. However, few studies have focused on the investigation of LJ applied in the construction of VSLs [15, 16].

The design and construction of a VSL incorporating LJ has some challenges that have not been addressed in the literature. These challenges are not trivial and must be solved before implementing VSLs in a functional cobot arm. The first challenge is to ensure that the VSL does not constrain the motion of the LJS in such a way that can alter the stiffness variation capability. The second challenge is to ensure that the VSL properly supports all the load conditions that may be present in the link of a robot arm. The third challenge is reducing the volume of the VSL and making it less bulky and free of protrusions.

The VSL concepts proposed in this chapter address the design challenges described above. It is important to note that the VSL Concept B was implemented in the impact tests presented in Chapter 5, and the VSL Concept C was implemented in the construction of a VSL robot arm that is presented in Chapter 6.

The following sections describe the challenges of designing a VSL with LJSs.

4.1.1 Attaching adjacent links without locking the layers

A VSL must have a structure that allows the attachment of joints at both ends to mount adjacent links. This simple mechanical function is not trivial for an LJS. Figure 4.1 illustrates what happens when bolts are used for joining an LJS with other bodies. The bolts in the proximal end can keep the layers together, attach the sheets to the proximal joint and allow for the relative slipping of the layers when the LJS is bent. However, if bolts are also implemented at the distal end, these bolts will prevent the relative slip of the layers, locking the layers, increasing the stiffness of the LJS, and impeding the variation of stiffness. This limitation also exists in the LJS proposed in Chapter 3. The effect would be the same if the bolts were replaced by other attachment methods, such as pins or glue.

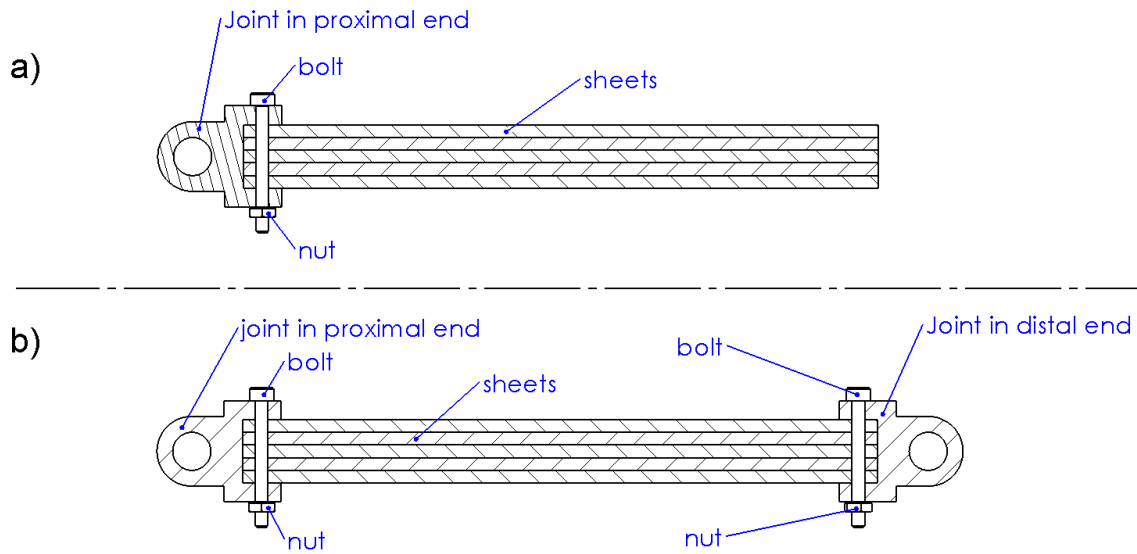


FIGURE 4.1: Constraint of the slip between the layers in a LJS. a) bolt joint in the proximal end. b) bolt joint at both ends.

The only practical solution is to use only one of the sheets in the distal end for joining other bodies, as seen in Figure 4.2. However, all the force from the adjacent link in the distal end will be supported by only one layer, which may fail because its thickness is usually very small, and in this work only plastic materials are considered. It is necessary to note that metal sheets were discarded because they exhibit too much pre-deformation, as was discussed in Section 3.3.1.

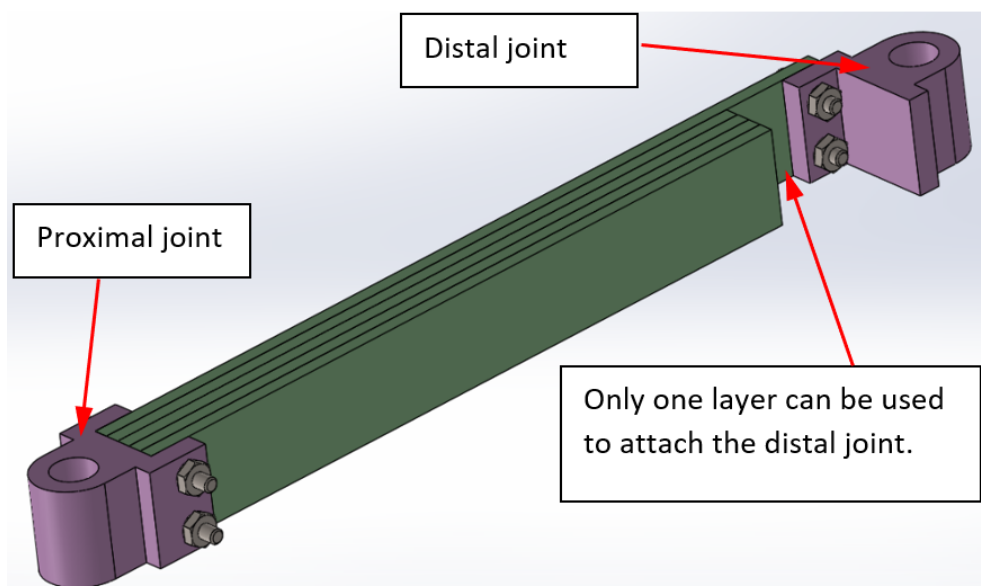


FIGURE 4.2: Use of only one layer to attach a distal joint.

The solution to this limitation is the implementation of an interlocking LJS, also known as a double-link based layer jamming mechanism [43]. This type of LJS has two parts (proximal and distal). In this configuration, adjacent layers are not joined in any of their ends, as shown in Figure 4.3. This allows bodies to be attached to each end of the LJS without locking adjacent layers. Interlocking LJSs have been applied in wearable robots [19, 43], grippers [42] and robotic arms [15–17, 20].

[Production note: This figure is not included in this digital copy due to copyright restrictions.]

FIGURE 4.3: Interlocking LJS. Figure taken from [19].

4.1.2 Supporting Multiple Load Conditions

The links of robot arms must support forces and moments in all directions, even if the robot arm is designed to move in only one plane. This requirement could conflict with the variable stiffness capability of the VSL, even if this capability only occurs for one load condition. Most of the LJSs presented in Chapter 2 and the LJS presented in Chapter 3 do not provide enough rigidity for all conditions and loads (bending, axial force, torsion) in all directions.

The LJSs presented in Chapter 3 can support bending and axial forces. However, they may not be able to support high levels of transverse force and torsion about the longitudinal axes because they are slender, resulting in buckling because of the transverse force and excessive twisting because of torsion about the longitudinal axis. The solution to these limitations is the parallel guided beam architecture. This architecture supports higher transverse forces and torsion moments without failing [20]. Figure 4.4 illustrates the single beam and the parallel guided beam under transversal force and torsion about the longitudinal axis. It can be seen how the width (b) of the parallel improves the resistance to buckling and twisting. the hability of the parallel guided architecture to withstand torsion load will be investigated in Section 4.5.

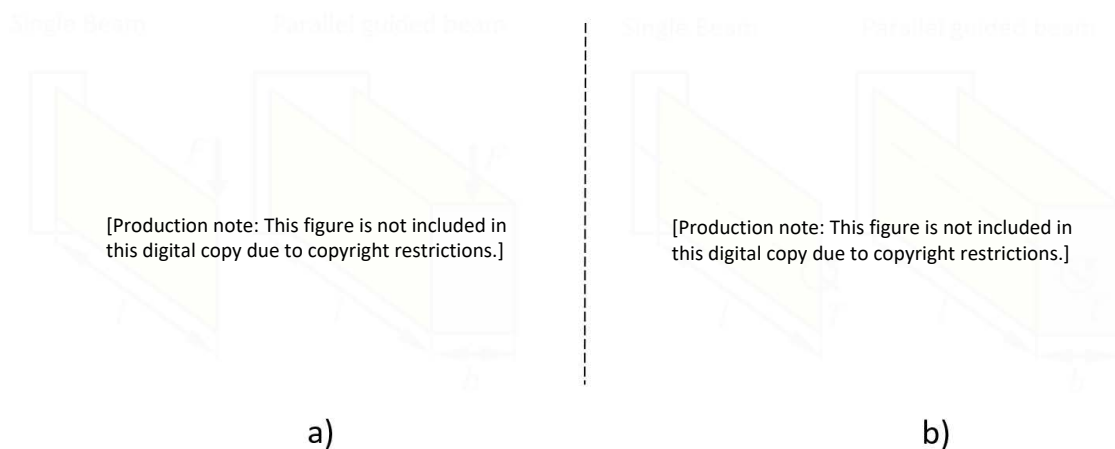


FIGURE 4.4: Single beam and parallel guided beam a) under transverse vertical force. b) under torsion about the longitudinal axis. Figure taken from [20]

VSLs with parallel guided beam architecture have been implemented using interlocking LJSs based on vacuum pressure [15, 16, 20]. These studies have demonstrated the capacity of the VSL to support bending moments and to vary the bending stiffness, but they did not investigate how much transverse force and how much axial force can be supported by the VSL. However, it is reasonable to suppose that, when the chamber is at atmospheric pressure, this type of VSL cannot support high axial and transversal forces in the free end because such loads will be resisted by solid cores with very thin cross-sections, and by the LJS envelopes, which may fail easily because they are usually made of a very thin plastic film or silicone.

4.1.3 Avoiding Protrusions

VSLs should be free from protrusions or sharp edges because they could generate considerable injuries in the case of an impact with a human being [78].

The LJSs presented in Chapter 3 have pneumatic cylinders for driving the trapezoidal pin or the flat clamp. These actuators were selected because they were the smallest cylinders in the market. However, they still make the LJS bulky. In addition, they protrude from the LJS, which may be more dangerous in the case of a collision with a human being. Pneumatic cylinders also add significant weight to the LJS because they are made of aluminium and must be robust enough to support the air pressure.

Other types of linear actuators present the same problems as pneumatic cylinders. For example, solenoids are also bulky and heavier than pneumatic cylinders. Vacuum pressure-activated LJSs do not have this problem since the vacuum pump does not have to be mounted on the LJS. However, it should be noted again that this type of LJS has a flexible membrane that covers the whole link length. This membrane may be torn during an impact, which eliminates the vacuum pressure, leading to the loss of the stiffness variation capability in the LJS.

4.2 VSL Concept A

The VSL that is proposed in this chapter consists of a parallel-guided beam. The components of this VSL are illustrated in Figure 4.5. The design features two interlocking LJSs. The mechanism to lock/unlock the layers is the direct action of the pneumatic actuator that is in contact with the LJSs. In addition, there are frames placed along the LJS. The overall dimensions of the link are; length 236 mm, width 61 mm, and height 58.6 mm.

The general characteristics of each component of the LJ mechanism are described as follows.

Layers: Each interlocking LJS has five sheets made of ABS plastic with a length of 192 mm, width of 50 mm, and thickness of 1.5 mm. The material has a Young's modulus of 180 GPa and a density of 1030 kg/m³.

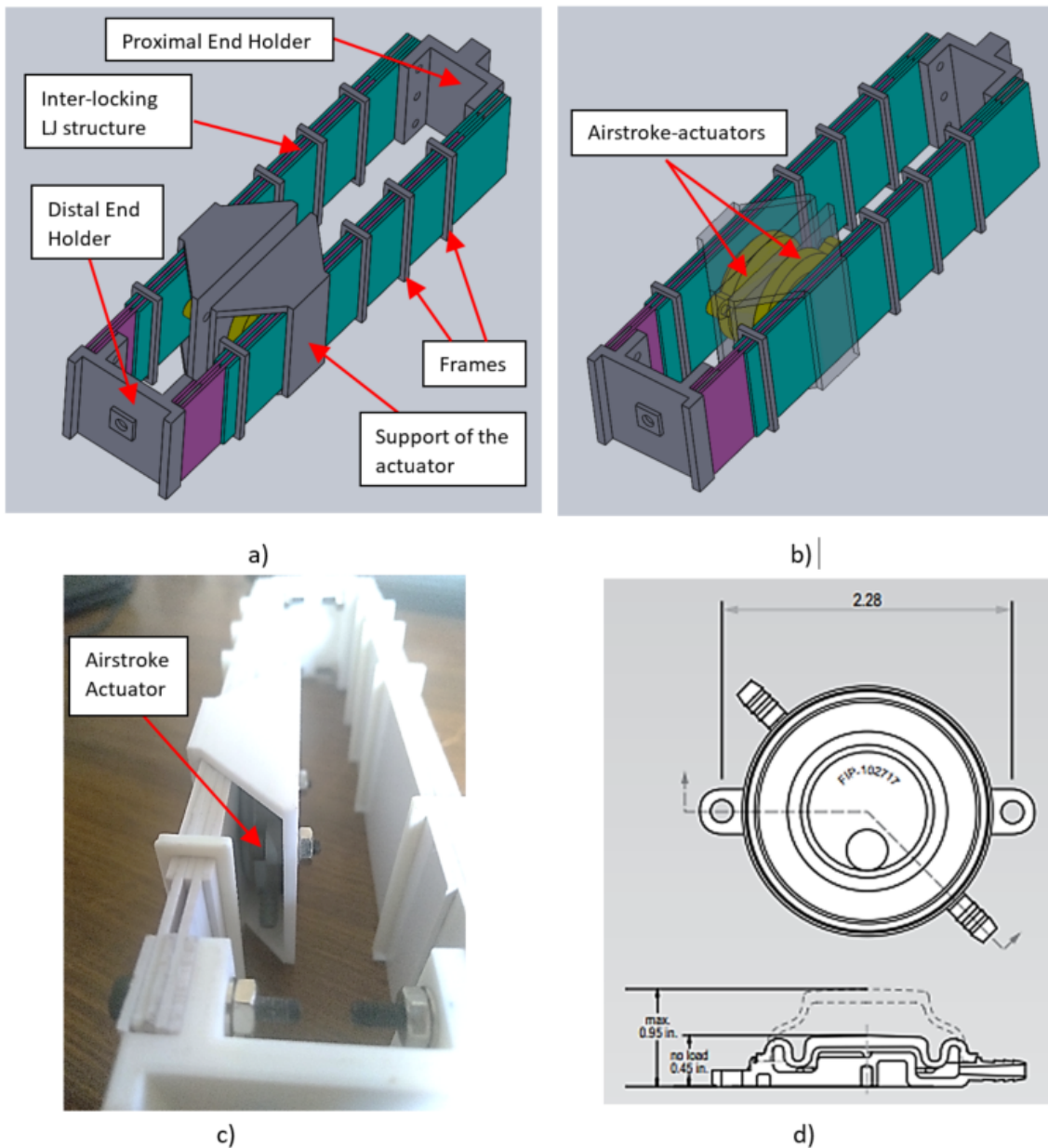


FIGURE 4.5: VSL Concept A. a) Components. b,c) Detail of the Airstroke actuators in the VSL. d) Diagram of minimum and maximum stroke of the Airstroke actuator (50-P-10).

Frames: Similarly to the LJS presented in Chapter 3, the main function of the frames is to avoid independent buckling of the layers by keeping them together in one stack. However, the frames also keep both parts of the interlocking LJSs (fixed and free end) together. This additional function will be discussed later in this section.

Airstroke (50-P-10) : Reducing the weight and volume of the actuators and increasing the lock/unlock force is a desirable objective in the design of VSLs based on LJSs. The combination

of trapezoidal pin and pneumatic actuator should be optimised to achieve this objective. Pneumatic cylinders are easy to couple with the trapezoidal pin, but they become bulky if more force is required. Other pneumatic actuators, such as air bellows actuators, can provide larger forces while being smaller and lighter than pneumatic cylinders. However, coupling the air bellows with the trapezoidal pins could be more difficult, and the trapezoidal pins would need to be redesigned for this purpose.

The Airstroke is a pneumatic actuator that is also known as an "Air Spring" and manufactured by Firestone (Nashville-USA). The Airstroke is a single-effect actuator with a bellows that inflates when pressurised. The actuator inflates in a perpendicular direction to the actuator's body. In addition, the bellows is bonded to an upper bed plate in such a way that the bed plate is usually placed in contact with the element that must be pushed by the actuator. When the Airstroke is depressurised, the bellows returns to its original shape, and the upper bed plate returns to its initial position. Figure 4.5d illustrates the Airstroke actuator; it can be observed that the Airstroke has a length of only 0.45 in (11.56 mm) when the actuator is depressurised. This actuator was implemented in this link because its length is about 25% of the length of the shortest pneumatic cylinder available in the market, making the whole link narrower and less bulky. In addition, the Airstroke can apply 3-4 times more force than the shortest pneumatic cylinder.

Figure 4.6 illustrates the Airstroke actuator when it is depressurized and pressurized. It can be seen that the bellow is flexible, but the top part of the actuator is rigid due to the upper bed plate that has a circular shape, which means that the actuator and the layers keep a large circular contact area when the actuator is pressurized and pushes against the LJSs. Therefore, the VSL Concept A does not need a flat clamp because the Airstroke actuator itself acts as a clamp, which simplifies the design of the link.

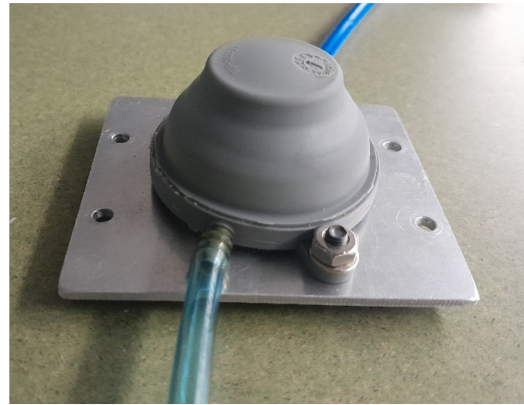
Support of the Airstroke Actuator: This part is bonded to the bottom layer of the LJS only. The support has enough height to accommodate the stack of layers and the Airstroke when it is not pressurised. This short height reduces the width of the link and also allows the Airstroke to release the maximum force that occurs when the upper bed plate is at the lowest position, as can be seen in the performance graph of the Airstroke in the Appendix A. The

support of the actuator also contributes to keeping both parts of the interlocking LJSs together. This additional function will be discussed later in this section.

The frames, the support of the actuators and the ends of the links were manufactured by 3D printing (FDM technology) and the material was PLA. The ABS sheets were cut with a CNC router and a CNC drill. Laser cutting for ABS was avoided because of the generation of toxic fumes. The LJSs were joined to the end of the links by using bolts, as can be seen in Figure 4.5c.



a)



b)

FIGURE 4.6: Airstroke actuator a) depressurized state b) pressurized state.

As mentioned above, the frames and the support of the actuator have an additional function that consists of constraining the relative motion between the proximal end and the distal end of the LJSs. Figure 4.7a illustrates what happens if the interlocking LJS does not have the frames and the support of the Airstroke when a vertical transverse force is applied on the distal end. In this case, the distal end can move relative to the proximal end in the vertical plane, leading to the disintegration of the structure. Therefore, the frames and the support of the actuators keep both ends of the VSL together when transverse force is applied and contribute to the rigidity of the link in relation to this load condition. However, the frames and the support of the actuator cannot constrain the axial motion between the proximal end and the distal end when axial force is applied, as shown in Figure 4.7b.

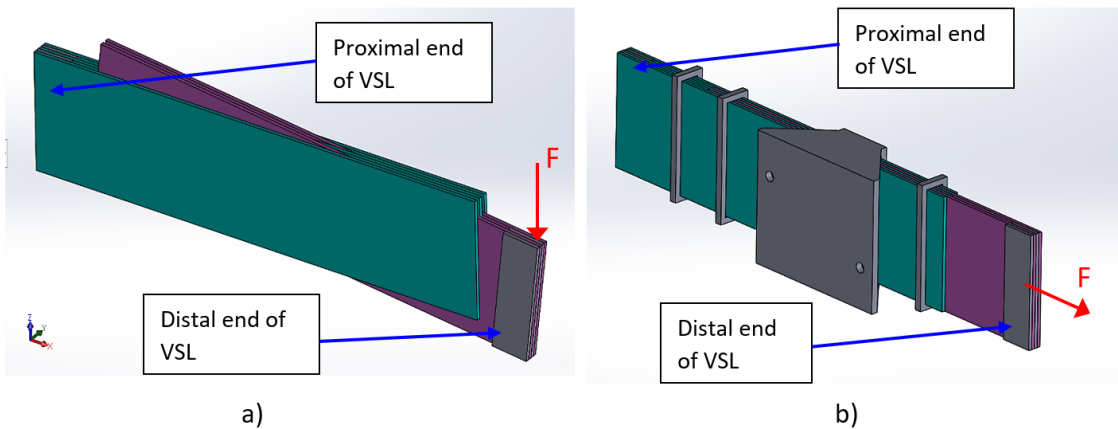


FIGURE 4.7: a) Transverse force applied to interlocking LJS without frames and Airstroke support. b) Axial force applied to the interlocking LJS with frames and Airstroke support.

Each LJS of the VSL Concept A has four frames, as can be seen in Figure 4.8. This number of frames was defined by the result of the analysis carried out in Section 3.7.2 whose conclusion was that 3 frames distributed along a normal LJS is the optimal option. However, an additional frame (frame 1) is necessary in the interlocking LJS to avoid the local buckling of the top layer of the proximal end when the VSL is bent. For the same reason, frame 1 and frame 4 should be placed close to the ends of the overlapping section of the interlocking LJS.

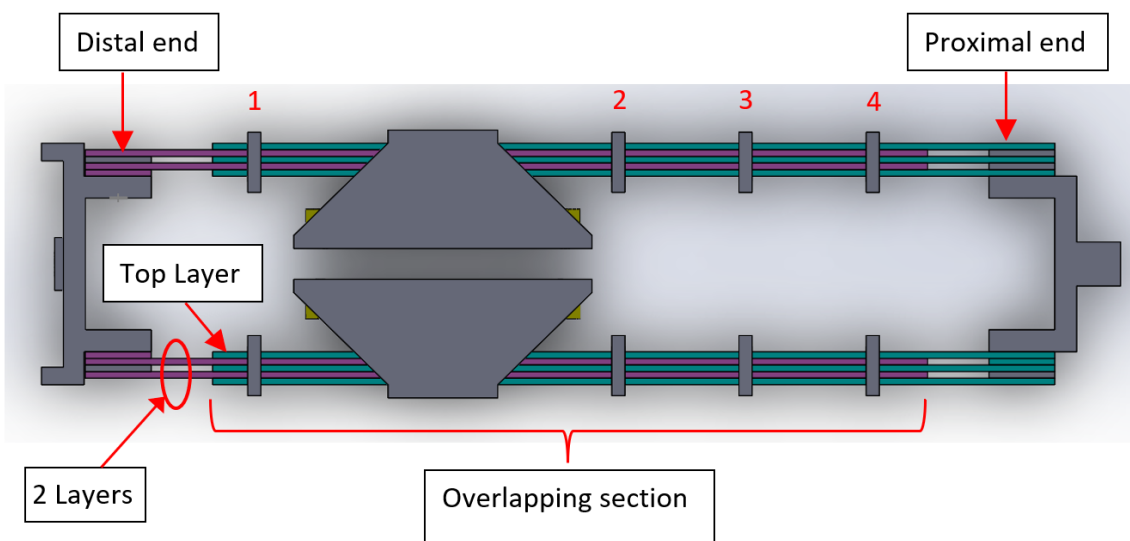
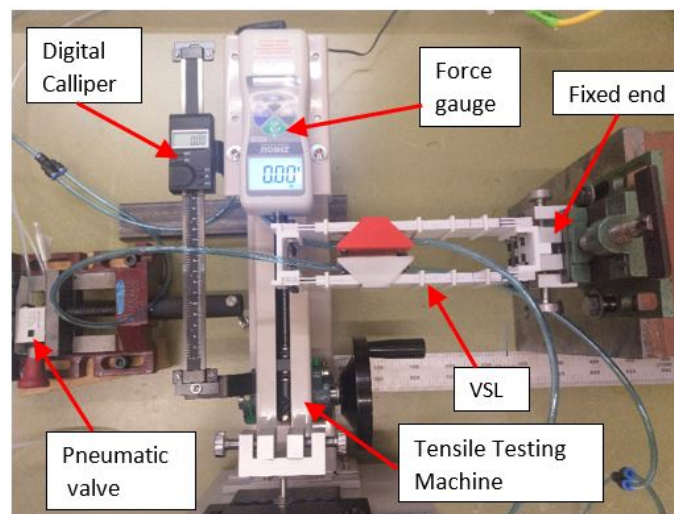


FIGURE 4.8: Location of frames in the interlocking LJS of VSL Concept A.

4.2.1 Experiment Setup

The purpose of the experiment was to determine the variation in the stiffness of the VSL as a function of the air pressure in the Airstroke actuator. The experimental setup is illustrated in Figure 4.9. This experimental setup has the same components of the experimental setup presented in Section 3.5, such as the tensile testing machine, the force gauge, the digital caliper, the pneumatic valve, and the air pressure regulator.



a)



b)

FIGURE 4.9: Experimental setup of bending test. a) components of the experimental setup. b) Deformation of VSL Concept A due to lateral deflection imposed by the load frame.

4.2.2 Experiment Procedure

The experiment of force vs deflection consisted on the application of a complete load-unload cycle at 0 kPa, 69 kPa (10 psi), 138 kPa (20 psi), 207 kPa (30 psi), and 276 kPa (40 psi) of pressure in the Airstroke actuators. The test begins with the loading procedure, where the deflection increases every 2 mm from 0 mm to 24 mm, which is about 10% of the total length of the link. Then, the unloading procedure begins by reducing the deflection every 2 mm from 24 mm until a deflection where the force gauge measures 0 N. It is important to know that these values were recorded after the force has reached a stable value. For this reason, it can be considered that the VSL structure is loaded and unloaded quasi-statically.

Figure 4.10 illustrates the results of this experiment for a locking pressure of 0 kPa in the Airstroke actuator. The upper branch of the curve is the loading procedure. The lower branch of the curve represents the unloading procedure. Three trials were conducted at each pressure value. The points illustrated in Figure 4.10 correspond to the average of the forces obtained in the three trials for a given deflection. The error is illustrated in Figure 4.10 through the error bars that reflect the range of force values obtained across the three trials for a given deflection. A similar procedure to illustrate the error in stiffness tests was implemented by [73].

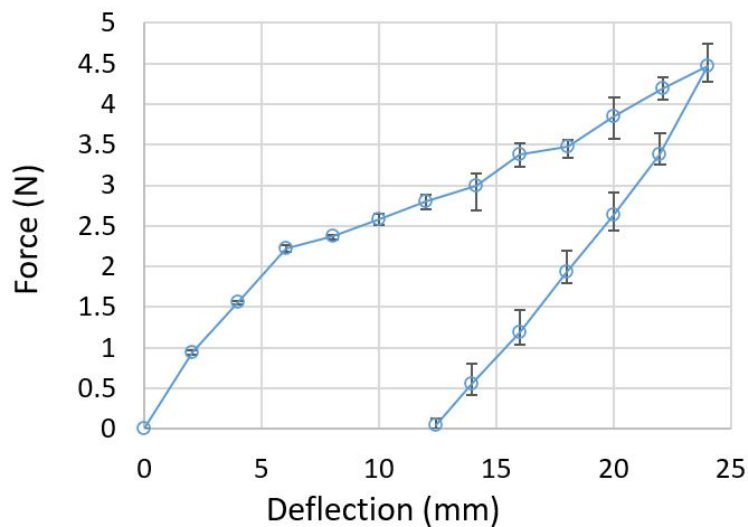


FIGURE 4.10: Results of the force-deflection experiment for VSL Concept A at 0 kPa.

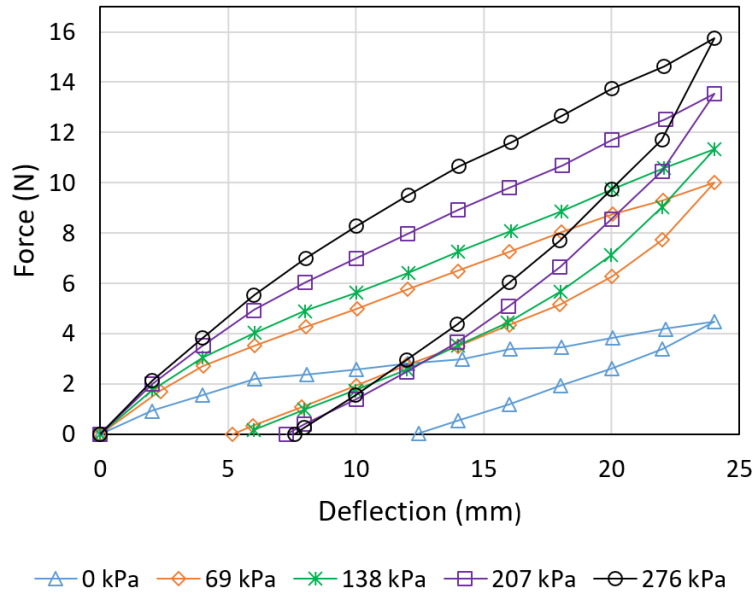


FIGURE 4.11: Results of the force-deflection experiment for all values of pressure in the Airstroke actuators.

The bending experiments revealed a problem with VSL concept A. After each test, there was a displacement of the free end of the link in the axial direction, making the VSL longer by 2-3 mm. This axial motion occurs because no physical bodies constrain the length between the fixed and free ends of the interlocking LJSs that form the VSL, as illustrated in Figure 4.7b. The free end of the VSL was manually placed in its original position between consecutive tests to ensure that the VSL always had the same length in each test.

4.2.3 Finite Element Simulation of VSL Concept A

FE simulations have been carried out to study VSLs with parallel guided architectures. For example, a VSL formed by vacuum pressure-activated LJSs was simulated in FE software to study how the dimensions of the robot link affect the torsional stiffness and the critical vertical buckling load [20].

An FE model was built in Ansys with the same dimensions and components as the VSL that was tested in the previous sections. The link was modelled in SolidWorks and imported to Ansys. The Airstroke actuators were very difficult to model exactly because of the flexible membrane. Therefore, the Airstroke actuators were modeled as traditional pneumatic cylinders with pistons,

as shown in Figure 4.12. The diameter of the piston is the same as the top side of the Airstroke that comes in contact with the layers.

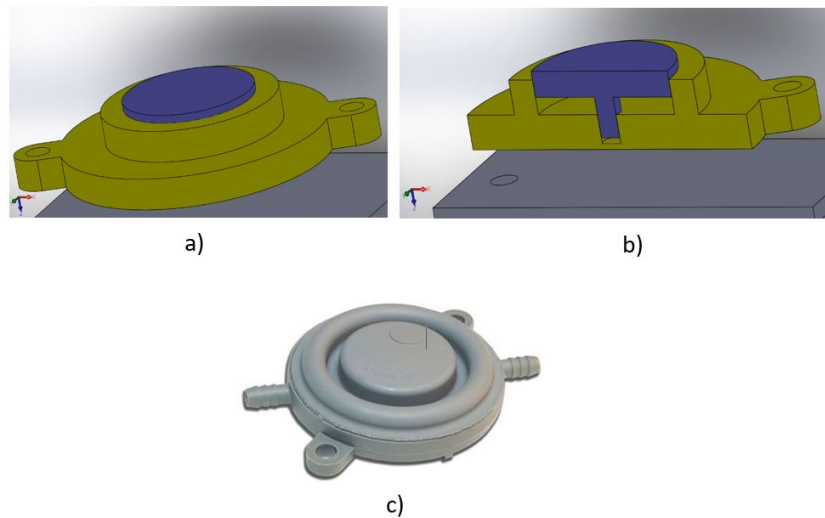


FIGURE 4.12: CAD model of the Airstroke a) general view of CAD model. b) cross sections of CAD model. c) real sample of an Airstroke actuator.

The FE model could not be simplified to one half of the CAD model because the VSL does not have symmetry planes. In particular, The Airstroke actuator is not symmetric. Concerning the mesh. The size of the element in the layers was 1.25 mm. As shown in Figure 4.13, only one element across the thickness of the layers was necessary because the element order was quadratic.

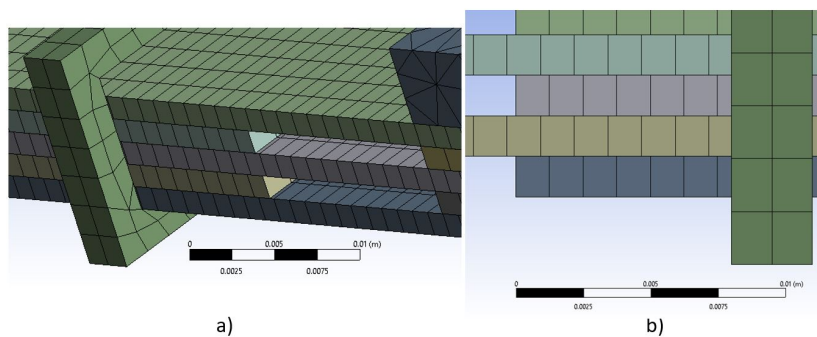


FIGURE 4.13: Mesh of the FE model of VSL Concept A.

The FE model has the same load and boundary conditions that were implemented in the experiment. These conditions are the following: the VSL model is fixed at one of its ends; deflection is imposed at the free end following the same values that were imposed in the experiment; the

pressure in the pneumatic cylinder is calculated as the equivalent pressure that would generate the same locking force that the real Airstroke applies according to its force vs displacement graph. Figure 4.14 illustrates the load and boundary conditions implemented in the FE model.

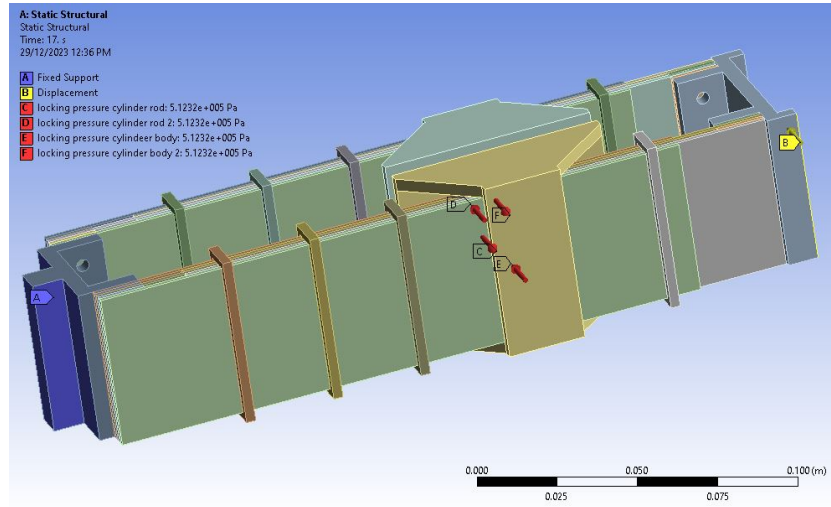


FIGURE 4.14: Loads and boundary conditions imposed on the FE model of VSL Concept A

The most relevant settings in the simulations are equal to the settings described in Section 3.6.2. The only difference is the COF between the Airstroke actuator and the top layer of the LJS, which was 0.251. This value of COF was measured using an inclined plane friction device [74].

The result of the simulation is the force associated with each value of the enforced deflection. Figure 4.15 illustrates the deformed shape obtained in the FE simulation when the lateral displacement of the free end was 24 mm (the maximum enforced in the test).

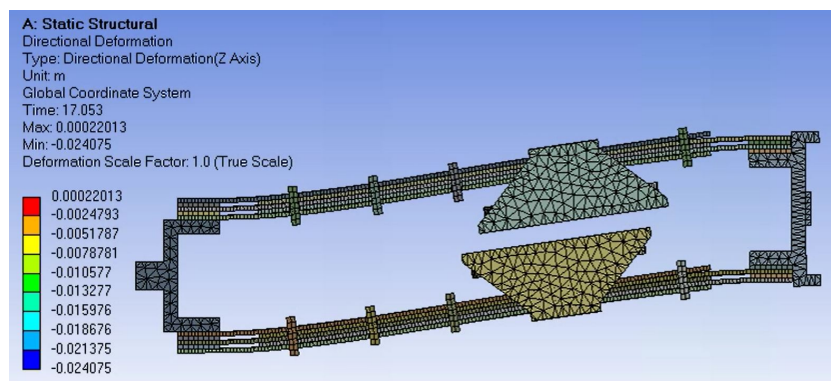


FIGURE 4.15: Resulting shape of the VSL at 69 kPa from the FE simulation when deflection of the free end is 24 mm.

Figure 4.16 illustrates the results of the FE simulations and the experiment for the VSL at 69 kPa. It can be observed that the simulation results agree well with the experimental results. Both results were linearised by the least squares method to define a stiffness of $k=0.4456$ N/mm in the experiment and a stiffness $k=0.427$ N/mm in the simulation. Therefore, the error of the simulation relative to the experiment is about 4.1% in this case.

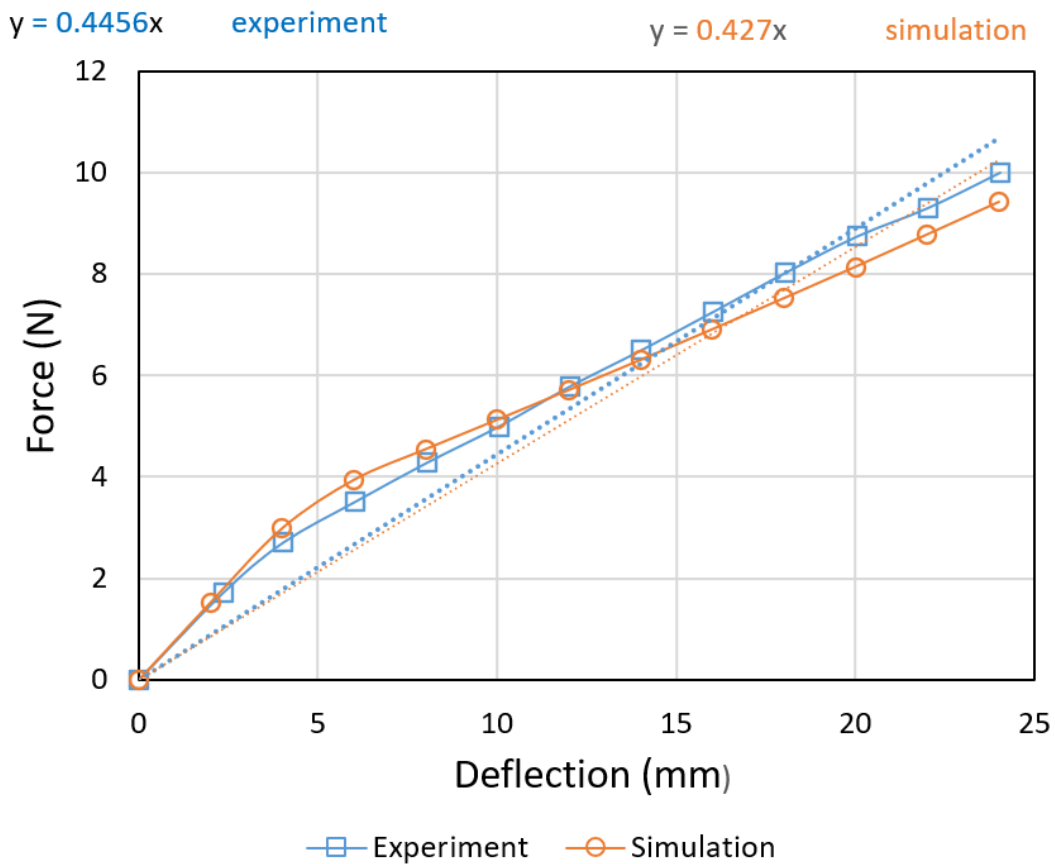


FIGURE 4.16: Comparison of stiffness from experiments and FE simulations, VSL Concept A at 69 kPa.

Figure 4.17 compares the experimental and the simulation values of stiffness for all the pressure states tested in the experiment. It can be seen that the results of the simulations match well with the results of the experiment. In addition, Table 4.1 shows that the maximum error between the experiment and the simulations is 8.83% and occurred at 207 kPa (30 psi).

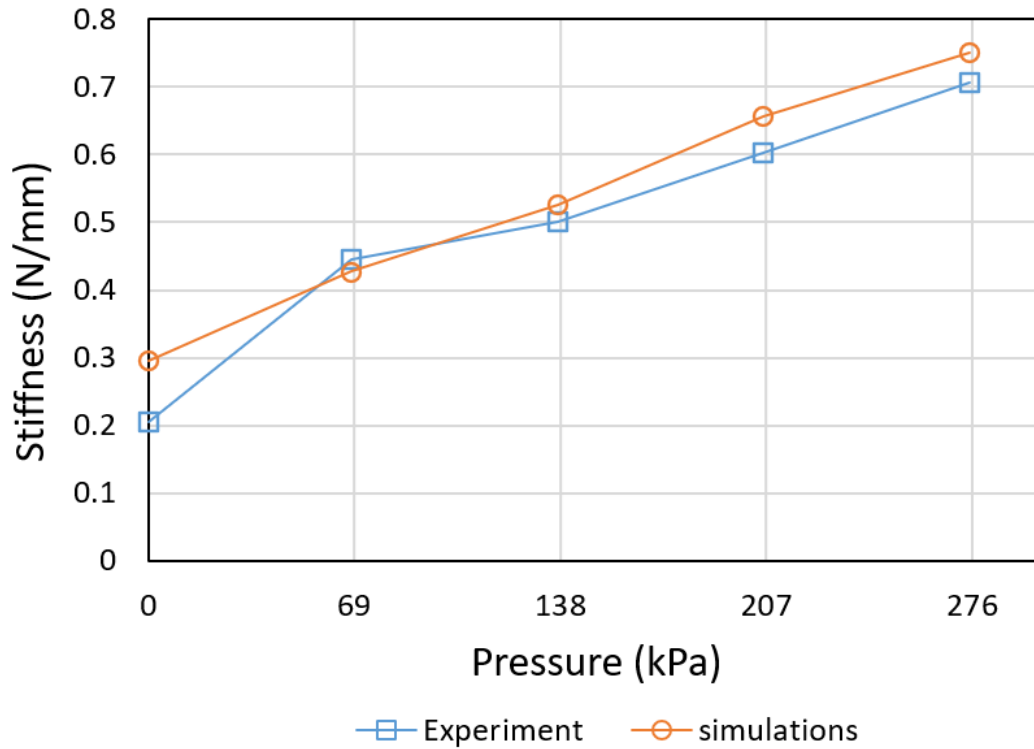


FIGURE 4.17: Comparison of bending stiffness from experiments and FE simulations.

TABLE 4.1: Error from the simulations results relative to experimental results in the VSL Concept A

Pressure (kPa)	0	69	138	207	276
Stiffness: experiment (N/mm)	0.2051	0.4456	0.5002	0.6031	0.7073
Stiffness: simulations (N/mm)	0.295	0.427	0.5254	0.6564	0.7511
Error	4.38%	4.17%	5.03%	8.83 %	6.19%

Based on the experimental values from Table 4.1, the stiffness ratio between the maximum stiffness state (276 kPa) and the minimum stiffness state (0 kPa) is 3.44.

4.3 VSL Concept B

VSL Concept B keeps two characteristics from VSL Concept A: the interlocking LJSs and the parallel guided beam architecture. It also incorporates the trapezoidal pin mechanism to modulate the stiffness of the link. These trapezoidal pins are also driven by pneumatic cylinders. Figure 4.18 illustrates the components of VSL Concept B. The overall dimensions of the link are; length 344 mm, width 159 mm, and height 58.6 mm. The sheets of the LJSs are made of ABS plastic with the same properties as for VSL Concept A described in Section 4.2. It can be appreciated that the length and width of this link are larger than the corresponding dimensions of VSL Concept A because it was necessary to accommodate the trapezoidal pin and the pneumatic actuators.

Similarly to VSL Concept A, each LJS of VSL Concept B has two frames located very close to the ends of the overlapping section in order to avoid the local buckling of the top layer of the proximal end of the LJS when the VSL is bent.

VSL concept B implements a trapezoidal pin with an angle of 30° as can be seen in Figure 4.18b. This angle was selected because Section 3.7.1 demonstrated that the highest stiffness in normal LJS occurs at 30° for pressures higher than 500 kPa. Each trapezoidal pin is driven by a double-acting pneumatic cylinder (SMC-model CDQSB12-5D, Manufacture by SMC, Aichi-Japan).

VSL Concept B was also designed to be used in the impact tests presented in Chapter 5. Therefore, the width of the link was increased to create enough room for additional components necessary for the impact tests.

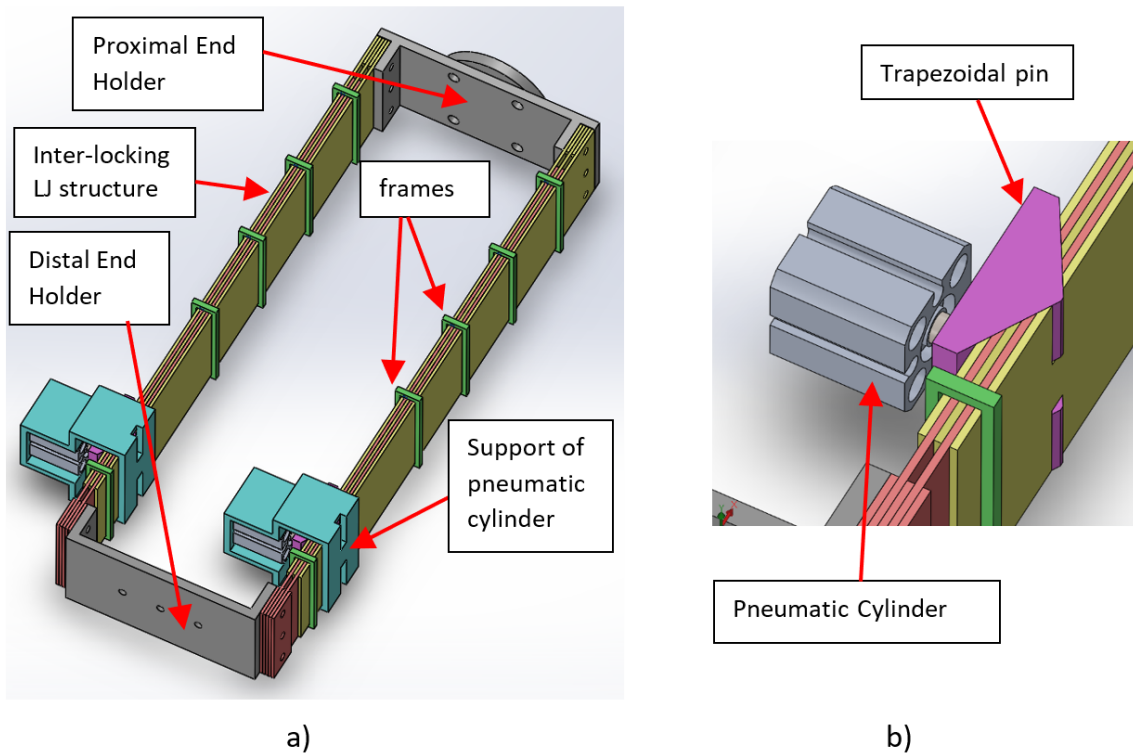


FIGURE 4.18: VSL Concept B. a) components. b) Detail of the actuator and the trapezoidal pin (support of pneumatic cylinder is hidden).

4.3.1 Bending Experiment

Bending experiments were carried out to determine the bending stiffness of VSL Concept B. The experimental setup was very similar to the experimental setup presented in Section 3.5. The only difference is the use of an IMADA ZTA-50N force gauge that is manufactured by IMADA (Aichi-Japan), as seen in Figure 4.19.

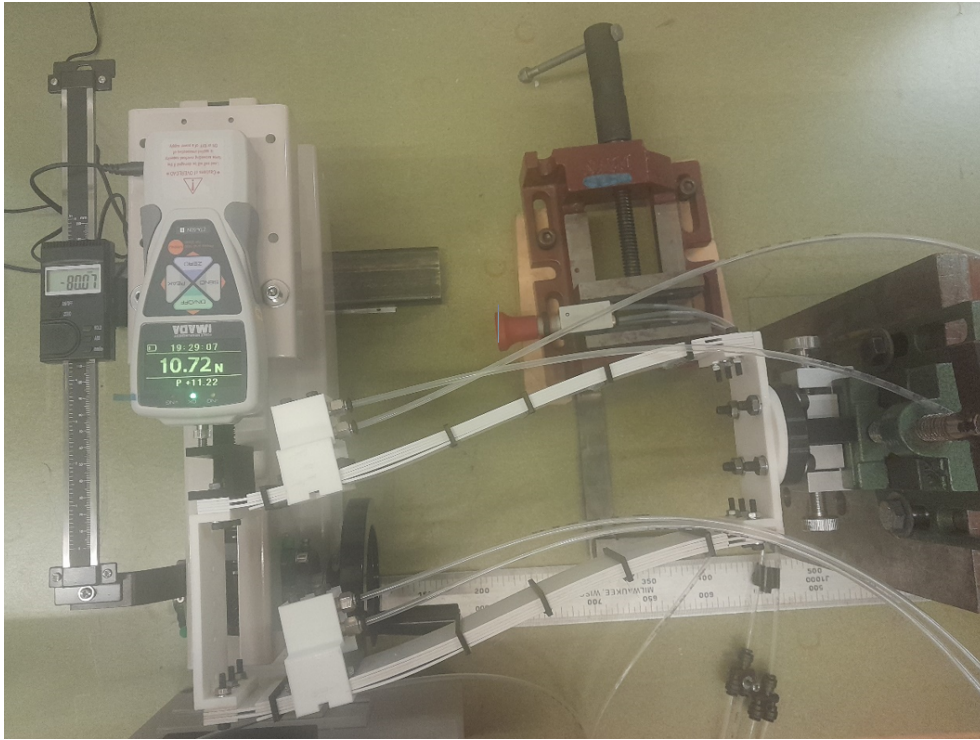


FIGURE 4.19: Experimental setup for measuring the bending stiffness of VSL Concept B.

The experiment of force vs deflection consisted on the application of a complete load-unload cycle at 0, 100, and 600 kPa of pressure in the pneumatic cylinders. These pressure values were selected because they produce the maximum and minimum stiffness states necessary to use the VSL in the impact tests presented in Chapter 5. The test begins with the loading procedure, where the deflection increases every 2 mm from 0 mm to 12 mm, and then every 4 mm up to 48 mm, which is about 10% of the total length of the link. Then, the unloading procedure begins by reducing the deflection every 4 mm from 48 mm to 12 mm, then every 2 mm until a deflection where the force gauge measures 0 N. It is important to know that these values must be recorded after the force has reached a stable value. For this reason, it can be considered that the LJS is loaded and unloaded quasi-statically.

Similarly to the experiments presented in Section 4.2.2. Three trials were conducted at each value of deflection, and the average of these values defines the force values that correspond with the given deflection. The results of the bending experiments are illustrated in Figure 4.20.

VSL Concept B presented the same problem observed in VSL Concept A, which consists of the axial separation of the free end of the VSL relative to the fixed end of the VSL. This

displacement was observed after each test, and it was more pronounced in the tests at 0 kPa because the trapezoidal pin was not engaged with the LJSs. The free end of the VSL was manually placed in its original position between consecutive tests to ensure that the length of the VSL was always the same.

The results were linearised by the least squares method to calculate the stiffness considering only the first section of the curve from 0 mm to 8 mm, as shown in Figure 4.20b. A similar approach to calculate the stiffness was carried out in Section 4.2.3.

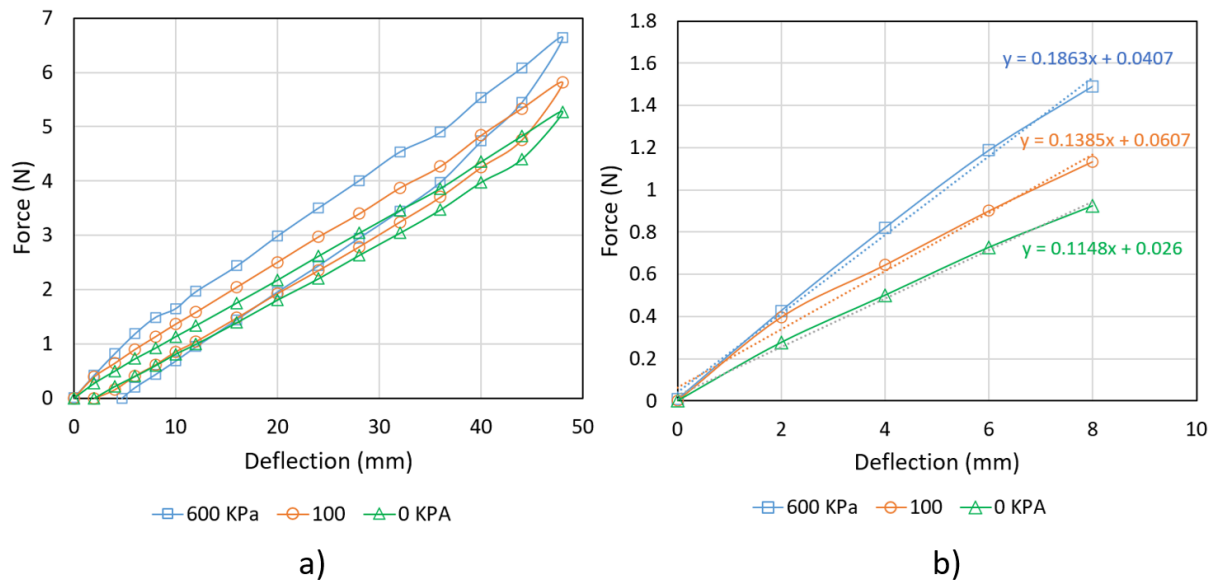


FIGURE 4.20: Results of the force-deflection experiment for VSL Concept B.

Figure 4.20 shows the stiffness of the VSL calculated for each pressure. The stiffness ratio between the maximum stiffness state (600 kPa) and the minimum stiffness state (100 kPa) is 1.34. The stiffness at 0 kPa was not considered as the minimum stiffness state because the link at 0 kPa does not have practical application in impact tests, as will be explained in Chapter 5.

4.4 VSL Concept C

VSL Concept A and the VSL Concept B were combined in a new VSL design. This VSL is a parallel guided beam, and each beam is composed of an interlocking LJS with a trapezoidal pin

driven by an Airstroke actuator. This combination allows the implementation of the trapezoidal pin mechanism in a link with a smaller width than the VSL with pneumatic cylinders (VSL Concept B). As a result, the link presented in this section is less bulky than the predecessors.

Figure 4.21 illustrates the components of the proposed link. The VSL is a parallel guided beam that is composed of two interlocked LJSs, each LJS having five sheets made of ABS plastic. The Airstroke actuator is located in the centre of the beam because this is the position where the actuator may generate the maximum stiffness in DLJ structures [9]. The support of the Airstroke actuator is bonded to the bottom layer and made through 3D printing (FDM technology) using PLA material. The airstroke actuator drives a trapezoidal pin that sits on trapezoidal slots that were machined in the sheets of the LJS. The overall dimensions of the link are: length 291 mm, width 87.9 mm, and height 78.6 mm. The material for the laminates of the LJSs is ABS plastic with the same mechanical properties as in VSL Concept A that were described in Section 4.2.

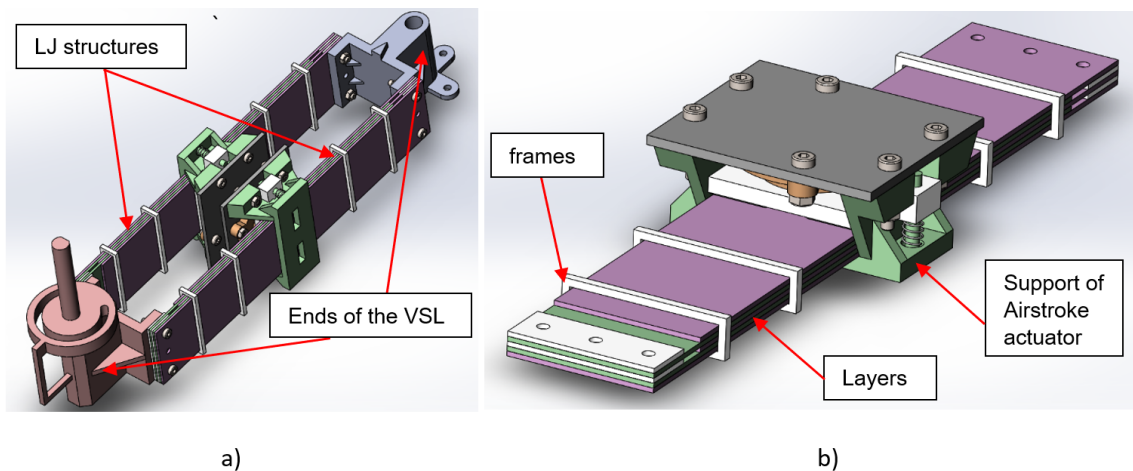


FIGURE 4.21: VSL Concept C. a) design of the whole link. b) Components of each LJS.

Similarly to VSL Concept B, the VSL Concept C also implements a trapezoidal pin with an angle of 30° . This angle was selected because Section 3.7.1 demonstrated that the highest stiffness in normal LJSs occurs at 30° for pressures higher than 500 kPa.

The number and the location of the frames in the VSL Concept C are similar to the VSL Concept A and follow the same reasoning. In particular, two frames are placed very close to the ends of the overlapping section in order to avoid the local buckling of the top layer of the proximal end of the LJSs when the VSL is bent.

Figure 4.22 illustrates another important feature of the new VSL, which is the bottom layer of the LJS that extends between both ends of the link. The front part of the link therefore cannot be separated from the back part of the link. This feature avoids the problem that was present in VSL Concept A and VSL Concept B, in which both ends of the VSL separated after a bending test. Another consequence of this feature is that VSL Concept C does not require manual adjustment after bending or impact test to set up its original length while the VSL Concept A and VSL Concept B require such adjustment as explained in Section 4.2.2 and Section 4.3.1. It should be noted that this modification does not constrain the relative slip between the layers during bending deformation. Therefore, it does not eliminate the variable stiffness capability of the LJS for bending.

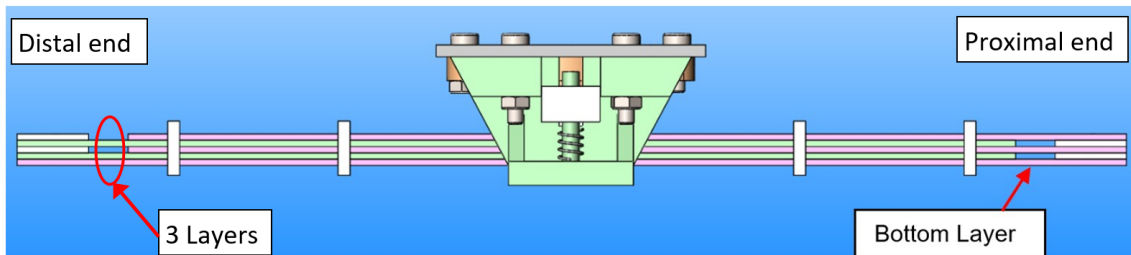


FIGURE 4.22: Bottom layer of one of the LJSs in VSL Concept C.

The top surface of the Airstroke, which moves up when the actuator is pressurised, was not designed to be attached to another body, which means that this actuator is able to push an object, but it cannot pull an object. Therefore, the support of the Airstroke actuator was designed to execute the retraction motion. This function is carried out by a pair of compression springs that can be seen in Figure 4.23. The support has two cylindrical protrusions that keep the springs in place and guide the motion of the trapezoidal pin. The design of the trapezoidal pin also includes two holes on both sides to allow the compression of the springs. The cylindrical protrusions and the slots on the sides of the support contribute to the guidance of the trapezoidal pin. Finally, the Airstroke actuator is attached to an aluminium lid, which is attached to the support utilising bolts and nuts.

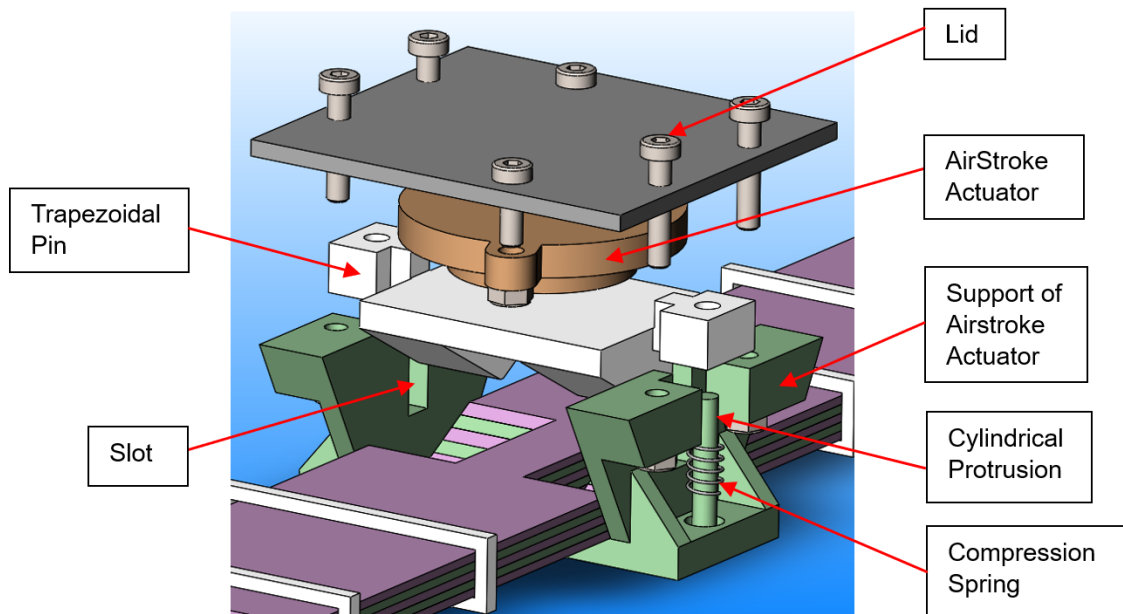


FIGURE 4.23: Components of the mechanism to vary the stiffness in VSL Concept C.

The mechanism to change the stiffness of the new version of the VSL works as follows. First, it should be noted that the compression springs keep the trapezoidal pin in contact with the Airstroke actuator. Then, when the Airstroke actuator is pressurised, the actuator pushes the trapezoidal pin until it sits in the trapezoidal slots of the stack of sheets. When the Airstroke is depressurised, the top face of the actuator returns to its original position, and the compression springs push the trapezoidal pin back until the initial position. It is important to note that the stiffness of the springs is low, which means that the springs do not apply too much force against the Airstroke actuator when it is pressurised. The springs apply just enough force to push back the trapezoidal pin when the pneumatic actuator is depressurised.

4.4.1 Bending Experiment

Bending experiments were carried out to determine the bending stiffness of VSL Concept C. The experimental setup was very similar to the experimental setup presented in Section 4.3.1. The only difference is the use of a 2/2-way manually-actuated pneumatic valve, as seen in Figure 4.24

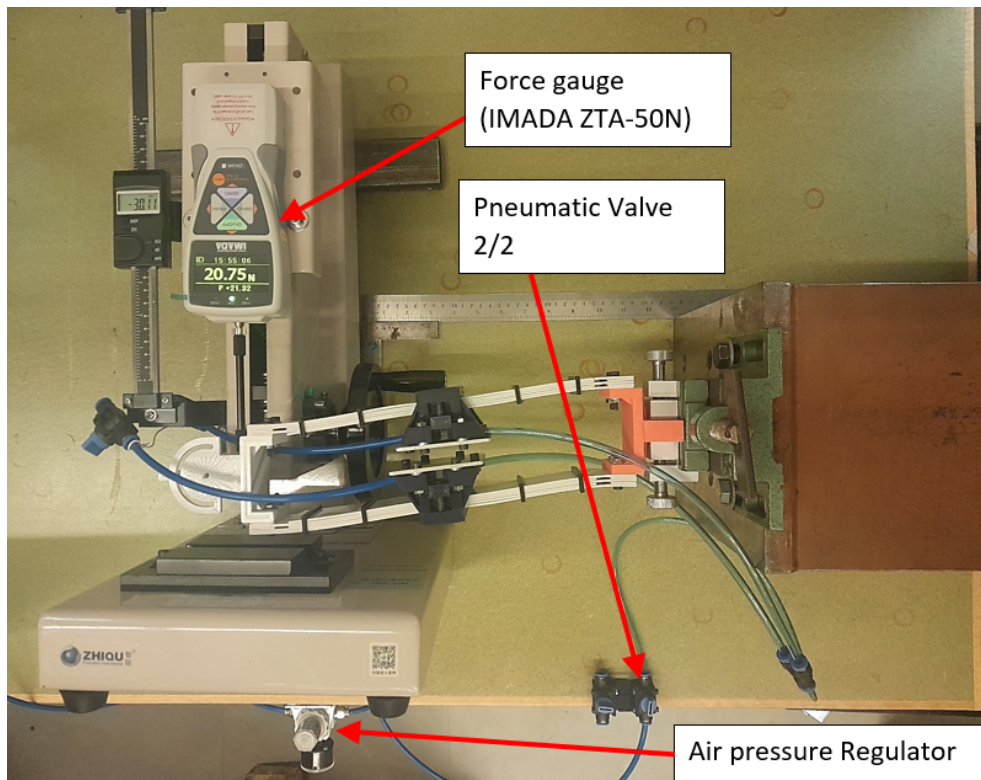


FIGURE 4.24: Experimental setup for measuring the bending stiffness of the VSL Concept C

The experiment of force vs deflection consisted on the application of a complete load-unload cycle at 0 kPa, 276 kPa (40 psi), and 345 kPa (50 psi) of pressure in the Airstroke actuators. 0 kPa and 345 kPa were selected because they produce the minimum and the maximum stiffness states necessary to use the VSLs in the tests presented in Chapter 6. 276 kPa was selected for comparison with the VSL Concept A, which was pressurised at the same pressure. The test begins with the loading procedure, where the deflection increases every 2 mm from 0 mm to 30 mm which is about 10% of the total length of the link. Then, the unloading procedure begins by reducing the deflection every 2 mm from 30 mm until a deflection where the force gauge measures 0 N. It is important to know that these values are recorded after the force has reached a stable value. For this reason, it can be considered that the VSL is loaded and unloaded quasi-statically.

Five trials were conducted at each value of deflection, and the average of these values defines the force values that correspond with the given deflection. The average force values of the bending experiments are illustrated in Figure 4.25. The results were linearised by the least squares method to calculate the stiffness as shown in Figure 4.25b where the slope of the straight lines

corresponds to the stiffness of the VSL for a given value of pressure in the Airstorke actuators. A similar approach to calculate the stiffness was carried out in Section 4.2.3.

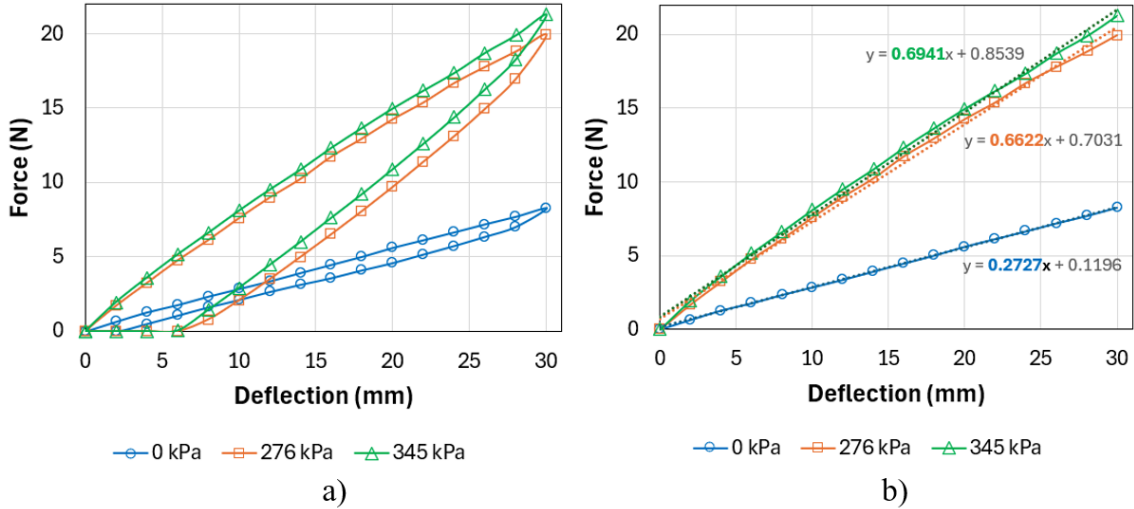


FIGURE 4.25: Results of the force-deflection experiment for VSL Concept C.

The stiffness ratio between the maximum stiffness state (345 kPa) and the minimum stiffness state (0 kPa) is 2.54. The stiffness ratio between the VSL at 276 kPa and the minimum stiffness is 2.42. These values of stiffness ratio will be discussed in Section 4.7

4.5 Torsional Stiffness of VSL Concept C

All the VSL Concepts presented in this chapter have a parallel guided beam architecture. This feature was implemented to increase the torsional stiffness in comparison to VSLs composed of a single beam. In addition, the VSL concepts could also change the torsional stiffness despite this is not the main purpose that motivates their development. Therefore, this section presents torsion tests that were carried out to study the difference in torsional stiffness between these two architectures and to investigate the effect of the mechanisms to change the bending stiffness in the torsion stiffness. The VSL Concept C link was selected for these tests.

Figure 4.26 shows the components of the experimental setup. The VSL was fixed at one end and twisted at the other end by a UR3 robotic arm (manufactured by Universal Robots, Odense-Denmark). The torque applied at the free end of the VSL was measured by an F/T ATI Axia80 M20

sensor that has a resolution of 0.005 Nm (manufactured by ATI Industrial Automation, North Carolina-USA). The torque measured by the sensor is collected by the ATI FT Data viewer program. A coupling between the torque sensor and the free end of the vSL was printed in 3D. This coupling allowed the application of torque by the UR3 without generating other types of loads in the VSL, such as bending. The air pressure in the Airstroke actuators is controlled by a 2/2 way manually-actuated pneumatic valve and an air pressure regulator.

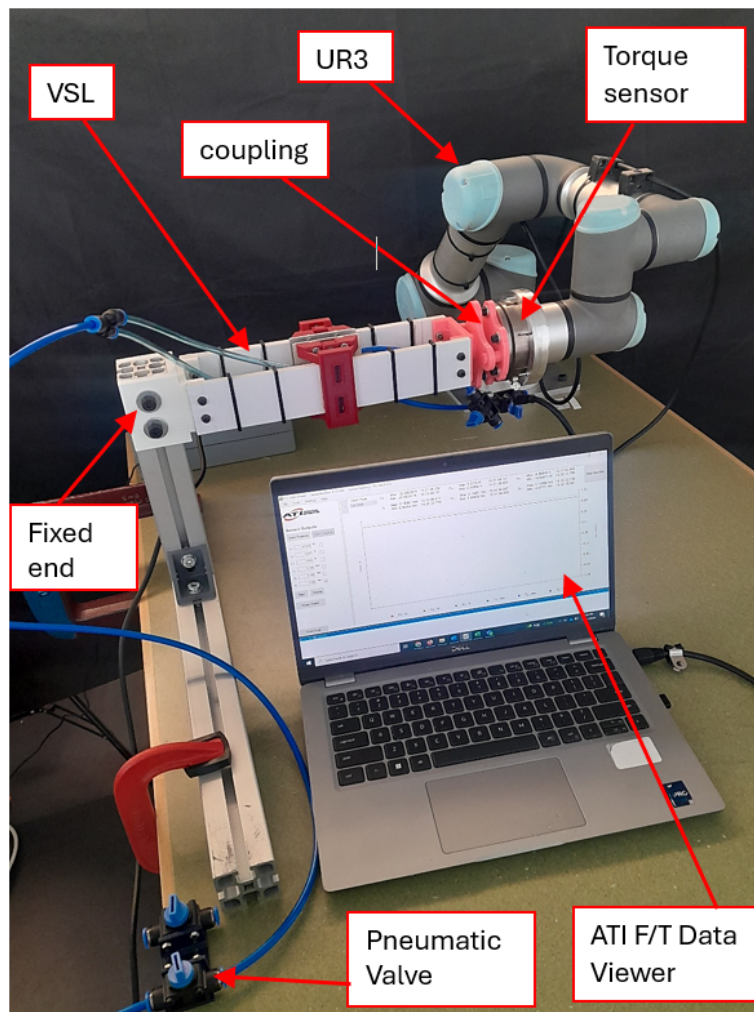


FIGURE 4.26: Experimental setup of the torsion experiment.

The experiment was carried out on the VSL Concept C and a VSL formed by a single LJS, as can be seen in Figure 4.26 and Figure 4.27, respectively. Each link was tested at 0 kPa and 345 kPa to study the minimum torsional stiffness and the maximum torsional stiffness respectively. The experiment procedure consisted in coupling the end effector of the robot arm with the free

end of the VSL. Then, the wrist of the UR3 twists for 9.1 s until reaching an angle of 6.5° and stops in this position for 0.7 seconds as shown in Figure 4.27b; finally, the wrist of the UR3 returns to the initial position (0°). This procedure was repeated 5 times for each experiment.

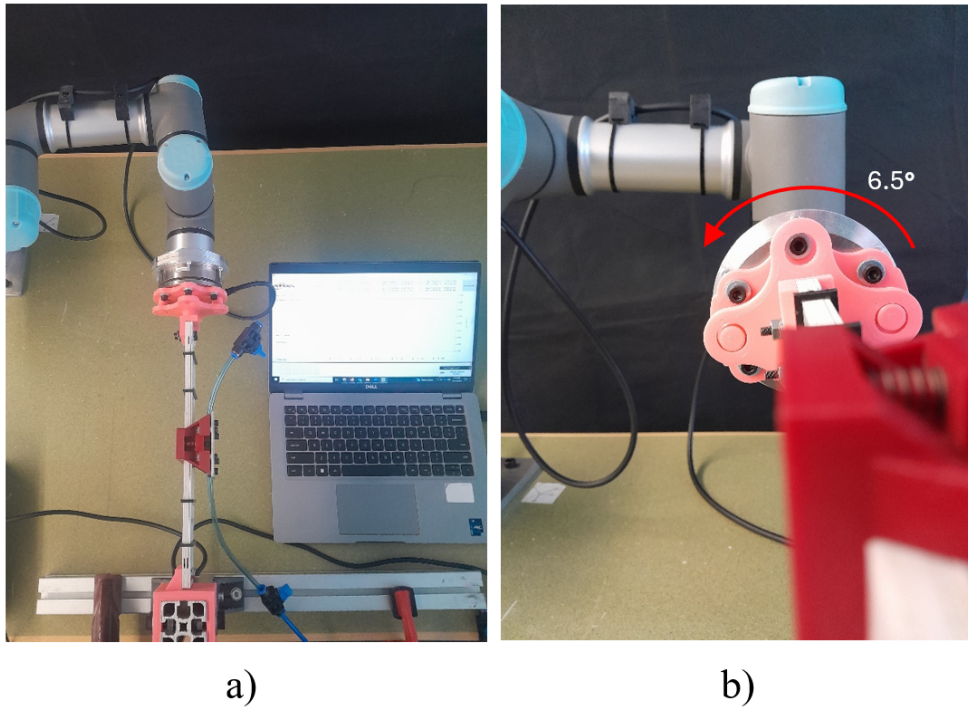


FIGURE 4.27: Torsion experiment of the single beam VSL

Table 4.2 and Figure 4.28 show the results of the torsion experiment. The torsion stiffness for each case was calculated as the average of the measured torques divided by 6.5° .

TABLE 4.2: Results of the torsion experiment

Pressure (kPa)	single beam VSL Torsional Stiffness (Nm/rad)	Parallel guided beam VSL (VSL Concept C) (Nm/rad)
0	1.1	11.9
345	1.7	13.2
Torsional stiffness ratio (max/min)	1.56	1.11

The stiffness ratio that is shown in Table 4.2 is calculated as the ratio between the maximum torsional stiffness and the minimum torsional stiffness. For both types of links, the torsional stiffness when the Aistroke actuators are pressurized is higher than the torsional stiffness when the actuators are depressurized, demonstrating that the trapezoidal pin mechanism also varies

the torsional stiffness despite being designed to change the bending stiffness. However, the stiffness ratio of the VSL Concept C is low in comparison with its bending stiffness ratio (2.54), showing that this type of VSL has limited capacity to vary the stiffness ratio.

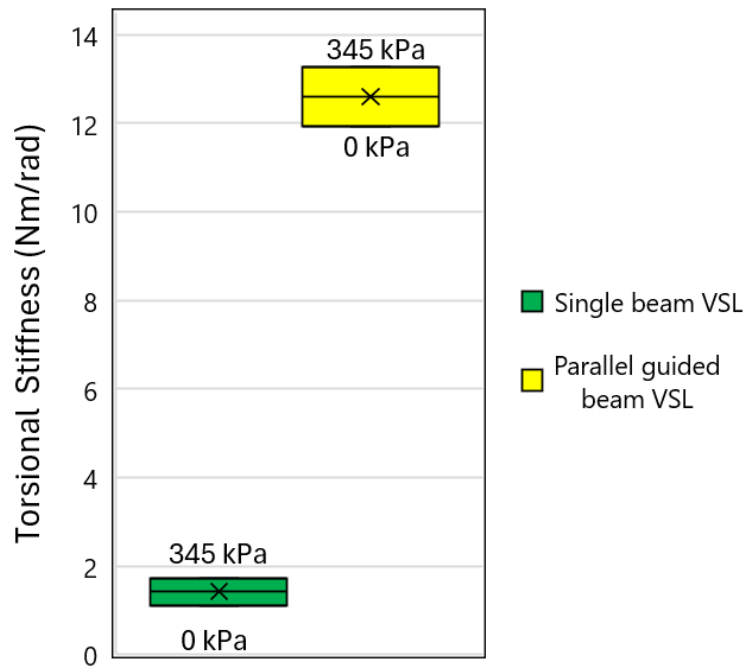


FIGURE 4.28: Torsional Stiffness for Parallel guided Beam link and single link at 0 kPa and 345 kPa.

Figure 4.28 shows an evident difference between the torsional stiffness of the single beam link and the parallel guided beam link. The stiffness of the parallel guided beam link is about 9 times larger than the stiffness of the single beam link. This result agrees with the FE simulations of similar VSLs based on vacuum pressure [20].

4.6 Manufacturing of VSLs

The manufacturing of the VSL Concept B and VSL Concept C was particularly challenging due to the trapezoidal slots in the laminates. This section describes the manufacturing process of the LJSs and the problems during this process.

The process to cut the trapezoidal slots of the LJS was very similar to the process that was described in the Section 3.4.2, which consists of a fixture that is composed of two sacrificial

plates that are made of brass. Figure 4.29 illustrates the assembly of the fixture for the case of VSL Concept C. A similar fixture was used for the machining of VSL Concept B. VSL Concept A did not require this type of fixture for machining because it does not have trapezoidal slots. It can be seen that this fixture has bolts on both ends of the LJS, while the fixture presented in section 3.4.2 has bolts only on one side of the LJS. The reason for this difference is that VSL Concept B and VSL Concept C are based on the interlocking LJS.

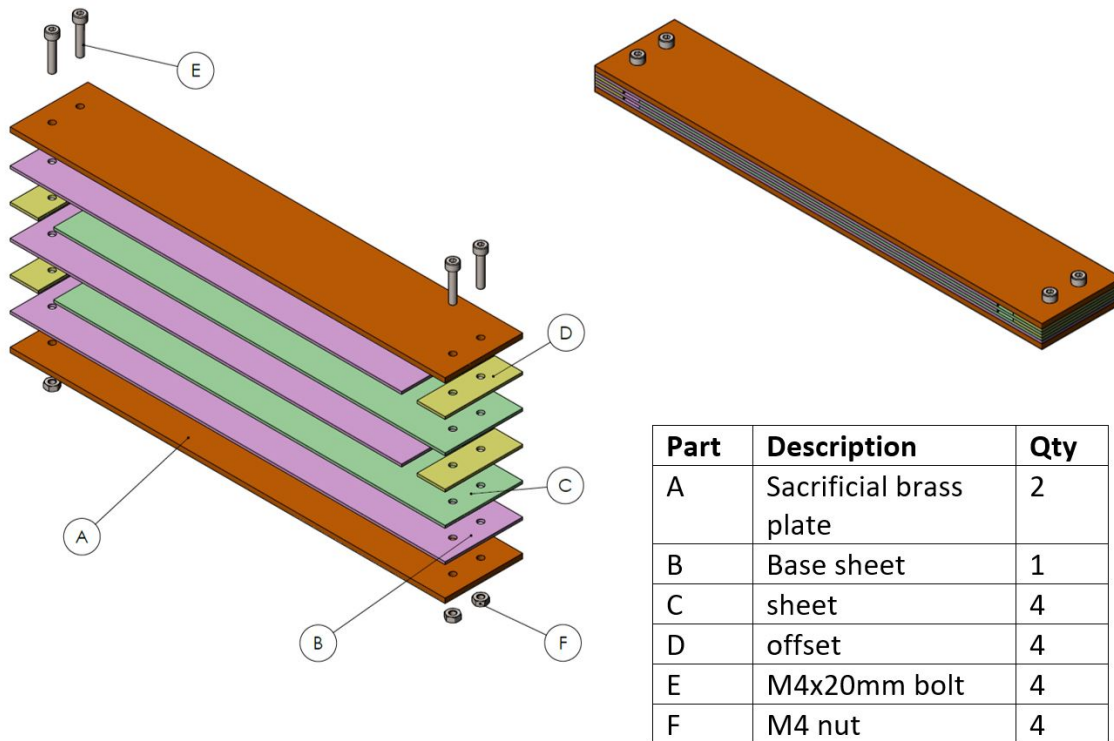
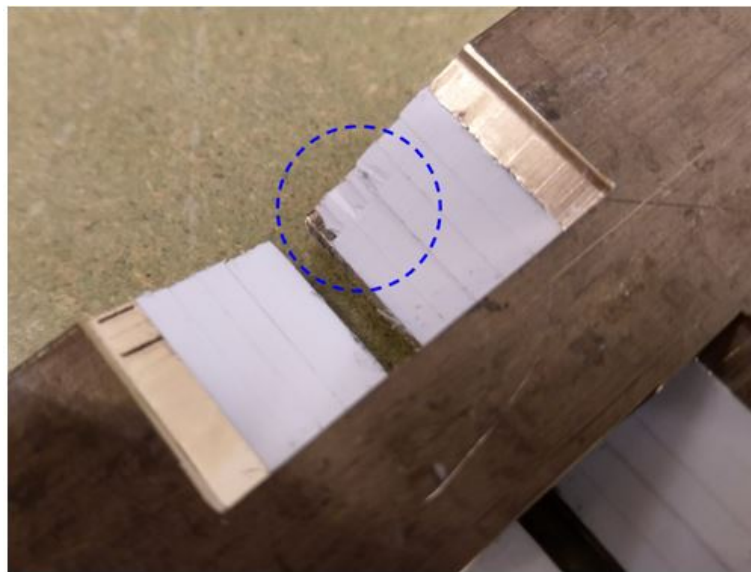
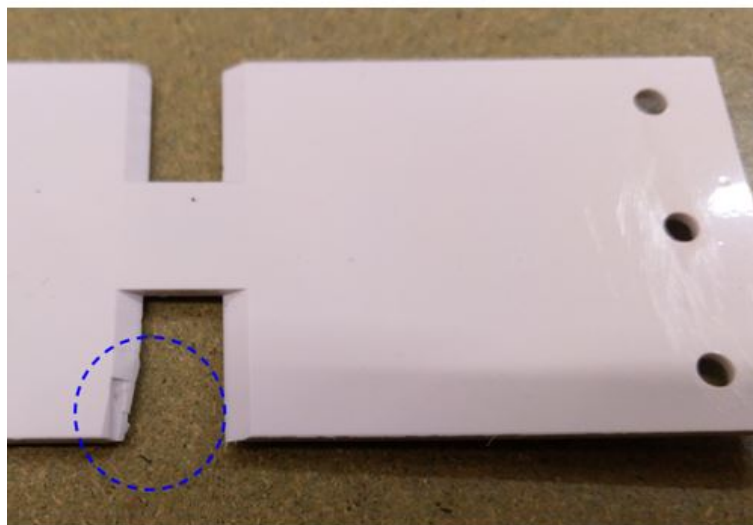


FIGURE 4.29: Assembly of the fixture to cut the trapezoidal slot in the LJS that formed VSL Concept C.

The machining of the LJS had a success rate of 50%. This means that the manufacturing of 50% of the samples failed because the milling tool tears the layers during the machining of the trapezoidal slot. Figure 4.30 illustrates the effects of the tearing in the layers. This type of defect may affect the performance of the trapezoidal pin mechanism because the contact area between the layers and the trapezoidal pin is reduced. These LJSs were therefore discarded.



a)



b)

FIGURE 4.30: Tearing defect in the layers of the VSL Concept C generated during the machining of the trapezoidal slots

4.7 Summary of VSL Design Concepts

Table 4.3 shows a summary of the main characteristics of the VSL concepts presented in this chapter. It should be noted that VSL Concept A does not have a pin or clamp because the Airstroke actuator itself acts as a clamp. It must also be noted that VSL Concept C does not

experience axial separation because the bottom layer is extended along the whole length of the link.

All the VSL concepts have in common the interlocking LJSs, the parallel guided beam architecture, the presence of frames, and the material of the laminates: ABS plastic whose properties are described in Section 4.2.

TABLE 4.3: Summary of VSL concepts

Aspect	Concept A	Concept B	Concept C
Type of actuator	Airstroke	Double-effect pneumatic cylinder	Airstroke
Type of pin	Flat clamp	Trapezoidal-30°	Trapezoidal-30°
Return to initial position	Through actuator	Through actuator	Through compression springs
Presence of axial separation	Yes	Yes	No
Use	No particular use	Impact test in chapter 5	Robot arm with VSL in chapter 6
Location of the actuator along the length	Distal end	Distal end	Middle
Stiffness ratio	3.44	1.34	2.54

The bending performance of the VSLs presented in this chapter is evaluated through the stiffness ratio which is presented in Table 4.3. It can be seen that the higher stiffness ratio corresponds to VSL Concept A, and the minimum stiffness ratio corresponds to VSL Concept B. The most likable cause for the low stiffness ratio of VSL Concept B is that this VSL has pneumatic cylinders while the other VSLs have the Airstroke actuators that are able to generate higher forces than pneumatic cylinders. It can be noted that VSL Concept C has a lower stiffness ratio than VSL Concept A. This difference is probably caused by the bottom layers of the LJSs of the VSL Concept C that extend along the whole length of the link, which increases the number of layers that support the bending in the distal end of each LJS to three as Figure 4.22 shows, while only

two layers support the bending in the distal end of each LJS of the VSL Concept A as can be seen in Figure 4.8.

Although the bottom layers of the VSL Concept C can reduce its stiffness ratio in comparison with VSL Concept A, they prevent the separation of the distal and proximal parts of the link, which is a significant advantage over the VSL Concept A. This separation problem that occurs in VSL Concept A and VSL Concept B reduces significantly their practical application in robotics because they can not keep their original length after load application.

4.8 Conclusions

A new VSL was designed and manufactured. The final design was called “VSL Concept C” and combines a set of features that make it adequate for the construction of a robot arm with VSLs. The main novelty of this design is that it incorporates the trapezoidal pin mechanism and the frames that were presented in the previous chapter.

Two important mechanical challenges were identified in the design of the VSL. First, the difficulty of attaching another link at the distal end of a normal LJS. Second, the necessity for supporting all types of loads generated by adjacent links like torsion, axial force, and bending moments in all axes. Two features were incorporated in the design of VSL Concept C to address these challenges. The first feature is the interlocking LJS that allows the attachment of another link at the distal end. The second feature is the parallel guided beam architecture that supports axial torsion and transverse vertical force better than a single beam. Torsional tests carried out on the VSL Concept C demonstrated that the torsional stiffness of the parallel guided beam is about 9 times larger than the stiffness of a single beam link.

VSL Concept C also incorporates an Airstroke actuator, which is a pneumatic actuator that is shorter than a typical pneumatic cylinder. This advantage in combination with the parallel guided beam, makes it possible to place the actuators inside the link, which eliminates external protrusions, making the link safer in the case of an impact with a human operator.

Another important feature of VSL Concept C is that the bottom layers of the LJSs extend along the whole length of the link. This feature solves one of the main problems of interlocking LJS,

which is the separation of the distal and proximal parts of the links when the mechanism to lock the layers is disengaged.

VSL Concept C was developed as a result of two iterations in the design of the link: VSL Concept A and VSL Concept B. VSL Concept B was also developed to be tested in the impact test that will be presented in Chapter 5. VSL concept C is used in the construction of a VSL robot arm that is presented in Chapter 6.

Chapter 5

Application of VSLs to Mitigate Impacts

All the previous chapters have presented the response to the first research question, which was about how to create robot links with variable stiffness. Chapter 4 presented a set of VSL concepts that incorporate the novelties presented in Chapter 3 to achieve variable stiffness in LJSs such as the trapezoidal pin mechanism and frames.

This chapter presents part of the response to the second research question, which was about how to exploit VSLs to improve the performance of robots in human-robot interactions. To answer this question, VSL Concept B presented in Chapter 4 is used to investigate its capacity to reduce the impact force during a collision against a human being.

The lessons from this chapter are applied in Chapter 6 where a robot arm with VSLs is built and tested to completely respond to the second research question.

5.1 Impacts Between Robot Arms with VSLs and Human Beings

This section briefly reviews the most important aspects of the impact tests between VSLs and human operators, including the indicators that determine the damage caused by impacts on

human beings, the design of the test bench, passive and active compliance, and the use of soft cover materials for the robot arm.

Chapter 1 and Chapter 2 discussed some of the technologies that have been developed to mitigate the effects of the impacts between human beings and robots during the last decades. Some of these technologies consist of the variation of the stiffness of the robot, and this capability has been implemented through two approaches: VSJs and VLS. VSJs have been widely studied in human-robot interaction by [2, 26, 27, 29]. VSLs have been recently explored by [15, 16, 62, 79–81]. A comparison of performance between VSJ and VSL robots in human-robot impact presented by [62] demonstrates that a VSL robot can generate lighter injuries than a VSJ robot for the same given design parameters.

The investigation of impact between robot arms with VSLs and human beings has consisted mainly of carrying out impact tests. The result of these tests has been the determination of indicators of the damage produced to the human being during the impact. One of these indicators is the head impact criterion (HIC) [62, 80], which is based on measuring the acceleration of the human head during an impact and was created by the automobile industry. The use of the HIC criterion has shown some ambiguities and confusion when applied to impacts between robot arms and human beings. For example, a low value of HIC does not necessarily mean that a cobot is safe. HIC is only appropriate when the contact against the head happens in a large enough area in order to avoid penetration or puncture of the skull, and it is not applicable to situations where the head is trapped between the robot and a wall or any other rigid body [78].

Impact force is another criterion that has been used to evaluate the effects of an impact between a human being and a robot arm [82]. The impact force can be directly related to the biomedical limits of bone fracture. Therefore, the impact force was selected as the indicator to measure the effects of the impact tests that are presented in this chapter.

Impact test benches have been developed to carry out the impact tests of VSL. These impact tests usually involve a prototype of the VSL that is being tested and a dummy of the human head. The design of the test bench can be classified into two groups. One group is characterised by the motorisation of the VSL in order to reach the impact velocity [16, 62, 80]. Another group is characterised by a pendulum design where the VSL swings by the effect of gravity [79, 83] to reach the impact velocity. Both types of test bench are illustrated in Figure 5.1.

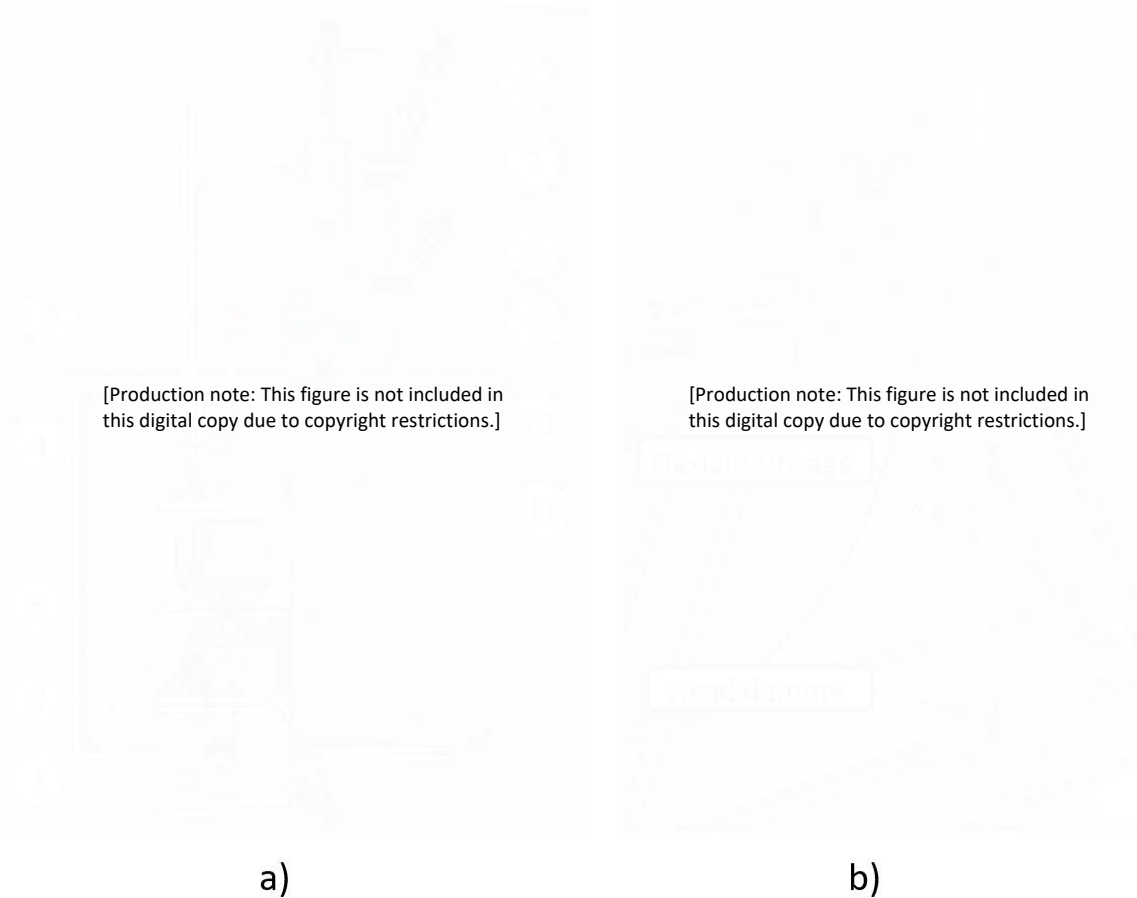


FIGURE 5.1: Types of test bench for impact between VSLs and human beings. a) Motorised design with VSL driven by an electric motor (1 is the motor, 3 is the VSL, and 6 to 10 are the components of the dummy head system). b) Pendular design with VSL driven by gravity.

Two strategies exist to implement compliance in safe robot arms for attenuating collisions. The first approach is active compliance, which consists of detecting the collision and then controlling the stiffness of the arm appropriately. This strategy involves using various types of sensors to detect the collision, and actuation mechanisms to dynamically respond to the impact. The second strategy is passive compliance, which consists of mechanical components that absorb the excessive collision force. Examples of passive components are springs, dampers, and soft covers. Passive compliance provides fast and reliable responses to collisions, but the response cannot be controlled during the impact because the stiffness of these components is usually tuned before the operation of the robot, or it is a permanent property of the component [79, 80].

As was explained above, covering the links of robot arms with a soft material is a passive method to reduce the effects of the impact in human-robot interactions. The damage reduction

is represented by the decrease in contact force and acceleration of the human body during the impact. The covering materials that have been used in impact tests are polyurethane foam [79, 83] and silicone [62]. The level of mitigation depends on the thickness of the soft material and has been extensively investigated through analytical models [79].

5.2 Impact Experiment

An impact test bench was designed and built to measure the impact force of the proposed VSL against a human head dummy. The test bench consists of a VSL that swings about a pivot and collides with a dummy of the human head, as can be seen in Figure 5.2. The dummy head consists of a car made of steel plates. The impact force is measured by an ATI FT Axia80 M20 sensor (manufactured by ATI Industrial Automation, North Carolina-USA) that is mounted in the steel car. The stiffness of the VSL is controlled by a pneumatic circuit that is composed of an air regulator and a 5/2 manual control valve.

The steel car and the sensor weight is 3.25 kg, which is the assumed value for the weight of the human head dummy in studies that present similar experiments [79, 83]. The steel car slides effortlessly along the aluminium rails since the wheels have ball bearings in their axles to ensure low friction losses. Figure 5.2 shows a pair of compression springs that were placed at the back of the steel car to replicate the stiffness of the neck, each spring has a stiffness of 230 N/m. The springs are combined in a parallel arrangement whose stiffness is 460 N/m, which is the same value that was assumed in similar impact experiments and models [79, 83].

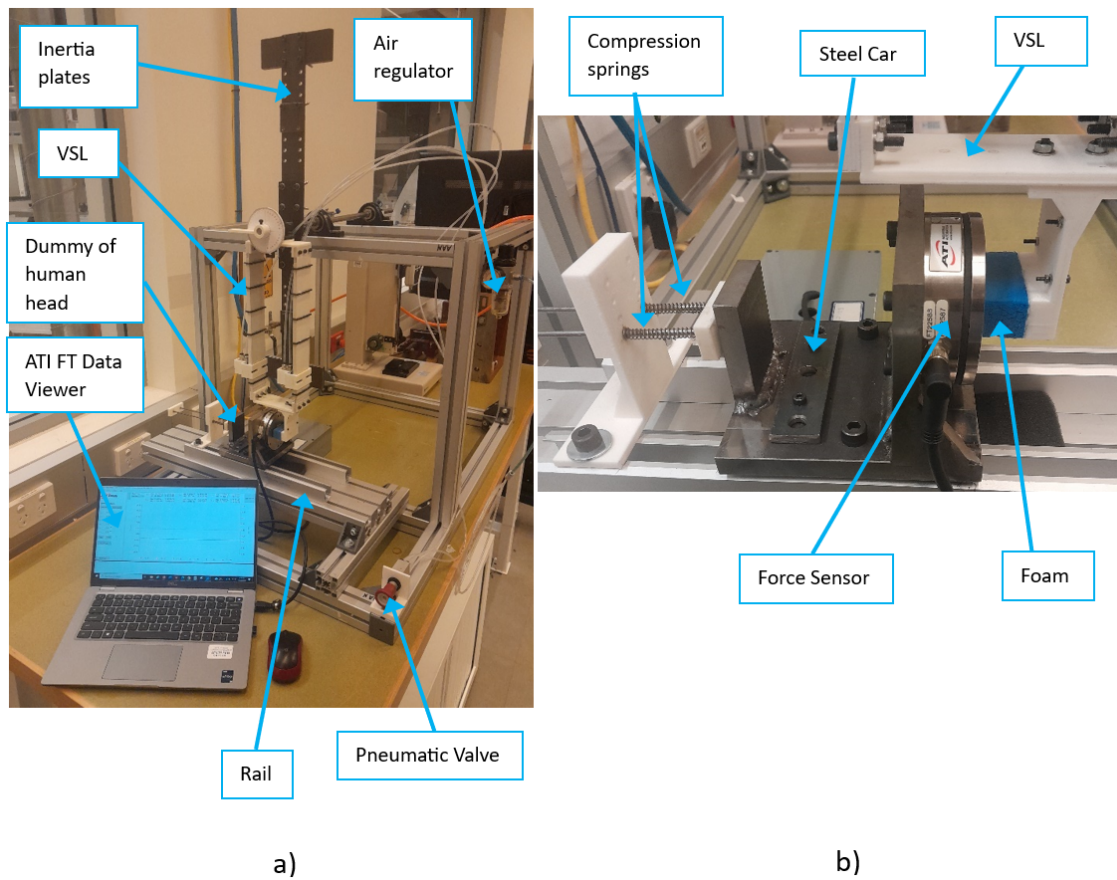


FIGURE 5.2: Assembly of VSL Concept B, PLA support, and inertia plates

The ATI FT Axia80 M20 is a force-torque sensor with all the electronics that are necessary for signal processing built into the sensor body. For the impact experiment, the sensor was set at its maximum sampling frequency of 7812 Hz, and a force range of 800 N in the Z axis. The forces measured by the ATI Axia80 sensor were processed through a program that is provided by the manufacturer of the sensor (ATI FT Data Viewer).

VSL Concept B is attached to the inertia plates through a support that is made of PLA (3D printed). This assembly is illustrated in Figure 5.3. The inertia plates are made of steel, and their purpose is to replicate the inertia of a robot arm. The whole assembly pivots about a calibrated steel bar that is supported on ball bearings. The steel bar is fixed to the aluminium frame through a bracket. The steel bar is therefore static, and the VSL revolves around the

steel bar. Grease was applied on the contact surfaces between the bar and the VSL to ensure low friction.

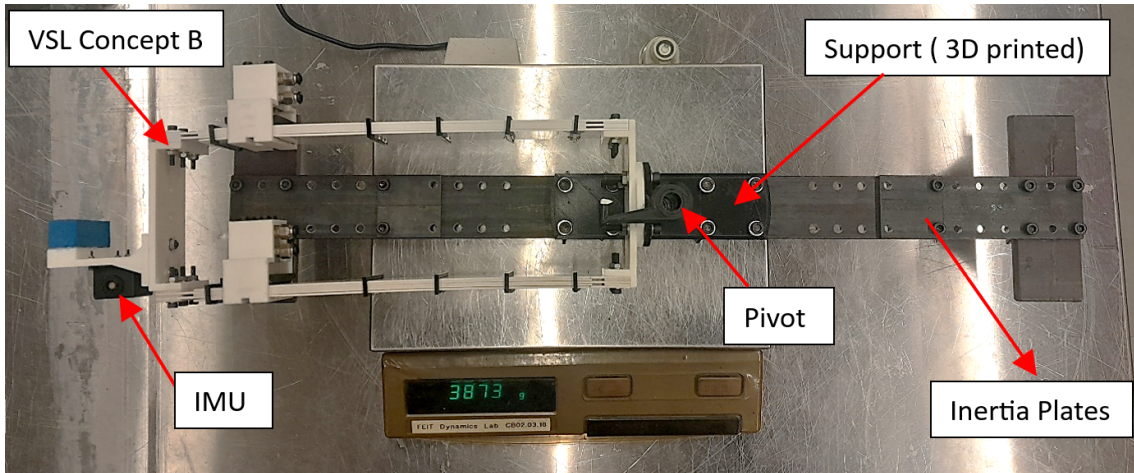


FIGURE 5.3: Assembly of VSL Concept B and inertia plates

The purpose of the experiment was to determine the impact force as a function of the impact velocity and the stiffness of the VSL. The main parameters of the impact test bench and the impact experiment are summarised in Table 5.1.

TABLE 5.1: Parameters of impact test bench and impact experiment

Parameter	Value
Mass of steel car	3.25 kg
Combined stiffness of compression springs	460 N/mm
Mass of assembly VSL Concept B and inertia plates	3873 kg
Distance from the pivot to the impact point	429 mm
Moment of inertia of VSL and inertia plates about the pivot (calculated in SolidWorks)	$0.25129 \text{ kg} \cdot \text{m}^2$
Air pressure for maximum stiffness	600 kPa
Air pressure for minimum stiffness	100 kPa
Impact velocities	1.8 m/s
	2.0 m/s
	2.2 m/s

It is important to note that VSL concept B was modified to be used in the impact test bench. The modification consisted of attaching an impactor that will come in contact with the dummy head during the impact. Figure 5.4 illustrates the impactor and a piece of ethylene-vinyl acetate (EVA) foam that was bonded to the impactor. The function of this foam is to replicate the soft material that is used to reduce the effect of the impact as was described in Section 5.1. The effect of the foam thickness was not investigated in the impact experiments presented in this section because this variable has been extensively studied [79]. However, a compression test and a tension test on this foam are presented in Appendix C to support future research in this field, such as impact simulations.

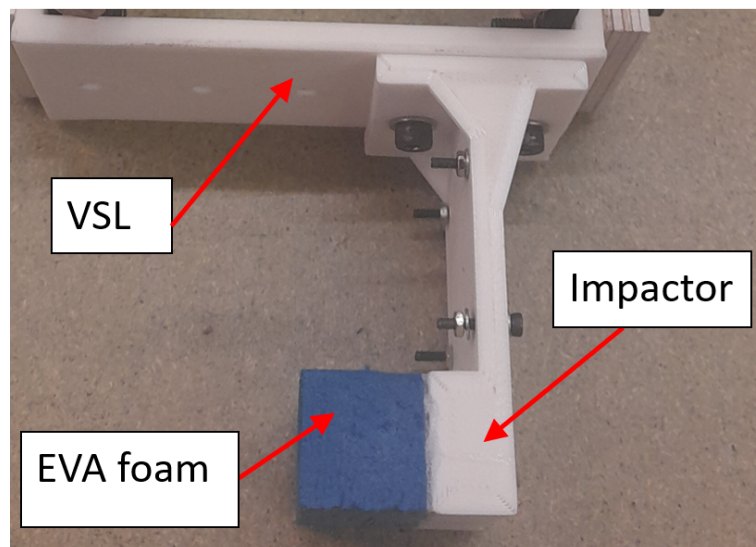


FIGURE 5.4: Modification of the VSL for its application in the impact test.

5.2.1 Experimental Procedure

The impact experiment consists of generating an impact between the VSL and the dummy of the human head. The impact velocity can be controlled by releasing the VSL from different angles. In addition, the stiffness of the VSL is controlled by setting the air pressure in the pneumatic cylinder through the pneumatic regulator. The experiment procedure can be appreciated in the following video <https://youtube.com/shorts/HISRWoiCv-w>

Preliminary experiments were carried out to determine the angles that produced an impact velocity of 2.2 m/s, 2.0 m/s, and 1.8 m/s, which is the range of collision velocities that were

studied in similar experiments [83]. The impact speeds were measured by an Orientus-Inertial Measurement Unit (IMU) that is produced by the company Advanced Navigation (Sydney-Australia), this IMU was placed in the free end of the VSL and measured the angular velocity of the VSL.

The impact experiments were carried out for 100 kPa and 600 kPa of air pressure in the pneumatic cylinder and for the velocities that were mentioned above. Each experiment was repeated three times. The impact force is defined as the maximum force that was measured during the experiment. Then, the average force of the three experiments is taken as the impact force for the given values of air pressure and impact velocity.

It is important to note that the swing motion of VSL Concept B and the impact against the dummy head generate the displacement of the distal part of the link from the proximal part of the link in the axial direction. Therefore, the distal part of the link had to be placed back manually in the correct position after each test. As discussed in the previous chapter, a remedy for this problem has been implemented in the design of VSL Concept C.

The axial separation of the distal and proximal parts of VSL Concept B that occurs during the impact test is even more pronounced at 0 kPa of pressure in the pneumatic cylinders because the trapezoidal pin is not engaged with the layers. As a result, the impact tests at 0 kPa were not carried out. The VSL Concept B unit used in this experiment had a similar problem during the bending tests that were described in Section 4.3.1. The cause of both problems is the same: no components join the distal end and the proximal end of the interlocking LJS that forms the VSL.

The axial separation of the VSL Concept B after bending and impact tests prevents the use of this link to build the VSL robot arm with 2 DoF that will be presented in Chapter 6.1. The VSL robot arm will be used to conduct about 480 stiffness tests and about 40 impact tests. Therefore, the use of the VSL Concept B in those experiments would be impractical because it would require resetting the original length of the links about 1040 times.

VSL concept B was modified to make it completely rigid. The modification involved attaching two timber members in an “X” configuration to the link, as shown in Figure 5.5. The addition of these members prevents the bending of the VSL under a transverse load and they also constrain

the axial separation of the VSL. Impact experiments were also carried out with this link at the same velocities that were described above.

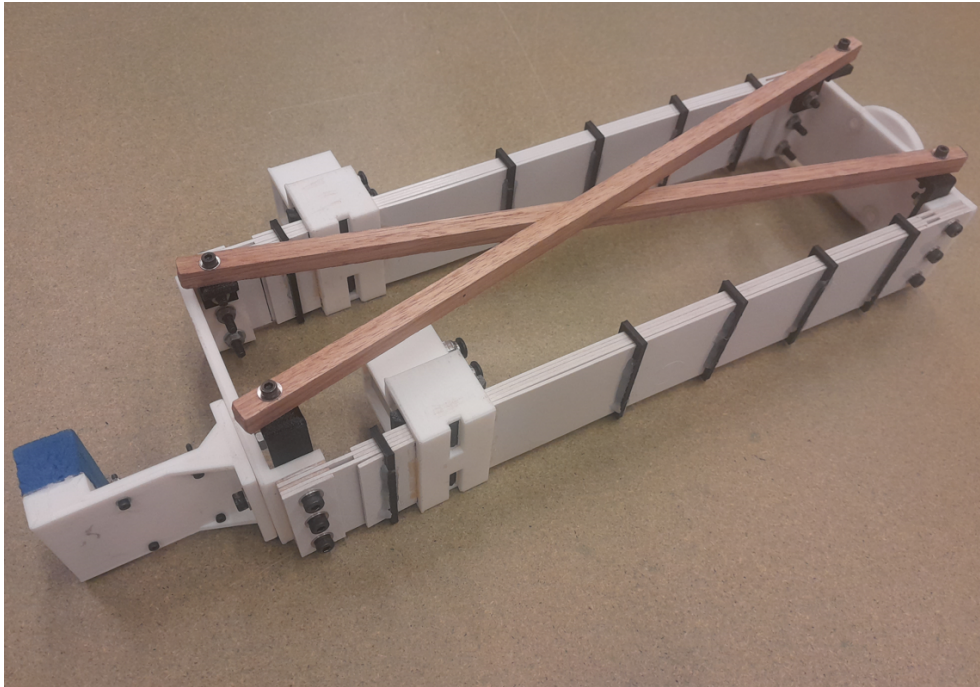


FIGURE 5.5: Modification of VSL Concept B to make it completely rigid.

5.2.2 Results of Experiments

Figure 5.6 shows the results of one of the experiments when the impact velocity is 2.2 m/s and the air pressure in the pneumatic cylinders is 600 kPa. Only the first peak of contact force is illustrated in the figure because it is the peak that reaches the maximum force in all cases. The impact force in this experiment is determined as the maximum value contact force, which is 50.75 N in the example shown.

Figure 5.7 illustrates the results of the impact experiments for the VSL at its maximum stiffness state (600 kPa in the pneumatic cylinders) and its minimum stiffness state (100 kPa in the pneumatic cylinders). In addition, this figure shows the results of the experiment for the rigid link.

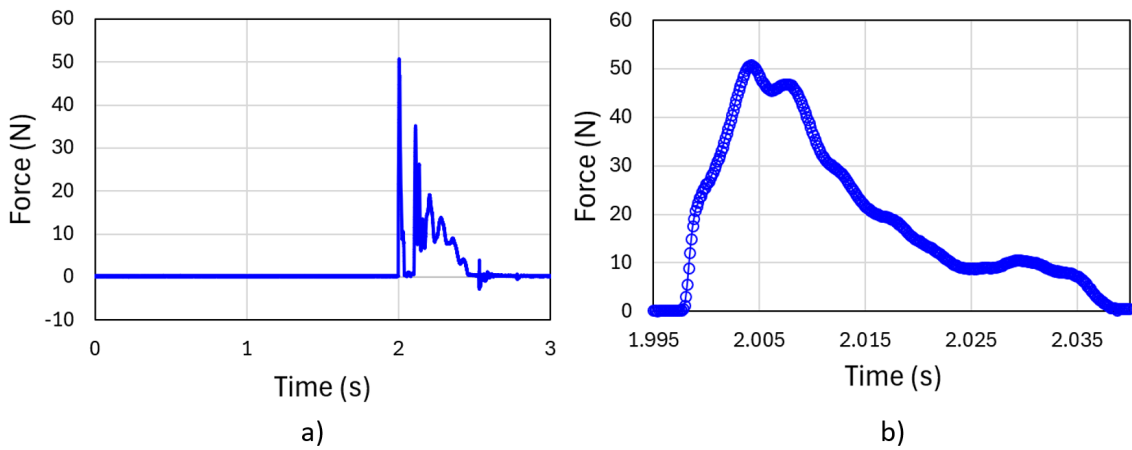


FIGURE 5.6: Data collected from the force sensor during one of the impact experiments at collision velocity $v=2.2$ m/s and 600 kPa of pressure in the pneumatic cylinders. a) Multiple peaks were registered during the collision. b) First force peak used to calculate the impact force.

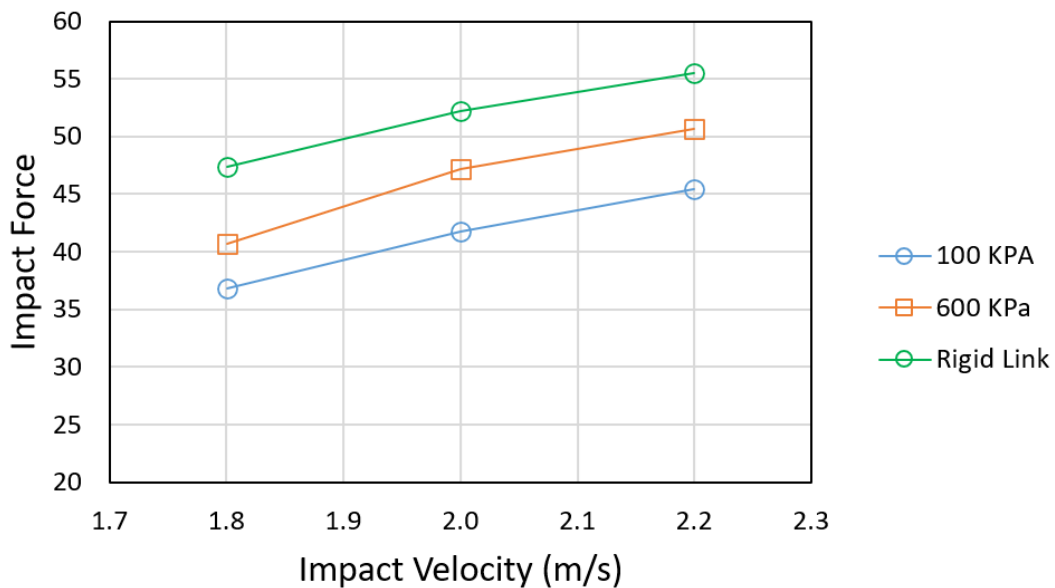


FIGURE 5.7: Results of impact experiment.

5.3 Discussion

Figure 5.7 shows that the VSL at 600 kPa generates a higher impact force than the VSL at 100 kPa at all velocities. The biggest difference occurs at 2 m/s, where the impact force at the minimum stiffness state (100 kPa) is about 88% of the impact force at the maximum stiffness

state (600 kPa). These results show that the proposed trapezoidal pin mechanism and the design of the VSL are able to reduce the impact force during a collision.

It should be noted that the stiffness ratio of VSL Concept B between 600 kPa and 100 kPa is 1.34 as it was discussed in Section 4.3.1, which can be considered a low value in comparison with other VSLs based on LJ [15]. However, this variation of stiffness is enough to produce a reduction in the impact force of 12% at 2 m/s.

Figure 5.7 also shows that the impact forces generated by the rigid link are significantly higher than the impact forces generated by the VSL. In particular, the maximum difference between the rigid link and the VSL occurs at 1.8 m/s where the stiffness of the VSL at 100 kPa is about 78% of the stiffness of the rigid link. It should be noted that the VSL and the rigid link have almost the same mass and the same overall dimensions. This demonstrates that the proposed VSL can be safer than rigid links without diminishing the mass or the dimensions of the link.

The purpose of the experiments presented in this chapter was not to measure the damage to the human being due to a collision with the proposed VSL but to measure the variation in the impact force due to the change in the stiffness of the VSL. However, It is important to note that the maximum impact force generated by the VSL was about 50 N, as can be seen in Figure 5.6 and Figure 5.7. This force value is significantly lower than the fraction forces for the maxilla facial bone and frontal cranial bone, which are 600 N and 4000 N, respectively. These values of fraction forces have been adopted in some studies as safety criteria in human-robot interaction [82]. Therefore, the results obtained suggest that the proposed VSL may not generate significant damage in the event of a collision with the head of a human operator. It must be noted that better quantification of the injuries due to impact would require a force sensor with superior performance in aspects such as a higher sampling rate.

The low impact force generated by the proposed VSL may be due to the use of the EVA foam that covers the impactor. This piece of foam was 20 mm thick, as illustrated in Figure 5.4. Another study demonstrates that the reduction of the foam thickness could result in a significant increment of the impact force [79]. An additional impact test was carried out to verify this behaviour. The impactor was covered with an EVA foam with a thickness of 10 mm. The result was an impact force of 63.7 N at 600 kPa and an impact velocity of 2.2 m/s. This value

represents an increase of about 13% in the impact force relative to the experiment with a foam thickness of 20 mm.

The capacity of soft covers to reduce the impact force in a cobot is limited. Even if a cobot arm is completely covered with a soft material, the impact can still occur through the payload which may be a rigid object. Therefore, rigid impacts against human beings cannot be completely avoided by only covering the cobot arm with soft materials.

5.4 Conclusions

This chapter presents the impact tests that were carried out with one of the VSL concepts presented in Chapter 4. These experiments were conducted to determine if the proposed VSL (VSL concept B) is able to reduce the impact force in the case of a collision with a human being and quantify such reduction.

The experiments demonstrate that VSLs based on the LJS concept with a trapezoidal pin mechanism are able to reduce the impact force by 12% when the LJS transitions from a high stiffness state to a low stiffness state. It is important to note that VSL Concept B has a low stiffness ratio (1.34). However, it was demonstrated that VSL Concept B is able to reduce the impact force significantly despite its low stiffness ratio.

The experiments also showed that VSL Concept B in its lowest stiffness state is able to reduce the impact force by 22% in comparison with an equivalent rigid link, showing the effectiveness of the VSL in significantly reducing the impact force in the case of a collision with a human being.

The impact test also highlighted that VSL Concept B presents a problem of the separation between the distal end and the proximal end of the link. This problem occurs because there are no components that join both parts of the link. This problem has been solved in VSL Concept C that will be implemented in a robot arm in Chapter 6.

Chapter 6

Robot arm with Variable Stiffness

Links

The previous chapter focused on responding to the second research question, which is about how to exploit VSLs in human-robot interaction – in particular, how to exploit this type of link in the case of an impact between a human being and a robot arm. To answer this question, an impact test bench was built where VSL Concept B collided with a dummy of the human head and the impact force was measured. The results of the experiments demonstrate the capacity of VSL Concept B to mitigate the impact force of a collision between a human being and a robot arm. However, these experiments, and other experiments in the literature, are limited to the investigation of one link rather than investigating a robot arm with multiple VSLs.

To overcome the limitations of the literature, this chapter presents a 2-degree-of-freedom (DoF) robot arm formed by two VSLs whose design corresponds to VSL concept C that was presented in Chapter 4. A stiffness test was carried out to investigate the stiffness of the proposed robot arm in multiple poses and different stiffness levels in each link. Another experiment was conducted to estimate the destiffening time of the proposed robot arm during a collision.

The integration of multiple VSLs into a robot arm raises some questions that have not been investigated. For example, what would be the contribution of each link to the stiffness of the robot arm, and how does the stiffness of the robot arm change according to the pose of the

robot arm, the direction of the force and the stiffness state of each link?. This chapter presents answers to these questions for the particular case of the proposed VSL robot arm.

The destiffening time of the proposed VSL robot arm was estimated through experimental methods. This estimation will allow us to determine if the proposed robot arm can effectively reduce the damage caused to a human being due to a collision against the robot arm. This aspect of VSL Concept C is very important because other mechanisms to vary the stiffness in LJSs have demonstrated significant limitations in the speeds of stiffening and destiffening as it was discussed in Chapter 2. These limitations raise questions about the suitability of these existing LJ mechanisms to be applied in robot arms that may work together with human beings.

6.1 Review of VSL Robot Arms

Multiple studies have been carried out in relation to the design, construction and performance of VSLs [16, 18, 20, 81, 84–89]. These studies are based on many of the methods to vary the stiffness in soft robotics that were described in Table 2.1. Some of these VSLs are based on LJSs [15, 16, 18, 20] and were described in Chapter 2 and Chapter 4.

Most of the studies about VSLs focused on the behaviour of only one link; there are few studies that investigate a complete robot arm that is formed from multiple VSLs [90–94]. The research on robots with multiple VSLs focuses mainly on inflatable manipulators. Some of the studies present experiments where a VSL robot arm was built and tested [90, 91], and some studies focus only on the modelling and simulation of a VSL robot arm [93, 94].

Some studies have presented insights into how to exploit the capabilities of a VSL robot arm according to the operation that is being executed. For example, a robot arm that is performing a pick-and-place operation usually moves in three stages. In the first stage, the robot accelerates from the initial position until reaching a maximum speed. In the second stage, the robot moves at a constant maximum speed. In the third stage, the robot decelerates to stop at the final position. The manipulator has low speed in the first stage due to the inertia of the robot, high speed in the second stage for maximum efficiency, and low speed in the last stage to stop accurately in the final position. In the case of a collision with a human being, the robot arm may minimise the damage of an impact if it has low stiffness at high velocities. At low velocities,

the robot arm could have high stiffness because the damage depends more on the velocity rather than on the stiffness. Therefore, the profile of the stiffness in this task should be stiff in the first stage, flexible in the second stage, and stiff in the third stage [62, 95].

As was explained in Section 5.1, the strategies for introducing compliance into safe robot arms can be classified as passive compliance or active compliance. Some studies that have adopted the strategy of passive compliance combine multiple passive elements to make robot arms with VSLs [79, 80]. There are also studies that have adopted VSLs with active compliance [16, 90, 95]. The investigation of the destiffening time of VSLs is more relevant in the active strategy than in the passive strategy, because active VSLs require a suitably fast destiffening time in order to be effective, while passive VSLs rely on the initial stiffness setup of their passive elements.

6.2 Stiffness Experiment on the VSL Robot Arm

The purpose of this experiment is to determine how the stiffness in the proposed VSL robot arm changes due to the pose of the robot arm, the stiffness states in the links, and the direction of the external forces. This section describes the experiment and its results.

6.2.1 Experimental Setup

The objective of this experiment is to investigate the stiffness of a robot arm whose links have variable stiffness capabilities. The stiffness of the proposed VSL robot arm changes in function of the pose of the robot, the direction of the external force, and the stiffness of each link. A test bench was therefore developed to measure the stiffness of the robot arm when these three variables change.

The main component of the test bench is a 2-DoF robot arm whose links are VSL Concept C that was described in section 4.4. The links of the robot arm can be placed manually in any pose. This pose can be fixed by tightening the fasteners that lock the joints in the desired position. Figure 6.1 illustrates the details of the robot arm, where it can be seen that the robot arm has a SCARA configuration.

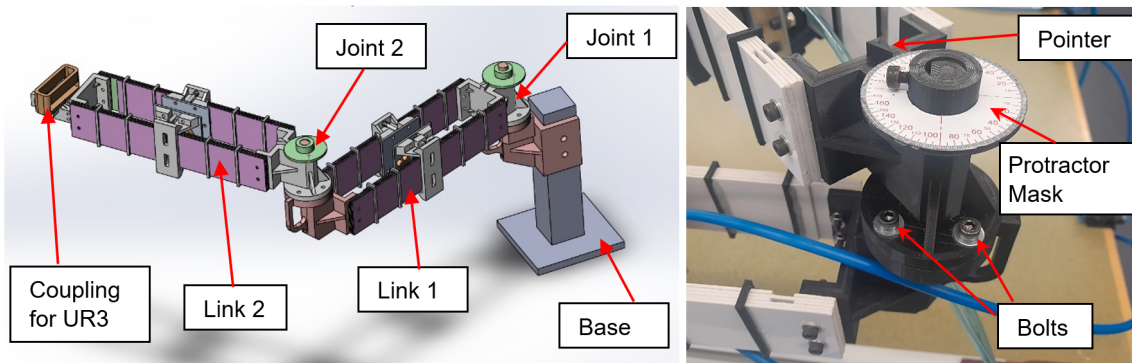


FIGURE 6.1: Robot arm with VSLs. a) Components of the robot arm. b) Detail of joint 2.

The VSL Concept B was not used to build the VSL robot arm because the distal and proximal parts of the link separate in the axial direction after bending tests or after impact tests, as explained in the section 5.2.1. Therefore, the length of the link has to be reset manually after each test, which would be impractical in the VSL robot arm due to the high number of tests that must be carried with this robot. In contrast, the VSL Concept C does not have the problem of separation of the distal and proximal parts, which makes it adequate for the VSL robot arm because resetting the length of the VSLs is not necessary.

Figure 6.2 illustrates the components of the test bench. The UR3 robot arm and the 2-DoF robot arm were firmly attached to a table. The function of the UR3 (Manufactured by Universal Robots, Odense-Denmark) is to apply forces on the end effector of the 2-DoF robot arm. The force that the UR3 applies to the 2-DoF robot arm is measured by an ATI FT Axia80 M20 force sensor that is attached to the UR3 arm. This sensor is able to measure the force in three orthogonal axes simultaneously. The other end of the force sensor is attached to a coupling that transfers the force to the end effector of the 2-DoF robot arm.

The 2-DoF robot arm deflected and twisted excessively because of gravity in some poses. This deformation makes the coupling with the UR3 difficult. It was therefore necessary to include a support for the robot arm that consisted of a column that was attached to the end effector of the arm. The base of the column is a platform that has three steel ball caster wheels that allow motion of the platform in any direction with minimal resistance. These supports prevent excessive vertical deflection and twist of the free end of the 2-DoF robot arm without adding resistance to the motion in the horizontal plane.

With regards to the control and instrumentation of the test bench, the force sensor is directly connected to a laptop that runs the ATI FT Data viewer program, which shows and records the force values as a function of time. The UR3 robot arm is controlled through the pendant of the robot. The stiffness of the 2-DoF robot arm is controlled through pneumatic manual valves. The stiffness of each link in the 2-DoF robot arm was controlled independently because the links were connected to two different air pressure regulators.

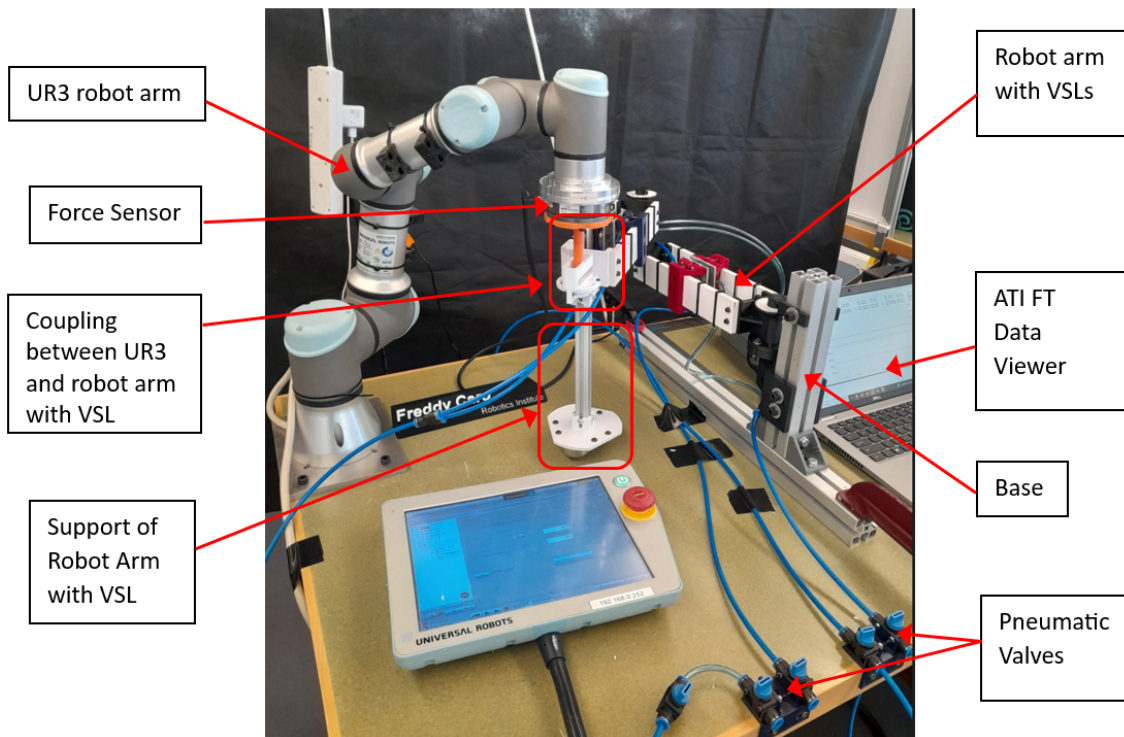


FIGURE 6.2: Experimental setup to measure the stiffness of the VSL robot arm

6.2.2 Experimental Procedure

The experiment consisted on the application of force on the free end of the 2-DoF robot arm in multiple directions. The steps to carry out the experiment are described as follows.

1. Place the 2-DoF robot arm in a specific pose and fix the joints. Five poses of the robot were investigated, they were defined by θ_2 equal to 0° , 45° , 90° , 135° , and 180° .

2. Define the direction of the force that will be applied to the 2-DoF robot arm. The UR3 was programmed to apply force in eight directions as follows: 0° , 45° , 90° , 135° , 180° , 225° , 270° , and 315° .
3. Set the stiffness of the 2-DoF robot arm. Two states of stiffness were defined for each link: a maximum stiffness state that occurs when the air pressure is set at 345 kPa, and a minimum stiffness state that occurs when the air pressure is set up at 0 kPa. Therefore, four stiffness state combinations were investigated for each pose of the robot arm.
4. For a given direction, the end effector of the UR3 robot arm is programmed to move 25 mm along a straight line, wait in that position for 5 s then move back to the original position. The force that the UR3 applies on the 2-DoF robot arm during this motion sequence is measured by the force sensor. This experiment is repeated three times in each direction.

Figure 6.3 illustrates the layout of the experiment when the 2-DoF robot arm is in the pose defined by $\theta_2 = 135^\circ$. It can be seen how the UR3 robot pushes the 2-DoF robot arm in eight directions in order to determine the stiffness in each direction. One of the experiments carried out in this pose is presented in the following video. <https://youtube.com/shorts/NPWmbeYY8cQ>

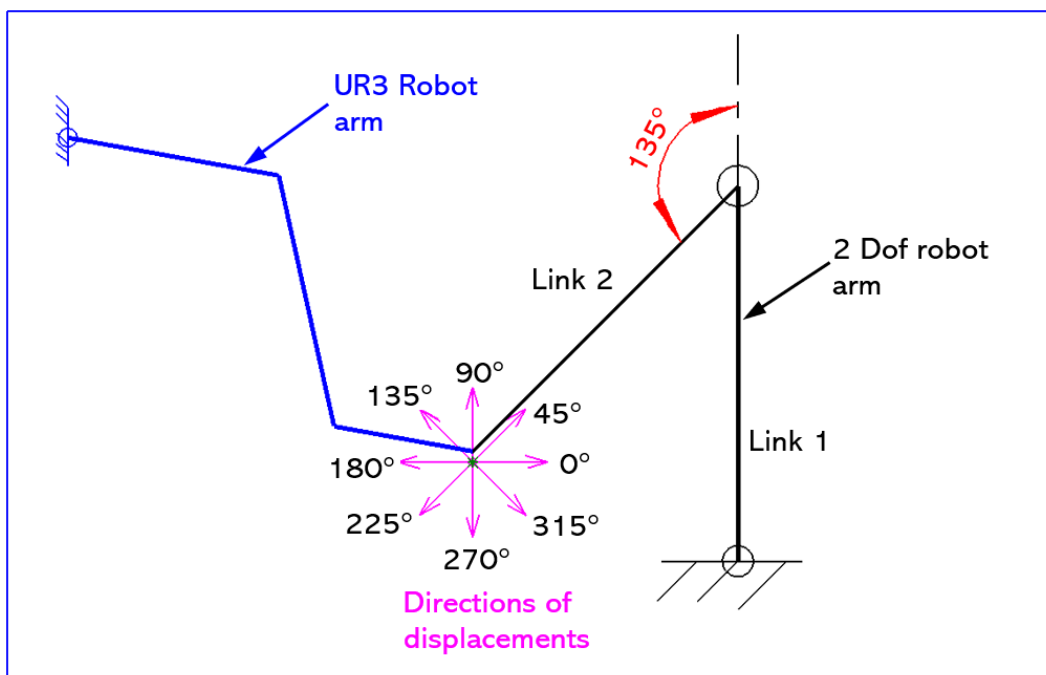


FIGURE 6.3: Stiffness experiment layout for $\theta_2=135^\circ$.

6.2.3 Results of the Experiment

Figure 6.4 illustrates the data from the force sensor for one of the stiffness tests. The experiment has four stages that are defined by the linear trajectory that was programmed in the UR3 robot arm. The result of the experiment is the value F (magnitude of the vector sum of F_y and F_x in the sensor coordinate system), which is the force that is necessary to generate a deflection of 25 mm in the end effector of the VSL robot arm in the given direction. The experiment was repeated three times. Then, the average force value (F) from the three experiments is calculated, this average value is divided by the displacement (25 mm), which yields the stiffness in the given direction.

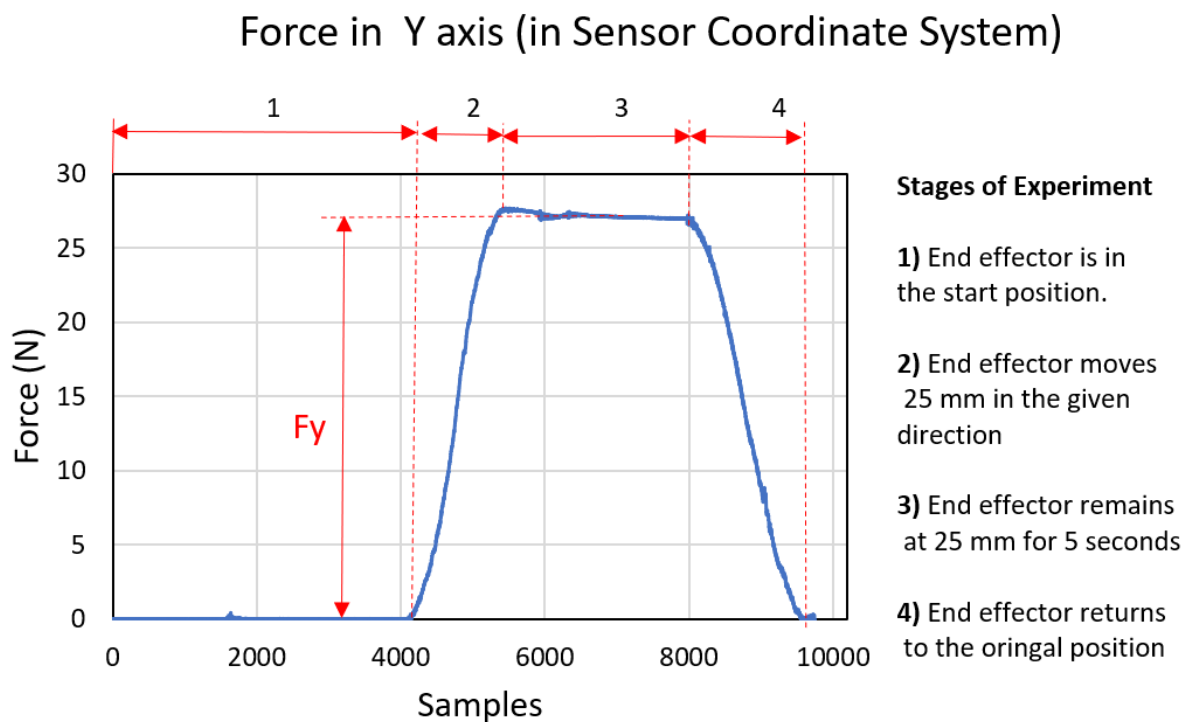


FIGURE 6.4: Data from the force sensor for one of the stiffness tests at $\theta_2=135^\circ$, L1 345 kPa, L2 345 kPa, and 45° for the direction of the displacement.

Figure 6.5 illustrates the results of the stiffness experiment when $\theta_2=135^\circ$, and the stiffness of the links is maximum (345 kPa in both links). The stiffness has been represented as an arrow

whose direction corresponds with the direction of the displacement generated by the end effector of the UR3, and the length of the arrow indicates the value of the stiffness.

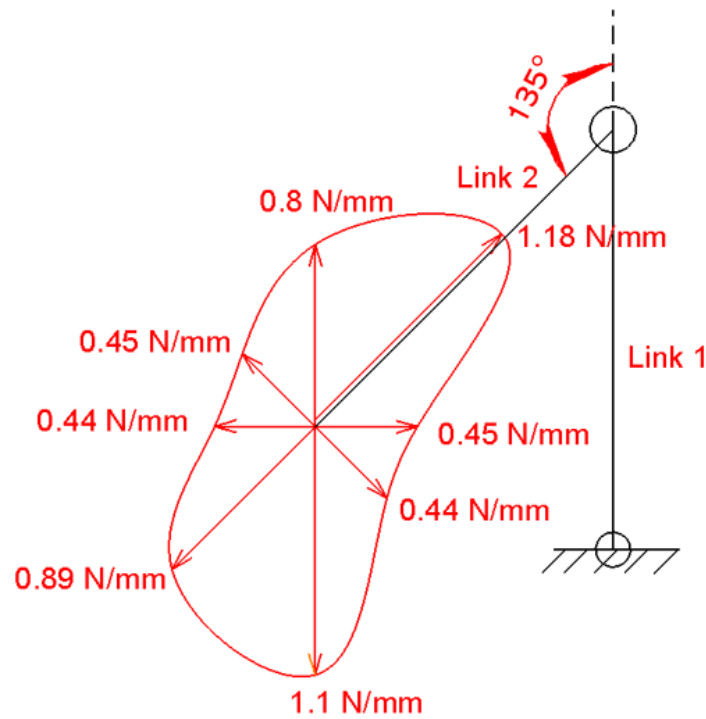


FIGURE 6.5: Results of stiffness experiment when $\theta_2=135^\circ$. The pressure in Link 1 is 345 kPa, and the pressure in Link 2 is 345 kPa.

Figure 6.6 illustrates the results of the stiffness experiments in five poses of the VSL robot arm. The stiffness states of the robot arm were represented by colour and correspond with the possible combinations of stiffness in the links (L1 and L2 at high stiffness, L1 at low stiffness and L2 at high stiffness, L1 at high stiffness and L2 at low stiffness, L1 and L2 at low stiffness). It should be noted that the high stiffness states occur when the pressure in the Airstroke actuators is 345 kPa, which is the maximum operational pressure of these actuators, and the low stiffness states occur when the air pressure in the Airstroke actuators is 0 kPa.

The stiffness experiments presented a limitation in the poses of the VSL robot arm where the links are aligned. As can be seen in Figure 6.6, these poses correspond to $\theta_2=0^\circ$, and $\theta_2=180^\circ$. The limitation consists in the impossibility of applying force along the axial direction of the links (force at 0° and 180°). The VSLs are stiff at these poses when the external forces are applied in

the axial direction because the links would be completely under tension or compression. As a result, applying force through the UR3 robot arm in these directions could damage the 2-DoF robot or the force sensor.

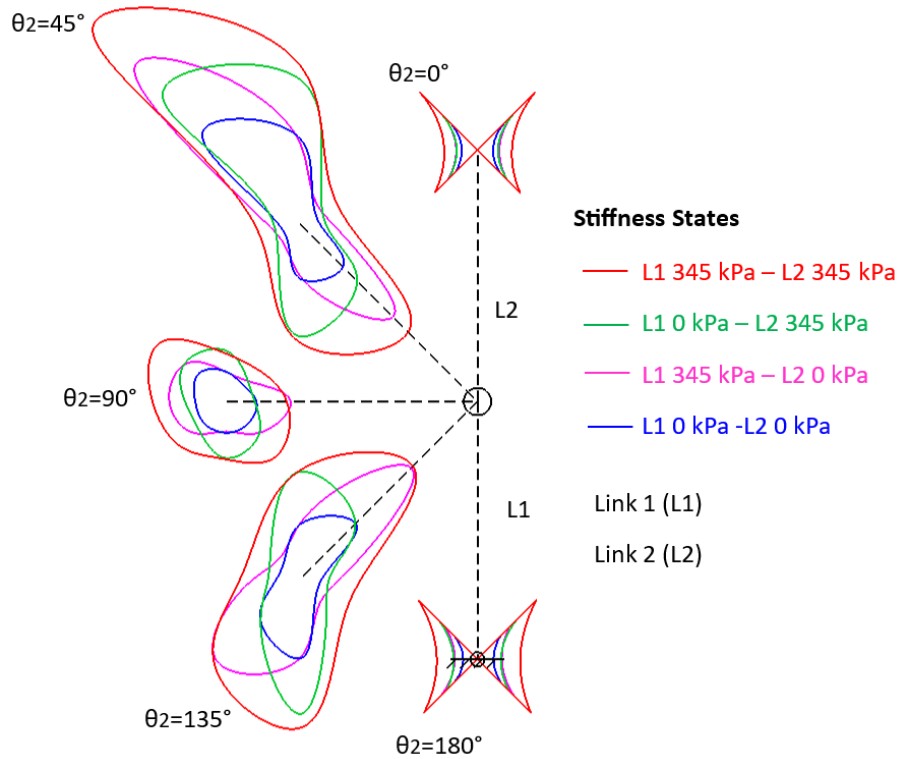


FIGURE 6.6: Results of stiffness experiment for all poses of the 2-DoF robot arm and all states of stiffness.

6.2.4 Discussion

The term “stiffness envelope” will be used to designate the curves that can be seen in Figure 6.6. The stiffness envelope graphically represents the stiffness in all directions for the robot arm for a given combination of stiffness states in the links. Following this terminology, Figure 6.5 would show the stiffness envelope at $\theta_2=135^\circ$ when link 1 (L1) and link 2 (L2) are in a high stiffness state.

Figure 6.6 shows that the stiffness envelope when both links are at their maximum stiffness states contains all the other envelopes in all the poses of the robot arm. This means that the maximum stiffness of the robot arm occurs when the stiffness of its links is maximum.

The results of the stiffness experiments show that there are some directions where most of the stiffness of the robot arm comes from one link while the other link makes a very small contribution to the stiffness of the whole arm. Figure 6.7 illustrates a pose where this phenomenon is very evident. It can be seen that the purple envelope touches the red envelope in direction A, and the green envelope touches the red envelope in direction B. This means that the stiffness of the VSL robot arm at 315° (direction A) is generated mainly by link 1 that is in its high stiffness state, while the stiffness of the VSL robot arm at 0° (direction B) is generated mainly by the link 2 that is in its high stiffness state.

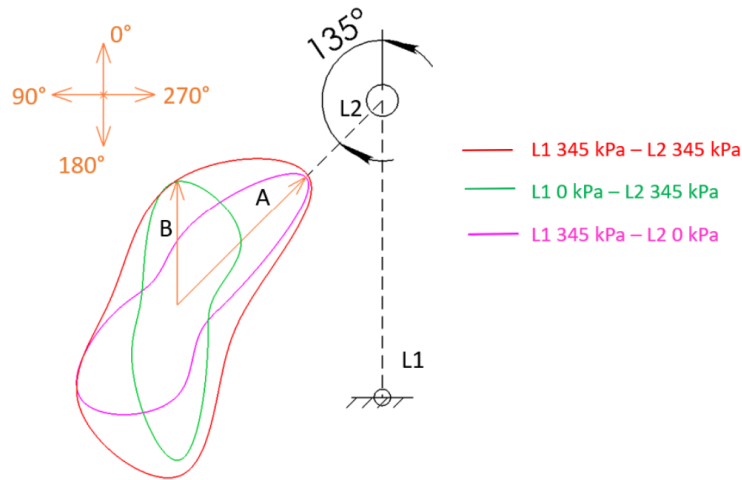
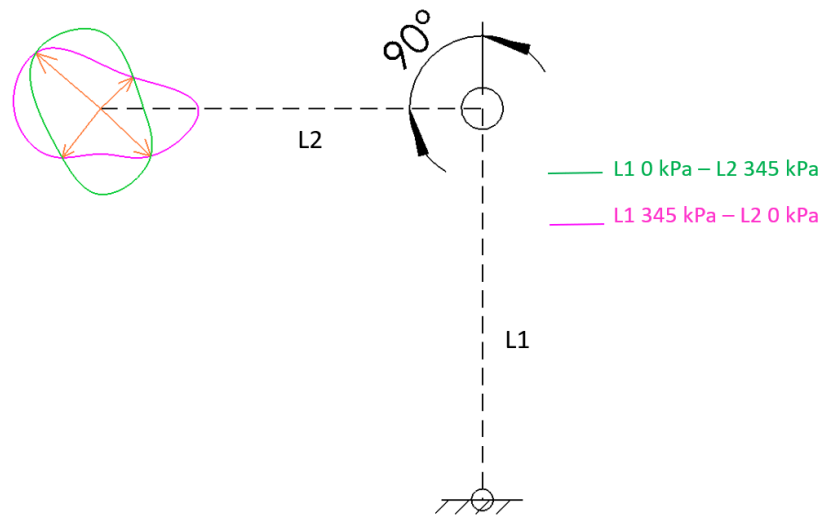


FIGURE 6.7: Stiffness envelopes at $\theta_2=135^\circ$.

Figure 6.6 also shows that there are directions where the entire stiffness of the robot arm could come from any of the two links. This phenomenon is clearly illustrated in Figure 6.8. It can be seen that the stiffness envelopes intersect each other in four points. This means that there are four directions where the stiffness of the robot arm is the same for the case when only link 1 is at high stiffness (L1 345 kPa - L2 0 kPa), and for the case when only link 2 is at high stiffness (L1 0 kPa - L2 345 kPa).

The results of the experiment also show that the stiffness of the robot arm depends significantly on the pose and the direction of the application of the external force. Figure 6.6 shows that the pose at $\theta_2=45^\circ$ generates the highest stiffness values in the robot arm. While the pose at $\theta_2=90^\circ$ has some of the lowest values of stiffness. In relation to the direction of the external force. The

FIGURE 6.8: Stiffness envelopes at $\theta_2=90^\circ$.

stiffness of the robot arm is higher when the force is aligned with the links of the robot arm, and it is low when the external force is more perpendicular to the links. When the external force is more aligned with the axial direction of the links, the links are more under tension or compression than under bending. When the links are under axial load (tension or compression), the stiffness is higher than when the links are under bending. The difference in stiffness between these two conditions could be of various orders of magnitude because VSL Concept C was designed to be rigid in the axial direction and to have variable stiffness capabilities in bending on the horizontal plane.

6.2.5 Use of the Stiffness Envelope in the Execution of a Task

Changing the stiffness characteristics of the robot arm by modulating its stiffness envelope could be utilised to increase efficacy and efficiency when a specific task is executed. This section presents an example of how to use the stiffness envelope in a specific task.

As an example, consider the task of cleaning a glass window or erasing a whiteboard, as can be seen in Figure 6.9. The end effector of the robot arm would hold a sponge or an eraser, respectively. The stiffness in the perpendicular direction to the surface (glass or board) should be low so that position errors do not generate large forces. The stiffness in the direction parallel

to the surface (glass or board) should be high to maintain good position control despite the variation in frictional force.

In the case of the task illustrated in Figure 6.9a (top), the glass window is in a vertical orientation, which means that low stiffness is required in the horizontal direction towards the right while high stiffness is required in the vertical direction upwards and downwards. This requirement could be taken to the stiffness envelope (bottom), which shows that the envelope that satisfies both requirements is the green one, which corresponds to the high stiffness in link 2 and low stiffness in link 1. Any other configuration of stiffness will not satisfy both requirements simultaneously. Figure 6.9b illustrates the example when the orientation of the glass window (or board) is horizontal. A similar reasoning could be applied, which results in the selection of the purple envelope as the best solution. The purple envelope corresponds to high stiffness in link 1 and low stiffness in link 2.

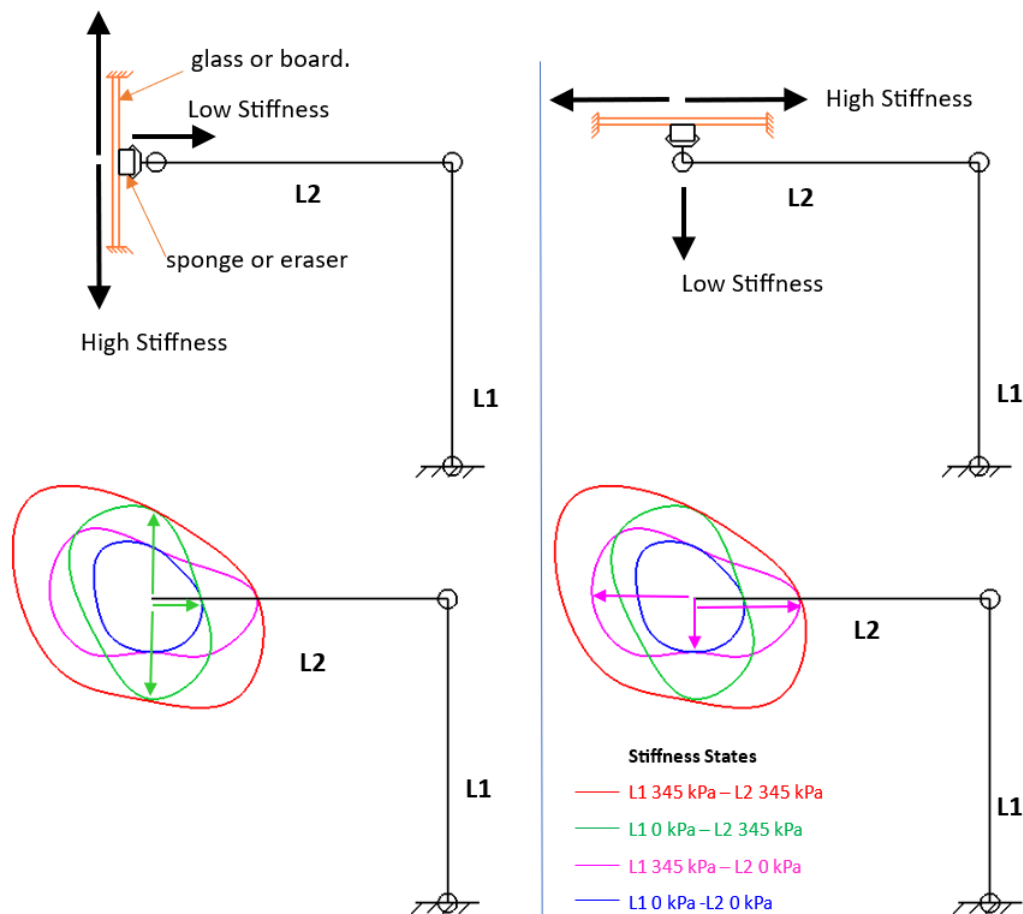


FIGURE 6.9: Use of stiffness envelope when the VSL robot arm executes a task.

6.3 Destiffening Time Experiment for the VSL Robot Arm

The objective of this experiment is to determine if the destiffening speed of the VSL robot arm is fast enough to reduce the impact force of a collision against a human being. This section describes the experiment and its results.

6.3.1 Experimental Setup

A test bench was developed to measure the destiffening time of the proposed VSL robot arm during an impact. Figure 6.10 illustrates the components of the test bench. The main component is the VSL robot arm that was presented in the section 6.2.1. The airflow to the AirStrokes actuators is controlled by a 3/2 Emerson-ASCO solenoid valve (Model E314K121S1V01). A manual air pressure regulator controls the air pressure in the Airstroke actuators of both links. A UR3 robot arm is used to generate a collision against the VSL robot arm. The impact force is measured by an ATI Axia80 M20 force sensor that is attached to the end effector of the UR3 and has a sampling frequency of 7812 samples per second. The force measured by the sensor is collected by the ATI FT Data viewer program. The UR3 is controlled by a program that is executed from its pendant. The solenoid valve is connected to a digital output of the control box of the UR3 robot arm.

The VSL robot arm was modified by attaching an impactor in order to receive the impact from the UR3. Figure 6.11 shows a piece of foam between the impactor and the sensor force mounted in the VSL robot arm. This piece of foam replicates the soft covers used in Cobots as a passive measure to reduce the impact forces in the case of collision against a human being. The thickness of this piece of foam is recorded in Table 6.1.

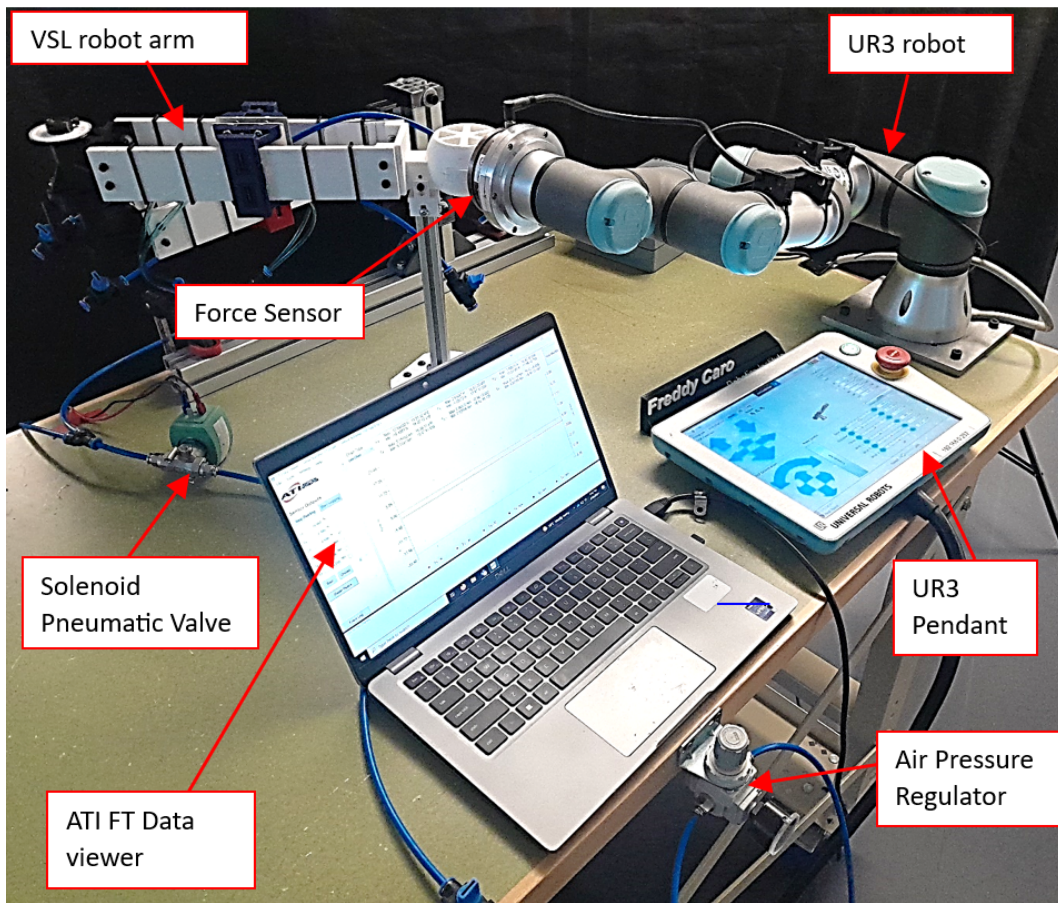


FIGURE 6.10: Experimental setup of the destiffening time experiment for the VSL robot arm.

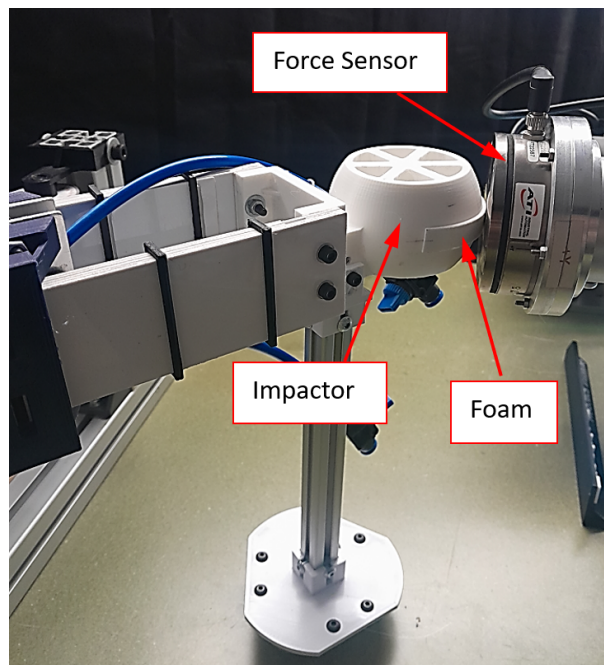


FIGURE 6.11: Detail of the impact area between the VSL robot arm and the UR3 robot arm.

6.3.2 Experimental Procedure

The experiment consists of generating an impact between the UR3 robot arm and the VSL arm. The stiffness of the VSL is reduced just before the impact. Then, the impact force during the collision is measured, and the destiffening time of the VSL robot arm is estimated. The steps of the experiment are described as follows.

1. The VSL is placed in the pose $\theta_1=0^\circ$ deg, $\theta_2=135^\circ$ deg. The joints of the robot are fixed in this pose.
2. The UR3 robot arm is taken to the initial position of its trajectory, as can be seen in Figure 6.12.
3. The logging of the data from the force sensor starts in the ATI FT Data viewer that is running on the laptop. After this, the program that controls the motion of the UR3 and the solenoid valve is executed in the pendant.
4. The program of the UR3 starts by turning on the solenoid valve, which generates a high stiffness state in the VSL robot arm. Then, after 1.4 s, the UR3 starts to rotate about the base joint.
5. The UR3 robot arm moves according to the parameters presented in the Table 6.1. It should be noted that the motion of the UR3 consists of rotating the base joint only. The trajectory followed by the UR3 is illustrated in Figure 6.12. It should be noted that two sets of experiments were carried out, they were called Experiment 1 and Experiment 2. Experiment 1 was characterised by an impact velocity of 0.58 m/s, and Experiment 2 was characterised by an impact velocity of 0.84 m/s.
6. When the UR3 reaches a deactivation angle that has been specified in the program, the solenoid valve is turned off through a command that is sent from the program, which starts the destiffening process of the VSL robot arm. Then, the UR3 continues its travel toward the VSL robot arms until the collision occurs at the angle of impact. The UR3 keeps moving until it stops at the final angle. The angular velocities of the joint at the moment of passing through the deactivation angle and the angle of impact are recorded by the program of the UR3.

7. After stopping at the final angle, the UR3 robot arm retracts to a position where it loses contact with the VSL robot arm. Then the recording of the information from the force sensor is stopped in the ATI FT Data viewer.
8. This experiment is repeated three times for each deactivation angle. A video of One of the impact experiments can be seen in the following link. <https://youtube.com/shorts/pO8-VEw23Rg>

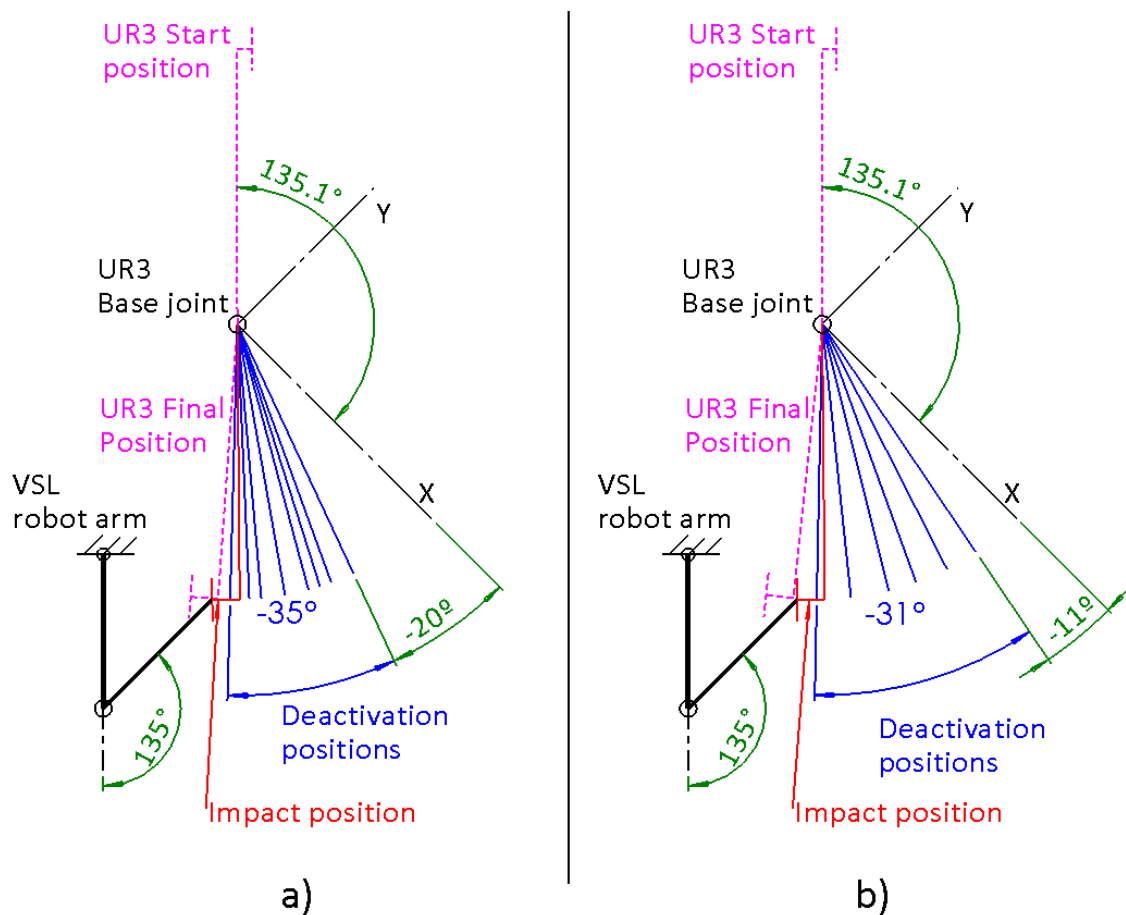


FIGURE 6.12: Layout of the destiffening experiment during a collision. a) Positions of the UR3 robot arm in experiment 1. b) Positions of the UR3 robot arm in experiment 2. X-Y is the base coordinate system of the UR3.

In addition to the previous procedure, two baseline impact experiments were carried out to determine the impact force during the collision between both arms when the VSL robot arm was in its minimum stiffness state (Airstroke actuators depressurised) and its maximum stiffness state (Airstroke actuators pressurised). For simplicity, these stiffness states will be called flexible

TABLE 6.1: Parameter of destiffening time experiments

Parameter	Experiment 1	Experiment 2
Impact velocity	v=0.58m/s	v=0.84 m/s
Pressure in the actuators	200 kPa	345 kPa
Angular acceleration (UR3 base joint)	360 °/s/s	540 °/s/s
Maximum angular velocity (UR3 base joint)	170°/s	170°/s
Initial angle (UR3 base joint)	135.1°	135.1°
Deactivation angles (UR3)	-20° (-0.236 s)	
	-25° (-0.198 s)	-11° (-0.256 s)
	-27.5° (-0.183 s)	-18° (-0.203 s)
	-30° (-0.159 s)	-25° (-0.15 s)
	-35° (-0.118 s)	-31° (-0.111 s)
	-40° (-0.063 s)	-39° (-0.055 s)
	-42.5° (-0.023 s)	46.15° (0.022 s)
	-46.5° (0.037s)	
Angle of impact (UR3 base joint)	-44.5°	-44.4°
Final angle (UR3 base joint)	-49°	-51°
Foam thickness	2 mm	4 mm

state and rigid state respectively. The stiffness of the VSL robot arm was set up at the beginning of the experiment, and the UR3 moves with the same parameters that are presented in Table 6.1. However, the rotation of the UR3 robot arm did not command the deactivation of the solenoid valve. Therefore, there was no change in the stiffness of the VSL prior to collision. These experiments were also repeated three times for each stiffness state.

6.3.3 Results of the Experiment

The processing of the data from the experiments consists of determining the impact force of the collision and estimating the time of destiffening of the VSL robot arm.

Figure 6.13 illustrates the data generated by the sensor during one of the impact tests. The data corresponds to the collision at v=0.84 m/s and a deactivation angle of -39°. The maximum

impact force (MIF) is determined as the maximum value of the first peak of the contact force, as can be seen in Figure 6.13b.

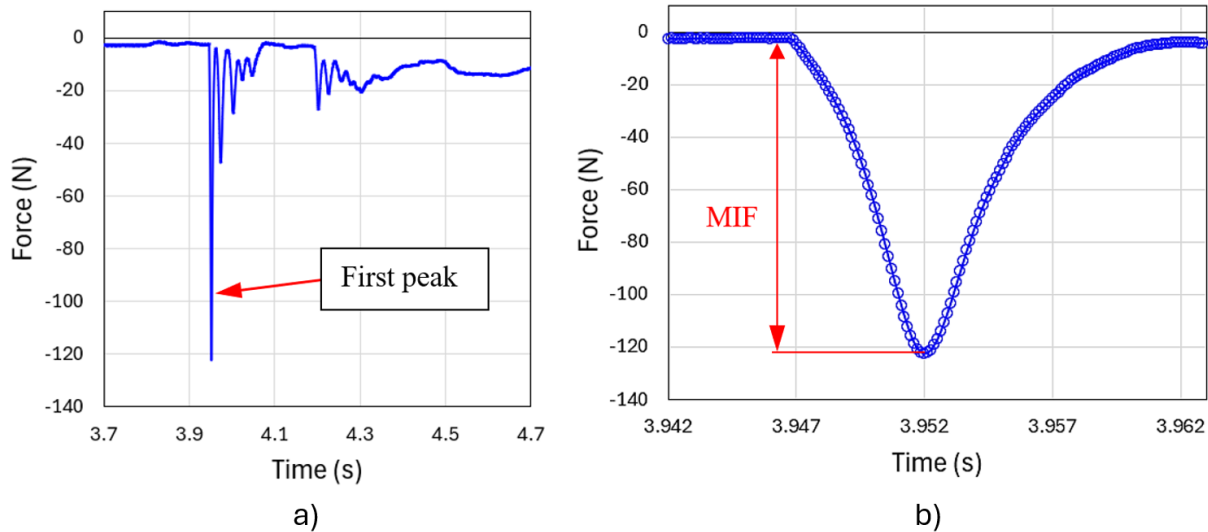


FIGURE 6.13: Data collected from the force sensor during one of the experiments at impact velocity $v=0.84$ m/s and deactivation angle equal to -39° (-0.055 s). a) Multiple force peaks were registered during the collision. b) First force peak used to calculate the maximum impact force (MIF).

The time from the deactivation of the solenoid valve until the collision against the VSL robot arm is calculated from the angular velocities recorded by the program that controls the UR3 robot arm. The user manual of the UR3 robot arm and the velocities recorded during the experiments reveal that the base joint is decelerating at a constant rate from the deactivation angles until the collision position. Therefore, circular motion equations with constant angular acceleration can be applied to calculate the time between these two positions. Table 6.1 shows the destiffening time associated with each deactivation angle, taking the impact moment as reference ($t=0$ s).

The results of all the experiments are presented in a graph of force vs time, as can be seen in Figure 6.14 and Figure 6.15. The purpose of these figures is to illustrate when the reduction of the impact forces occurs. The points that are represented in the graphs correspond to the average of the MIF measured in the three experiments that were carried out for each deactivation angle. Time $t=0$ s corresponds to the moment of the collision between the UR3 and VSL robot arm. The time axis in these graphs represents the moment of the deactivation of the solenoid valve relative to the moment of the collision ($t=0$). A negative time means that the solenoid valve was

deactivated before the UR3 collided with the VSL robot arm. A positive time means that the solenoid valve was activated after the collision. Table 6.1 shows the time that is associated with each deactivation angle. The impact force is matched with the corresponding deactivation time of the experiment. It should be noted that all the impact forces occur at the moment of the collision (close to $t=0$). However, the impact forces are not drawn at $t=0$ s but they are drawn at the deactivation time of the experiment.

Figure 6.14 and Figure 6.15 show the impact forces measured when the VSL robot arm was in its maximum stiffness state and its minimum stiffness state. They are represented by the red band and the blue band, respectively. It should be noted that these impact forces are also measured as the moment of the impact ($t=0$). However, they are presented as a band only for the purpose of comparison with the impact forces recorded in the experiments where the solenoid valve was deactivated.

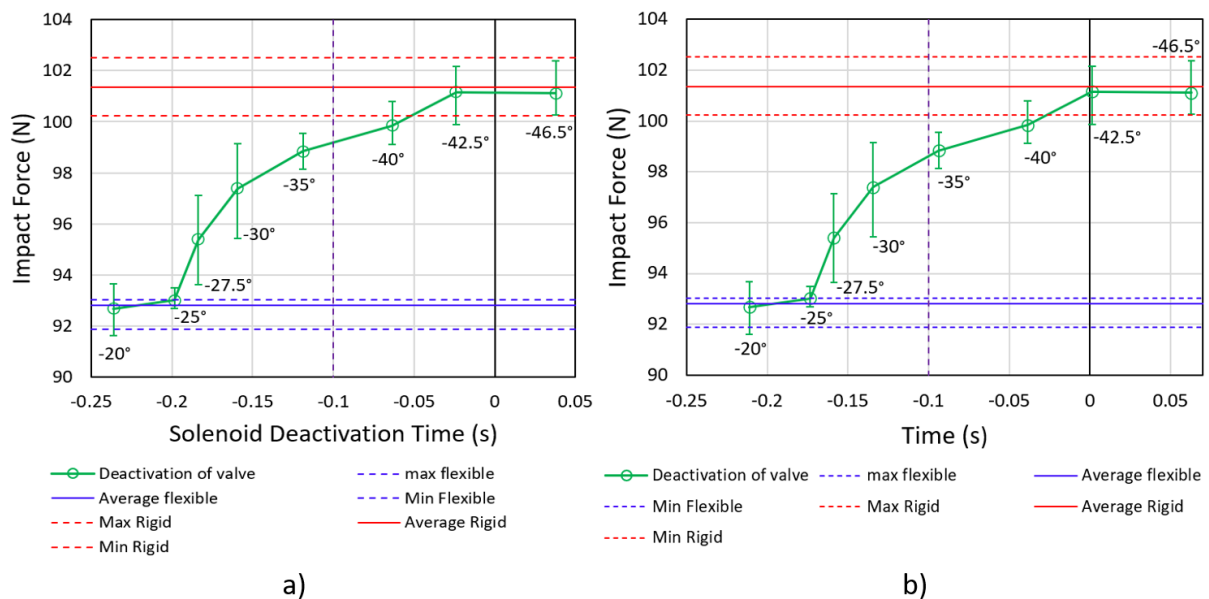


FIGURE 6.14: Results of the destiffening time experiment at impact velocity $v=0.58$ m/s. a) including the switching time of the solenoid valve. b) without including the switching time of the solenoid valve.

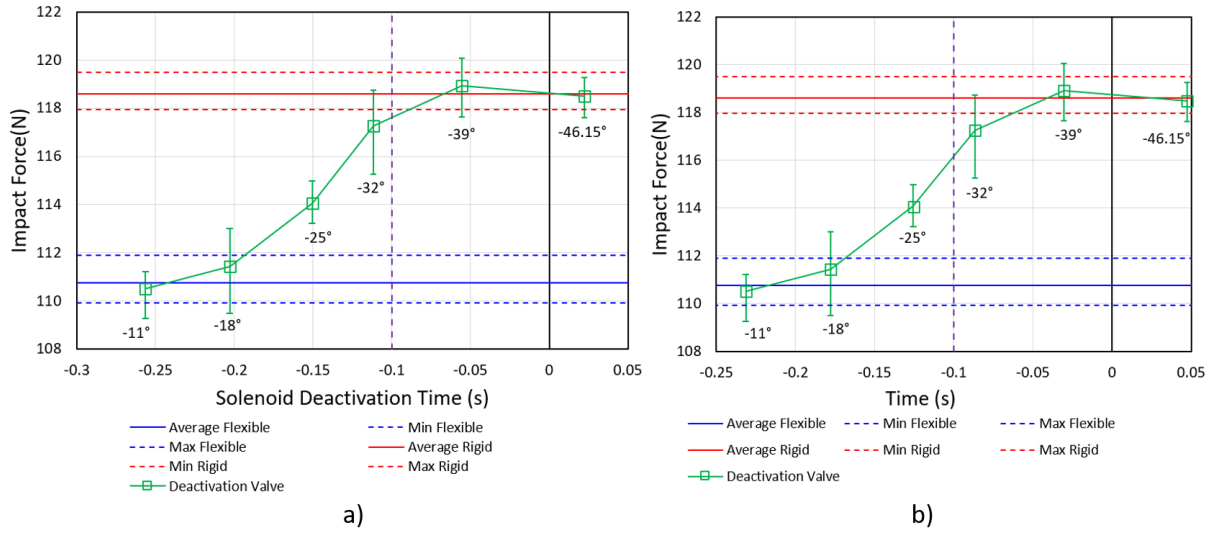


FIGURE 6.15: Results of the destiffening time experiment at impact velocity $v=0.84\text{m/s}$. a) including the switching time of the solenoid valve. b) without including the switching time of the solenoid valve.

6.3.4 Discussion

The change of stiffness of the VSL robot arm is an event that does not occur immediately after the activation or deactivation of the solenoid valve, but rather is a sequence of events. In the particular case of the destiffening process, the first step is the switching of the internal mechanism of the solenoid valve, which takes 25 ms according to the information provided by the manufacturer as can be seen in Appendix B. Then, the air in the Airstroke actuators and the pneumatic hoses starts to evacuate through the pneumatic valve, and the air pressure in the pneumatic circuit decreases until reaching atmospheric pressure. At some point during the decompression process, the Airstroke actuators start to retract and lose contact with the sheets of the LJSs. At this point, the stiffness of the robot arm decreases from the maximum stiffness state to the minimum stiffness state. It is very difficult to theoretically predict the exact moment when the trapezoidal pins loses contact with the sheets of the LJS because the manufacturer of the Airstroke actuator does not provide information about the time response of the actuators. In addition, the destiffening process of the robot arm also depends on other factors that are difficult to characterize such as the force of the compression springs located in the support of the actuators and the length of the pneumatic hoses. For this reason, the estimation of the

destiffening time is carried out through the experiments presented in this section rather than analytical models or simulations.

The destiffening time can be estimated by observing Figure 6.14a and Figure 6.15a. These figures illustrate the moments when the reduction of stiffness starts and finishes. For example, in the case of Experiment 1, Figure 6.14 shows that the experiment at -42.5° has an impact force that coincides with the rigid band, which means that the VSL robot arm is still rigid, although the solenoid valve was deactivated 23 ms before the impact. The experiment at -40° has an impact force that is very close to the rigid band, but it is clearly below the rigid band, which means that the reduction in the stiffness of the VSL robot arm begins to be effective when the valve was deactivated 63 ms before the impact. It is clear that for the experiment at -20° , the impact force coincides with the flexible band, which means that the robot arm is flexible at the moment of the impact when the solenoid valve was deactivated 236 ms before the impact. Therefore, for Experiment 1, it is possible to conclude that once the solenoid valve is turned off, the destiffening process starts at about 63 ms (-40°) and finishes at about 198 ms (-25°). Following a similar reasoning for Experiment 2, the destiffening process starts at about 111 ms (-32°) and finishes at about 203 ms (-18°) after the solenoid valve is turned off. It should be noted that these periods of time include the switching time of the solenoid valve.

Figure 6.14b and Figure 6.15b illustrate the impact forces associated with each deactivation position, but the deactivation time does not include the response time of the solenoid valve. This means that there is an offset of 25 ms in relation to Figure 6.14a and Figure 6.15a, respectively. These figures show the deactivation time of the pneumatic circuit that is formed by the pneumatic hoses and the airstroke actuators only. Therefore, in Experiment 1, the reduction in the stiffness of the VSL robot arms starts about 38 ms and finishes about 173 ms. In Experiment 2, the destiffening process starts at about 86 ms and finishes at about 178 ms. The comparison between Figure 6.14a and Figure 6.14b also shows what happens when the valve is deactivated 23 ms before the collision. The solenoid valve is still switching its internal mechanisms. Thus, the evacuation of the air has not begun, and the Airstroke actuators are still applying 100% of the pressure on the trapezoidal pins, which keeps the VSL robot arm rigid at the moment of the collision.

The results of the experiments demonstrate that the destiffening process of the trapezoidal pin

mechanism presented in Section 3.4 is significantly faster than the vacuum pressure mechanisms detailed in the literature. Of the existing lock/unlock mechanisms detailed in Chapter 2, the vacuum pressure mechanism has the fastest destiffening speed to vary the stiffness of the LJSs, with its destiffening speed characterised by a time constant of about 0.5 s [45]. In comparison, the trapezoidal pin mechanism can complete the destiffening process in 198 ms (including the activation time of the solenoid valve), making the trapezoidal pin mechanism more than two times faster than the vacuum pressure mechanism in terms of the reduction of LJS stiffness.

The results of the destiffening experiments also demonstrate the potential of the proposed VSL robot arm to effectively reduce the damage in the case of a collision with a human being. As explained in Chapter 2, the damage due to an impact between robot arms and human beings takes about 100 ms [2]. Figure 6.14 and Figure 6.15 show a vertical line at 0.1 s (100 ms) in order to compare the deactivation times against the time of the damage due to collisions. It can be seen in Figure 6.14a that the reduction of the impact forces starts at about 63 ms. This figure also shows that the reduction of the impact force is about 26% of the impact force variation (difference in the impact force between the rigid and the flexible states) at 100 ms; it should be taken into account that Figure 6.14a includes the response time of the solenoid valve (25 ms). If the response time of the solenoid valve is not considered, Figure 6.14b and Figure 6.15b show the impact force reduction is about 33.3% and 33.1% of the impact force variation respectively within a period of 100 ms. This reduction may be improved by using additional measures to speed up the destiffening time of the VSL robot arm.

6.3.5 Additional Measures to Reduce the Destiffening Time of the VSL Robot Arm

The destiffening time of the VSL robot arm can be shortened in order to reduce the impact forces within a period of 100 ms, which in turn would reduce the damage to humans due to a collision against the robot arm. The measures to achieve a faster destiffening are described as follow.

- Increase the stiffness of the springs that push the trapezoidal pin back to its initial position during the depressurisation of the Airstroke actuators. This measure implies a disadvantage; increasing the stiffness of the springs could reduce the force that the Airstroke actuators apply to push the trapezoidal pin because the springs work against the actuators. However, this reduction of force could be very small in comparison with the force that the actuators are able to apply when they are pressurised.
- Introducing multiple solenoid valves in different parts of the pneumatic circuit to evacuate the air pressure faster during depressurisation. A good place to locate these additional solenoid valves could be the discharge port of each Airstroke actuator. A disadvantage of this measure is the additional weight, cost and complexity of the added valves.
- Reduce the length of the pneumatic hoses that connect the Airstroke actuator with the solenoid valves. The response time for the pressurisation and depressurisation of the pneumatic circuit depends on the length of the pneumatic hoses. If the pneumatic hoses are shortened, less air has to be evacuated during the depressurisation and the destiffening process could be completed in less time.
- Implement solenoid valves with a shorter response time. The solenoid valve used in this section has a response time of 25 ms, but there are faster solenoids in the market with a response time between 10 ms and 15 ms [96].

6.4 Conclusions

This chapter responds to the second research question formulated in Chapter 1, which was about how to exploit the VSLs to improve the performance of a robot arm in human-robot interactions, particularly in relation to the problem of an impact between a human being and a robot arm. This chapter presents a stiffness experiment and a destiffening time experiment. To conduct both experiments, a 2-DoF VSL robot arm is developed. Each link of the robot arm is a sample of VSL Concept C that was presented in Section 4.4.

The stiffness experiment leads to the formulation of the stiffness envelopes, which is a method for visualisation of the stiffness of the proposed robot arm with VSLs. In general terms, all the

links contribute to the stiffness of the robot arm, but the contribution of each individual link depends on the pose of the robot and the direction of the force. The stiffness envelopes illustrate how each link contributes to the stiffness of the robot arm.

The stiffness envelopes could be used to determine how the stiffness in the links should be modulated in order to accomplish the requirements of a specific task. An example consisting of cleaning a window or erasing a board was described. The stiffness envelopes of the robot arm determined that one VSL must be rigid and the other VSL must be flexible to satisfy the requirements of these example tasks.

The mechanical design of a VSL is usually designed to provide variable stiffness capabilities for one load condition. However, the link must be stiff enough for the rest of the load conditions in order to have a practical use. In the case of the robot arm presented, the links have variable stiffness capabilities in bending. They are stiff enough to support axial loads, but they are not rigid enough to support torsion about the longitudinal axis. It is evident that the design of VSL Concept C should be improved in this aspect.

This chapter also presents a destiffening time experiment during impacts. The purpose of this experiment was to determine if the VSL robot arm was able to reduce its stiffness fast enough to attenuate the damage to a human being in the case of a collision. The experiment consisted of depressurising the Airstroke actuators in the VSL robot arm just before the impact against a UR3 robot arm and measuring the impact force.

The experiments demonstrated that the trapezoidal pin mechanism that is implemented in the VSL robot arm can achieve an impact force reduction of about 33% of the impact force variation (difference in the impact force between the rigid case and the flexible case) within a period of 100 ms. The arm was able to completely transition from its rigid to flexible state within a period of 173 ms. LJSs with a vacuum pressure mechanism could have a destiffening time characterised by a time constant of 0.5 s, and the damage from a collision between a human being and a robot arm takes about 100 ms. Therefore, the trapezoidal pin mechanism implemented in VSL Concept C has a destiffening speed that is faster than the vacuum pressure mechanism, and because the impact force can be reduced within 100 ms it also has the potential to reduce damage to a human during a collision.

Chapter 7

Conclusions

Traditional robot arms have been characterised by structural elements with constant and high stiffness in order to withstand high loads with minimum deformation. However, traditional robots have limitations in accomplishing other desirable functions such as being adaptable to variable operation conditions or grasp objects with irregular shapes. Robots with flexible structures could perform properly in those functions where rigid robots are not useful, but they do not have the capacity to support high loads without yielding or presenting significant deformation. Variable stiffness has emerged as a promising approach to solve this duality between rigid robots and flexible robots. Having a robot that can change its stiffness accordingly with the situation will make it possible to take advantage of both conditions.

Human-robot interaction is one of the fields that could take advantage of variation-of-stiffness technologies. There has been a desire for humans and robots to work in the same space, but due to safety concerns they have been kept isolated. Only in the relatively recent past have collaborative robots that can work with humans come to market. This has raised a set of problems about how robots and humans interact. One of these problems is the reduction in damage during an impact between a human being and a robot. This problem is critical because human beings could suffer serious or even fatal injuries if they receive a rigid impact from a robot. In addition, the impact could cause serious damage to the mechanical adjustment of the robot. A practical solution to reducing the risk is for manipulators to have mechanical compliance.

Variable stiffness capabilities can be implemented in robot arms through two approaches: VSJs and VSLs. VSJs have been widely studied in relation to the attenuation of impacts between human beings and robot arms while VSLs have been only recently explored. This research therefore aims to explore the implementation of VSLs in robot arms and their application in the reduction of impact between a human operator and a robot arm. These aims were formulated through two research questions.

The solution to the first research question was developed in Chapter 2, Chapter 3, and Chapter 4. The response to the second research question was presented in Chapter 5 and Chapter 6.

In this concluding chapter, a summary of the main contributions is presented in Section 7.1. Section 7.2 discusses the limitations of this research. Section 7.3 discusses future research directions and recommendations in the area of robot arms with VSLs.

7.1 Summary of Contributions

This section summarises the contributions to knowledge that resulted from this research.

7.1.1 Creation of the Trapezoidal Pin Mechanism

This contribution is the result of Chapter 2 and Chapter 3. Chapter 2 identified multiple technologies to vary stiffness in robotics. Among these technologies, LJSs were selected for this research because of their high stiffness ratio and manufacturability through conventional methods. The existing mechanisms to control the stiffness of an LJS have been demonstrated to be effective in achieving variation of stiffness. However, they also have shown some limitations in human-robot interactions. For example, in the case of the vacuum pressure mechanics, which is the fastest lock/unlock mechanism in LJSs, the main limitation is the destiffening time, which is not short enough to effectively reduce the impact force due to a collision between a human being and a robot arm. In addition, the envelope that generates vacuum pressure can be damaged easily during impacts, and the LJS itself must be manually returned to ambient pressure after transitioning from the rigid state to the flexible state.

The limitations of the existing mechanisms to modulate the stiffness of an LJS has motivated the creation of a new mechanism that was called the “Trapezoidal Pin Mechanism”. This mechanism was investigated in Chapter 3 and consists of a pneumatic actuator that drives a trapezoidal pin to interfere mechanically with the layers and, in turn, modulate the stiffness of the LJS. This mechanism also implements another novelty, which is the location of frames along the LJS. These frames do not apply normal pressure to the layers. They only avoid the separation or buckling of the layers. Another LJS with a flat clamp mechanism is presented to compare the mechanical behaviour of both mechanisms.

Force-deflection tests were conducted to characterise variations in bending stiffness in the LJSs due to changes in air pressure in the pneumatic cylinder. The results demonstrated that the maximum stiffness ratio of the trapezoidal pin is about 15% larger than the maximum stiffness ratio of the flat clamp. In addition, the experiments showed that the stick-slip phenomenon occurs in the flat clamp mechanism, but it is not present in the trapezoidal pin mechanism.

FE simulations were developed in Ansys to investigate the trapezoidal pin mechanism. The results of the FE simulations match well with the test results. Therefore, computational case studies were performed using FE simulations to study the effect of the angle of the trapezoidal pin in the LJS. The simulations show that the 30° trapezoidal pin has the highest stiffness for pressures greater than 500 kPa, while the 75° and 90° trapezoidal pins have the highest stiffness for pressures lower than 200 kPa.

Another computational study was carried out to investigate the effect of the number of frames placed along the LJS with a trapezoidal pin mechanism. FE simulations show that incrementing the number of frames results in an increased average of the stiffness range. Furthermore, the stiffness ratio reaches a maximum value when there are three frames in the LJS, showing an increase of about 11.5% relative to the minimum stiffness ratio. Overall, altering the number of frames is a practical and novel method of modulating the stiffness range without including more actuators in the LJS.

The behaviour of the proposed mechanism when deflections are large was also analysed through FE analysis. The simulations demonstrate that the stiffness of the LJS diminishes when the deflection increases beyond 10% of the length of the LJS. In addition, it is evident that at large

deflections, the layers of the LJS push the pin upwards, and the pin keeps contact only with the first top layers.

Compared with a vacuum pressure mechanism, the proposed mechanism does not require an air-tight chamber. It is therefore not vulnerable to sealing damage due to contact with rough edges. In addition, trapezoidal pin mechanisms have the potential to change the stiffness faster than the vacuum pressure mechanism, which makes the proposed mechanism adequate for mitigating impacts between robot arms and human beings.

7.1.2 Design of a Variable Stiffness Link

This contribution is the result of Chapter 4 and consists of a new design of a VSL. This new design is called “VSL Concept C”. It was developed as a result of two iterations in the design of the link, which were named VSL Concept A and VSL Concept B. This VSL Concept C combines a set of features that make it adequate for the construction of a robot arm with VSLs. The main novelty of this design is that it incorporates the trapezoidal pin mechanism and the frames that were presented in Chapter 2.

Two relevant mechanical problems were identified in the design of VSLs. First, the difficulty of attaching another link at the distal end of a typical LJS. Second, the requirement of supporting all types of forces generated by adjacent links such as axial force, bending moments, and torsion in all axes. Two characteristics were included in the design of VSL Concept C to address these challenges. The first characteristic is the interlocking LJS that allows the attachment of another link at the distal end. The second characteristic is the parallel guided beam architecture that supports axial torsion and transverse vertical force better than a single beam.

VSL Concept C also integrates a new type of pneumatic actuator known as “Airstroke”. This type of actuator is shorter than a normal pneumatic cylinder. The length of the Airstroke, in combination with the parallel guided beam, permits the location of the actuators inside the link, which eliminates external protrusions, making the VSL safer in the case of a collision with a human operator.

Another relevant characteristic of VSL Concept C is that the bottom sheets of the LJSs extend along the whole length of the link. This characteristic solves one of the fundamental problems

of interlocking LJSs, which is the separation of the distal and proximal parts of the link when the mechanism to lock the sheets is not activated.

VSL Concept B was developed to be tested in the impact test that is presented in Chapter 5. VSL concept C is used in the construction of a VSL robot arm that is presented in Chapter 6.

7.1.3 Experimental Quantification of Impact Reduction of a VSL

This contribution is the result of Chapter 5. The capacity of VSL Concept B to attenuate the impact force in the case of a collision with a human being was evaluated through an impact experiment. The experiment was carried out in an impact test bench where VSL concept B collides with a dummy of the human head.

The impact tests proved that VSLs based on the concept of an LJS with a trapezoidal pin mechanism can diminish the impact force by 12% when the LJS transitions from a high stiffness state to a low stiffness state. It is important to note that VSL concept B has a low stiffness ratio (1.34). Thus, it was proved that VSL concept B can significantly reduce the impact force despite its low stiffness ratio.

The impact tests also demonstrated that VSL concept B in its lowest stiffness state can reduce the impact force by 22% in comparison with an equivalent rigid link, demonstrating the efficacy of the VSL to mitigate the impact force significantly in the case of a collision with a human being.

The impact experiments also demonstrate that VSL concept B has the problem of the separation between the proximal end and the distal end of the link. This problem happens because there are no components that join both parts of the link.

7.1.4 Formulation and Use of the Stiffness Envelope to Analyse and Modulate the Robot Arm Stiffness

This contribution is one of the results from Chapter 6. A robot arm composed of two samples of VSL Concept C was built to conduct a stiffness experiment. This stiffness test leads to the formulation of stiffness envelopes, which is a method for visualisation of the stiffness of

the proposed VSL robot arm. Overall, all the links contribute to the stiffness of the robot arm. However, the contribution of each individual link is determined by the pose of the robot arm and the direction of the external force. The stiffness envelopes illustrate how each link contributes to the stiffness of the robot arm.

The stiffness envelopes were used to analyse the results of the stiffness experiment, showing some relevant aspects of the stiffness of the developed VSL robot arm. For instance, there are poses of the VSL robot arm where almost the entire stiffness of the robot arm in some directions is generated by one link while the other link makes a marginal contribution to the arm stiffness. There are also poses of the robot arm where the entire stiffness of the arm in some directions can be generated by any of the links.

The stiffness envelopes can also be used to analyse the ability of the robot arm to modulate its stiffness in order to satisfy the requirements of a specific task. An example consisting of erasing a board or cleaning a window was described. The stiffness envelopes of the robot arm were used to determine that one VSL must be rigid and the other VSL must be flexible to satisfy the requirements of the task.

7.1.5 Estimation of the Destiffening Time of a VSL Robot Arm

This contribution is another result of Chapter 6. The VSL robot arm composed of two samples of VSL Concept C was used to conduct a destiffening time experiment during impacts. The objective of this test was to determine if the VSL robot arm was able to decrease its stiffness fast enough to reduce the damage to a human being in the case of a collision. The test consisted of depressurising the Airstroke actuators in the VSL robot arm just before the impact against a UR3 robot arm and measuring the impact force.

The tests demonstrated that the trapezoidal pin mechanism that is implemented in the VSL robot arm can achieve an impact force reduction of about 33% of the impact force variation (difference in the impact force between the rigid case and the flexible case) within a period of 100 ms, and can completely transition from its rigid to flexible state within a period of 173 ms. LJSs based on existing vacuum pressure mechanisms could have a destiffening time characterised by a time constant of 0.5 s, but the damage from a collision between a human being and a robot

arm takes about 100 ms. Thus, the trapezoidal pin mechanism implemented in VSL Concept C has a destiffening speed that is faster than the vacuum pressure mechanism, and because the impact force can be diminished within a period of 100 ms it has the potential to mitigate the damage to a human being during a collision.

7.2 Discussion and Limitations

This section discusses the limitations of the work in this research.

7.2.1 Multiple Load Conditions Applied in VSL Robot Arms

The mechanical design of a VSL is usually designed to provide variable stiffness capabilities for one load condition. However, the link must be stiff enough for the rest of the load conditions in order to have a practical use. In the case of the robot arm presented in Chapter 6, the links have variable stiffness capabilities in bending, and they are stiff enough to support axial loads, but they are not rigid enough to support torsion about the longitudinal axis. As a result, it was necessary to use a support for the end effector. Thus, the VSL robot arm developed has limited practical applications in its current form.

Any modification that is implemented to make a VSL more rigid for one load condition may have an effect on the variable stiffness capabilities of the VSL for another load condition. A good example was the modification implemented in VSL Concept B that was presented in Section 6.2.1 to make it rigid. This modification, intended to cancel the variable stiffness capabilities of the link for bending, also increased the stiffness of the VSL for torsion which was not the objective of this modification.

7.2.2 VSL Actuators

The mechanical performance of the mechanism to vary the stiffness of LJSs depends significantly on the type of actuators that are used to drive the mechanism. This dependency also affects the performance of VSLs that integrate LJSs to achieve variable stiffness capabilities. In the case of

VSLs presented in this research, the stiffness ratio and the destiffening time of the VSL depend on the type of pneumatic actuator (pneumatic cylinder or Airstroke).

The type of actuator may also determine the methodology of the research to some extent. For instance, the actuators used in the developed VSLs are not specifically designed for this application. Therefore, the information about the actuation time is not usually provided by the manufacturer of the actuator, which limits the possibilities of developing analytical models or computational models for the research of the VSL. This is a research limitation that leads to an experimental methodology that is more intensive in resources and time-consuming.

The mechanical performance of the mechanism in varying the stiffness of the LJSs does not depend only on the type of actuator, but also depends on the systems or components that are associated with the actuator. In the case of the VSL robot arm presented in Section 6.3, the stiffness ratio depends on the maximum pressure of the pneumatic installation, and the destiffening time depends on the solenoid valve that is used to control the Airstroke actuator. An increase in the maximum pressure of the pneumatic circuit and the use of a faster solenoid valve is expected to increase the stiffness ratio and make the destiffening time shorter. Optimisation of the performance of the robot arm should therefore take into account the whole actuation system, and not only the actuator of the variable stiffness mechanism.

7.2.3 Manufacturing of the LJS

Section 1.4 explained that the scope of this research does not cover the manufacturing or the materials of the LJSs or the VSLs. However, the production of samples of LJSs for the experiments provided useful lessons in this regard.

The LJS with a conical pin mechanism that was described in Section 3.3 had an important problem related to the use of metallic sheets. The layers were made of stainless steel and they were curved due to the manufacturing process of the raw material. The curved shape of the sheets may have an influence on the mechanical behaviour of the LJS that is difficult to predict. This problem does not mean that it is impossible to manufacture an LJS with metallic sheets, but it demonstrates the challenges of working with very thin metal sheets.

It should be noted that the reduction in the thickness of the layers would increase the stiffness ratio of the LJS because more layers can be accommodated in a given thickness of the stack of layers. However, working with very thin metal sheets implies challenges like undesirable curvature of the sheets.

Another problem was the machining of the trapezoidal slots in the LJSs described in Section 3.4.2 and Section 4.6. In this case, the manufacturing of the trapezoidal slot drove the design of the LJS. The selected design allowed the machining of the slots from the sides of the LJS, which generates the necessity of having one slot on each side of the LJS. Cutting a trapezoidal slot in the center of the LJS is not possible with conventional milling machines or laser cutting machines.

The machining of the slots was also challenging because it required a fixture to cut all the layers at the same time. In the case of the interlocking LJSs implemented in VSL Concept B and VSL Concept C, the machining with the fixture led to a failure rate of 50% due to the tearing and fluttering of the sheets.

The main lesson from these problems is that the manufacturing of the LJSs is a critical problem that could determine the feasibility of a particular variable stiffness mechanism or the convenience of using a specific material.

7.3 Future Directions and Recommendations

This section discusses three areas of research that are potentially useful in the application of LJSs in the mitigation of impact between human beings and robots. Furthermore, some recommendations for future research are suggested.

7.3.1 VSLs for Multiple Load Conditions

The majority of the VSLs are designed to have variable stiffness for one particular load type. This feature limits the functionality and performance of the robot arm based on such VSLs. For example, VSL Concept C has variable stiffness capabilities for bending in the horizontal plane only. The stiffness envelope of the 2-DoF robot arm based on VSL Concept C shows that there

are poses of the robot arm where the robot is very rigid if force is applied in the axial direction of the links. This is the direct consequence of having links that only have variable stiffness capabilities for bending.

Developing robot links with variable stiffness for multiple load conditions will produce robots with improved performance in terms of their stiffness capabilities. The VSL would multiply the stiffness ratio of the robot arm in all poses and in all directions of external forces. For example, if variable stiffness in the axial direction is implemented in VSL Concept C, the stiffness envelope of the 2-DoF robot arm presented in Chapter 6 will be different in two aspects. First the envelope would be bigger in all stiffness states and in all poses of the robot. Second, the stiffness ratio would also be higher in all the cases; there will not be poses where the robot arm is completely stiff in one direction.

Developing VSLs based on LJSs that have variable stiffness for multiple conditions would require a more complex mechanical design, but it is still a task that is viable with the existing LJ mechanisms, including the trapezoidal pin mechanism developed in this thesis. For instance, the joint design that integrates LJS activated by vacuum pressure [17], can provide stiffness control in two orthogonal axes and could be modified to make a VSL that provides bending stiffness in two orthogonal planes.

Another strategy to improve the variable stiffness capabilities of a robot arm is to combine VSLs that have variable stiffness capabilities for different types of loads. For example, combining a VSL for bending with a VSL for axial loads. The combination of multiple variable stiffness technologies could help the development of this strategy.

It should be noted that attempts to develop manipulators that have variable stiffness for multiple load conditions in multiple directions and that are based on vacuum pressure LJSs have resulted in the creation of continuum robots. However, continuum robots are used for applications that require dexterity, such as minimally invasive surgery, while VSL robot arms are focused on the typical task of rigid robot arms, such as pick-and-place operations.

7.3.2 Active Compliance

Most of the studies about safe robot arms that can mitigate the impacts through their links have adopted a passive strategy. The studies of robot arms with VSLs that have implemented an active strategy are more scarce.

More work is necessary for the development of VSL robot arms with active compliance because they are more versatile than VSL robot arms with passive compliance. Robots with active compliance in the links can tune their VSLs during the operation of the robot, while a passive strategy depends more on the initial setup of the passive components. For example, in a passive compliance robot arm that uses foam for covering the links, it is necessary to replace the foam if the requirements of the impact attenuation change, which requires stopping the operation of the robot arm to replace the foam.

VSL robot arms with active compliance require sensors that can detect a collision and mechanisms that can vary the stiffness of the links in less than 0.1 s in order to be effective in the attenuation of impacts with human beings. The trapezoidal mechanism that was implemented in the VSL robot arm presented in this research can effectively attenuate the impact force during a collision. Therefore, it is effective to protect a human being in this type of incident. However, more work should be done with this mechanism to increase the attenuation of the impact force within a period of 0.1 s. More work is also necessary in the implementation of sensors that can detect the impact fast enough.

Research on other mechanisms to vary the stiffness of robot arms should also characterise the time response of the mechanism, and work toward achieving time responses shorter than 0.1 s in order to be effective in the attenuation of impacts between human beings and robots.

7.3.3 Improvement of Existing Lock/Unlock Mechanisms

It is necessary to note that all the technologies mentioned in Chapter 2 still have room for improvement regarding specific criteria. The appropriate combination of factors usually generates space for improvement. For example, FE simulations demonstrate that LJSs with heating blankets could reach a stiffness variation larger than 20 if the LJS has a low slenderness ratio,

relatively thick polymer layers, and cover layers with high extensional stiffness [70]. Another example is the functional dependencies established in LJSs that are activated by vacuum pressure [7]. These functional dependencies show that the full-slip and pre-slip stiffness scaled with N and N^3 , respectively, where N is the number of layers. Furthermore, full-slip stiffness scales with μ^2 (coefficient of friction) and P (pressure on the LJS). Therefore, changing N , μ , or P could improve the performance of the LJS significantly.

Considering the limitations of the actuators that were mentioned in Section 7.2.2. Another method for improving the existing lock/unlock mechanism is exploring other types of actuators. In the case of the trapezoidal pin mechanism, piezoelectric actuators could be used to drive the trapezoidal pin and achieve high speeds of stiffening and destiffening. In the case of DLJ, piezoelectric actuators are being considered as well to drive the flat clamp mechanism[9].

Another method that could be used to improve the existing lock/unlock mechanisms is to explore more materials and more manufacturing processes for the sheets of the LJS. For instance, 3D printing of metallic alloys could be a solution for the problems of the LJS with stainless steel sheets that were described in Section 3.3.1.

7.3.4 New Lock/Unlock Mechanisms

Section 2.5 demonstrates that LJ based on vacuum pressure is the dominant lock/unlock mechanism for applications in robotics, particularly in the application of robot arms. However, vacuum pressure-activated LJSs have two problems to be overcome to be completely adequate for this application. First, the LJSs do not have short enough destiffening and stiffening times to be useful in active compliance robots. Second, there are problems with the envelope, such as full sealing, easy damage caused by contact with rough edges, and the necessity to manually return the device to ambient pressure after the transition from the rigid state to the flexible state. To overcome these problems, new locking mechanisms have been developed or proposed in recent years, such as DLJ [9, 59], and the trapezoidal pin mechanism presented in this thesis and its associated publications [72, 97]. These mechanisms seek a rapid change in the stiffness of the LJS. For example, further development of DLJ will use piezoelectric actuators that could have a very fast action [9].

The development of new LJ mechanisms for the mitigation of impacts between robot arms and human beings should follow three strategies. The first one is the combination of LJ fundamental mechanisms. Some of these combinations have been investigated for this particular application, such as the case of the trapezoidal pin mechanisms developed in this thesis and its associated publications [72, 97]. The second strategy is the combination of LJ with other variable stiffness methods for robot arms. Some investigations have already been carried out in this direction, such as robot arms with variable stiffness joints formed by LJSs [17] and the VSL that combines airtight chamber, shape morphing, and LJ [18]. The third strategy is the implementation of existing LJ mechanisms, different from the basic vacuum pressure mechanism, to modulate the stiffness of a robot arm. The research on LJSs applied to other areas of robotics could serve as inspiration for the implementation of this strategy since some LJ mechanisms have shown significant improvements in relevant aspects such as speed of stiffening/destiffening and stiffness variation. For instance, the application of LJSs based on electrostatic force in haptic gloves has demonstrated to have very short actuation and release times (5 ms and 15 ms respectively) [64], and wearable gloves that combine a vacuum pressure mechanism with the mechanical interference mechanism have shown stiffness variations up to 26.3 [98]. These LJ mechanisms could be applied to robot arms and allow faster and more effective mitigation of impacts between robots and human beings.

7.3.5 Control of Robot Arms Composed of LJSs

Research on the control of VSLs that can mitigate impacts on human beings is scarce. Particularly in the case of VSLs based on LJSs. One of the few studies in this regard is a parallel guided link that is composed of LJSs. This link has been characterised to develop control algorithms of link motion and to carry out experiments in order to measure force and acceleration during impacts against a human being [16]. More developments of control algorithms for this type of link are expected in the coming years since they represent the evolution of research from the mechanical characterisation of LJSs to their application in the impact between human beings and robots. In addition, the research on control is fundamental for VSL robot arms that implement the active compliance strategy in the problem of collisions with human operators.

The investigation of robot arms with joints formed by LJSs has also progressed towards the control of the robot arm [17], showing that the robot arm is able to control the end effector impedance in orthogonal directions by tuning the stiffness of the LJSs in the joints. In addition, the same joint could be used to control the impact response of the robot by setting the yield force threshold in different directions and by providing a tunable damping response. More developments of control algorithms for this type of joint are expected as well, particularly because it has demonstrated to be effective in attenuating the negative effects of impacts.

7.3.6 Recommendations

The following recommendations focus on LJ since this technology was selected in this thesis for the construction of robot arms with VSLs.

In Chapter 6, the speed of destiffening of a VSL robot arm with a trapezoidal pin mechanism was measured. However, this task has not been carried out for other types of VSLs based on LJSs. Future research on VSL robot arms based on LJ mechanisms should measure quantitatively the speed of stiffening and destiffening. The measurement of these criteria will provide valuable information to determine if a particular lock/unlock LJ mechanism is suitable for the development of active compliant robot manipulators or for use in dynamic applications. In this way, it would be possible to progress beyond the passive compliance robots that have dominated the implementation of LJSs in robotics. This recommendation is also applicable to VSL robot arms that are based on other technologies different from LJ since the majority of studies of VSL robot arms focus on other aspects of the link performance, such as the stiffness ratio or precision.

Another recommendation is to test the LJSs directly on the particular application of interest. For the case of impact between human beings and robots, there is scarce information on the performance of different lock/unlock mechanisms of LJSs in this application.

The modelling of LJ mechanisms is progressing towards the formulation of methodologies to guide the design process of LJSs applied to robotic applications. The development of these strategies has resulted in computational tools to design LJSs that satisfy a specific set of performance requirements. The research community should use these tools in order to speed up the implementation of LJ in various robotic fields. Unfortunately, these methodologies are focused

only on LJ based on vacuum pressure. For the rest of the LJ mechanisms, FEA is still the most practical tool for design.

Manufacturing and testing of VSLs based on LJSs also should be documented better. This thesis and its associated articles about LJSs based on the trapezoidal pin mechanism described in detail the manufacturing process [72, 97]. The manufacturing process of an LJS activated by vacuum pressure has been described as well [7]. However, some publications about the application of LJSs in different fields of robotics do not provide enough details about manufacturing. These discussions of LJSs are not clear about how the final designs were settled on. For example, there is no indication of the manufacturing problems, the design alternatives that were tried before the definition of the final design, or of the materials that were tested. In addition, few publications present information about how the performance of a particular LJS degrades with time. For instance, the study presented in [41] explains that LJSs composed of paper or sandpaper present problems of repeatability and durability because these materials exhibit significant wear when they are bent. This type of observation could be very useful for future research in order to avoid the same mistakes and improve the repeatability of the LJSs.

Appendix A

Airstroke Actuator

The Airstroke actuator is produced by Firestone. Figure A.1 illustrates the dimensions of the Airstroke 50-P-10 and the Force vs Height curve.

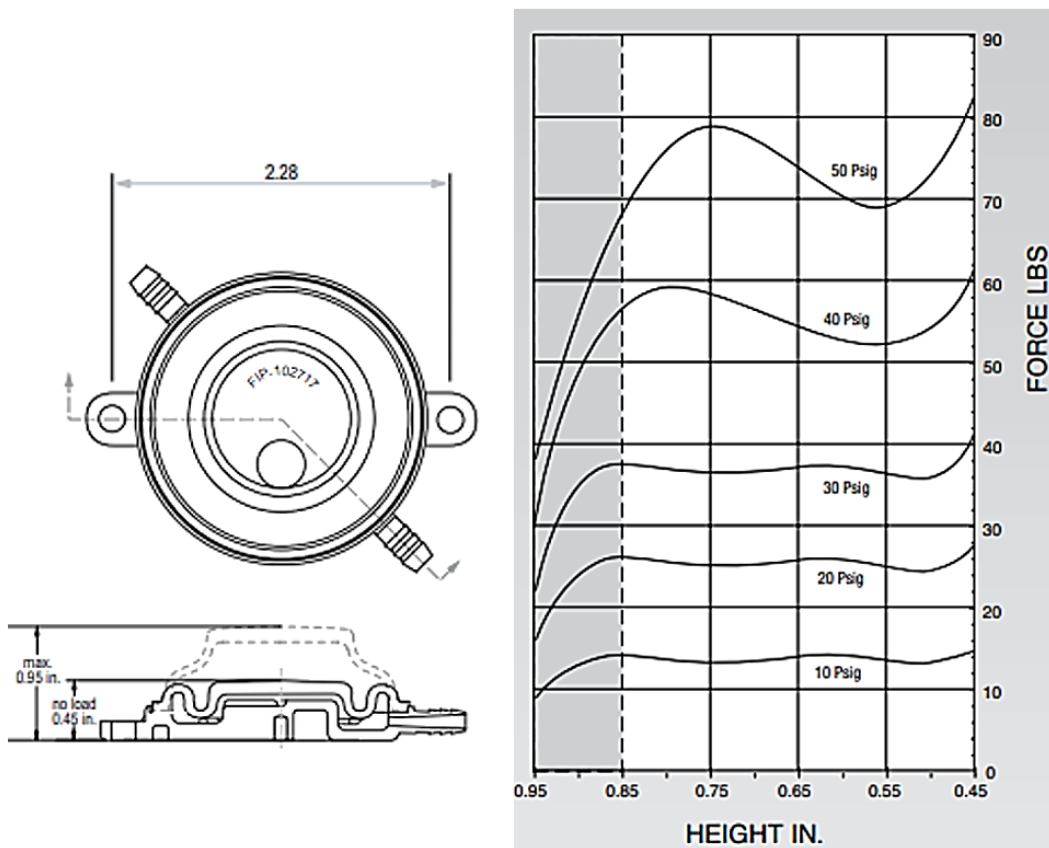


FIGURE A.1: Airstroke actuator

Appendix B

Solenoid Valve

The solenoid valve is produced by the company ASCO. Figure B.1 illustrates the specifications of the ASCO valve model E314K121S1V01.



Attribute	Value
Supply Voltage	24 V dc
Number of Ports	3
Connection Size	1/4in
Connection	1/4 in G Female
Operation	Direct
Default Valve Position	NC
Suitable Applications	Air, Oil, Water
Type	3/2
Orifice Diameter	2.4mm
Body Material	Stainless Steel
Series	E314K
Maximum Working Pressure	10 (Air) bar, 6 (Oil) bar, 8 (Water) bar
Operating Temperature Range	-25 → +90 °C
Maximum Operating Temperature	+90°C
Connection Gender	Female
Minimum Operating Temperature	-25°C
Thread Standard or Connection Type	G
Flow Factor Kv	0.17m ³ /h
Maximum Opening Time	25ms

FIGURE B.1: Solenoid Valve

Appendix C

EVA Test

Ethylene-Vinyl Acetate (EVA) is the foam used to cover the impactor during the impact test presented in Chapter 5. EVA is a closed-cell foam that is produced by multiple manufacturers around the world. EVA is commonly used for vibration dampening, impact absorption, production protection and packaging, thermal insulation and more.

EVA properties vary considerably according to the manufacturer. EVA manufacturers usually provide general mechanical properties such as density and tensile strength. However, characteristic curves such as Force vs Deformation in compression and tension are rarely available. For this reason. It was necessary to experimentally characterize the EVA foam that was used in the impact experiment.

The compression experiment consisted of applying a compression load on a sample of the EVA foam. The sample used in the compression experiment was a cylinder with a diameter of 56mm and a thickness of 20 mm. This sample was cut from the same EVA sheet that was used in the impact experiment. The experiment was carried out in a Shimadzu AGX50 Universal Testing Machine, and the load was applied at a deformation rate of 4mm/s. Figure C.1 illustrates the results of the experiment.

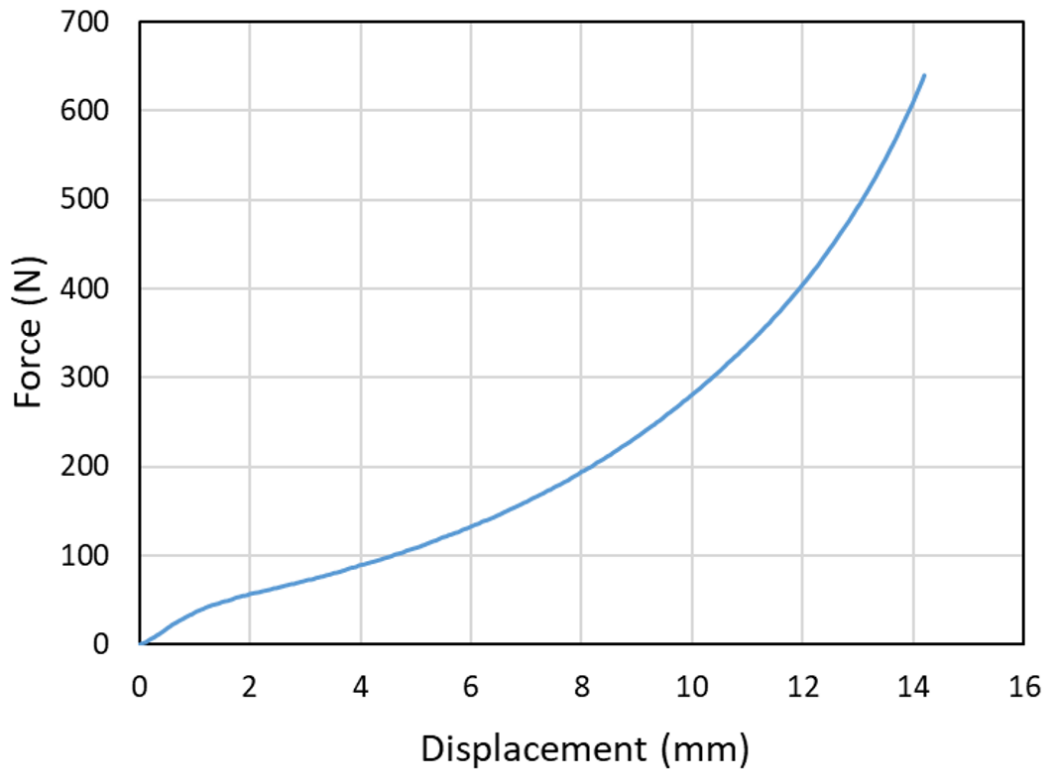


FIGURE C.1: Compression test of EVA Foam

The EVA foam was also tested for tension. The dimensions of the sample are illustrated in Figure C.2; the dimensions of the sample correspond to the type A sample that is specified in the standard ASTM D412; the thickness of the sample was 8 mm. This sample was cut from the same EVA sheet that was used in the impact experiment. The tensile test was carried out according with the test method specified in the standard ASTM D3575. The tension test was conducted in the Shimadzu AGX50 Universal Testing Machine, The deformation rate was 4mm/s. The results can be seen in Figure C.3.

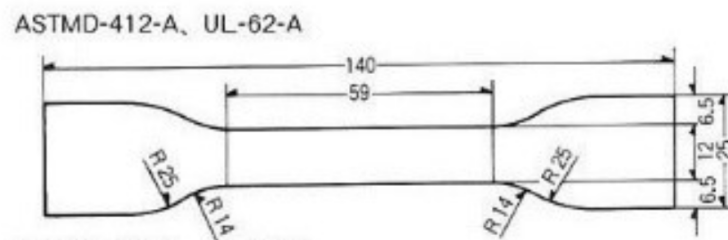


FIGURE C.2: Sample of EVA Foam for tension test

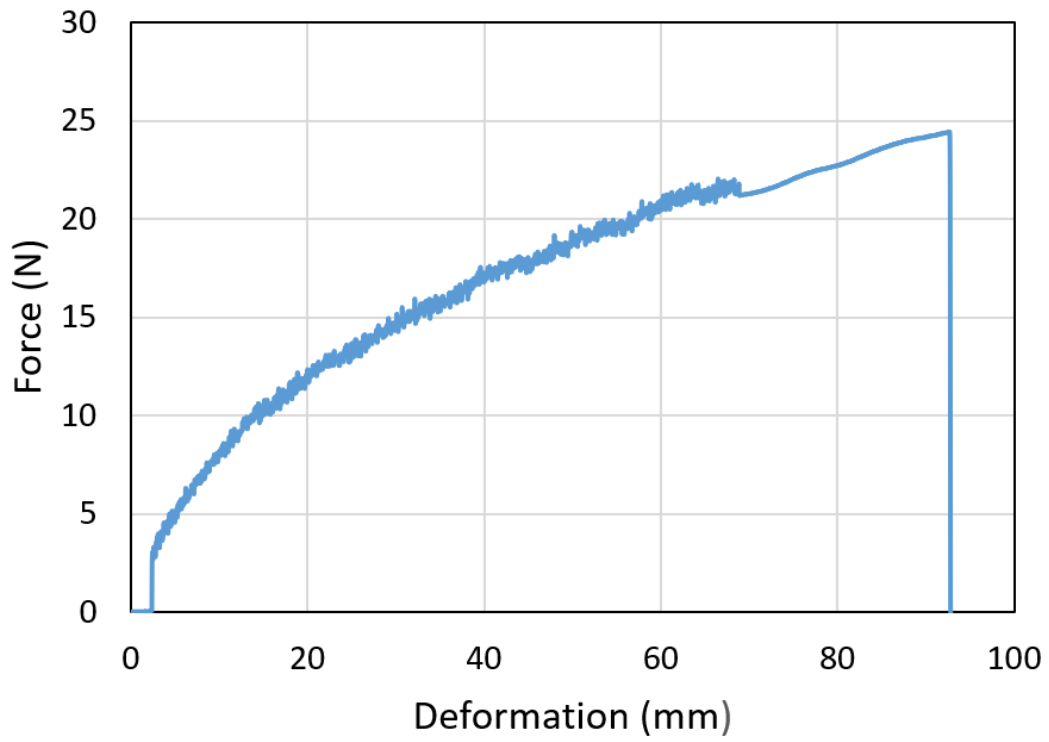


FIGURE C.3: Tension test results of EVA foam

Bibliography

- [1] Bram Vanderborght, Ronald Van Ham, Dirk Lefeber, Thomas G. Sugar, and Kevin W. Hollander. Comparison of mechanical design and energy consumption of adaptable, passive-compliant actuators. *The International Journal of Robotics Research*, 28(1):90–103, 2009. doi: 10.1177/0278364908095333.
- [2] Alin Albu-Schaffer, Oliver Eiberger, Markus Grebenstein, Sami Haddadin, Christian Ott, Thomas Wimbock, Sebastian Wolf, and Gerd Hirzinger. Soft robotics. *IEEE Robotics Automation Magazine*, 15(3):20–30, 2008. ISSN 1070-9932.
- [3] Myrel Alsayegh, Freia Irina Mues, Jörn Malzahn, and Torsten Bertram. Analytic forward and inverse kinematics of a multi-elastic-link robot arm. pages 425–430. ISBN 3800742314.
- [4] Jörn Malzahn and Torsten Bertram. Collision detection and reaction for a multi-elastic-link robot arm. *IFAC Proceedings Volumes*, 47(3):320–325, 2014. ISSN 1474-6670. doi: <https://doi.org/10.3182/20140824-6-ZA-1003.01545>.
- [5] M. Manti, V. Cacucciolo, and M. Cianchetti. Stiffening in soft robotics: A review of the state of the art. *IEEE Robotics Automation Magazine*, 23(3):93–106, 2016. ISSN 1070-9932. doi: 10.1109/MRA.2016.2582718.
- [6] Markus Henke and Gerald Gerlach. On a high-potential variable-stiffness device. *Microsystem Technologies*, 20(4):599–606, 2014. ISSN 1432-1858. doi: 10.1007/s00542-013-1995-5.
- [7] Yashraj S. Narang, Joost J. Vlassak, and Robert D. Howe. Mechanically versatile soft machines through laminar jamming. *Advanced Functional Materials*, 28(17):1707136, 2018. doi: 10.1002/adfm.201707136.

-
- [8] Osamu Tabata, Satoshi Konishi, Pierre Cusin, Yuichi Ito, Fumie Kawai, Shinichi Hirai, and Sadao Kawamura. Micro fabricated tunable bending stiffness devices. *Sensors and Actuators A: Physical*, 89(1):119–123, 2001. ISSN 0924-4247. doi: [https://doi.org/10.1016/S0924-4247\(00\)00538-0](https://doi.org/10.1016/S0924-4247(00)00538-0).
- [9] Yitong Zhou, Leon M. Headings, and Marcelo J. Dapino. Discrete Layer Jamming for Variable Stiffness Co-Robot Arms. *Journal of Mechanisms and Robotics*, 12(1), 10 2019b. ISSN 1942-4302. doi: 10.1115/1.4044537. 015001.
- [10] Jessie Lee C. Santiago, Isuru S. Godage, Phanideep Gonthina, and Ian D. Walker. Soft robots and kangaroo tails: Modulating compliance in continuum structures through mechanical layer jamming. *Soft Robotics*, 3(2):54–63, 2016. doi: 10.1089/soro.2015.0021.
- [11] M Henke and G Gerlach. A multi-layered variable stiffness device based on smart form closure actuators. *Journal of Intelligent Material Systems and Structures*, 27(3):375–383, 2016. doi: 10.1177/1045389x15577645.
- [12] Farhan Gandhi and Sang-Guk Kang. Beams with controllable flexural stiffness. *Smart Materials and Structures*, 16(4):1179–1184, 2007. ISSN 0964-1726 1361-665X. doi: 10.1088/0964-1726/16/4/028.
- [13] M. Jiang and N. Gravish. Sliding-layer laminates: A robotic material enabling robust and adaptable undulatory locomotion. In *2018 IEEE/RSJ International Conference on Intelligent Robots and Systems (IROS)*, pages 5944–5951. ISBN 2153-0866. doi: 10.1109/IROS.2018.8594421.
- [14] Mingsong Jiang and Nicholas Gravish. Reconfigurable laminates enable multifunctional robotic building blocks. *Smart Materials and Structures*, 30(3):035005, feb 2021. doi: 10.1088/1361-665x/abdc3f.
- [15] Carter Hurd. *Variable stiffness robotic arm for safe human-robot interaction using layer jamming*. PhD thesis, The Ohio State University, 2017.
- [16] Siyang Song, Xianpai Zeng, Yu She, Junmin Wang, and Hai-Jun Su. Modeling and control of inherently safe robots with variable stiffness links. *Robotics and Autonomous Systems*, 120:103247, 2019. ISSN 0921-8890. doi: <https://doi.org/10.1016/j.robot.2019.07.017>.

-
- [17] Buse Aktaş and Robert D. Howe. Flexure mechanisms with variable stiffness and damping using layer jamming. In *2019 IEEE/RSJ International Conference on Intelligent Robots and Systems (IROS)*, pages 7616–7621, 2019. doi: 10.1109/IROS40897.2019.8967759.
- [18] Yitong Zhou, Leon M. Headings, and Marcelo J. Dapino. Hybrid jamming variable-stiffness link for safe co-robots. In *2021 IEEE International Conference on Real-time Computing and Robotics (RCAR)*, pages 1224–1229, 2021. doi: 10.1109/RCAR52367.2021.9517445.
- [19] I. Choi, N. Corson, L. Peiros, E. W. Hawkes, S. Keller, and S. Follmer. A soft, controllable, high force density linear brake utilizing layer jamming. *IEEE Robotics and Automation Letters*, 3(1):450–457, 2018. ISSN 2377-3766. doi: 10.1109/LRA.2017.2761938.
- [20] Xianpai Zeng, Cart Hurd, Hai-Jun Su, Siyang Song, and Junmin Wang. A parallel-guided compliant mechanism with variable stiffness based on layer jamming. *Mechanism and Machine Theory*, 148:103791, 2020. ISSN 0094-114X. doi: <https://doi.org/10.1016/j.mechmachtheory.2020.103791>.
- [21] Loïc Blanc, Alain Delchambre, and Pierre Lambert. Flexible medical devices: Review of controllable stiffness solutions. *Actuators*, 6(3):23, 2017. ISSN 2076-0825.
- [22] Izabela K. Kuder, Andres F. Arrieta, Wolfram E. Raither, and Paolo Ermanni. Variable stiffness material and structural concepts for morphing applications. *Progress in Aerospace Sciences*, 63:33–55, 2013. ISSN 0376-0421. doi: <https://doi.org/10.1016/j.paerosci.2013.07.001>.
- [23] R. V. Ham, T. G. Sugar, B. Vanderborght, K. W. Hollander, and D. Lefeber. Compliant actuator designs. *IEEE Robotics Automation Magazine*, 16(3):81–94, 2009. ISSN 1070-9932. doi: 10.1109/MRA.2009.933629.
- [24] B. Vanderborght, A. Albu-Schaeffer, A. Bicchi, E. Burdet, D.G. Caldwell, R. Carloni, M. Catalano, O. Eiberger, W. Friedl, G. Ganesh, M. Garabini, M. Grebenstein, G. Grioli, S. Haddadin, H. Hoppner, A. Jafari, M. Laffranchi, D. Lefeber, F. Petit, S. Stramigioli, N. Tsagarakis, M. Van Damme, R. Van Ham, L.C. Visser, and S. Wolf. Variable impedance actuators: A review. *Robotics and Autonomous Systems*, 61(12):1601–1614, 2013. ISSN 0921-8890. doi: <https://doi.org/10.1016/j.robot.2013.06.009>.

- [25] Songyuan Zhang, Shuxiang Guo, Muye Pang, Baofeng Gao, and Ping Guo. Mechanical design and control method for sea and vsa-based exoskeleton devices for elbow joint rehabilitation. *Neuroscience and Biomedical Engineering*, 03:1–1, 05 2015. doi: 10.2174/2213385203666150514235041.
- [26] F. Petit, M. Chalon, W. Friedl, M. Grebenstein, A. Albu-Schäffer, and G. Hirzinger. Bidirectional antagonistic variable stiffness actuation: Analysis, design and implementation. In *2010 IEEE International Conference on Robotics and Automation*, pages 4189–4196. ISBN 1050-4729. doi: 10.1109/ROBOT.2010.5509267.
- [27] Florian Patrick Petit. *Analysis and control of variable stiffness robots*. Thesis, 2014.
- [28] Sebastian Wolf, Thomas Bahls, Maxime Chalon, Werner Friedl, Markus Grebenstein, Hannes Höppner, Markus Kühne, Dominic Lakatos, Nico Mansfeld, Mehmet Can Özparpucu, Florian Petit, Jens Reinecke, Roman Weitschat, and Alin Albu-Schäffer. Soft robotics with variable stiffness actuators: Tough robots for soft human robot interaction. In Alexander Verl, Alin Albu-Schäffer, Oliver Brock, and Annika Raatz, editors, *Soft Robotics*, pages 231–254. Springer Berlin Heidelberg. ISBN 978-3-662-44506-8.
- [29] R. Schiavi, G. Grioli, S. Sen, and A. Bicchi. Vsa-ii: a novel prototype of variable stiffness actuator for safe and performing robots interacting with humans. In *2008 IEEE International Conference on Robotics and Automation*, pages 2171–2176. ISBN 1050-4729. doi: 10.1109/ROBOT.2008.4543528.
- [30] A. S. Phung, J. Malzahn, F. Hoffmann, and T. Bertram. Data based kinematic model of a multi-flexible-link robot arm for varying payloads. In *2011 IEEE International Conference on Robotics and Biomimetics*, pages 1255–1260. doi: 10.1109/ROBIO.2011.6181460.
- [31] Juan Carlos Cambera, Daniel Feliu Talegon, Saddam Gharab, and Vicente Feliu Batlle. Flexible link arm with a passive gravity compensation mechanism: design and modeling. *Actas de las XXXIX Jornadas de Automática, Badajoz, 5-7 de Septiembre de 2018*, 2018.
- [32] D. Kragic, P. Marayong, M. Li, A. M. Okamura, and G. D. Hager. Human-machine collaborative systems for microsurgical applications. *The International Journal of Robotics Research*, 24(9):731–741, 2005. doi: 10.1177/0278364905057059.

-
- [33] Rainer Müller, Matthias Vette, and Matthias Scholer. Inspector robot – a new collaborative testing system designed for the automotive final assembly line. *Assembly Automation*, 34(4):370–378, 2014. Copyright - © Emerald Group Publishing Limited 2014; Last updated - 2023-11-25.
- [34] A. Chu, H. Kazerooni, and A. Zoss. On the biomimetic design of the berkeley lower extremity exoskeleton (bleex). In *Proceedings of the 2005 IEEE International Conference on Robotics and Automation*, pages 4345–4352, 2005. doi: 10.1109/ROBOT.2005.1570789.
- [35] A. Bicchi and G. Tonietti. Fast and "soft-arm" tactics [robot arm design]. *IEEE Robotics Automation Magazine*, 11(2):22–33, 2004. doi: 10.1109/MRA.2004.1310939.
- [36] Collin Mikol and Hai-Jun Su. An actively controlled variable stiffness structure via layer jamming and pneumatic actuation. In *2019 International Conference on Robotics and Automation (ICRA)*, pages 7555–7561, 2019. doi: 10.1109/ICRA.2019.8794340.
- [37] Freddy Caro and Marc G. Carmichael. A review of mechanisms to vary the stiffness of laminar jamming structures and their applications in robotics. *Actuators*, 13(2), 2024. ISSN 2076-0825. doi: 10.3390/act13020064.
- [38] Walter D. Pilkey. *Formulas for stress, strain, and structural matrices*. John Wiley Sons, Hoboken, NJ, 2nd ed. edition, 2005. ISBN 0-470-34610-8.
- [39] S. Kawamura, T. Yamamoto, D. Ishida, T. Ogata, Y. Nakayama, O. Tabata, and S. Sugiyama. Development of passive elements with variable mechanical impedance for wearable robots. In *Proceedings 2002 IEEE International Conference on Robotics and Automation (Cat. No.02CH37292)*, volume 1, pages 248–253 vol.1. doi: 10.1109/ROBOT.2002.1013369.
- [40] Y. Kim, S. Cheng, S. Kim, and K. Iagnemma. Design of a tubular snake-like manipulator with stiffening capability by layer jamming. In *2012 IEEE/RSJ International Conference on Intelligent Robots and Systems*, pages 4251–4256. ISBN 2153-0866. doi: 10.1109/IROS.2012.6385574.
- [41] Lucas Gerez, Geng Gao, and Minas Liarokapis. Laminar jamming flexure joints for the development of variable stiffness robot grippers and hands. In *2020 IEEE/RSJ International Conference on Intelligent Robots and Systems (IROS)*.

-
- [42] Yuan Gao, Xiguang Huang, Ishan Singh Mann, and Hai-Jun Su. A novel variable stiffness compliant robotic gripper based on layer jamming. *Journal of Mechanisms and Robotics*, 12(5), 2020. ISSN 1942-4302. doi: 10.1115/1.4047156.
- [43] Choi Won Ho, Kim Sunghwan, Lee Dongun, and Shin Dongjun. Soft, multi-dof, variable stiffness mechanism using layer jamming for wearable robots. *IEEE robotics and automation letters*, 4(3):2539–2546, 2019. ISSN 2377-3766. doi: 10.1109/LRA.2019.2908493.
- [44] L. Gerez, G. Gao, A. Dwivedi, and M. Liarokapis. A hybrid, wearable exoskeleton glove equipped with variable stiffness joints, abduction capabilities, and a telescopic thumb. *IEEE Access*, 8:173345–173358, 2020. doi: 10.1109/ACCESS.2020.3025273.
- [45] Igor Zubrycki and Grzegorz Granosik. *Novel Haptic Device Using Jamming Principle for Providing Kinaesthetic Feedback in Glove-Based Control Interface*, volume 85. 2016. doi: 10.1007/s10846-016-0392-6.
- [46] Jae Hyuck Jang, Altair Coutinho, Yeong Jae Park, and Hugo Rodrigue. A positive and negative pressure soft linear brake for wearable applications. *IEEE transactions on industrial electronics (1982)*, 70(1):688–698, 2023. ISSN 0278-0046. doi: 10.1109/TIE.2022.3148746.
- [47] Yeman Fan, Dikai Liu, and Lin Ye. A novel continuum robot with stiffness variation capability using layer jamming: Design, modeling, and validation. *IEEE access*, 10:130253–130263, 2022. ISSN 2169-3536. doi: 10.1109/ACCESS.2022.3228775.
- [48] Bin Fang, Fuchun Sun, Linyuan Wu, Fukang Liu, Xiangxiang Wang, Haiming Huang, Wenbing Huang, Huaping Liu, and Li Wen. Multimode grasping soft gripper achieved by layer jamming structure and tendon-driven mechanism. *Soft robotics*, 9(2):233–249, 2022. ISSN 2169-5172. doi: 10.1089/soro.2020.0065.
- [49] Y. S. Narang, A. Degirmenci, J. J. Vlassak, and R. D. Howe. Transforming the dynamic response of robotic structures and systems through laminar jamming. *IEEE Robotics and Automation Letters*, 3(2):688–695, April 2018. ISSN 2377-3766. doi: 10.1109/LRA.2017.2779802.
- [50] Yang Yang, Yazhan Zhang, Zicheng Kan, Jieli Zeng, and Michael Yu Wang. Hybrid jamming for bioinspired soft robotic fingers. *Soft robotics*, 7(3):292–308, 2020. ISSN 2169-5172. doi: 10.1089/soro.2019.0093.

-
- [51] Mingzhu Zhu, Mengying Xie, Yoshiki Mori, Junyue Dai, Sadao Kawamura, and Xiaokui Yue. A variable stiffness soft gripper based on rotational layer jamming. *Soft robotics*, 2023. ISSN 2169-5172. doi: 10.1089/soro.2022.0232.
- [52] Xianpai Zeng and Hai-Jun Su. A high performance pneumatically actuated soft gripper based on layer jamming. *Journal of mechanisms and robotics*, 15(1), 2023. ISSN 1942-4302. doi: 10.1115/1.4053857.
- [53] Mingzhu Zhu, Yoshiki Mori, Tatsuhiko Wakayama, Akira Wada, and Sadao Kawamura. A fully multi-material three-dimensional printed soft gripper with variable stiffness for robust grasping. *Soft robotics*, 6(4):57–519, 2019. ISSN 2169-5172. doi: 10.1089/soro.2018.0112.
- [54] Takashi Mitsuda and Hareruya Tanaka. Mesh layer jamming to cover and secure curved surfaces without wrinkles. *Advanced Engineering Materials*, 25(20):2300513, 2023. doi: <https://doi.org/10.1002/adem.202300513>.
- [55] Callum JC Heath, Ian P Bond, and Kevin D Potter. Interlocking electro-bonded laminates. *Journal of Intelligent Material Systems and Structures*, 28(11):1524–1529, 2017. doi: 10.1177/1045389X16672733.
- [56] Yi Sun, Xiongxiang Wu, Ben Lu, Min Wang, Jiheng Ding, Huayan Pu, Wenchuan Jia, Yan Peng, and Jun Luo. Electrostatic layer jamming variable stiffness enhanced by giant electrorheological fluid. *IEEE/ASME Transactions on Mechatronics*, pages 1–11, 2023. doi: 10.1109/TMECH.2023.3275961.
- [57] Xiongxiang Wu, Ben Lu, Ningbin Liao, Wenchuan Jia, Min Wang, Jiheng Ding, Huayan Pu, Yan Peng, Jun Luo, and Yi Sun. Enhanced elasticstatic layer jamming for variable stiffness using ac excitation. In *2023 9th International Conference on Electrical Engineering, Control and Robotics (EECR)*, pages 1–5, 2023. doi: 10.1109/EECR56827.2023.10149952.
- [58] Cheng Chen, Dongliang Fan, Hongliang Ren, and Hongqiang Wang. Comprehensive model of laminar jamming variable stiffness driven by electrostatic adhesion. *IEEE/ASME Transactions on Mechatronics*, pages 1–10, 2023. doi: 10.1109/TMECH.2023.3319650.
- [59] Y. Zhou, L. M. Headings, and M. J. Dapino. Discrete layer jamming for safe co-robots. In *2019 International Conference on Robotics and Automation (ICRA)*, pages 6124–6129, 2019a. doi: 10.1109/ICRA.2019.8793908.

- [60] Kunal Singh and Shilpa Gupta. Discrete stiffness control of soft actuators using laminar jammers made of abrasive materials. *Materials today : proceedings*, 2023. ISSN 2214-7853. doi: 10.1016/j.matpr.2023.02.109.
- [61] Markus Henke, Jörg Sorber, and Gerald Gerlach. *Multi-layer beam with variable stiffness based on electroactive polymers*, volume 8340 of *SPIE Smart Structures and Materials + Nondestructive Evaluation and Health Monitoring*. SPIE, 2012.
- [62] Yu She. *Compliant robotic arms for inherently safe physical human-robot interaction*. Thesis, 2018.
- [63] David J. Levine, Gokulanand M. Iyer, R. Daelan Roosa, Kevin T. Turner, and James H. Pikul. A mechanics-based approach to realize high-force capacity electroadhesives for robots. *Science Robotics*, 7(72):eabo2179, 2022. doi: 10.1126/scirobotics.abo2179.
- [64] Ronan Hinchet and Herbert Shea. High force density textile electrostatic clutch. *Advanced materials technologies*, 5(4):n/a, 2020. ISSN 2365-709X. doi: 10.1002/admt.201900895.
- [65] A Bergamini, R Christen, B Maag, and M Motavalli. A sandwich beam with electrostatically tunable bending stiffness. *Smart materials and structures*, 15(3):678, 2006.
- [66] Luigi Di Lillo, Wolfram Raither, Andrea Bergamini, Manuel Zündel, and Paolo Ermanni. Tuning the mechanical behaviour of structural elements by electric fields. *Applied Physics Letters*, 102(22):224106, 2013.
- [67] Brian H. Do, Inrak Choi, and Sean Follmer. An all-soft variable impedance actuator enabled by embedded layer jamming. *IEEE/ASME Transactions on Mechatronics*, 27(6):5529–5540, 2022. doi: 10.1109/TMECH.2022.3183576.
- [68] Xiaoyi Liu and Zehao Liang. Soft actuator using sponge units with constrained film and layer jamming. *Industrial Robot: the international journal of robotics research and application*, 49(4):616–624, 2022.
- [69] Niccolò Pagliarani, Giacomo Picardi, Syeda Shadab Zehra Zaidi, and Matteo Cianchetti. Variable kinematics enabled by layer jamming transition in a soft bending actuator. In *2023 IEEE International Conference on Soft Robotics (RoboSoft)*, pages 1–7, 2023. doi: 10.1109/RoboSoft55895.2023.10121943.

- [70] Gabriel Murray and Farhan Gandhi. Multi-layered controllable stiffness beams for morphing: energy, actuation force, and material strain considerations. *Smart Materials and Structures*, 19(4):045002, 2010. ISSN 0964-1726 1361-665X. doi: 10.1088/0964-1726/19/4/045002.
- [71] Ziqi Wang, Xiangjie Zhou, Zejian Zhou, Yan Zhang, Yuru Zhang, and Dangxiao Wang. Matejam: Multi-material teeth-clutching layer jamming actuation for soft haptic glove. *IEEE transactions on haptics*, 16(2):276–286, 2023. ISSN 1939-1412. doi: 10.1109/TOH.2023.3269063.
- [72] Freddy. Caro and Marc G. Carmichael. A novel multi-layer beam mechanism for variable stiffness robotic arms. *Australasian Conference on Robotics and Automation, ACRA*, 2021-December, 2021. ISSN 1448-2053.
- [73] *Design of a Multi-Directional Variable Stiffness Leg for Dynamic Running*, volume Volume 10: Mechanics of Solids and Structures, Parts A and B of *ASME International Mechanical Engineering Congress and Exposition*, 11 2007. doi: 10.1115/IMECE2007-41318. URL <https://doi.org/10.1115/IMECE2007-41318>.
- [74] P.J. Blau. *Friction Science and Technology: From Concepts to Applications, Second Edition*. Mechanical Engineering. ISBN 9781420054101.
- [75] Saquib Rouf, Ankush Raina, Mir Irfan Ul Haq, Nida Naveed, Sudhanraj Jeganmohan, and Aysha Farzana Kichloo. 3d printed parts and mechanical properties: Influencing parameters, sustainability aspects, global market scenario, challenges and applications. *Advanced Industrial and Engineering Polymer Research*, 5(3):143–158, 2022. ISSN 2542-5048. doi: <https://doi.org/10.1016/j.aiepr.2022.02.001>.
- [76] S Haddadin, A Albu-Schaffer, M Frommberger, J Rossmann, and G Hirzinger. The ”dlr crash report”: Towards a standard crash-testing protocol for robot safety - part ii: Discussions. In *2009 IEEE International Conference on Robotics and Automation*, pages 280–287. IEEE, 2009. ISBN 1424427886.
- [77] Fabio Caruso, Giacomo Mantriota, Luciano Afferrante, and Giulio Reina. A theoretical model for multi-layer jamming systems. *Mechanism and machine theory*, 172:104788, 2022. ISSN 0094-114X. doi: 10.1016/j.mechmachtheory.2022.104788.

-
- [78] Dalong Gao and Charles W. Wampler. Head injury criterion. *IEEE Robotics Automation Magazine*, 16(4):71–74, 2009. doi: 10.1109/MRA.2009.934824.
- [79] Javier López-Martínez, José Luis Blanco-Claraco, Daniel García-Vallejo, and Antonio Giménez-Fernández. Design and analysis of a flexible linkage for robot safe operation in collaborative scenarios. *Mechanism and Machine Theory*, 92:1–16, 2015. ISSN 0094-114X. doi: <https://doi.org/10.1016/j.mechmachtheory.2015.04.018>.
- [80] Jung-Jun Park, Byeong-Sang Kim, Jae-Bok Song, and Hong-Seok Kim. Safe link mechanism based on nonlinear stiffness for collision safety. *Mechanism and Machine Theory*, 43(10): 1332–1348, 2008. ISSN 0094-114X. doi: 10.1016/j.mechmachtheory.2007.10.004.
- [81] Xianpai Zeng, Tyler N. Morrison, and Haijun Su. Mechanical solutions to variable stiffness robotic arms. 2019.
- [82] Yu She, Siyang Song, Hai-Jun Su, and Junmin Wang. A Comparative Study on the Effect of Mechanical Compliance for a Safe Physical Human–Robot Interaction. *Journal of Mechanical Design*, 142(6):063305, 03 2020. ISSN 1050-0472. doi: 10.1115/1.4046068.
- [83] J. López-Martínez, D. García-Vallejo, A. Giménez-Fernández, and J. L. Torres-Moreno. A Flexible Multibody Model of a Safety Robot Arm for Experimental Validation and Analysis of Design Parameters. *Journal of Computational and Nonlinear Dynamics*, 9(1):011003, 09 2013. ISSN 1555-1415. doi: 10.1115/1.4025285.
- [84] Agostino Stilli, Helge A. Wurdemann, and Kaspar Althoefer. A novel concept for safe, stiffness-controllable robot links. *Soft robotics*, 4(1):16–22, 2017. ISSN 2169-5172.
- [85] Yu She, Hai-Jun Su, Deshan Meng, and Cheng Lai. Design and Modeling of a Continuously Tunable Stiffness Arm for Safe Physical Human–Robot Interaction. *Journal of Mechanisms and Robotics*, 12(1):011006, 10 2019. doi: 10.1115/1.4044840.
- [86] *A Continuously Tunable Stiffness Arm With Cable-Driven Mechanisms for Safe Physical Human-Robot Interaction*, volume Volume 10: 44th Mechanisms and Robotics Conference (MR) of *International Design Engineering Technical Conferences and Computers and Information in Engineering Conference*, 08 2020. doi: 10.1115/DETC2020-22035. URL <https://doi.org/10.1115/DETC2020-22035>.

- [87] Ruiqi Hu, V Venkiteswaran, and H-J Su. A variable stiffness robotic arm using linearly actuated compliant parallel guided mechanism. In *Mechanism Design for Robotics: Proceedings of the 4th IFToMM Symposium on Mechanism Design for Robotics*, pages 33–40. Springer, 2019.
- [88] T. Morrison, C. Li, X. Pei, and H. Su. A novel rotating beam link for variable stiffness robotic arms. In *2019 International Conference on Robotics and Automation (ICRA)*, pages 9387–9393, May 2019. doi: 10.1109/ICRA.2019.8793833.
- [89] Tyler Morrison and Hai-Jun Su. Stiffness modeling of a variable stiffness compliant link. *Mechanism and Machine Theory*, 153:104021, 2020. ISSN 0094-114X. doi: <https://doi.org/10.1016/j.mechmachtheory.2020.104021>.
- [90] A. Stilli, L. Grattarola, H. Feldmann, H. A. Wurdemann, and K. Althoefer. Variable stiffness link (vsl): Toward inherently safe robotic manipulators. In *2017 IEEE International Conference on Robotics and Automation (ICRA)*, pages 4971–4976. doi: 10.1109/ICRA.2017.7989578.
- [91] Morgan T. Gillespie, Charles M. Best, and Marc D. Killpack. Simultaneous position and stiffness control for an inflatable soft robot. In *2016 IEEE International Conference on Robotics and Automation (ICRA)*, pages 1095–1101, 2016. doi: 10.1109/ICRA.2016.7487240.
- [92] Juan M. Gandarias, Yongjing Wang, Agostino Stilli, Alfonso J. García-Cerezo, Jesús M. Gómez-de Gabriel, and Helge A. Wurdemann. Open-loop position control in collaborative, modular variable-stiffness-link (vsl) robots. *IEEE Robotics and Automation Letters*, 5(2): 1772–1779, 2020. doi: 10.1109/LRA.2020.2969943.
- [93] Siyang Song, Yu She, Junmin Wang, and Hai-Jun Su. Toward Tradeoff Between Impact Force Reduction and Maximum Safe Speed: Dynamic Parameter Optimization of Variable Stiffness Robots. *Journal of Mechanisms and Robotics*, 12(5):054503, 05 2020. ISSN 1942-4302. doi: 10.1115/1.4046839.
- [94] Pierpaolo Palmieri, Mario Troise, Matteo Gaidano, Matteo Melchiorre, and Stefano Mauro. Inflatable robotic manipulator for space debris mitigation by visual servoing. In *2023 9th*

-
- International Conference on Automation, Robotics and Applications (ICARA)*, pages 175–179, 2023. doi: 10.1109/ICARA56516.2023.10125753.
- [95] Yu She, Zhaoyuan Gu, Siyang Song, Hai-Jun Su, and Junmin Wang. Design, Modeling, and Manufacturing of a Variable Lateral Stiffness Arm Via Shape Morphing Mechanisms. *Journal of Mechanisms and Robotics*, 13(3):031020, 03 2021. ISSN 1942-4302. doi: 10.1115/1.4050379.
- [96] Norgren. 3/2 solenoid valve, 2024. URL https://cdn.norgren.com/pdf/en_5_2_040_MICROSOL.pdf.
- [97] Freddy Caro and Marc G. Carmichael. Laminar jamming with trapezoidal pin mechanism for variable stiffness robotic arms. In *2022 IEEE International Conference on Robotics and Biomimetics (ROBIO)*, pages 1061–1066, 2022. doi: 10.1109/ROBIO55434.2022.10011709.
- [98] Xiangxiang Wang, Linyuan Wu, Bin Fang, Xiangrong Xu, Haiming Huang, and Fuchun Sun. Layer jamming-based soft robotic hand with variable stiffness for compliant and effective grasping. *Cognitive Computation and Systems*, 2(2):44–49. doi: <https://doi.org/10.1049/ccs.2020.0003>.